8-2016

3D Multi-Scale Behavior of Granular Materials using Experimental and Numerical Techniques

Andrew Michael Druckrey
University of Tennessee, Knoxville, adruckre@vols.utk.edu

To the Graduate Council:

I am submitting herewith a dissertation written by Andrew Michael Druckrey entitled "3D Multi-Scale Behavior of Granular Materials using Experimental and Numerical Techniques." I have examined the final electronic copy of this dissertation for form and content and recommend that it be accepted in partial fulfillment of the requirements for the degree of Doctor of Philosophy, with a major in Civil Engineering.

Khalid A. Alshibli, Major Professor

We have read this dissertation and recommend its acceptance:

Dayaker Penumadu, Angel Palomino, Eric C. Drumm

Accepted for the Council:
Dixie L. Thompson

Vice Provost and Dean of the Graduate School

(Original signatures are on file with official student records.)

3D Multi-Scale Behavior of Granular Materials using Experimental and Numerical Techniques

A Dissertation Presented for the

Doctor of Philosophy

Degree

The University of Tennessee, Knoxville

Andrew Michael Druckrey

August 2016

ACKNOWLEDGEMENTS

I would first and foremost like to express my sincere gratitude to my advisor, Dr. Khalid Alshibli. Dr. Alshibli has guided me in molding my technical, research, and personal skills that I will use for my entire lifetime. I am forever grateful to him for his mentorship through my graduate study. I would also like to thank my committee members Dr. Dayaker Penumadu, Dr. Angel Palomino, and Dr. Eric Drumm for the respected and highly regarded input towards this dissertation.

I would also like to thank Dr. Mark Rivers for all of his help during experiments at Advanced Photon Source, Riyadh Al-Raoush for his help in data analysis, the Department of Defense for financial support of the Multi-University Research Initiative (MURI) project that I was part of, and all of the MURI project and team members for their suggestions and guidance on my research.

I would also like to thank my colleagues at UT, family, and friends for their support and helping me to keep sane during my research.

ABSTRACT

Constitutive modeling of granular material behavior has generally been based on global response of laboratory-size specimens or larger models with little understanding of the fundamental mechanics that drive the global response. Many studies have acknowledged the importance of micro-scale and meso-scale mechanics on the constitutive behavior of granular materials. However, much knowledge is still missing to develop and improve robust micromechanical constitutive models. The research in this dissertation contributes to this knowledge gap for many potential applications using novel experimental techniques to investigate the three-dimensional (3D) behavior of granular materials. Critical micromechanics measurements at multiple scales are investigated by combining 3D synchrotron micro-computed tomography (SMT), 3D image analysis, and finite element analysis (FEA).

At the single particle level (micro-scale), particle fracture was examined at strain rates of 0.2 mm/min and 2 m/s using quasi-static unconfined compression, unconfined mini-Kolsky bar, and x-ray imaging techniques. Surface reconstructions of particles were generated and exported to Abaqus FEA software, where quasi-static and higher rate loading curves and crack propagation were simulated with good accuracy. Stress concentrations in oddly shaped particles during FEA simulations resulted in more realistic fracture stresses than theoretical models. A nonlinear multivariable statistical model was developed to predict force required to fracture individual particles with known internal structure and loading geometry.

At the meso-scale, 3D SMT imaging during in-situ triaxial testing of granular materials were used to identify particle morphology, contacts, kinematics and inter-particle behavior. Micro shear bands (MSB) were exposed during pre-peak stress using a new relative particle displacement concept developed in this dissertation. MSB for spherical particles (glass beads) had larger thickness ($3d_{50}$ to $5d_{50}$) than that of angular sands (such as F35 Ottawa sand, MSB thickness of $1d_{50}$ to $3d_{50}$). Particle morphology also plays a significant role in the onset and growth of shear bands and global fabric evolution of granular materials. More spherical particles typically exhibit more homogeneous internal anisotropy. Fabric of particles within the shear band (at higher densities and confining pressures) exhibits a peak and decrease into steady-state. Also, experimental fabric produces more accurate strength and deformation predictions in constitutive models that incorporate fabric evolution.

TABLE OF CONTENTS

LIST OF TABLES

LIST OF FIGURES

INTRODUCTION

Motivation

Constitutive models for granular materials have traditionally included global inputs such as laboratory or field scale testing measurements to define Mohr-Coulomb shear strength parameters, which is generally used in professional practice. Stress-dilatancy models have also been developed to better describe the behavior of sands (i.e. Bolton 1986). These types of classical models, however, are conservative and treat granular material as a continuum rather than an assembly of discrete particles that interact in a complex fashion across length scales. Particles align themselves to resist macro-scale loading, rotate and translate, and react in a multitude of other methods at various length scales for various loading conditions. A fundamental approach for better understanding of the strength and behavior of granular material is to determine and analyze mechanical behavior at smaller scales such as the meso-scale and the micro-scale (single particle scale).

Micromechanical modeling of granular material commences at assessing mechanical properties of individual particles, especially for loading conditions that involve high strain rates or stresses that cause particle fracture. Investigation of the fundamental mechanisms involved in particle fracture lead to a better understanding of the macro-scale behavior of the granular materials. In reference to particle fracture, this dissertation focuses on the influences of loading rate, particle morphology, and mineralogy on the fracture properties of individual particles. Synchrotron micro-computed tomography (SMT) imaging of the particles before and after fracture aids in

assessing mechanisms of fracture, as well as a method of integrating 3D particle shape into FEA modeling. FEA modeling provides means to analyze stresses within the particle before and during fracture.

Global behavior of granular materials is highly influenced by micro- and meso-scale behavior. The importance and significance of smaller scales is well established in the literature (e.g. Oda and Iwashita 1999; Hill and Selvadurai 2005). However, limited research that considers actual particle shapes using SMT imaging during in-situ loading has been published. High resolution SMT imaging allows for analysis of micromechanics of laboratory scale experiments at the meso-scale. Particle and contact measurements during in-situ loading are calculated and used to quantify particle kinematics and fabric. Tools were developed to extract properties from 3D experiments using SMT imaging and the data was used to provide a framework for developing micromechanical constitutive models that account for the fundamental mechanics of granular material.

Objectives

The main objectives of this dissertation are to: 1) Develop new tools to analyze real granular materials; 2) Characterize micromechanical material properties, particle kinematics, and interaction behavior; 3) Link behavior of granular materials across the micro- and meso-scales; and 4) Provide a basis for robust multi-scale constitutive modeling and implement findings into current models. These objectives are achieved by investigating the response of sand at various length scales using the following experimental and numerical techniques.

- **Micro-scale**: defined as properties involving a single particle that can be used to assess larger scale phenomena. Physical particle characteristics are quantified using SMT imaging. Particle fracture is investigated at various strain-rates using experimental and numerical techniques. This dissertation provides new information to the geotechnical engineering community regarding particle physical characteristics and fracture including:
    - Quantification of particle morphology (sphericity and roundness) using 3D images of particles.
    - A methodology to analyze real granular material particle fracture using SMT imaging and finite element analysis (FEA).
    - Accurate determination of particle tensile strengths for use in constitutive models involving particle fracture.
    - In-depth analyses of particle fracture mechanisms and the affect of particle morphology and mineralogy on particle fracture at various loading rates.
- **Meso-scale**: defined as properties involving interaction of particles that are in contact (particle-to-particle interactions), such as the contact network of granular material or particle kinematics (displacements and rotations). Meso-scale properties of granular material (such as strain localization or fabric) can be incorporated into micro-scale constitutive models for granular material. Micro-scale effects (such as particle morphology) is integrated into the analysis at the meso-scale. Specifically the objectives of the dissertation are to:

- Develop an accurate method for characterizing particle and contact properties, as well as develop computer code to track particles throughout triaxial testing.
- Develop a computer code to analyze strain localization within sheared granular materials and investigate onset and evolution of shear bands.
- Calculate fabric tensors of actual (not assumed) experimental granular material for use in micromechanical constitutive modeling.
- Incorporate experimental fabric evolution into current anisotropic critical state constitutive models.

Properties of granular material at the micro- and meso-scales influence the global macro-scale behavior, such as continuum strength and deformation. An overview of the research plan and dissertation objectives for single particle fracture and meso-scale properties of granular materials is presented in Figure I.1, which is generally divided into the two scales. The basis of commonality of this research is the utilization of 3D imaging techniques. Along the micro-scale track, 3D imaging of single particles before, during, and after fracture at various loading rates is employed to analyze fracture mechanisms and model real particle shapes. At the meso-scale, 3D imaging of axisymmetric triaxial experiments acts as the origin of quantitative analysis, which includes complex particle kinematics and fabric evaluation.

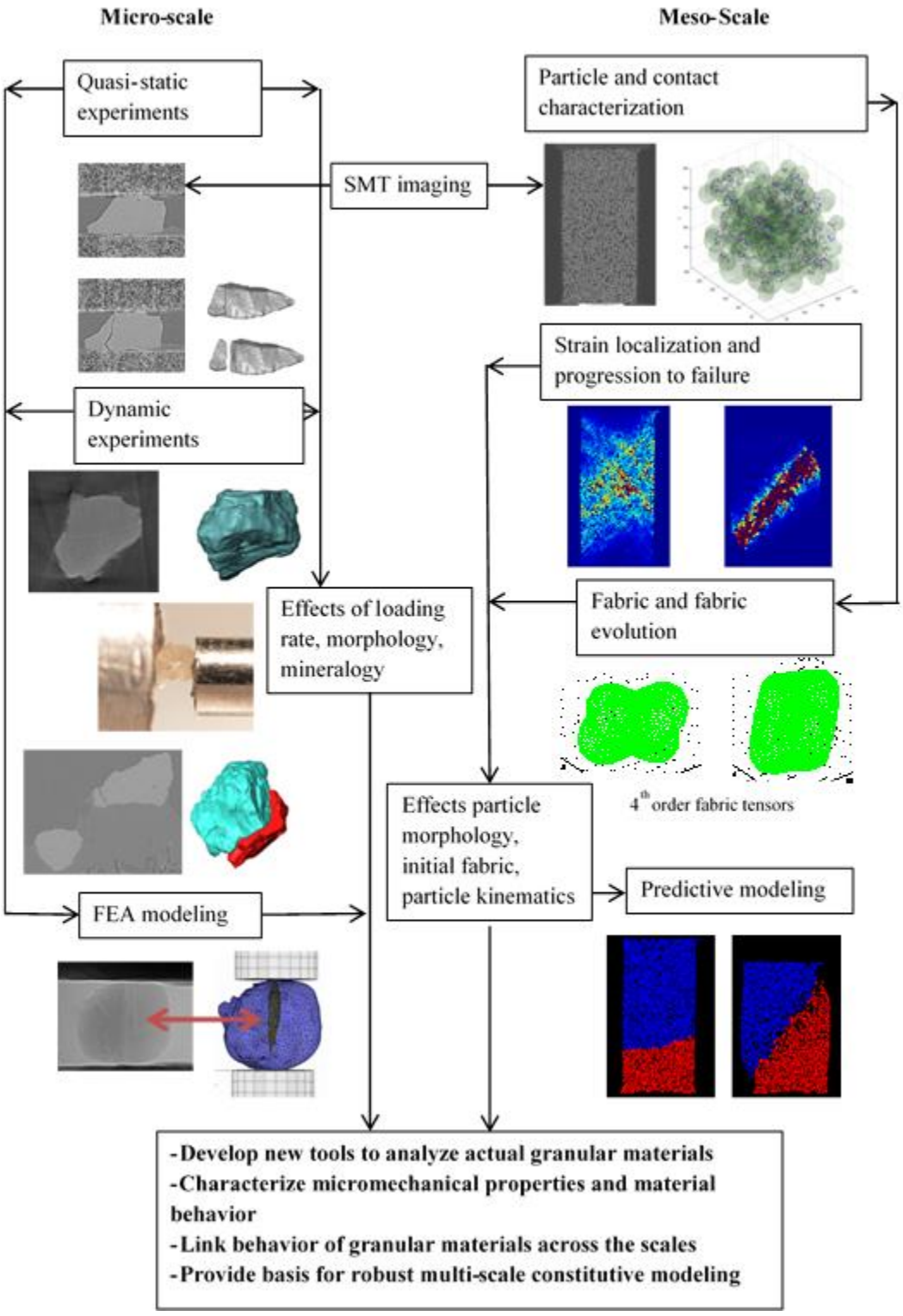

Figure I.1. Overview of proposed research and expected outcomes

Literature Review

The following sub-sections present a brief review of particle-scale fracture mechanics, characterization of particles and particle contacts, strain localization, and fabric evolution of granular materials. The importance of each aspect is established, as well as methodology to develop constitutive models based on these parameters. Knowledge gaps in the current published literature are described along with how the proposed research will fill the knowledge gap.

Particle-scale

Constitutive behavior of granular materials is highly influenced by the material properties at the micro-scale. For example, McDowell and Bolton (1998) updated the relative density index that was proposed by Bolton (1986) to include the mean tensile strength of particles, which provides an enhanced micromechanical insight into the dilatant behavior of crushable soils. Loading of a granular material causes particles to rearrange into force chains that carry the majority of the applied external stresses (Edwards and Grinev 1999; Yoshida 2005; Antony 2007; Tordesillas and Muthuswamy 2009; Maeda et al. 2010). As the applied compressive stresses increase, force chains transmit larger forces between particles, eventually leading to particle fracture within the force chains (Peters et al. 2005; Cooper 2011; Wang et al. 2011; Cil and Alshibli 2014). The first step for modeling particle fracture within force chains in a granular material using actual particle morphology is to model and understand the micromechanics of compression and fracture of individual particles.

Quasi-static particle fracture

Fracture mechanics of particles when subjected to quasi-static compression is controlled by several mechanisms. Particle morphology (texture, shape, and sphericity) is a primary determinant of fracture strength. The mechanics of loading of an irregularly shaped particle differs from loading of a sphere such that during uniaxial compression of a single particle, such that a sphere has one contact at each loading plate while a real particle may have multiple. Mechanics of irregular particles during uniaxial compression has been thoroughly investigated in the literature (e.g. Shipway and Hutchings 1993; McDowell and Bolton 1998; Cavarretta and O'Sullivan 2012; Zhao et al. 2015). Many theories and approaches have been reported in the literature to describe quasi-static particle fracture. The most common approach is to relate the failure stress within the particle to the applied failure force and particle size (or flaw size, if a flaw is present). McDowell and Bolton (1998) presented a study of the micromechanical behavior of crushable soils and found that tensile strengths of particles of different size and mineralogy are consistent with Weibull statistics of brittle fracture. Brzesowsky et al. (2011) developed theoretical models that describe particle strength using Weibull statistics based on data that were collected from experiments. Cavarretta and O'Sullivan (2012) used a micromechanical approach to describe the compression of individual particles and developed models that incorporated frictional sliding, bulk particle compression, and fragmentation based on geometry and kinematic degradation of stiffness.

Most of the published research has included statistical descriptions of failure or assumed particle geometries and has not integrated real particle morphology into failure determination of individual particles. Alshibli et al. (2013) used 3D x-ray diffraction to measure strains within individual silica particles in compression and calculated stresses based on particle strain, inherently incorporating experimental particle shape. Druckrey and Alshibli (2015) used 3D SMT during in-situ compression of sand particles to model particle fracture using the extended finite element method (XFEM), capturing actual particle shapes through image processing and importing into FEA software. Zhao et al. (2015) used x-ray CT to thoroughly investigate sand particle fracture and found that initial particle morphology, heterogeneity, and mineralogy are important factors that influence fracture patterns.

Based on current research available in the literature for quasi-static particle fracture, there are knowledge gaps that are filled by this study. Analyzing particle stresses and fracture of real particle shapes (not assumed) using FEA has not be published by others in the literature. Analysis that incorporates real particle shapes will lead to more accurate determination of particle failure strength than what is currently known and methodology to predict fracture propagation in irregularly shaped particles.

Particle fracture under dynamic loading

Fracture and progressive comminution (reduction to minute fragments) of sand particles is well known to affect the constitutive and deformation behavior of granular materials during quasi-static loading as well as high-rate loading conditions (Allen et al.

1957; Cooper and Breaux 2010; Antoun 2012; Iskander et al. 2015). During blast loading, energy dissipates partially through sand particle fracture and comminution (Braslau 1970; Børvik et al. 2011). Fracture of individual particles could affect the dynamic behavior of the ejecta resulting from buried explosives (Regueiro et al. 2014) and therefore affect the loading applied to an object such as an armored vehicle. Particle fracture occurs in many other high strain rate loadings on granular materials such as projectile penetration into sand (Allen et al. 1957; Cole 2010; Cooper and Breaux 2010), drilling and mining applications, and impact such as dynamic compaction. Assessing dynamic properties of fracture at the particle level is an essential step in understanding the behavior of bulk granular materials that experience high strain rates and plays a critical role in improving design against such dynamic forces.

As described earlier, behavior of granular materials is highly influenced by the material properties at the micro-scale (particle scale). For example, particle shape influences granular material packing density, stiffness, and strength (Cho et al. 2006). However, little is known about the micromechanics of granular materials, especially when they are subject to high strain rates. High-rate experimental fracture testing of individual sand particles provides the initial particle-scale information that can be used in dynamic modeling across the scales. In particular, high-rate tests can be used to calibrate and validate high fidelity particle-scale poly-ellipsoidal discrete element models (DEM) that include particle fracture, which in turn can be used to develop lower fidelity soil blast models at larger scale to replace costly and time consuming full scale testing (Antoun

2012). Important input parameters to the particle-scale DEM include particle shape, loading direction, fracture strength, and fracture mode resulting from dynamic loading.

Although the importance of particle fracture during dynamic loading is well-known (Allen et al. 1957; Braslau 1970; Cole 2010; Cooper and Breaux 2010), very little research on the dynamic fracture behavior of individual sand particles has been published. Some researchers have investigated the high strain rate behavior of sand using techniques such as the split-Hopkinson pressure bar (SHPB) on laboratory-scale specimens (Charlie et al. 1990; Martin et al. 2009; Luo et al. 2011). Luo et al. (2011) found that the grain size distribution shifted significantly, suggesting that many particles fractured during SHPB testing at high strain rates.

Few studies have been published concerning the behavior of single particle failure under dynamic loading. Recently, Parab et al. (2014) used a mini-Kolsky bar to dynamically compress confined particles during in-situ high speed phase contrast imaging (PCI). Two approximately spherical Ottawa sand particles were placed in an aluminum housing and were subjected to dynamic loading while 2D radiographs and load versus time data were collected. Visual assessments of damage propagation were conducted and when particles were tested under dry conditions, and one of the two particles had extensive interfacial cracking before pulverization. Wet sand particles broke into relatively large fragments followed by pulverization.

The published literature regarding dynamic fracture of single particles is limited. Very little research has been published involving dynamic experimental fracture of single

particles. Data in the literature is limited to few tests with confined loading of semi-spherical particles. This study will contribute to the body of knowledge by including higher loading rate experiments on single particles and analysis of loading rate and micro-scale properties on observed fracture loads. FEA modeling of dynamic fracture of individual particles is presented and stresses experienced during dynamic compression are compared to theoretical stresses within particles.

Meso-scale Behavior

Particle gradation, mineralogy, morphology, and contacts are major factors that contribute to the fabric of granular materials and to a rather complex interaction between particles, which traditionally has been difficult to analyze at the micro-scale. Accurate characterization of particles and their interaction is essential for the development of micromechanics-based constitutive models for granular materials. X-ray CT image acquisition and processing has greatly advanced the quantification of different engineering properties of granular materials.

Characterization of particles and particle contacts

Extensive research has been published to quantify individual particle characteristics such as particle size, shape, spatial coordinates, and orientation using both 2D and 3D CT imaging (Thompson et al. 2006; Al-Raoush 2007; Cox and Budhu 2008; Bloom et al. 2009; Cnudde and Boone 2013; Alshibli et al. 2014). Recently, particle-to-particle contacts and evolution of the contacts during loading are considered as important

factors in fabric evolution and force transmission in granular materials. Few researchers have developed methods to determine particle coordination number (CN) and track the CN of individual particles as a test progresses based on CT and SMT imaging. However, identifying particle contacts and their spatial coordinates do not provide full insight into how particles interact with neighboring particles. A more comprehensive definition of contact would include location as well as orientation of the contact in 3D space. Moreover, calculating the location of the contact and the normal and tangential directions to the contact would provide the necessary measurements to quantitatively define the contact between two particles. Only few experimental studies have proposed a method to quantify particle contact orientation. Viggiani et al. (2013) presented a method to determine the orientation of contact based on CT particles composed of voxels (~5000 voxels per particle) by fitting a plane to the contact voxels between two particles. The distribution of the normal unit vector varies based on the type of algorithm that was used to separate particles. Vlahinić et al. (2014) used mathematical level set functions on the greyscale 3D x-ray CT image to determine the orientation of a given contact.

Particle kinematics and strain localization into shear bands

Particle translation and rotation have a significant influence on the constitutive behavior of granular materials (Oda et al. 1997; Hall et al. 2010; Hasan and Alshibli 2012). Resistance to sliding and rolling between particles is the major contributor to shear strength of granular materials, and incorporating their contribution into constitutive models has yielded better predictions of the behavior of granular materials (Tordesillas

and Walsh 2002; Anandarajah 2004). Accurate experimental quantification of particle kinematics during shearing will be a significant contribution to constitutive and numerical modeling.

Tracking the displacement and rotation fields of particles has drawn extensive research in recent years. X-ray micro-tomography imaging during in-situ testing has aided researchers in the ability to track localized displacement and rotation within experimental specimens in 3D. Digital image correlation (DIC) and digital volume correlation (DVC) based on experimental imaging has been used to determine localized deformation and rotation of granular materials, particularly near and within the shear band (Rechenmacher 2006; Sjödahl et al. 2012). However, DIC and DVC present a continuum approach to the deformation and rotation fields within a sample, ignoring the discrete particle kinematics and interaction that occurs between particles.

Furthermore, research focusing on evolution of particle kinematics while subjecting granular mass to in-situ loading has been investigated using x-ray CT. For example, Hasan and Alshibli (2010) used SMT to image a plane strain specimen, quantified particle orientation within the shear band, and assessed particle-to-particle interaction. Hall et al. (2010) acquired multiple in situ CT images of a triaxial specimen composed of Hostun RF sand, discretized particles, and analyzed discrete and continuum deformation within the specimen. Andò et al. (2012) expanded on Hall's approach and developed the ID-Track computer code to quantify particle kinematics at multiple loading stages for many particles within triaxial specimens composed of Hostun RF (angular) and

Caicos Ooid (rounded) sands. Similarly, Druckrey and Alshibli (2014) developed an algorithm to track kinematics of ASTM 20-30 sand based on SMT images during triaxial testing. The failure shear band in many different granular materials has been well defined and analyzed in the literature based on particle kinematics; however, a comprehensive understanding of the formation of localized shearing during pre-peak loading and specimen bulging is still lacking.

Although the transformation of strain localization into specimen failure via shear band during softening and critical states based on particle kinematics has been well-studied, no investigation exists into the many localized preliminary shear bands that develop during the hardening regime and progress into the final failure shear band. Also, internal strain localization during specimen bulging has not been investigated. This information is new to the geotechnical engineering community and will prove useful in bifurcation analysis of granular materials.

Fabric and fabric evolution in granular materials

Fabric of a granular material is a general term that characterizes microstructure at the meso-scale. The micromechanical fabric of granular materials has a profound influence on their global mechanical and hydraulic behavior (Oda 1972). Fabric tensors are commonly used as a metric to quantitatively describe granular material fabric in tensorial form. Directional data, such as contact normal vectors, can be characterized by fabric tensors and several definitions have been proposed in the literature. Kanatani (1984) established methods for mathematically quantifying tensors that describe

directional data distributions and applied them to characterize inter-particle contact distribution in granular materials. Many researchers have adopted a form of Kanatani's fabric tensor of the first kind, or moment tensor, and have applied it to characterize the fabric of granular materials based on various geometrical features (Liou and Pan 2003; Fonseca et al. 2013; Li and Yu 2014; Fu and Dafalias 2015).

Extensive research has been published emphasizing the effect of fabric on mechanical properties granular material, such as strength and dilatancy, for many loading conditions. Oda (1972) varied sample preparation methods to vary the fabric, fixed the specimens with resin and quantified fabric of different soils based on thin sections. Effects of the initial fabric on deformation behavior and shear strength of soils were analyzed and found that the different initial fabrics of the same sand greatly influence mechanical properties of mobilized strength, dilatancy rate, and secant deformation modulus. Similarly, Mehrabadi et al. (1982) observed that it is easier to relate the fabric tensor and its elements to macroscopic quantities than to relate stress directly to kinematic quantities. More recently, the discrete element method (DEM) has been utilized to investigate the effect of fabric on macroscopic properties of granular material. Yimsiri and Soga (2001) found that DEM soil fabric has a profound influence on the undrained behavior of sand and Yimsiri and Soga (2010) found that sand becomes stiffer, stronger, and more dilative when sheared in the direction of particle contact normal. Many others have also used DEM to investigate effects of granular material fabric on various properties (e.g. Theocharis et al. (2014), Yang et al. (2014)).

Constitutive behavior of granular materials can be modeled based on the micromechanics defined by fabric tensors. Several research studies have derived relationships between macro-scale measurements, such as global stress and dilatancy, and fabric of granular material during loading. Mehrabadi and Nemat-Nasser (1983) derived a general dilatancy model that directly involves branch vectors as a measure of fabric and successfully relates their derivations to experimental results found in the literature. Nemat-Nasser (2000) developed a 2D micromechanics based constitutive model for frictional deformation of granular material with four material functions, one of which is a parameter defines the evolution of the fabric tensor. Nemat-Nasser and Zhang (2002) furthered this approach for the 3D deformation and dilatant behavior of granular material and found that the model produced results in reasonable agreement with experimental observations. Li and Yu (2013) mathematically derived a stress-force-fabric relationship for accurately predicting the stress state for 2D DEM granular materials.

Accurate prediction of constitutive behavior of granular materials based on fabric approaches would require knowledge of 3D fabric in actual granular materials. Most studies focus on granular material fabric using 2D or DEM approaches, neither of which can fully integrate actual particle shape and contacts. Of the many studies of granular material fabric, few have directly measured the 3D fabric of granular material and investigated fabric evolution during loading. Fonseca et al. (2013) used CT and image analysis tools to investigate stress transmission in granular materials by extracting cores from triaxial specimens impregnated with resin. Stershic et al. (2015) modeled the

evolution of ion particle contact in a battery using a fabric tensor approach. They used CT scans to develop fabric tensors based on spherical and ellipsoidal approximations of particles and analyzed fabric tensor evolution with increasing pressure on the particles. However, very little research has been published on the experimental 3D measurement of granular material fabric during in-situ SMT.

A limited literature exists that incorporates full 3D experimental fabric tensor analysis of actual granular material during in-situ loading. Incorporation of measured fabric and fabric tensors calculated based on measured 3D fabric would lead to more accurate fabric-based micromechanical constitutive models involving granular material. This study quantifies experimental fabric evolution during triaxial compression and incorporates the evolution into a constitutive model defined in the literature (Li and Dafalias 2011).

Dissertation Outline

This dissertation is composed of Chapters focusing on individual components described earlier that fulfill the overall objectives. Versions of each Chapter either has been or will be published in peer-reviewed technical journals. Chapters 1 and 2 involve SMT characterization of granular material. Chapters 3 and 4 present single particle fracture experimentation and modeling. Chapters 5 through 7 encompass analysis and modeling of triaxial compression using SMT imaging. A brief summary of each Chapter is presented as follows.

Chapter 1 presents a detailed methodology of 3D SMT imaging and image processing. Details of image processing for discretization of individual particles are presented, as well as micro-scale particle and contact quantification. Imaging, image processing, and measurements of granular material described in Chapter 1 are used throughout the dissertation.

Chapter 2 presents morphology (sphericity and roundness) and surface roughness quantification of granular materials that were used in this dissertation. These measurements are related to observed responses and were used as input to statistical models in Chapters 4 and 7. chapters.

Chapter 3 presents methodology for quasi-static unconfined compression of single particles using FEA that incorporates real particle shape. The extended finite element method (XFEM) is used to simulate crack initiation and propagation. Results are compared with ideal spherical particles.

Chapter 4 presents unconfined compression of individual particles at higher loading rates using mini-Kolsky bar techniques. A statistical model is developed to predict fracture force based on micro-scale characteristics and loading geometry. FEA fracture analysis at observed loading rates is conducted and fracture stresses are compared with theoretical results.

Chapter 5 presents an extension of traditional particle kinematics that exposes intricate zones of localized shearing during the hardening phase of axisymmetric triaxial

compression and the subsequent evolution of localized strain into the final shear band. Influence of particle morphology on shearing behavior is assessed and discussed.

Chapter 6 includes quantification of fabric and subsequent evolution during axisymmetric triaxial compression. Contact normal vectors are quantified (Chapter 1) and employed in fabric quantification of granular materials for incorporation into a current constitutive model.

Chapter 7 builds on the work of Chapter 6 and incorporates experimental fabric evolution into the anisotropic critical state theory (ACST) model. Model prediction accuracies are compared with theoretical fabric evolution.

References

Al-Raoush, R. (2007). "Microstructure characterization of granular materials." *Physica A: Statistical Mechanics and its Applications*, 377(2), 545-558.

Allen, W. A., Mayfield, E. B., and Morrison, H. L. (1957). "Dynamics of a Projectile Penetrating Sand." *Journal of Applied Physics*, 28(3), 370-376.

Allen, W. A., Mayfield, E. B., and Morrison, H. L. (1957). "Dynamics of a Projectile Penetrating Sand. Part II." *Journal of Applied Physics*, 28(11), 1331-1335.

Alshibli, K., Cil, M., Kenesei, P., and Lienert, U. (2013). "Strain tensor determination of compressed individual silica sand particles using high-energy synchrotron diffraction." *Granular Matter*, 1-14.

Alshibli, K., Druckrey, A., Al-Raoush, R., Weiskittel, T., and Lavrik, N. (2014). "Quantifying Morphology of Sands Using 3D Imaging." *Journal of Materials in Civil Engineering*, 04014275.

Anandarajah, A. (2004). "Sliding and Rolling Constitutive Theory for Granular Materials." *Journal of Engineering Mechanics*, 130(6), 665-680.

Andò, E., Hall, S., Viggiani, G., Desrues, J., and Bésuelle, P. (2012). "Grain-scale experimental investigation of localised deformation in sand: a discrete particle tracking approach." *Acta Geotechnica*, 7(1), 1-13.

Antony, S. J. (2007). "Link between single-particle properties and macroscopic properties in particulate assemblies: role of structures within structures." *Phil. Trans. R. Society*, 365, 12.

Antoun, T., Herbold, E., Johnson, S. (2012). "Dynamic Behavior of Sand: Annual Report FY 11." Lawrence Livermore National Laboratory.

Bloom, M., Russell, M., Kustau, A., Mandayam, S., and Sukumaran, B. "An X-ray computed tomography technique for the measurement of packing density in granular particles." *Proc., Instrumentation and Measurement Technology Conference, 2009. I2MTC '09. IEEE*, 74-79.

Bolton, M. D. (1986). "The strength and dilatancy of sands." *Geotechnique*, 36, 65-78.

Børvik, T., Olovsson, L., Hanssen, A. G., Dharmasena, K. P., Hansson, H., and Wadley, H. N. G. (2011). "A discrete particle approach to simulate the combined effect of blast and sand impact loading of steel plates." *Journal of the Mechanics and Physics of Solids*, 59(5), 940-958.

Braslau, D. (1970). "Partitioning of energy in hypervelocity impact against loose sand targets." *Journal of Geophysical Research*, 75(20), 3987-3999.

Brzesowsky, R. H., Spiers, C. J., Peach, C. J., and Hangx, S. J. T. (2011). "Failure behavior of single sand grains: Theory versus experiment." *Journal of Geophysical Research: Solid Earth*, 116(B6), B06205.

Cavarretta, I., and O'Sullivan, C. (2012). "The mechanics of rigid irregular particles subject to uniaxial compression." *Geotechnique*, 62(8), 11.

Charlie, W. A., Ross, C. A., and Pierce, S. J. (1990). "Split-Hopkinson Pressure Bar Testing of Unsaturated Sand." *Geotech. Test. J.*, 13(4), 291.

Cho, G.-C., Dodds, J., and Santamarina, J. C. (2006). "Particle Shape Effects on Packing Density, Stiffness, and Strength: Natural and Crushed Sands." *Journal of Geotechnical and Geoenvironmental Engineering*, 132(5), 591-602.

Cil, M. B., and Alshibli, K. A. (2014). "3D evolution of sand fracture under 1D compression." *Géotechnique*, 351-364.

Cnudde, V., and Boone, M. N. (2013). "High-resolution X-ray computed tomography in geosciences: A review of the current technology and applications." *Earth-Science Reviews*, 123(0), 1-17.

Cole, R. P. (2010). "Ballistic Penetration of a Sandbagged Redoubt Using Silica Sand and Pulverized Rubber of Various Grain Sizes." M.S.M.E., University of South Florida.

Cooper, W. (2011). "Communication of Stresses by Chains of Grains in High-Speed Particulate Media Impacts." *Dynamic Behavior of Materials, Volume 1*, T. Proulx, ed., Springer New York, 99-107.

Cooper, W., and Breaux, B. (2010). "Grain fracture in rapid particulate media deformation and a particulate media research roadmap from the PMEE workshops." *International Journal of Fracture*, 162(1-2), 137-150.

Cox, M. R., and Budhu, M. (2008). "A practical approach to grain shape quantification." *Engineering Geology*, 96(1–2), 1-16.

Druckrey, A., and Alshibli, K. (2014). "3D Behavior of Sand Particles Using X-Ray Synchrotron Micro-Tomography." *Geo-Congress 2014 Technical Papers*, 2814-2821.

Druckrey, A. M., and Alshibli, K. A. (2015). "3D finite element modeling of sand particle fracture based on in situ X-Ray synchrotron imaging." *International Journal for Numerical and Analytical Methods in Geomechanics*.

Edwards, S. F., and Grinev, D. V. (1999). "The statistical-mechanical theory of stress transmission in granular materials." *Physica A: Statistical Mechanics and its Applications*, 263(1–4), 545-553.

Fonseca, J., O'Sullivan, C., Coop, M. R., and Lee, P. D. (2013). "Quantifying the evolution of soil fabric during shearing using directional parameters." *Géotechnique*, 487-499.

Fu, P., and Dafalias, Y. F. (2015). "Relationship between void- and contact normal-based fabric tensors for 2D idealized granular materials." *International Journal of Solids and Structures*, 63(0), 68-81.

Hall, S. A., Bornert, M., Desrues, J., Pannier, Y., Lenoir, N., Viggiani, G., and BéSuelle, P. (2010). "Discrete and continuum analysis of localised deformation in sand using X-ray mCT and volumetric digital image correlation." *Geotechnique*, 315-322.

Hasan, A., and Alshibli, K. (2012). "Three dimensional fabric evolution of sheared sand." *Granular Matter*, 14(4), 469-482.

Hasan, A., and Alshibli, K. A. (2010). "Experimental assessment of 3D particle-to-particle interaction within sheared sand using synchrotron microtomography." *Géotechnique*, 369-379.

Hill, J. M., and Selvadurai, A. P. S. (2005). "Mathematics and mechanics of granular materials." *Mathematics and Mechanics of Granular Materials*, J. M. Hill, and A. P. S. Selvadurai, eds., Springer Netherlands, Dordrecht, 1-9.

Iskander, M., Omidvar, M., and Bless, S. (2015). "Chapter 2 - Behavior of Granular Media Under High Strain-Rate Loading." *Rapid Penetration into Granular Media*, Elsevier, Oxford, 11-63.

Kanatani, K.-I. (1984). "Distribution of Directional Data and Fabric Tensors." *Int. J. Engng Sci.*, 22(2), 149-164.

Li, X., and Dafalias, Y. (2011). "Anisotropic Critical State Theory: Role of Fabric." *Journal of Engineering Mechanics*, 138(3), 263-275.

Li, X., and Yu, H.-S. (2014). "Fabric, force and strength anisotropies in granular materials: a micromechanical insight." *Acta Mech*, 225(8), 2345-2362.

Li, X., and Yu, H. S. (2013). "On the stress–force–fabric relationship for granular materials." *International Journal of Solids and Structures*, 50(9), 1285-1302.

Liou, J.-C., and Pan, Y.-W. (2003). "Fabric evolution of granular assembly under K0 loading/unloading." *International Journal for Numerical and Analytical Methods in Geomechanics*, 27(13), 1099-1122.

Luo, H., Lu, H., Cooper, W. L., and Komanduri, R. (2011). "Effect of Mass Density on the Compressive Behavior of Dry Sand Under Confinement at High Strain Rates." *Exp Mech*, 51(9), 1499-1510.

Maeda, K., Sakai, H., Kondo, A., Yamaguchi, T., Fukuma, M., and Nukudani, E. (2010). "Stress-chain based micromechanics of sand with grain shape effect." *Granular Matter*, 12(5), 499-505.

Martin, B. E., Chen, W., Song, B., and Akers, S. A. (2009). "Moisture effects on the high strain-rate behavior of sand." *Mechanics of Materials*, 41(6), 786-798.

McDowell, G. R., and Bolton, M. D. (1998). "On the micromechanics of crushable aggregates." *Geotechnique*, 667-679.

Mehrabadi, M. M., and Nemat-Nasser, S. (1983). "Stress, dilatancy and fabric in granular materials." *Mechanics of Materials*, 2(2), 155-161.

Mehrabadi, M. M., Nemat-Nasser, S., and Oda, M. (1982). "On statistical description of stress and fabric in granular materials." *International Journal for Numerical and Analytical Methods in Geomechanics*, 6(1), 95-108.

Nemat-Nasser, S. (2000). "A micromechanically-based constitutive model for frictional deformation of granular materials." *Journal of the Mechanics and Physics of Solids*, 48(6–7), 1541-1563.

Nemat-Nasser, S., and Zhang, J. (2002). "Constitutive relations for cohesionless frictional granular materials." *International Journal of Plasticity*, 18(4), 531-547.

Oda, M. (1972). "Initial fabrics and their relations to mechanical properties of granular material." *Soils and foundations*, 12(1), 17-36.

Oda, M., and Iwashita, K. (1999). *Mechanics of granular materials: An introduction*, A.A. Balkema, Rotterdam, Netherlands.

Oda, M., Iwashita, K., and Kakiuchi, T. (1997). "Importance of particle rotation in the mechanics of granular materials." *Proc., Powder and Grains*, A A Balkema Publishers, Rotterdam, Netherlands, 207-210.

Parab, N. D., Claus, B., Hudspeth, M. C., Black, J. T., Mondal, A., Sun, J., Fezzaa, K., Xiao, X., Luo, S. N., and Chen, W. (2014). "Experimental assessment of fracture of individual sand particles at different loading rates." *International Journal of Impact Engineering*, 68, 8-14.

Peters, J. F., Muthuswamy, M., Wibowo, J., and Tordesillas, A. (2005). "Characterization of force chains in granular material." *Physical Review E*, 72(4), 041307.

Rechenmacher, A. L. (2006). "Grain-scale processes governing shear band initiation and evolution in sands." *Journal of the Mechanics and Physics of Solids*, 54(1), 22-45.

Regueiro, R., Pak, R., McCartney, J., Sture, S., Yan, B., Duan, Z., Svoboda, J., Mun, W., Vasilyev, O., Kasimov, N., Brown-Dymkoski, E., Hansen, C., Li, S., Ren, B., Alshibli, K., Druckrey, A., Lu, H., Luo, H., Brannon, R., Bonifasi-Lista, C., Yarahmadi, A., Ghodrati, E., and Colovos, J. (2014). "ONR MURI Project on Soil Blast Modeling and Simulation." *Dynamic Behavior of Materials, Volume 1*, B.

Song, D. Casem, and J. Kimberley, eds., Springer International Publishing, 341-353.

Shipway, P. H., and Hutchings, I. M. (1993). "Attrition of brittle spheres by fracture under compression and impact loading." *Powder Technology*, 76(1), 23-30.

Sjödahl, M., Siviour, C. R., and Forsberg, F. (2012). "Digital Volume Correlation Applied to Compaction of Granular Materials." *Procedia IUTAM*, 4(0), 179-195.

Stershic, A. J., Simunovic, S., and Nanda, J. (2015). "Modeling the evolution of lithium-ion particle contact distributions using a fabric tensor approach." *Journal of Power Sources*, 297, 540-550.

Theocharis, A., Vairaktaris, E., Fu, P., and Dafalias, Y. F. (2014). "Comparison of fabric tensors for granular materials." *Geomechanics from Micro to Macro*, K. Soga, K. Kumar, G. Biscontin, and M. Kuo, eds., CRC Press, 153-158.

Thompson, K. E., Willson, C. S., and Zhang, W. (2006). "Quantitative computer reconstruction of particulate materials from microtomography images." *Powder Technology*, 163(3), 169-182.

Tordesillas, A., and Muthuswamy, M. (2009). "On the modeling of confined buckling of force chains." *Journal of the Mechanics and Physics of Solids*, 57(4), 706-727.

Tordesillas, A., and Walsh, D. C. S. (2002). "Incorporating rolling resistance and contact anisotropy in micromechanical models of granular media." *Powder Technology*, 124(1–2), 106-111.

Viggiani, G., Andò, E., Jaquet, C., and Talbot, H. (2013). "Identifying and following particle-to-particle contacts in real granular media: An experimental challenge." *AIP Conference Proceedings*, 1542(1), 60-65.

Vlahinić, I., Andò, E., Viggiani, G., and Andrade, J. (2014). "Towards a more accurate characterization of granular media: extracting quantitative descriptors from tomographic images." *Granular Matter*, 16(1), 9-21.

Wang, Z., Yang, X., Chen, Q., Zhang, Y., and Zhao, Y. "Study of the contact forces and grain size distribution during grain crushing." *Proc., Multimedia Technology (ICMT), 2011 International Conference on*, 2617-2622.

Yang, D. S., Li, X., and Yu, H. S. (2014). "Fabric evolution of 3D granular materials in rotational shear." *Geomechanics from Micro to Macro*, CRC Press, 85-90.

Yimsiri, S., and Soga, K. (2001). "Effects of Soil Fabric on Undrained Behavior of Sands." *International Conferences on Recent Advances in Geotechnical Earthquake Engineering and Soil Dynamics*San Diego, CA.

Yimsiri, S., and Soga, K. (2010). "DEM analysis of soil fabric effects on behaviour of sand." *Géotechnique*, 483-495.

Yoshida, Y. (2005). "Force chains and the fragmentation of granular materials." MSCE Master's Thesis, University of Pittsburgh.

Zhao, B., Wang, J., Coop, M., Viggiani, G., and Jiang, M. (2015). "An investigation of single sand particle fracture using X-ray micro-tomography." *Géotechnique*, 65(8), 625-641.

CHAPTER 1

3D CHARACTERIZATION OF SAND PARTICLE-TO-PARTICLE CONTACT AND MORPHOLOGY

A version of this chapter was originally published in: Druckrey, A. M., Alshibli, K. A., and Al-Raoush, R. I. (2016). "3D characterization of sand particle-to-particle contact and morphology." *Computers and Geotechnics*, 74, 26-35.

My primary contributions to this paper include (i) conduction of experiments as well as acquisition and processing 3D SMT images, (ii) modification of quantification code and assistance in porting to C++ programming language, (iii) verification and validation of code output, (iv) most of the writing.

Abstract

Particle morphology, orientation, and contact configuration play a significant role in the engineering properties of granular materials. Accurate three-dimensional (3D) characterization of these parameters for experiments has historically proven difficult, especially in the context of particle contact with small particle size. This paper describes a computer code that was developed to analyze 3D images of granular materials to measure particle lengths (size), volume, surface area, global centroid location and orientation; it also provides a method to calculate particle contact location and orientation. Measurements from the proposed code can define a state of the granular material's fabric that can be used as input for micro-mechanics based constitutive models and to validate numerical discrete element simulations. A fabric tensor and its evolution is calculated based on experimental contact normal vectors that were extracted from SMT imaging of an axisymmetric triaxial compression experiment on a natural silica sand known as F-35 sand.

Introduction

Granular materials are composed of discrete particles that interact with each other in a complex fashion. Particle gradation, mineralogy, morphology, and contacts are the major factors that contribute to the fabric of granular materials and to rather a complex interaction between particles and mechanical properties, which is difficult to analyze at the micro-scale. Accurate characterization of particles and their interaction is essential for the development of micro-mechanics based constitutive models for granular materials. X-ray computed tomography (CT) image acquisition and processing has greatly advanced the quantification of different engineering properties of granular materials.

Extensive research has been published to quantify individual particle characteristics such as particle size, shape, spatial coordinates, and orientation using both 2D and 3D CT imaging (e.g. Thompson et al. (2006); Al-Raoush (2007); Cox and Budhu (2008); Bloom et al. (2009); Cnudde and Boone (2013); Alshibli et al. (2014)). Furthermore, research focusing on fabric evolution while subjecting granular mass to in situ loading has been investigated using x-ray CT. For example, Hasan and Alshibli (2010) used synchrotron micro-computed tomography (SMT) to image a plane strain specimen, quantified particle orientation within the shear band, assessed particle-to-particle interaction. Hall et al. (2010) acquired multiple in situ CT images of a triaxial specimen composed of Hostun RF sand, discretized particles, and analyzed discrete and continuum deformation within the specimen. Andò et al. (2012) expanded on Hall's approach and developed ID-Track computer code to quantify particle kinematics at

multiple loading stages for many particles within triaxial specimens composed of Hostun RF (angular) and Caicos Ooid (rounded) sands. Similarly, Druckrey and Alshibli (2014) developed an algorithm to track kinematics of ASTM 20-30 sand based on SMT images during triaxial testing.

Recently, particle-to-particle contact and evolution of contact are considered as important factors in fabric evolution and force transmission in granular materials. Few researchers have developed methods to determine particle coordination number (CN) and track the CN of individual particles as test progresses based on CT and SMT imaging. However, identifying particle contact and its spatial coordinates do not provide full insight into how particles interact with neighboring particles. A more comprehensive definition would include location as well as orientation of contact in 3D space. Moreover, calculating the location of contact and the normal and tangential directions to contact would provide the necessary measurements to quantitatively define the contact between two particles. Few experimental studies have been proposed to quantify particle contact orientation. Viggiani et al. (2013) presented a method to determine the orientation of contact based on CT particles composed of voxels (~5000 voxels per particle) by fitting a plane to the contact voxels between two particles, in which the distribution of the normal unit vector varies based on the type of algorithm that was used to separate particles. Vlahinić et al. (2014) used mathematical level set functions on the greyscale 3D x-ray CT image to determine the orientation of contact.

Directional data, such as contact normal vectors, can be characterized by fabric tensors and several definitions have been proposed in the literature. Oda (1972) discussed the initial fabric of granular materials and how it relates to their mechanical properties. Kanatani (1984) established methods for mathematically quantifying tensors that describe directional data distributions and applied them to characterize inter-particle contact distribution in granular materials. Many researchers have adopted a form of Kanatani's fabric tensor of the first kind, or moment tensor, and have applied it to characterize the fabric of granular materials based on various geometrical features. Oda et al. (1985) used fabric tensors to investigate stress-induced anisotropy in granular masses of biaxial compression tests of oval rods using photo-elastic pictures and contact normals. Others have used discrete element method to investigate effects of granular material fabric on various properties (e.g. Yimsiri and Soga (2010), Theocharis et al. (2014), Yang et al. (2014)). Fonseca et al. (2013) used CT and image analysis tools to investigate stress transmission in granular materials by extracting cores from triaxial specimens impregnated with resin.

The accuracy of the current methods relies heavily on the resolution of the CT/SMT images, especially sharpness at particle boundaries (phase contrast). Blurry particle edges/contacts make it difficult to determine voxels that belong to a particular particle during particle separation. Industrial x-ray CT imaging produces unclear particle boundaries and questionable contact orientations. This paper presents a method that utilizes high-resolution 3D SMT image analysis to quantify individual particle

morphology and defines contact that includes contact location and orientation. It includes an experimental assessment of fabric evolution of F-35 sand undergoing axisymmetric triaxial compression during in situ SMT imaging using fabric tensor techniques.

Image Acquisition

In the last three decades, x-ray CT has emerged as a powerful non-destructive 3D scanning technique to visualize the internal structure of materials. It involves probing a specimen mounted on a rotating stage from different angles and collecting the attenuated x-ray using a detector system. Post-scan computer reconstruction and processing involve creating multiple slices through the scanned specimen that can be stacked to generate a 3D volume rendering of the specimen. In this paper, SMT images of silica sands were acquired at the Bending Magnet Beamline 13D (13 BMD) at the Advanced Photon Source (APS), Argonne National Laboratory (ANL), Chicago, USA. SMT imaging offers many advantages when compared to industrial x-ray CT imaging, which is well documented in the literature (e.g. Baruchel et al. (2006), Brunke et al. (2008), Cnudde and Boone (2013)). The main advantages include an almost parallel beam and high brilliance (which results in high photon flux on the specimen) yielding a much better image resolution and signal-to-noise ratio in the images (Baruchel et al. 2006). High flux monochromaters can tune the beam to monochromatic radiation for the desired energy level to suit specimen size and attenuation level.

Specimen sizes at beamline 13 BMD can range from a single particle with a resolution on the order of 1–2 μm/voxel to a 10 mm × 20 mm miniature triaxial test with

resolutions of 8–11 μm/voxel. Specimens can range from dry to fully saturated and can include a variety of particle morphologies. Specimens were rotated at a constant velocity and radiograph images are obtained by the detector at 0.2^{o} rotational increments. More information on the setup of beamline 13BMD can be found in Rivers et al. (2010).

SMT Image Analysis

Particle Identification

3D SMT images must be post-processed to transform the grayscale SMT image to a binary image and eventually to an image where each particle is individually identified and labeled. The labeled image will be used to compute particle properties as well as to characterize particle contacts. Accurate identification and calculations of individual particle morphology parameters and particle-to-particle association of the bulk material can then be defined and analyzed to provide critical parameters to feed in micro-mechanics-based constitutive models as well as provide validation for numerical modeling.

Grayscale SMT images were imported into Avizo Fire software using the built-in raw data read option (Figure 1.1a). To remove noise within the image while preserving particle edges and enhancing the contrast of the edges, an anisotropic diffusion filter was applied to the grayscale image. The anisotropic diffusion algorithm compares the value of each voxel with its six face-centered neighbors and diffuses the voxel as long as the difference does not exceed the input diffusion stop threshold value, which was

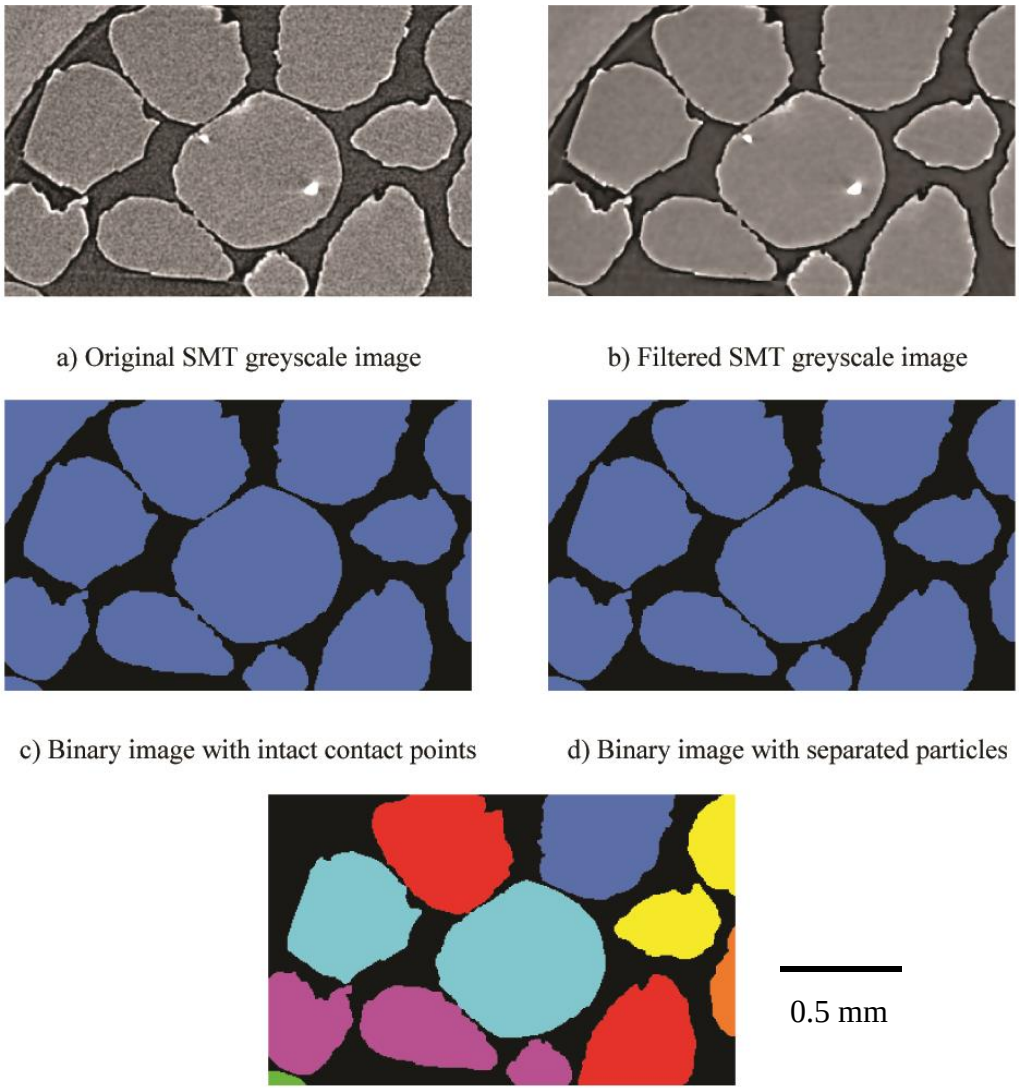

Figure 1.1. Steps of particle identification process

determined by a parametric study and error analysis (Figure 1.1b). The resulting image is a smoothed grayscale image with sharp particle edges between the solid particle material and the surrounding medium.

The next step in image processing was to segment the grayscale image in order to separate particles from the surrounding medium. Segmentation by interactive thresholding was employed to create a binary image assigning a voxel value of 1 for sand (having a higher x-ray attenuation) and 0 for the surrounding medium (usually air, which has a lower attenuation). The interactive thresholding produced a binary image that represents particles well. The binary image clearly shows particle contacts to the scale of image resolution. In other words, if particles are physically in contact at a point as small as the resolution, the binary image will represent this contact point. The segmentation process leaves small holes within some particles or small fragments of noise within the air surrounding particles. Further image processing using morphology operations on the image was implemented to remove noise from the images. First, Avizo Fire's 3D algorithm, Fill Holes, which fills all holes that are completely surrounded by material (solids) without affecting particle surfaces. Next all small noise must be removed so that it is not mistaken for actual particles; this is usually only a few voxels in volume within the surrounding air. The opening command was used to clean up other noise without affecting overall particle shape. The resulting binary image is depicted in Figure 1.1c and will be used later in image processing as a mask to ensure the final labeled image is accurate.

Now that the binary image accurately represents particles and surrounding void space, contacts between particles must be removed in order to label each particle. Avizo Fire's Separate Objects module is a combination of watershed, distance transform, and numerical reconstruction algorithms that can accurately remove the small area of contact between particles. It works well when particles are mono-sized and generally convex and results in separating the binary particles from each other similar to the image in Figure 1.1d. Next, the Border Kill module was applied to the image to remove all of the voxels connected to the edge of the 3D image. Finally, the particles were individually labeled from 1 through the number of particles, then particle-to-particle contact was reestablished. To omit the unnecessary expanded portions of the particle (regions of the particle boundary that were expanded excluding contact points), the image was masked with the binary image (Figure 1.1c) that precisely represents particle morphology and fabric. The resulting image (Figure 1.1e) accurately represents individually labeled in-contact particles.

Each particle label consists of connected voxels that have the same value, and each voxel occupies a cubical "point" in 3D space within the image. As a result of the high resolution and clarity of SMT images, the 3D voxel representation of particles captures morphology very well. Although measurements as small as surface texture cannot be accurately quantified using current SMT imaging, other properties such as volume, size, surface area, and contact can be accurately defined as demonstrated in the following sections. These properties were calculated using a computer code that was

developed by the authors. The code is divided into two "loops" one to define individual particle properties followed by a double loop to define contact properties. First, the labeled image was read into memory as a 3D matrix, and each particle label voxel was searched for with the first loop. In each iteration of the loop, the physical location of each particle's voxels were stored in an n×3 matrix, where n is the number of voxels belonging to a particular particle on that iteration of the loop. The three columns of the particle matrix are the x, y, and z coordinates of voxels that constitute the particle and can be easily used to calculate particle physical properties. For example, the volume of each particle was calculated as the summation of all voxels within the particle, or simply the length of the n×3 matrix. Particle volume was added to a vector containing all particle volumes from the preceding iterations after each iteration of the loop. This first loop also stores information about each particle surface that will be passed on to the contact definition loop.

Particle Center of Mass

Center of mass of each particle is the 3D volumetric center, or center of gravity in x, y, and z directions. The 3D matrix of particle voxel locations was used to determine the center of mass. An average spatial location was calculated by summing voxel locations in each direction (each column of the n×3 voxel location matrix) divided by the total volume of the particle (after Al-Raoush (2007)):

$$cg_i = \frac{\sum_i if(i,j,k)}{volume\ of\ particle} \qquad (1.1)$$

$$cg_j = \frac{\sum_j jf(i,j,k)}{volume\ of\ particle} \quad (1.2)$$

$$cg_k = \frac{\sum_k kf(i,j,k)}{volume\ of\ particle} \quad (1.3)$$

where cg_i, cg_j, and cg_k are the global center of mass of each particle $f(i,j,k)$ in the x, y, and z directions, respectively. An accurate determination of center of mass is essential in investigating particle kinematic behavior during shearing of granular materials. The proposed method determines the exact location of the particle center of mass in 3D space regardless of particle translation and/or rotation during testing and can provide valuable insight into behavior of granular material under any type of loading condition.

Particle Surface Area

Particle surface area influences the behavior of granular materials in many ways. Surface area can be used to quantify morphology (sphericity and roundness) of particles, which affects the strength and deformation characteristics of granular materials. Traditionally, particle surface area has been difficult to measure physically for small particles. Emergence of SMT imaging and analysis has greatly enhanced the ability to perform surface area measurements on small particles. The high resolution of SMT images provides virtual particles that very accurately portray particle shape via voxels, and measurements of surface area are not as elusive as before. To calculate the surface area of a particle, one must determine which voxels are on the boundary (surface) of the particle. Each voxel of the particle was analyzed to determine if it has any free faces in each iteration of the loop (free faced voxels have faces not directly adjacent to another

voxel that belongs to the same particle but rather either next to void space or another particle). To accomplish this analysis, each voxel of a particle was individually analyzed to determine if any part of that voxel was on the particle's surface. There are three situations where this can occur. The voxel face, as discussed earlier, can be directly on the surface, and there are six possible situations (six cubic faces) that occur where the face could be on the surface of the particle (Figure 1.2a). A voxel edge can be on the surface, which has 12 possible occurrences for the 12 edges of a cubic voxel (Figure 1.2b), or one of the eight voxel corners can be touching the surface (Figure 1.2c).

There are 26 total situations in which a voxel within a particle can be touching the surface. Representing these situations numerically entailed creating 26 matrices of length n, recalling that n is the total number of voxels within the particle. Six of the matrices store locations of the six voxels surrounding each voxel face. Twelve of the matrices store locations of the voxels connected to edges of each voxel. Eight of the matrices store locations of the voxels connected to corners of each voxel. Among all 26 matrices, the location of all voxels surrounding each particle voxel are known and can be searched to determine what, if anything, occupies them. If they do not contain the label ID of the particle being analyzed (i.e., they contain air or a different particle's voxel), then the voxel they surround is determined to be connected to the surface of the particle. Surface voxels are stored, and Figure 1.3 displays an example of voxels located on a particle surface. Surface area is calculated as the summation of voxels with free faces on the surface of the particle (excluding those with only corners and edges on the surface).

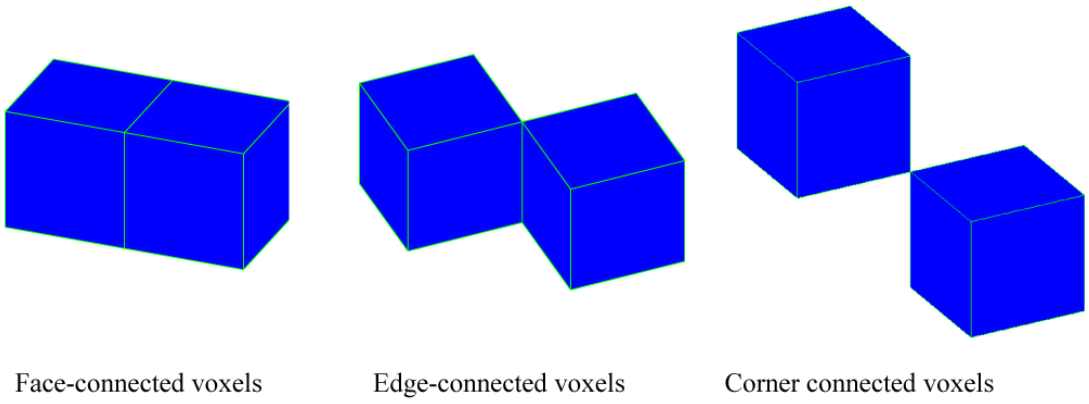

Figure 1.2. Example of three types of voxel connectivity

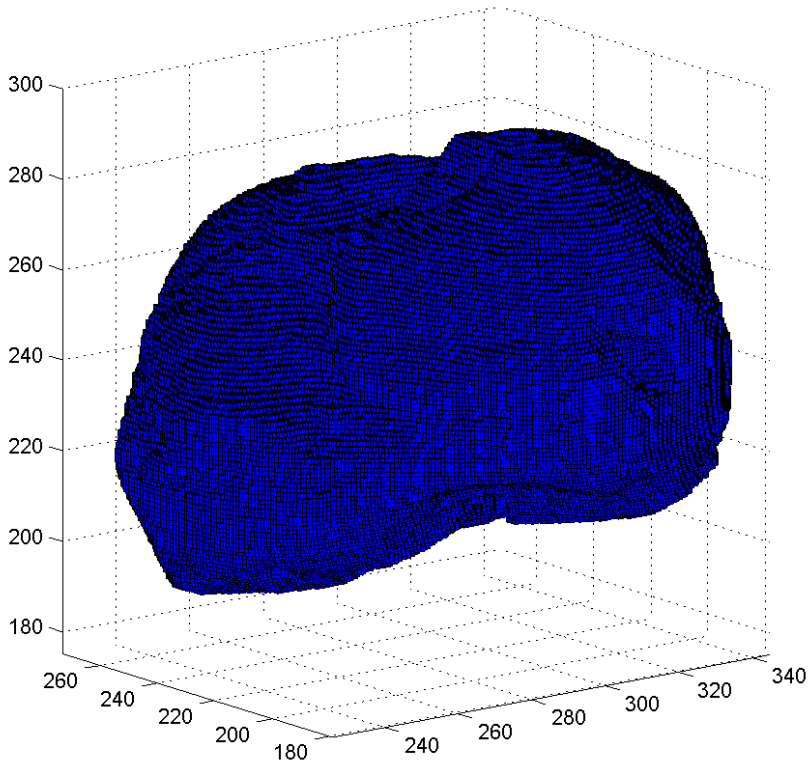

Figure 1.3. Voxel surface of a particle to compute surface area (axis units are in pixels, resolution = 10 μm/pixel)

Another matrix that includes the location of all voxels surrounding the particle, or a shell around the particle, is also stored for further use in contact determination. These are the voxels that come into contact with the particle at all voxel faces, corners, and edges.

A sphere made up of voxels (diameter of 151 voxels) was created and analyzed with the code to check its accuracy in calculating particle surface area. The code result was 71880 voxels^2, compared to a theoretical value of 71631.45 voxels^2, resulting in a 0.3% error between the calculated and theoretical values. The slight deviation is attributed to the voxel nature of the sphere.

Particle Lengths and Orientation

Orientations and sizes of particles in granular materials play a critical role in determining their behavior. Mostly, particle orientation and shape determines the initial fabric and its evolution during shearing. It contributes to the strength and dilatancy of granular materials as well as other engineering properties. Three principal lengths of a particle in 3D are defined as orthogonal and along the short, intermediate, and long axes of the particle.

Lengths and orientation of each particle are determined using the concept of Principal Component Analysis (PCA) on the multi-variant set of points that make up the particle voxels. PCA uses linear correlation between the points and applies a trend line to the long axis of the data by minimizing distances (x, y, and z) between the data points and the line using singular value decomposition. The principal component coefficients describe the global angle of the trend line determined by PCA, and the principal

component scores represent the fitted location of the voxels on the 1D trend line in principal space. The lengths of a particle were calculated as the difference between the maximum and minimum scores along each of the trend lines. There are two principal component coefficients in a 2D image of a particle governed by the x and y location of the points. For example, Figure 1.4 displays a 2D section of a particle composed of 6810 voxels, along with the results of 2D PCA displayed via a projected view that passes through the particle centroid. Principal component coefficients represent the global orientation of the particle lengths (vector directions shown in Figure 1.4) and lengths of the long and short axes are based on differences in extreme score values (extreme points fitted on trend line). The PCA method accurately represents how particles would be measured physically (twice the length of vectors shown in Figure 1.4) because it is the difference between extreme points of a particle as if measured by a micrometer. It is important to note that particle lengths obtained from PCA do not necessarily pass through the particle center of mass for non-spherical particles.

Three orthogonal principal components are defined along the three principal axes of the particle in 3D case, representing the long, intermediate, and short axes of a particle. Orientations of the three principal axes were calculated as the principal component coefficients of the PCA dataset. The long axis length of the particle is the difference between the extreme points that make up the first principal component. The intermediate and short axes lengths were calculated in the same manner on the second and third principal components, respectively. PCA yielded accurate measurements of the

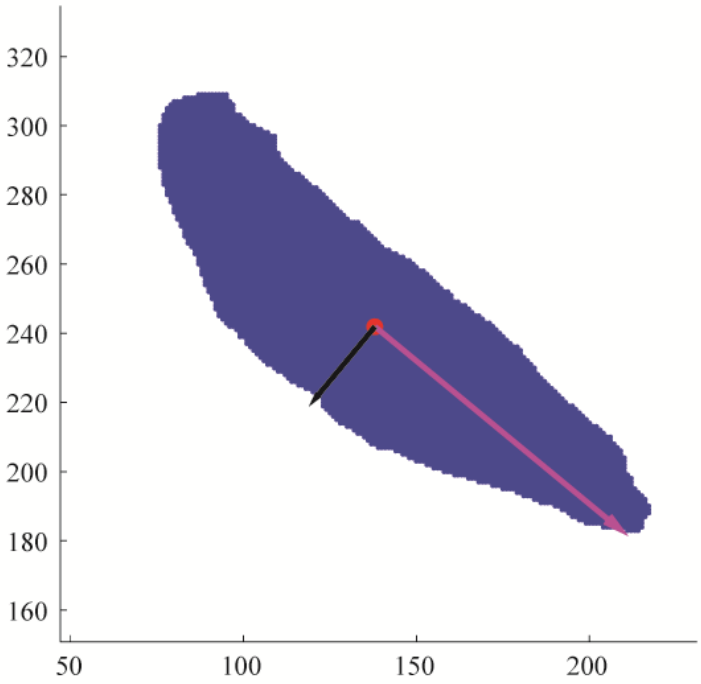

Figure 1.4. Example 2D PCA analysis on 6810 pixels of a particle cross section (axis units are pixels, resolution = 10 μm/pixel)

orientations and principal lengths of each of the particles in 3D. Figure 1.5 displays a 3D surface of a particle along with vectors that identify the particle's global orientation and length. The red, blue, and magenta vectors represent the orientations of the long, intermediate, and short axes of the particle, respectively (displayed through the particle center of mass). Principal components are orthogonal to each other and globally oriented based on the statistical computation by PCA. Global orientations of particles were extracted and can be used to represent fabric of granular materials as well as to calculate particle rotation during shearing.

A 3D SMT image of a triaxial experiment on ASTM 20-30 Ottawa sand was analyzed using the proposed code as a demonstration dataset. Resolution of the SMT image was 10.85 micron/voxel, and the image consisted of ~3400 particles. ASTM 20-30 Ottawa sand has a particle size between US sieves #20 (850 μm) and #30 (600 μm); therefore, particle sizes based on the SMT image should fall within that size range. Particle size distribution based on SMT image analysis is depicted in Figure 1.6, which shows a normal statistical distribution having sizes mostly between 600 and 800 μm with a small percentage larger than 850 μm. Particle size is determined from the SMT images based on the average of the small and intermediate lengths, which is used to compare particle size to mechanical sieving. Averaging these lengths better represents the physical process of mechanical sieving; for example, a particle's small axis length might fit through sieve mesh where its orthogonal intermediate axis might not. Based on this, a small portion of the particles are larger than what is expected.

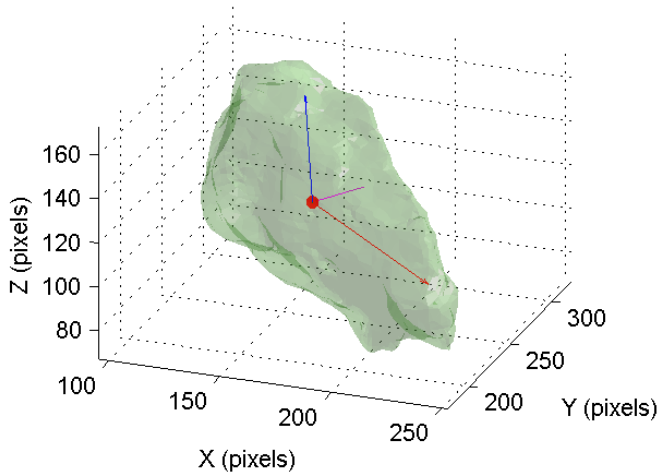

Figure 1.5. Illustrative example in 3D identifying particle global orientation and principal length.

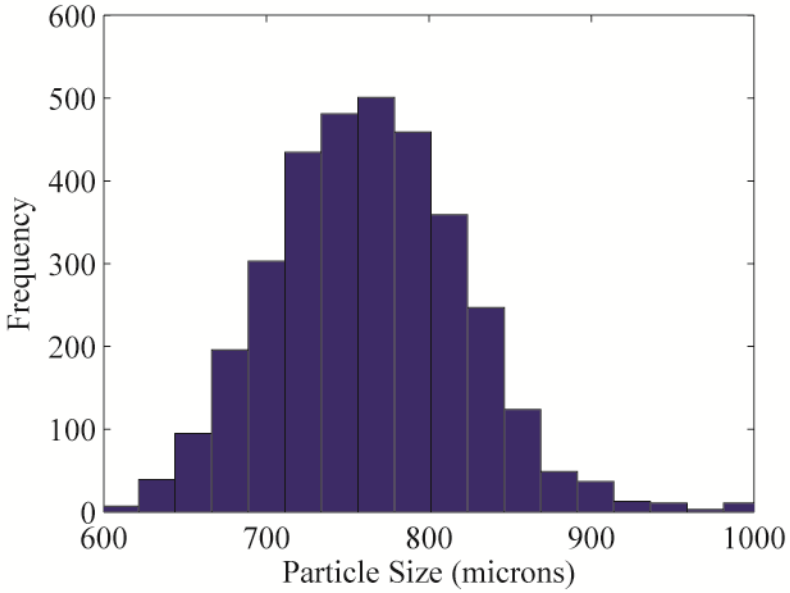

Figure 1.6. Particle size distribution of 3400 particles of ASTM 20-30 sand based on SMT image analysis.

Coordination Number and Particle-to-Particle Contact Definition

Identification of contact between particles involves analysis of the boundary shells that were described earlier for each particle. A matrix was generated that initially contained all voxels surrounding the particle surface (the shell around the particle determined from the first loop). The voxels of the shell that do not contain another particle (the void space) are then removed from the matrix based on the labeled image. What remains in the matrix is the portion of the shell that is occupied by other particles in contact with the particle being analyzed. Furthermore, data can be extracted on each particle that is in contact with the particle being analyzed by searching the original labeled image for the particle ID whose voxels occupy that space on the boundary. Coordination number is calculated as the total number of unique particle IDs within that matrix, which is the total number of particles in contact with the particle being analyzed.

The contact between particles was computed within the second loop of the code. Definition of contact between two particles consists of identifying which voxel faces, corners, and/or edges share a mutual face, corner, and/or edge with a neighboring particle and calculating the location and directions of that contact. The outer loop cycles through each particle and collects the spatial location indices of contact in a vector as well as a vector contains particle numbers which are in contact with the particle being analyzed. These two vectors were passed to inner loop that calculated contact properties. The code searches the labeled image to match a particle number to its contact location, and the number of voxels that defines the contact between two particles is a representation of a

surface between them. Even with high-resolution SMT images, this contact surface is only relative to the image and cannot be quantified with any real physical meaning. Figure 1.7b displays an example contact (shown in red) between two voxel particles. Contact location was calculated by adding the voxel locations in each direction (x, y, z) and dividing them by the total "area" of contact, similar to the calculation of particle centroids.

Contact between two particles is not always a single continuous surface. Roughness of particle surface or complex morphology could lead to several contact points, especially in very angular or rough granular materials. Considering that particle contacts may not be continuous, contact voxels do not lie in a plane as evident from Figure 1.7c. Although this definition of contact does not take into account the discontinuity of the contact surface, some researchers considered a global average of the voxel locations in calculating the contact and orientation. Contact area is relatively small and the global definition of contact between two particles will produce an overall average of the contact. This provides a good basis for determining fabric of a granular material, but may not prove as valuable for particle fracture assessment, since particle fracture depends heavily on contact and inter-particle forces. To define the contact between two particles, the 3D global direction of contact must be known as well as its location. The normal and tangent vectors to contact can play a significant role in determining how the particles will interact with each other upon loading and shearing. For example, if the loading direction is parallel to the vector normal to contact, then the forces transmitted

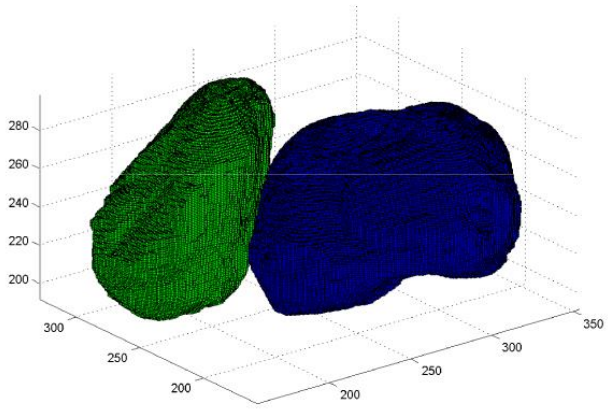

(a) Two particles in contact

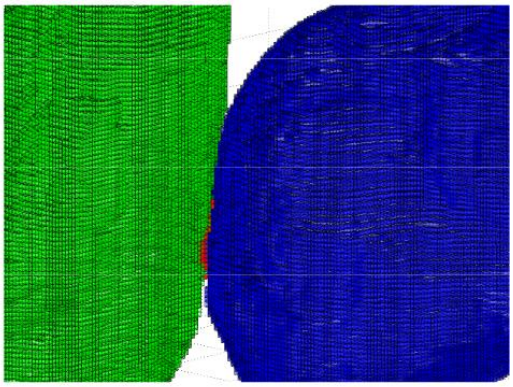

(b) Close up showing contact points

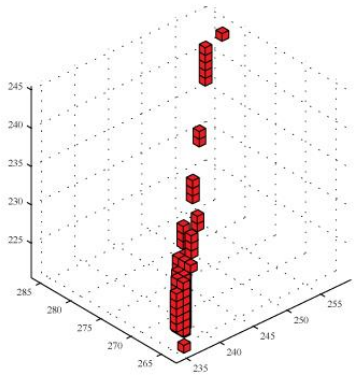

(c) Contact points between the two particles

Figure 1.7. Illustration of contact voxels between two particles (axis units are in pixels, resolution = 10 μm/pixel).

between particles will be higher than if the loading direction was perpendicular to the normal contact vector. A statistical analysis was conducted on the contact voxels using PCA to determine contact orientation. The first and third principal coefficients represent the tangent vector to contact (first principal component along long axis or plane of contact voxels) and the normal vector to contact (third principal component along shortest axis of voxels). Essentially, the 3D normal and tangent vectors are on the best fit plane as determined by PCA. Figure 1.8 shows example normal and tangent contact vectors located at the center of contact for the particles depicted in Figure 1.7. PCA of the contact voxels provides the global orientation of contact and insight into how particles interact with each other when they are loaded. Defining the global contact location and normal between particles is useful in determining force transfer through the granular material. Even if the contact is discontinuous, PCA determines the statistical center and normal/tangent vectors of contact. It represents the location and direction in which force will statistically be transmitted between particles, which is valuable input in micro-mechanics based constitutive models.

The code flow chart is shown in Figure 1.9. The code consists of two main loops. Input for the first loop is the labeled image, and volume, center of mass, surface area, coordination number, lengths and orientations are calculated for each particle and stored as output. Coordination number and contact voxel location are used as input for the second loop, which is a double for loop. The outer loop collects the contact locations for a particle, as well as particle numbers that are in contact with the particle being analyzed.

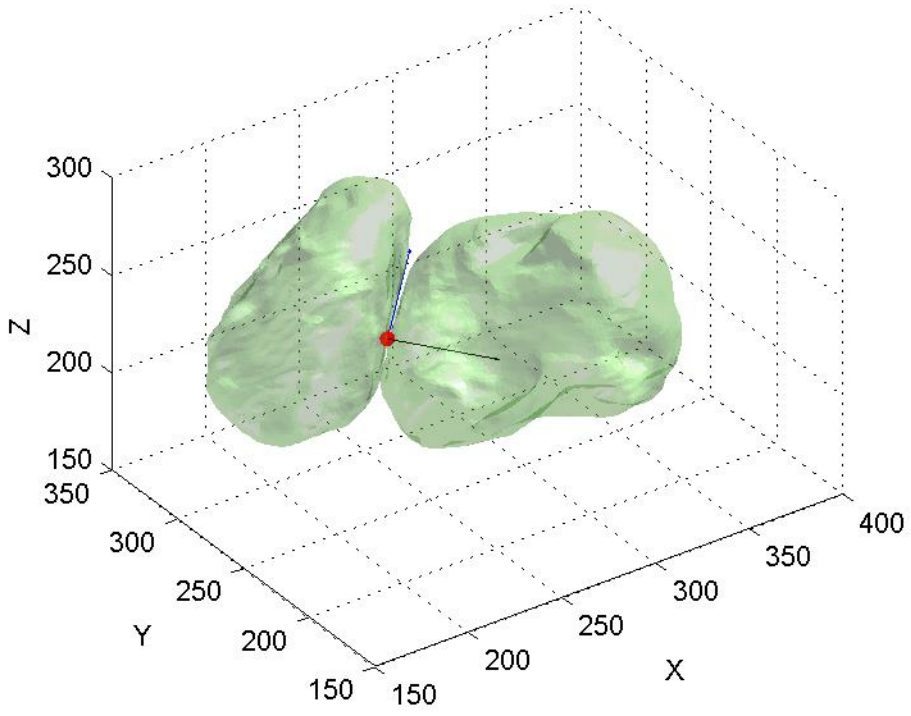

Figure 1.8. Normal and tangent contact vectors between two particles (axis units are in pixels, resolution = 10 μm/pixel).

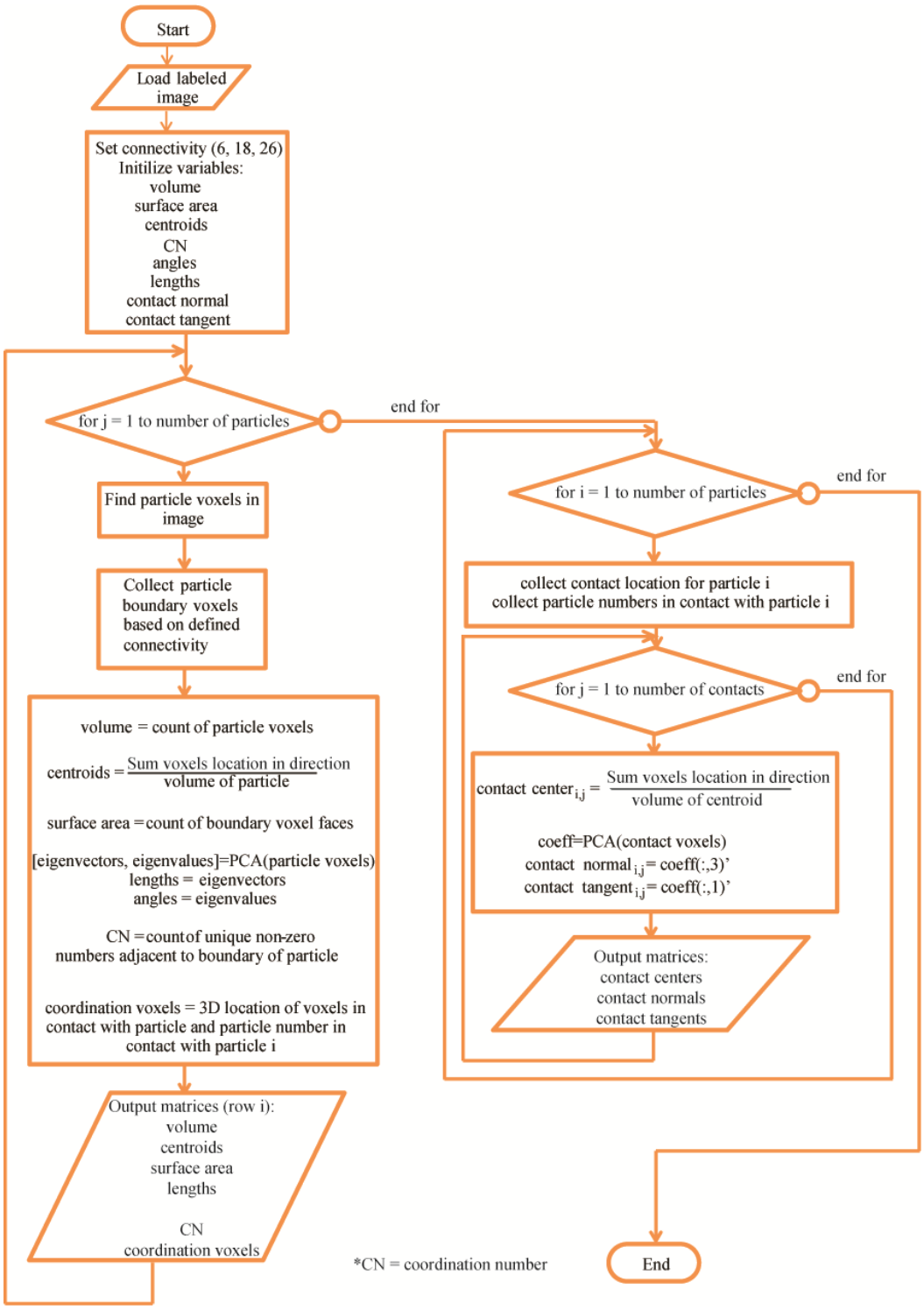

Figure 1.9. Flow chart of the code

The inner loop determines the contact orientation with PCA and the centroid of contact. Contact centroid and orientation is stored for each contact of each particle. Validation and verification of the code described in Figure 1.9 was conducted at each output, as described earlier.

Some difficulties were encountered in calculating contact between particles within the code. PCA requires more than one pixel being in contact for calculation of the three principal components. When contacts are limited to only one voxel, whether from pieces of noise within the image or a physically small contact (less than image resolution), those points are omitted from the analysis. They make up a negligible percentage of the total contacts within any SMT image using the current image processing analysis. Another situation that can possibly occur and cause errors in defining contact orientation is when a particle has an extremely concave surface and wraps around another particle. This type of contact does not accurately fit a plane to the contact voxels well; however, PCA statistically determines the best fit contact orientation. The types of sand used in analysis with this code can be chosen so that this error is not likely to occur.

Contact orientation of F-35 sand during axisymmetric triaxial compression

Many definitions of fabric for granular material are reported in the literature using various geometrical aspects of the material such as contact normal vectors, branch vectors (vector connecting centroids of contacting particles), particle orientation and void

space. This paper investigates the evolution of contact normal during axisymmetric triaxial compression experiment on F-35 sand from in situ SMT images. The experiment was conducted on 10 mm diameter x 20 mm height cylindrical dense specimen (relative density = 90%) that was subjected to 400 kPa confining pressure. Further description of the sand, experimental setup, and experiment can be found in Alshibli et al. (2014), Druckrey and Alshibli (2014) and Tordesillas et al. (2015). SMT images were acquired at axial strains of 0, 1, 2, 3.5, 5, 7, 9 and 17.5% and processed by the previously described methods. The SMT images had a resolution of 11.18 μm/pixel and the principal stress ratio (PSR) versus axial strain for the experiment is depicted in Figure 1.10. Peak stress is reached at ~5% axial strain and critical state was reached at approximately 13% axial strain.

Normal contact vectors were converted into spherical coordinate system with a rotated coordinate system in order to represent data in the loading direction (z-direction) with a full rose diagram (0 to 360 degrees, rather than 0 to 180 degrees). YZ direction was chosen in this paper due to limited pages of the paper and the normal contact vector and branch vector distributions are shown as rose diagrams in Figure 1.11 for axial strains of 0%, 2% (pre-peak stress state), 5% (peak stress state), and 17.5% (critical state). Before loading, contact normal vectors adduce a directional preference toward the horizontal which is expected as particles lay in the most stable position when they are deposited. As loading progresses, the directional preference of the contact normal vectors gravitates toward the loading direction (z-direction), and at peak and critical states

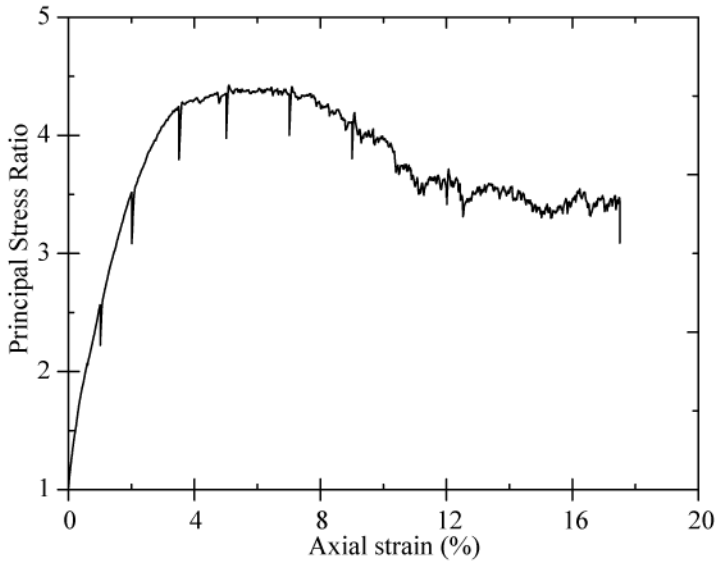

Figure 1.10. Axial strain versus principal stress ratio of axisymmetric triaxial compression experiment on F-35 sand.

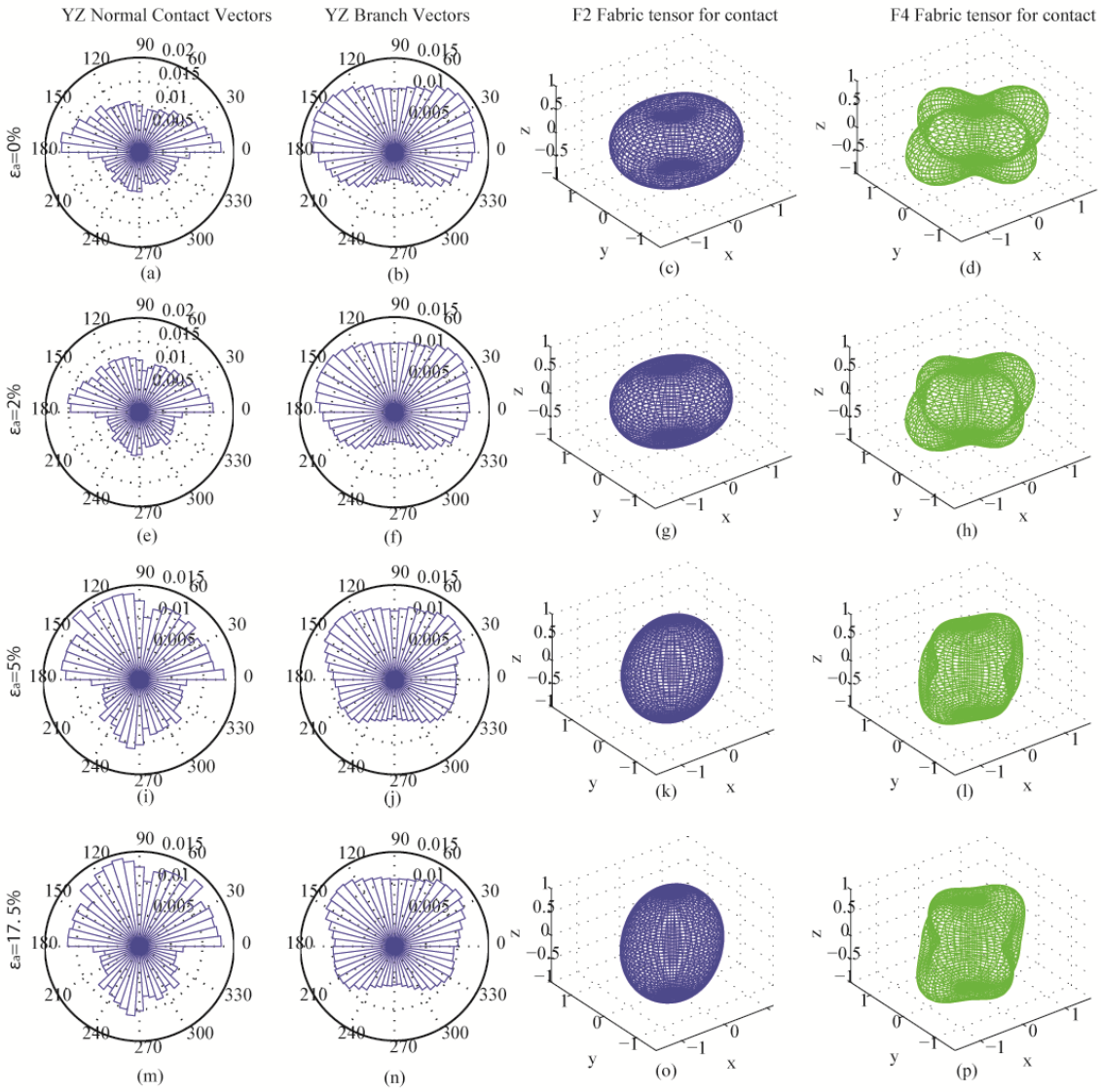

Figure 1.11. Distribution of fabric descriptors for axisymmetric triaxial compression experiment on F-35 sand at 0, 2, 5, and 17.5% axial strains.

contact normal vectors display a preference to resist the vertical load. This trend of contact normals aligning to resist the load agrees with published research on the evolution of contact normals (e.g. Kanatani (1984), Theocharis et al. (2014)). There is only a small difference between the contact vectors at 5% axial strain (peak principal stress ratio state) and 17.5% axial strain (critical state). At the peak state, the shear band has nearly fully developed and rotation and kinematics of particles outside the shear band is relatively constant; meaning all particles outside the shear band are either moving as a rigid body (above shear band) or not moving at all (below shear band). As a result, most particle contact vectors remain relatively constant outside the shear band. Branch vector orientations follow a similar trend, although not as dramatic as contact normal vectors. This is attributed to the angularity of the F-35 particles. If all particles were spherical, contact normal and branch vector distributions would be identical.

Kanatani (1984) fabric tensors were adopted in this paper. Fabric tensors of the first kind, which is the moment tensor of the contact normal vectors for each scan, is a symmetric tensor calculated as (second order):

$$N_{ij} = \frac{1}{N}\sum_{\alpha=1}^{N} n_i^{\alpha} n_j^{\alpha} \qquad (1.4)$$

where n_i^{α} is the αth contact normal vector and N is the number of contacts. Fabric tensors of the second kind order two is a deviatoric fabric tensor calculated as:

$$F_{ij} = \frac{15}{2}(N_{ij} - \frac{1}{3}\delta_{ij}) \qquad (1.5)$$

where δ_{ij} is the Kronecker delta. The second order probability density function (PDF) of the contact normal is:

$$f(n) \sim \frac{1}{4\pi} F_{ij} n_i n_j \qquad (1.6)$$

Moment tensors, deviatoric fabric tensors, and PDF can be calculated to any even order. Second order descriptions of directional data are limited to ellipsoidal shapes for 3D data, while fourth and higher orders can represent more complex distributions. Completely uniform directional data would be represented by a sphere in 3D, or circle in 2D. Second and fourth order deviatoric fabric tensor surface representations are displayed in Figure 1.11 for 3D contact normal vectors. Again, the second order tensor representation is limited to ellipsoidal shape while the fourth order tensor describes the data more accurately. Both orders show how the contact normal vectors are initially distributed more towards the horizontal and shift towards the vertical loading direction to resist the applied load.

To describe the evolution of internal structure anisotropy, the normalized second invariant of the second order deviatoric fabric tensor (F_{II}) was calculated at each loading stage, similar to Yang et al. (2014) and Theocharis et al. (2014). Figure 1.12 shows the evolution of F_{II} during shearing of the F-35 sand. Fabric anisotropy increases rapidly during pre-peak stress state and reaches a maximum at peak state. The fabric anisotropy neutralizes and is relatively constant during the post-peak regime, implying that once the peak stress is reached minimal changes in overall contact normal direction occur.

Computational Requirements

The code was originally developed using MATLAB R2012b for relatively small images. For example, a 300×300×300 voxel image with 120 particles requires

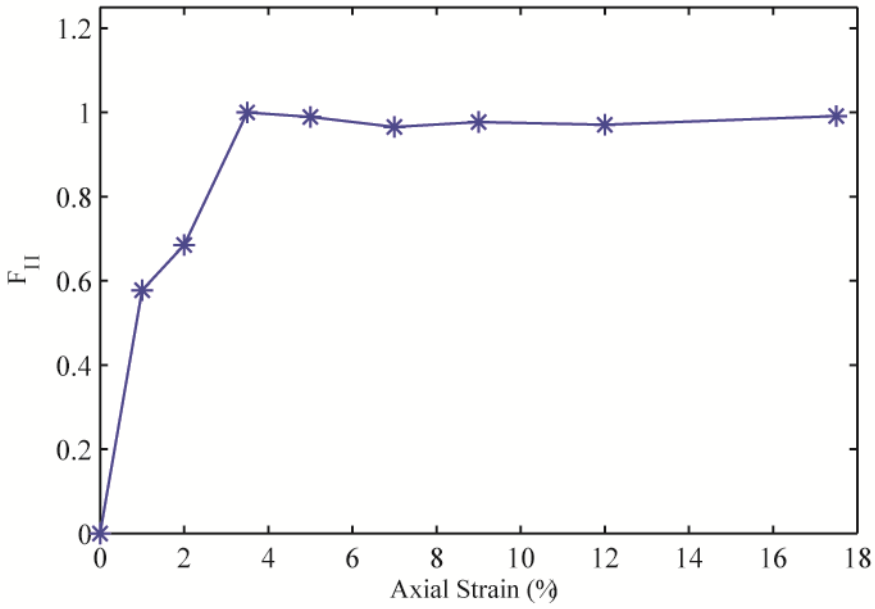

Figure 1.12. Evolution of F_{II} during axisymmetric triaxial test of F-35 sand.

approximately 1 GB of memory and ~2 minutes to process the data on a workstation with 48 GB RAM. As the images increase in size and the number of particles increases, the computational time increases because the images are loaded into memory and they are searched many times within the code. Some of the large SMT images can be in excess of 1920×1920×2600 voxels and contain over 100,000 particles. Running the MATLAB version of the code requires hundreds of gigabytes of RAM and several weeks of processing time. For this reason, the code was ported to C++ programming language. Once ported, analysis on the large images required approximately 70 GB RAM and 4– 5 hours of compute time. The C++ version of the code can analyze even the largest images available from current SMT technology.

Summary and Conclusions

The paper presented a method of 3D SMT image analysis to quantify particle morphology as well as particle contacts. High resolution SMT images were obtained and processed using Avizo Fire software. SMT imaging and anisotropic diffusion filtering provided grayscale images with very little noise and clear particle boundaries. The SMT images were processed, and individual particles were labeled with their contact points intact. A code was developed in Matlab and ported to C++ language to analyze the largest labeled images available from current SMT technology. Accurate values of particle volume, surface area, center of mass, lengths, and orientations were computed for individual particles. Contact was defined based on contact voxels between particles.

Those contact voxels were statistically analyzed using PCA to determine the normal and tangent vectors to contact.

Contact normal distributions were analyzed during in situ SMT imaging of triaxial compression of F-35 sand. Moment and fabric tensors were calculated to characterize the distribution. Contact normal distribution was initially oriented away from the loading direction, and upon compression the contact normal vectors oriented more in the loading direction to resist the load. Anisotropy of the fabric based on contact normal vectors increased dramatically until peak stress state was reached, then decreased to almost a constant value.

Quantitative particle characteristics described by this paper provides valuable insight into the fabric and failure mechanisms of granular material. Loading paths through granular material depend on particle shape, orientation, and contact, which are defined by the current study. Results from this analysis can be used in many future applications such as tracking particle kinematics at progressive loading, verifying numerical models, or input for force chain models, to name a few. This research provides a first step for future development of accurate micromechanical models that can eventually be used to design many different types of granular systems.

References

Al-Raoush, R. (2007). "Microstructure characterization of granular materials." *Physica A: Statistical Mechanics and its Applications*, 377(2), 545-558.

Alshibli, K., Druckrey, A., Al-Raoush, R., Weiskittel, T., and Lavrik, N. (2014). "Quantifying Morphology of Sands Using 3D Imaging." *Journal of Materials in Civil Engineering*, 04014275.

Andò, E., Hall, S., Viggiani, G., Desrues, J., and Bésuelle, P. (2012). "Grain-scale experimental investigation of localised deformation in sand: a discrete particle tracking approach." *Acta Geotechnica*, 7(1), 1-13.

Baruchel, J., Buffiere, J.-Y., Cloetens, P., Di Michiel, M., Ferrie, E., Ludwig, W., Maire, E., and Salvo, L. (2006). "Advances in synchrotron radiation microtomography." *Scripta Materialia*, 55(1), 41-46.

Bloom, M., Russell, M., Kustau, A., Mandayam, S., and Sukumaran, B. "An X-ray computed tomography technique for the measurement of packing density in granular particles." *Proc., Instrumentation and Measurement Technology Conference, 2009. I2MTC '09. IEEE*, 74-79.

Brunke, O., Brockdorf, K., Drews, S., Müller, B., Donath, T., Herzen, J., and Beckmann, F. "Comparison between x-ray tube-based and synchrotron radiation-based μCT." 70780U-70780U-70712.

Cnudde, V., and Boone, M. N. (2013). "High-resolution X-ray computed tomography in geosciences: A review of the current technology and applications." *Earth-Science Reviews*, 123(0), 1-17.

Cox, M. R., and Budhu, M. (2008). "A practical approach to grain shape quantification." *Engineering Geology*, 96(1–2), 1-16.

Druckrey, A., and Alshibli, K. (2014). "3D Behavior of Sand Particles Using X-Ray Synchrotron Micro-Tomography." *Geo-Congress 2014 Technical Papers*, 2814-2821.

Fonseca, J., O'Sullivan, C., Coop, M. R., and Lee, P. D. (2013). "Quantifying the evolution of soil fabric during shearing using directional parameters." *Géotechnique*, 487-499.

Hall, S. A., Bornert, M., Desrues, J., Pannier, Y., Lenoir, N., Viggiani, G., and BéSuelle, P. (2010). "Discrete and continuum analysis of localised deformation in sand using X-ray mCT and volumetric digital image correlation." *Geotechnique*, 315-322.

Hasan, A., and Alshibli, K. A. (2010). "Experimental assessment of 3D particle-to-particle interaction within sheared sand using synchrotron microtomography." *Géotechnique*, 369-379.

Kanatani, K.-I. (1984). "Distribution of Directional Data and Fabric Tensors." *Int. J. Engng Sci.*, 22(2), 149-164.

Oda, M. (1972). "Initial fabrics and their relations to mechanical properties of granular material." *Soils and foundations*, 12(1), 17-36.

Oda, M., Nemat-Nasser, S., and Konishi, J. (1985). "Stress-induced anisotropy in granular masses." *Soils and Foundations*, 25(3), 85-97.

Rivers, M. L., Citron, D. T., and Wang, Y. (2010). "Recent developments in computed tomography at GSECARS." *SPIE*, 3, 780409-780409.

Theocharis, A., Vairaktaris, E., Fu, P., and Dafalias, Y. F. (2014). "Comparison of fabric tensors for granular materials." *Geomechanics from Micro to Macro*, K. Soga, K. Kumar, G. Biscontin, and M. Kuo, eds., CRC Press, 153-158.

Thompson, K. E., Willson, C. S., and Zhang, W. (2006). "Quantitative computer reconstruction of particulate materials from microtomography images." *Powder Technology*, 163(3), 169-182.

Tordesillas, A., Pucilowski, S., Tobin, S., Kuhn, M., R., Andò, E., Viggiani, G., Druckrey, A., and Khalid, A. (2015). "Shear bands as bottlenecks in force transmission." *EPL (Europhysics Letters)*, 110(5), 58005.

Viggiani, G., Andò, E., Jaquet, C., and Talbot, H. (2013). "Identifying and following particle-to-particle contacts in real granular media: An experimental challenge." *AIP Conference Proceedings*, 1542(1), 60-65.

Vlahinić, I., Andò, E., Viggiani, G., and Andrade, J. (2014). "Towards a more accurate characterization of granular media: extracting quantitative descriptors from tomographic images." *Granular Matter*, 16(1), 9-21.

Yang, D. S., Li, X., and Yu, H. S. (2014). "Fabric evolution of 3D granular materials in rotational shear." *Geomechanics from Micro to Macro*, CRC Press, 85-90.

Yimsiri, S., and Soga, K. (2010). "DEM analysis of soil fabric effects on behaviour of sand." *Géotechnique*, 483-495.

CHAPTER 2

QUANTIFYING MORPHOLOGY OF SANDS USING 3D IMAGING

A version of this chapter was originally published in: Alshibli, K., Druckrey, A., Al-Raoush, R., Weiskittel, T., and Lavrik, N. (2014). "Quantifying Morphology of Sands Using 3D Imaging." *Journal of Materials in Civil Engineering*, 04014275.

My primary contributions to this paper include (i) surface roughness and SMT data collection, (ii) analysis of surface roughness and SMT data, (iii) determination of influence of particle morphology and surface roughness on granular material friction angle, (iv) some of the writing.

Abstract

Particle morphology plays a significant role in influencing engineering behavior of granular materials. Surface texture, roundness, and sphericity represent distinct multi-scale measures needed to fully describe particle morphology. Most studies reported in the literature rely on 2D projected images of particles with few 3D images that mostly focused on relatively large-size aggregate samples. In this paper, 3D Synchrotron Micro-Computed Tomography (SMT) was used to acquire high-resolution images of glass beads, F-35 Ottawa sand, #1 dry glass sand, GS#40 Columbia sand, Toyoura sand, and Hostun RF sand. New roundness and sphericity indices are proposed and calculated for the samples based on 3D measurements of surface area, volume, and three orthogonal diameters of particles. In addition, surface texture of particles was measured using optical interferometry technique. The measurements reported in this paper can serve as a good source for other researchers working on sands to build on these intrinsic particle properties to link engineering behavior of sands to their morphology.

Introduction

Morphology, mineralogy, and gradation of particles have a significant influence on engineering properties of granular materials. Sedimentologists generally express particle morphology in terms of surface texture (roughness), roundness, and sphericity. Surface texture is used to describe the surface of particles (e.g. polished, greasy, frosted, etc.) that are too small to affect the overall shape. Roundness refers to those aspects of particle surface (sharpness of corners and edges) that are on a larger scale than those classed as surface texture, but that are smaller than the overall dimensions of the particle. Sphericity is used to describe the overall form of the particle irrespective of the sharpness of edges and corners. It is a measure of the degree of conformity of particle shape to that of a sphere. Wadell (1932) was the first to point out that the terms *shape* and *roundness* were not synonymous, but rather include two geometrically distinct concepts. He defined roundness of a particle based on a 2D image as the ratio of the average of radii of all corners of the particle to the maximum radius of an inscribed circle..There are also are many other scale definitions for the roundness (e.g., Russel and Taylor 1937; Pettijohn 1949; Powers 1953, 1982). Powers (1953) emphasized that roundness does not depended on particle's shape instead it depends on the sharpness of edges. Wadell (1932) was also the first to choose the sphere as a standard. Ideally, the property of sphericity may be defined as the ratio of the volume of a sphere of the same volume as the fragment in question to the actual volume of the particle. Powers (1953) introduced the sphericity terminology to describe the shape as well as the roundness index. In 1982 Powers

modified this chart to include more classes for sphericity and assigned index numbers for the different roundness and sphericity classes.

A definition of particle shape in terms of sphericity and roundness is widely accepted. However, methods have not been standardized because of the tedious task of making numerous readings. Zavala (2012) presented a review of particle shape indices reported in the literature. Advances in digital imaging and computed tomography (CT) technqiues have served as valuable tools to characterize aggregate morphology based on 2D images (e.g., Kwan et al. 1999; Wang et al. 2005; Al-Rousan et al. 2006; Cox and Budhu 2008; Bessa et al. 2012; Sun et al. 2012) or 3D images (e.g., Komba et al. 2013; Garbout et al. 2013). Garboczi and Bullard (2013) acquired 3D images of spherical glass beads and calculated the the sphericity of the beads. Fonseca et al. (2012) compared 2D to 3D measurements of particle morphology of natural sands and found a clear difference between 2D and 3D shape measurements. Al-Raoush (2007) calculated sphericity and roundness indices of one sand sample based on 3D CT images.

The shape/roundness of granular particles can be evaluated using different indices such as the Form Factor (FF), which is widely used in the literature for 2D images:

$$FF = \frac{4\pi A}{p^2} \qquad (2.1)$$

Where *A* is the projected area of the particle and P is the perimeter of *A*. Sukumaran and Ashmawy (2001) quantified 2D particle shape using a normalized shape factor (SF) and angularity factor (AF) on projections of particles as well as ideal shapes such as circle, cross, and four pointed star. They fitted a polygon inside the particle projection and

measured lengths and angles at sampling various sampling intervals. Bloom et al. (2009) extended Sukumaran and Ashmawy (2001) approach to 3D by conducting the analysis on 2D cross sections throughout the particle and taking a statistical mean for the particle (not a true 3D measurement). They also used common methods such as Fourier analysis and invariant moments to compare the shapes.

Masad *et al.* (2001) introduced the surface Texture Index (TI) in which they referred to the fast Fourier transform, a good correlation between TI and the rutting resistance for hot-mix asphalt was found in their study. In 1998, Grigoriev *et al.* studied the surface texture at the nano-scale level and concluded that it affects the contact behavior between two surfaces. James and Vallejo (1997) defined the roughness as the general shape and surface irregularity and emphasized that roughness is an important characteristic that affects the mass behavior of the soil. The surface texture/roughness has been also mesured using more accurate and complicated methods such as Fractal Geometry, fuzzy uncertainty texture spectrum (Lee *et al.* 1998), Structural 3-D approaches (Hong *et al.* 1999), SURFASCAN 3D (Content & Ville 1995), photometric stereo acquisition and gradient space domain mapping (Smith 1999), and optical interferometry (Alshibli and Alsaleh, 2004).

This paper proposes new roundness and sphericity indices for glass beads and five silica sands including Ottawa sand, #1 dry glass sand, GS#40 Columbia sand, Toyoura sand, and Hostun RF sand based on high resolution 3D SMT images. Additionally, surface texture of the glass beads and the sands were quantified using optical

interferometry. The measurements reported in this paper can serve as a good source for other researchers working on sands to build on these intrinsic particle properties to link engineering behavior of sands to their morphology, state (density), applied stress condition, boundary condition, etc.

Sand Properties

Three silica sands known as F-35 Ottawa sand, #1 Dry Glass sand, and GS#40 Columbia grout sands were acquired and only size portion between US sieves #40 (0.429 mm) and #50 (0.297 mm) were used in this study (Table 2.1). These are silica sands with different morphology ranging from rounded to angular particle classes (Table 2.1). The authors plan to conduct triaxial experiments on these sands in the near future to investigate the influence of particle morphology on strength properties of poorly-graded (uniform) sand. Glass beads with similar grain size as these sands are also included in the investigation to provide baseline measurements for roundness and sphericity. In addition, samples of Toyoura and Hostun RF sands were analyzed. Toyoura sand is a poorly graded silica sand with a mean particle size (d_{50}) of 0.22 mm and has been extensively tested by Japanese geotechnical researchers under many loading and state conditions. Hostun RF sand is also a poorly graded sand with d_{50} = 0.34 mm and has been widely tested by many geotechnical researchers in France under complex loading paths and conditions. Figure 2.2 shows the grain size distribution curves for Toyoura and Hostun RF sands. Furthermore, many constitutive models reported in the literature have used Toyoura and Hostun RF sands for calibration and validation. Therefore, reporting

Table 2.1. Properties of sands and glass beads

Material	G_s	d_{50} (mm)	e_{min}	e_{max}	Source	Supplier	Grain Size
F-35 Ottawa Sand	2.650	0.36	0.570	0.763	Ottawa, IL, USA	US Silica Company	Size portion between US sieves #40 (0.42 mm) and #50 (0.297 mm)
#1 Dry Glass Sand	2.650	0.36	0.715	0.947	Berkeley Springs, WV, USA		
GS#40 Columbia Grout Sand	2.650	0.36	0.693	0.946	Columbia, SC, USA		
Glass beads	2.550	0.36	0.686	0.800	Soda lime glass	Jaygo inc.	
Hostun RF Sand	2.658[+]	0.34	0.592[+]	0.978[+]	France	Prof. Viggiani	Figure 2.2
Toyoura Sand	2.648[+]	0.22	0.621[+]	1.034[+]	Japan	Prof. Tatsuoka	Figure 2.2

[+] Duttine et al. (2008)

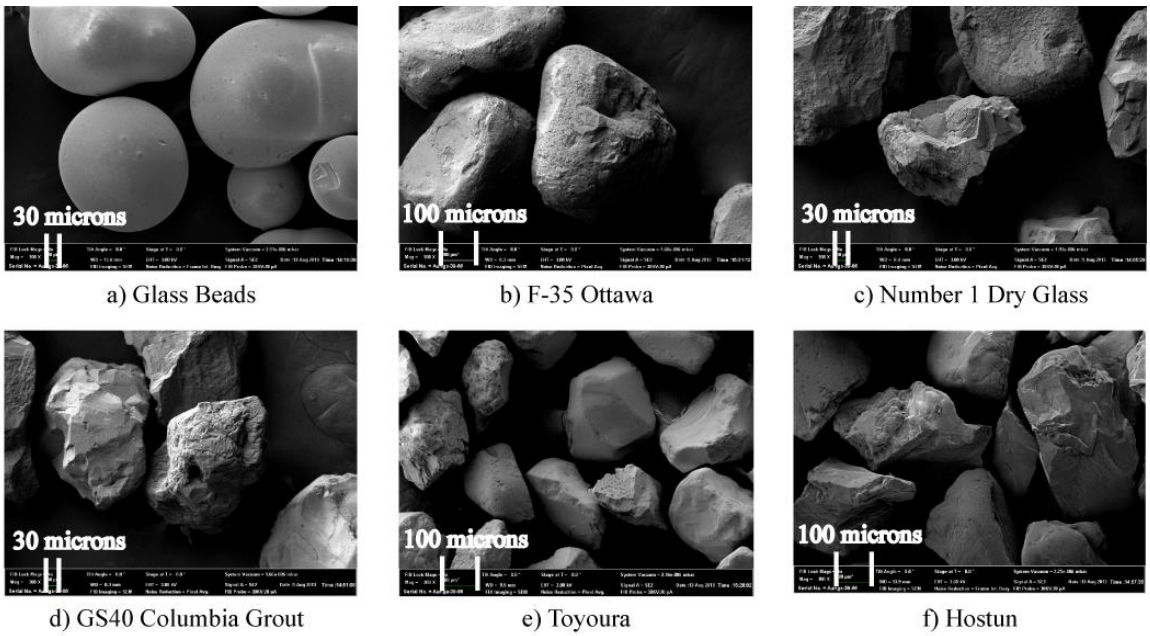

a) Glass Beads b) F-35 Ottawa c) Number 1 Dry Glass

d) GS40 Columbia Grout e) Toyoura f) Hostun

Figure 2.1. SEM images of the sands and the glass beads

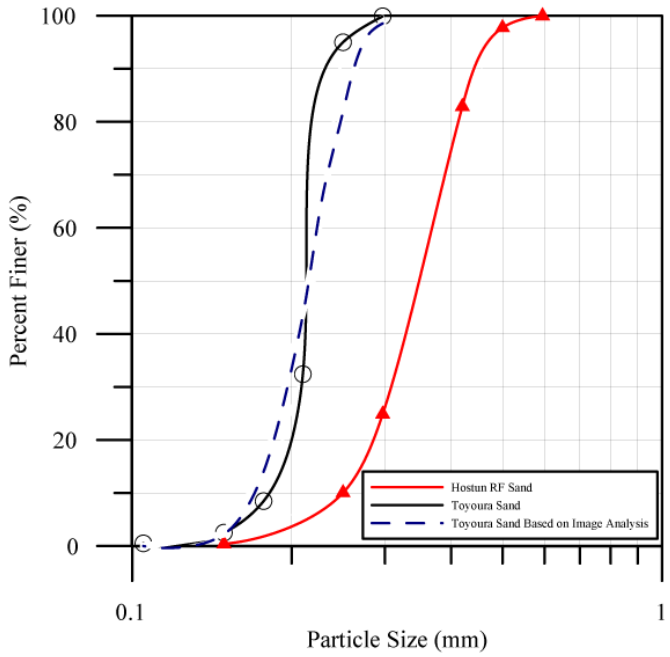

Figure 2.2. Grain size distribution curves for Toyoura and Hostun RF sands

morphology properties of these sands will have a broad impact and will be valuable measurements for future experimental studies.

Particle Roundness and Sphericity

Synchrotron Micro-computed Tomograhy (SMT) Image Acquisition and Processing

Since the early1990's, x-ray computed tomography (CT) has emerged as a powerful non-destructive 3D scanning technique to study geomaterials and visualize their internal structure. It is a technique in which the x-ray beam of a computerized tomography scanner passes through an object and is collected with a detector; the beam is rotated to produce the equivalent of a "slice" through the area of interest. The x-ray information collected during the rotation is then used by a computer program to reconstruct 3D image of the scanned object. X-ray CT has been extensively used to characterize geomaterials and there is extensive literature on the subject area. A significant enhancement to conventional x-ray tomography systems is the use of synchrotron radiation source which generates higher intensity beams (10^6 times greater than a conventional x-ray beam). This has several advantages over conventional x-ray sources, including high intensity of photon flux (number of photons per second), high degree of collimation (source divergence leads to image blur), and the ability to tune the photon energy over a wide range using an appropriate monochromator for obtaining specific-element measurements (Kinney and Nichols 1992). Synchrotron micro-computed tomography (SMT) produces images with higher resolution and less noise

when compared with conventional CT systems. SMT imaging also produces a relatively crisp boundary between solid and air phases which is beneficial for image analysis. Otani and Obara (2004), Desrues et al. (2006), and Alshibli and Reed (2010) reported the latest advances on applications of CT and SMT on soils, concrete, and rocks.

In this study, a sample of Toyoura sand was placed inside a capillary tube that has an inner diameter of 0.85 mm and scanned at Beamline 13D, Advanced Photon Source (APS), Argonne National Laboratory (ANL). The specimen was scanned at 20 KeV energy using 0.20 degree rotation increments with a spatial resolution of 2.01 micron/voxel. Since other sands and glass beads have larger grain size, they were placed inside an aluminum tube with inner diameter of 2.35 mm and scanned at 28 KeV energy yielding SMT images with a spatial resolution of 3.79 micron/voxel. Figure 2.3a&c show an example axial SMT image of F-35 Ottawa sand.

The 3D SMT images were post-processed using Avizo Fire software. Images were first filtered using an anisotropic diffusion filter which enhances the phase contrast at the boundary of particles as well as smoothes out noise within the particle continuum. Next, the images were segmented into solid and air phases using interactive thresholding. In the grayscale SMT image, solid material volumetric pixels (voxels) have higher intensities than air, and at some points it is difficult to differentiate between voxels belonging to solid and voxels belong to air. Errors resulting from incorrect segmentation can cause significant differences in particle shape, especially when conventional CT systems are used. This is because conventional CT systems sometimes do not provie 3D images with

clear material boundaries. However, voxel values between the solids and air in SMT are vastly different and boundaries are crisp as a result, especially after applying anisotropic diffusion filtering (Figure 2.3a&b). To demenstrate this, an error analysis on using different thresholding values on the effect on particle shape indices is presented later in this paper. After segmentation, particles were separated from each other using built-in separation algorithms and the tube and particles adjacent to the image boundaries were then removed to prevent partial particle count and the tube from being included in the calculations. Each of remaining particles was assigned a unique label that represents the actual particle shape very closely (Figure 2.3d). The 3D images were then saved for further processing and analysis using a special code that was developed by Al-Rausch (2007) using Matlab software. Particle volume was calculated by summing the voxels belonging to the particle. Similarly, particle surface area was computed as the summation of exterior faces of boundary voxels belonging to the particle. The shortest (d_S), intermediate (d_I), and longest (d_L) diameters of the particle that pass through the center of mass of the particle were calculated using the concept of principal component analysis on the 3D particle voxels. The three orthogonal directions were statistically calculated using singular value decomposition and the distances between the extreme points along those directions represent the three particle lengths. To demonstrate the accuracy of the code calculations, grain size distribution of Toyoura sand was calculated using d_S values and displayed in Figure 2.2 which shows that the images-based grain size distribution slightly deviates from sieve analysis. While shaking a sample in the sieve analysis, it is

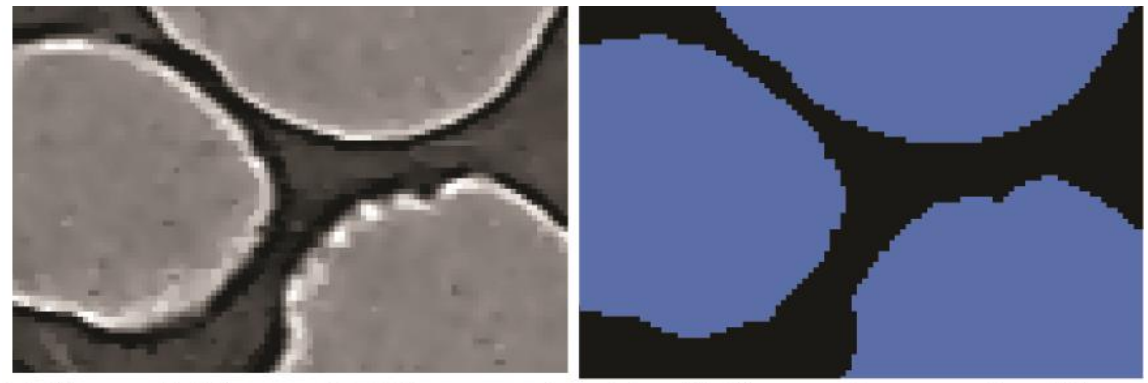

(a) Close up SMT image of F-35 Ottawa sand particles (b) Close up of segmented particles

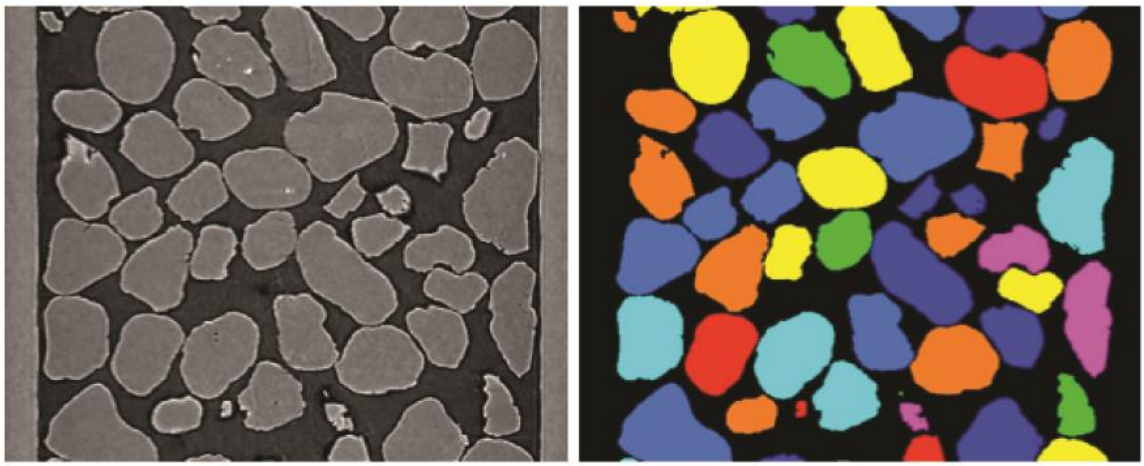

(c) SMT image of F-35 Ottawa sand (d) Processed image of F-35 sand particles

Figure 2.3. Example axial SMT image F-35 Ottawa sand and associated segmented image

difficult to align particles to pass through using their shortest diameter which caused the slight difference in grain-size distribution between image-based analysis and sieve analysis.

Roundness and Sphericity Measurements

In this paper, two new indices are introduced to define the sphericity and roundness of particles based on high-resolution 3D SMT images. The sphericity index (I_{sph}) is defined as:

$$I_{sph} = \frac{V_p}{V_s} \qquad (2.2)$$

Where V_p and V_s are the actual volume of the particle and the volume of sphere with a diameter equals to d_S, respectively. I_{sph} equals to unity for spherical particle. In most cases, I_{sph} has a value more than unity but it may have values less than unity for kidney-shaped and discoidal particles (e.g., Figure 2.4a). The roundness index (I_R) is defined as:

$$I_R = \frac{A_p}{4\pi(\frac{d_L+d_I+d_S}{6})^2} \qquad (2.3)$$

Where A_p is the actual 3D surface area of the particle. The denominator in Equation 2.3 represents the surface area of a sphere that has a diameter equals to the average of d_S, d_I and d_L. I_R equals to unity for a particle that has no asperities on its surface and has the same surface area as a sphere with an equivalent average diameter.

To demonstrate the effect of segmentation errors on particle shape indices, an image subset containing 70 particles of F35 sand was processed several times, with the only variation being the threshold value. The resulting sphericity and roundness indices

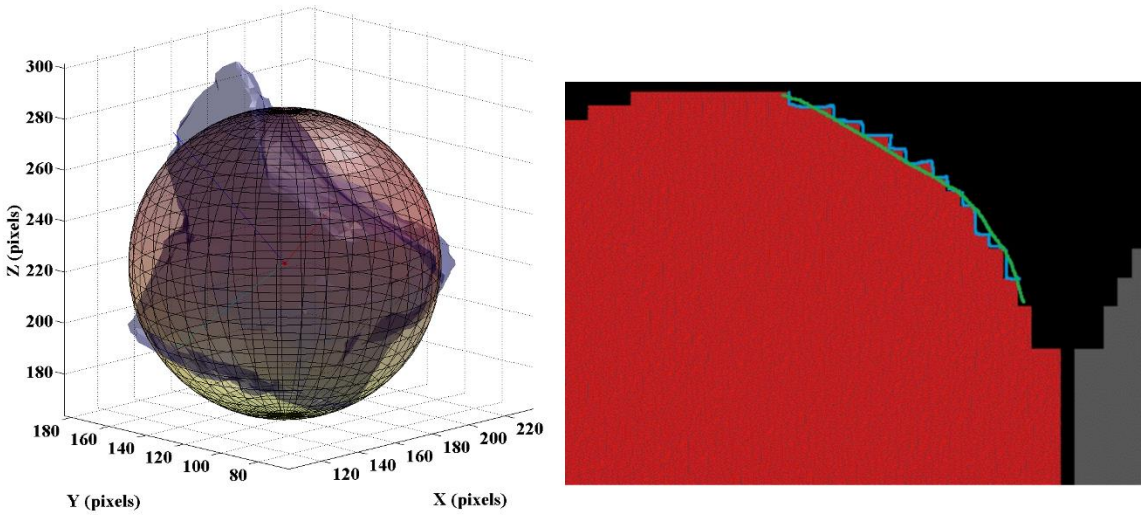

(a) (b)

Figure 2.4. (a) Example image showing a particle with I_{sph} <1; (b) Image demonstrate that a correction is necessary in particle perimeter calculation

were compared for each of the chosen values. The thresholding values chosen were at various voxel intensities close to the lower voxel range of solid material (where it begins to get difficult to determine whether a voxel belongs to solid phase or air phase). Once this value was estimated, a range of ± 200 intensity units was used to evaluate the effect on shape indices. The average error in sphericity between the lowest chosen thresholding value and the highest chosen thresholding value was less than 1% which demonstrates that the estimated thresholding value, as long as it is close the edge of solid material, has negligble effect on I_R and I_{sph} values.

Figure 2.5 and Table 2.2 show the normalized histograms and a summary of statistical parameters for I_{sph} and I_R, respectively. The mean value (MV) and standard deviation (SD) of I_R for glass beads are 0.965 and 0.043, respecively. The SEM images of glass beads (Figure 2.1a) revealed that the manufacturing and handling processes resulted in the beads not being perfectly spherical, rounded and smooth. Variation of the bead morphology from the processes produced a distribution in the sphericity, roundness, and surface roughness measurements. In fact, some beads are fused together which also explains the slight deviation of the MV of I_R from unity. The MV and SD of I_{sph} of glass beads are 1.096 and 0.433, respectively, where a higher SD is expected since roundness mainly measures the sharpness of particle corners whereas sphericity captures the overall volume of a particle normalized with respect to the volume of a sphere. Also, the distribution of I_{sph} is greatly skewed because of the fused particles ($V_p > V_s$), leading to the seemingly large SD. Figure 2.5 shows that I_R have normal distributions for all

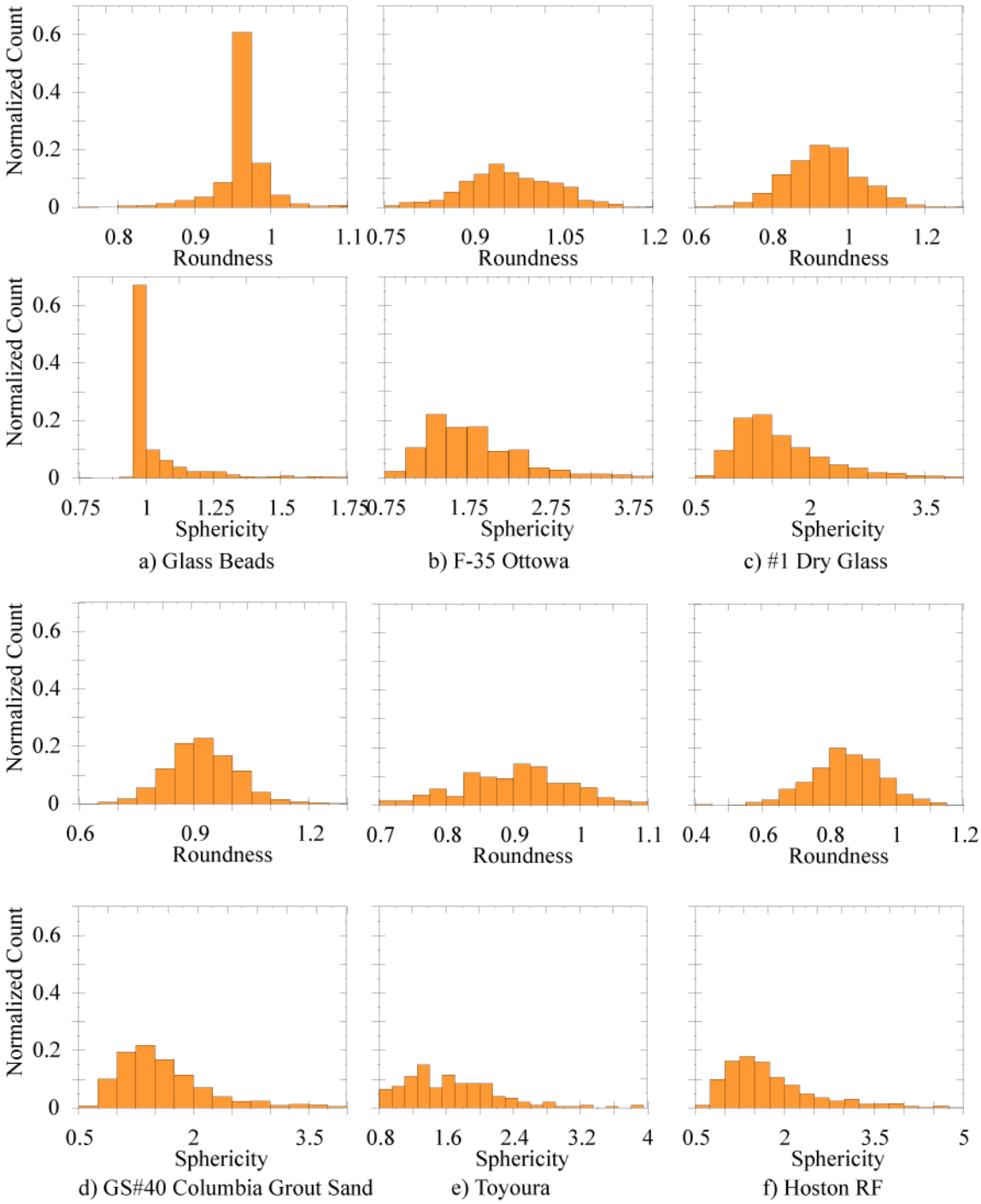

Figure 2.5. Normalized histograms of roundness and sphericity of the sands and the glass beads

Table 2.2. Statistical summary of roundess and sphericity measurements

		Current Study					Komba et al. (2013), Fonseca et al. (2012)	Garboczi and Bullard (2013)
Material	Parameter	d_S (mm)	d_I (mm)	d_L (mm)	I_{Sph}	I_R	3D Sphericity	Sph3D
Glass Beads	Minimum	0.151	0.165	0.1658	0.781	0.767	0.555	0.414
	Maximum	0.429	0.476	0.6673	7.879	1.515	1.089	1.136
	Mean	0.339	0.348	0.3696	1.096	0.965	0.996	0.995
	SD	0.042	0.039	0.061	0.433	0.043	0.045	0.063
F-35 Ottawa	Minimum	0.178	0.238	0.312	0.768	0.665	0.442	0.294
	Maximum	0.445	0.570	0.798	7.278	1.653	1.173	1.271
	Mean	0.331	0.433	0.545	1.872	0.959	0.872	0.817
	SD	0.048	0.049	0.073	0.732	0.083	0.070	0.097
Number 1 Dry Glass	Minimum	0.169	0.194	0.249	0.524	0.553	0.336	0.195
	Maximum	0.464	0.609	0.895	9.891	1.636	1.023	1.035
	Mean	0.309	0.417	0.535	1.704	0.937	0.773	0.682
	SD	0.050	0.054	0.091	0.859	0.106	0.085	0.110
GS40 Columbia Grout	Minimum	0.165	0.200	0.242	0.648	0.542	0.422	0.274
	Maximum	0.472	0.692	0.989	10.585	1.532	1.007	1.010
	Mean	0.309	0.412	0.530	1.674	0.924	0.796	0.712
	SD	0.049	0.055	0.0948	0.799	0.099	0.080	0.105
Toyoura	Minimum	0.123	0.160	0.207	0.795	0.623	0.464	0.316
	Maximum	0.251	0.327	0.564	3.877	1.373	1.102	1.157
	Mean	0.183	0.238	0.313	1.665	0.906	0.839	0.772
	SD	0.026	0.035	0.053	0.579	0.097	0.091	0.124
Hostun RF	Minimum	0.150	0.183	0.192	0.618	0.580	0.261	0.133
	Maximum	0.520	0.658	1.284	11.496	2.351	1.088	1.134
	Mean	0.315	0.442	0.575	1.833	0.904	0.773	0.683
	SD	0.066	0.068	0.102	0.971	0.136	0.091	0.118

sands and glass beads with Hostun RF sand has the highest SD whereas F-35 Ottawa sand has the lowest SD among the sands (Table 2.2). I_{sph} histograms (normalized) are skewed and have wider distribution ranges when compared to I_R (Figure 2.5) which is also manifested in higher SD where Hostun RF sand again has the highest SD followed by #1 dry glass sand (Table 2.2).

For each of the materials, Table 2.2 also compares I_{sph} to 3D sphericity as presented by Fonseca et al. (2012) and Komba et al. (2013), $\boldsymbol{sphericity} = \frac{\sqrt[3]{36\pi V^2}}{A}$, as well as $\boldsymbol{SPH3D} = \frac{6\pi^{1/2}V}{SA^{1.5}}$ presented by Barboczi and Bullard (2013). The mean of the new proposed measure, I_{sph}, deviates more from unity than the either of the sphericity indices presented in the literature, especially for as particles that are non-sphericial. The SD is also much larger for the new proposed I_{sph}. This is an indication that the proposed I_{sph} amplifies the effect of non-spherical particles. No comparison of roundness is presented in this paper because there is a lack of well-defined equations to calculate 3D roundness in the literature.

2D Versus 3D Roundness and Sphericity Measurements

It is common to use 2D images to quantify roundness and sphericity of granular materials. The question is: does 2D projection image of a particle yield a correct measure of particle roundess and sphericity? To answer the question, the roundess (I_{R-2D}) and sphericity (I_{sph-2D}) indices for 2D images are defined as:

$$I_{sph-2D} = \frac{A_a}{A_s} \qquad (2.4)$$

$$I_{R-2D} = \frac{0.78\ perimeter}{\pi(\frac{d_L+d_s}{2})} \quad (2.5)$$

Where A_a and A_s are the actual area of the particle and the area of a circle with a diameter equal to d_S, respectively. In a digital image (e.g., Figure 2.4b), square pixels are counted to calculate the perimeter of particles in 2D which slightly overestimates the value of perimeter; therefore a factor of 0.78 in Equation 2.5 is necessary to correct the perimeter measurement from digital images. It is found based on a simple calibration process by digitally calculating the perimeter of a spherical particle and comparing it to πd where d is particle diameter.

Figure 2.6 shows a comparison between 2D and 3D roundness and sphericity of all granular materials used in this study. Initial investigation of this data gives the impression that the 2D and 3D samples do not produce the same results (same mean and standard deviation), and warrants quantative statistical analysis. To test the null hypothosis that the two means are the same, a two-sample t-test was condcuted on each of the materials. The null hypothesis was rejected for every sample even at very low significance levels (<0.001). For spheres with smooth surfaces, one expects no difference between 2D and 3D analysis. However, the variance of morphology of the glass beads from the manufacturing process (Figure 2.1a) caused a statistical difference between 2D and 3D roundness and sphericity indices. However, there is a difference between 2D and 3D roundness and sphericity indices for the sands where were much more statistically different as determined by visual inspection of the histograms (Figure 2.6) and from the two-sample t-test analysis. I_R has smaller values than I_{R-2D} whereas I_{sph} has higher

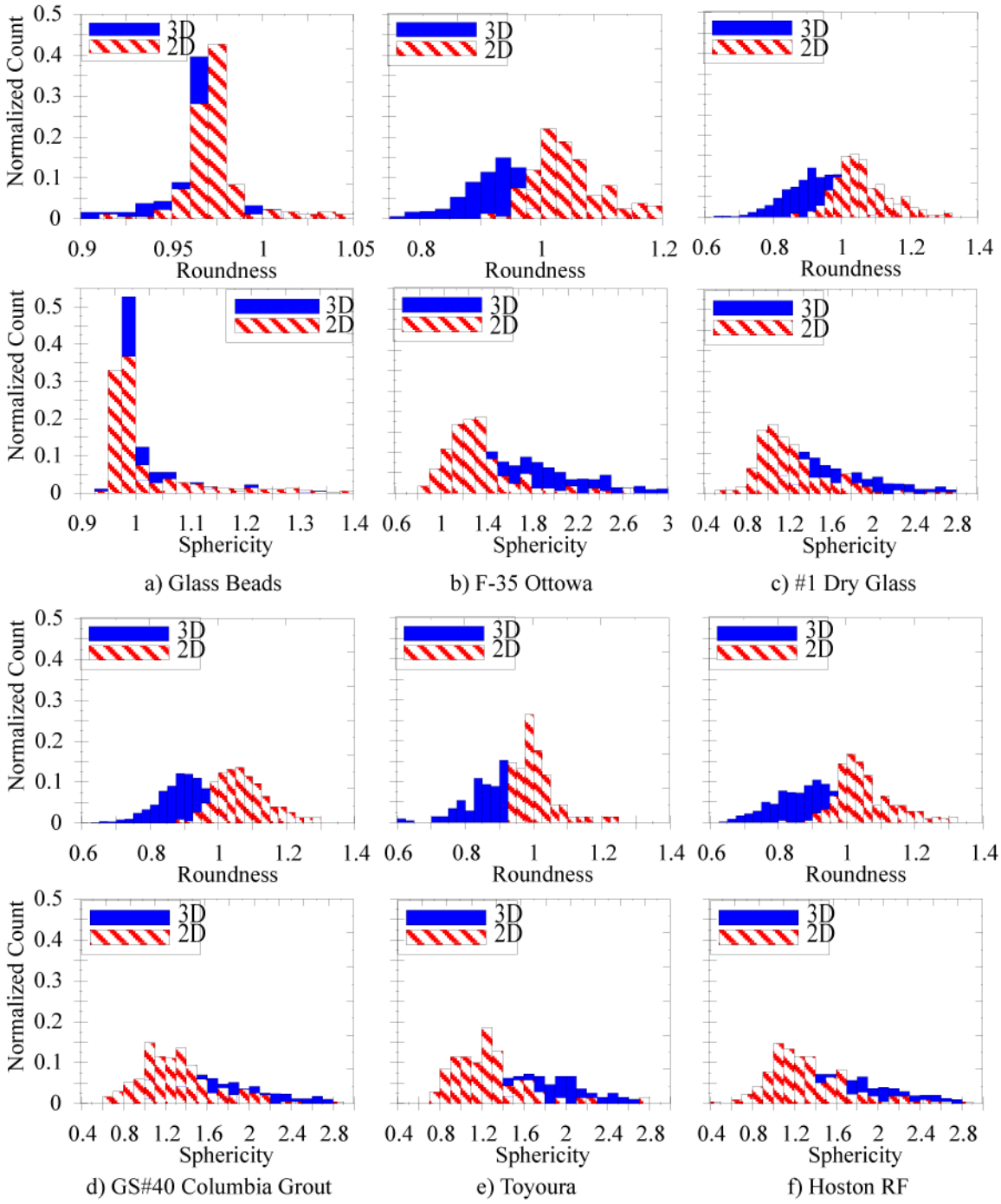

Figure 2.6. Comparison of 2D versus 3D sphericity and roundness indices for glass beads and F-35 sand

values than I_{sph-2D} and spreads over a wider range. These results demonstrate that quantifying particle sphericity and roundness based on 2D projection image of a particle will result in a different classification of particle morphology when compared to 3D for non-spherical particles and it is necessary to use 3D images to obtain accurate measures of roundness and sphericity. The differences between 2D and 3D are caused by several factors. In particular, the orientation of a particle in a 2D slice might not show the true short and/or long axes, which would certainly affect the roundness of the particle. This is evident from Figure 2.6 as the 3D roundness for each sample has a wider distribution. Also, indices based on 2D projects, even if aligned perfectly to display the shortest and longest axes of the particle, do not provide any information about the third dimension. If the third dimension had no effect on the particle morphology, the distributions could be the same. The effect of the third dimension and true particle lengths (short, intermediate, long) on the response of a granular system could be significant. For example, a cylindrical particle could have the same short and long diameters as a flat, platy particle. However, the platy particle will resist rolling in the intermediate direction much more than a cylindrical particle.

Surface Texture Measurements

Surface texture measurements were conducted using VEECO IMOA optical surface profiler of the Center for Nanophase Materials Sciences (CNMS) of Oak Ridge National Laboratory (ORNL). It is a non-contact optical profiler that uses two techniques to measure a wide range of surface heights. Figure 2.7 shows a photograph of the profiler.

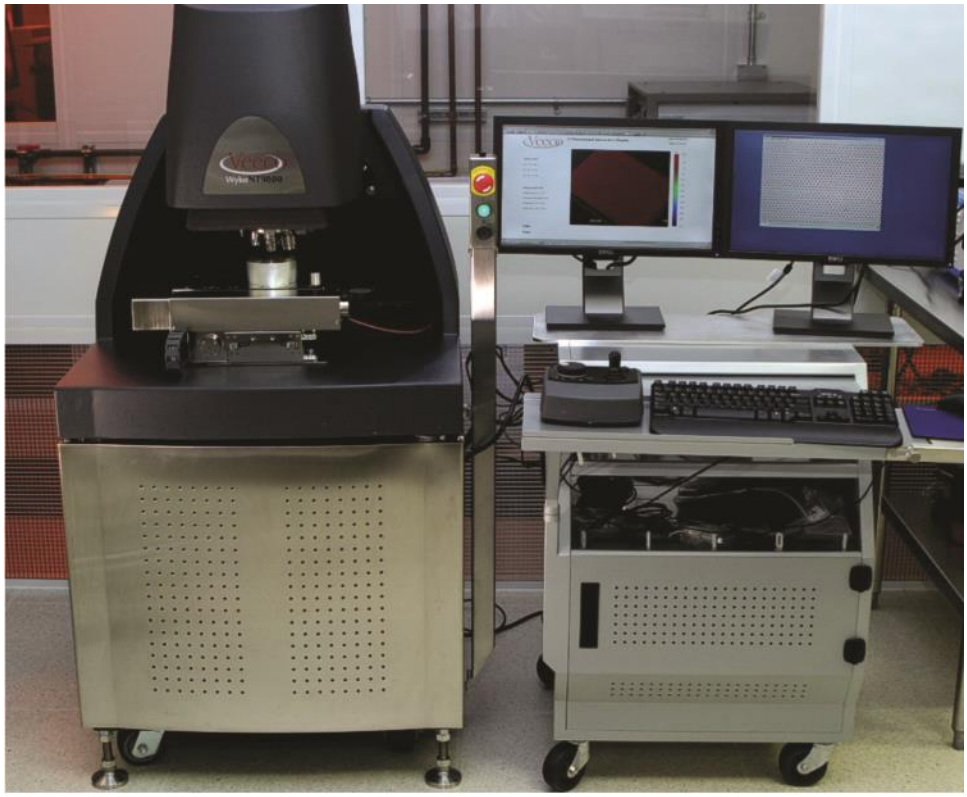

Figure 2.7. Photo of the Veeco optical profiler

It has two operating phase; Phase Shifting Interferometry (PSI) mode allows measuring smooth surfaces and steps, while the Vertical Scanning Interferometry (VSI) measures rough surfaces and steps up to millimeters high. Vertical scanning interferometry (VSI) measurement mode was used to collect spatial surface profile of the area. VSI is more ideal for capturing the surface profile for relatively rough surfaces (roughness greater than 100 μm) or surfaces with discontinuities greater than 135 nm, which is a common occurrence in natural particles. The maximum vertical scan range of VSI (10 μm) was needed because the particles were relatively large and discontinuities within the field of view (FOV) were often close to or exceeded 10 μm, especially if the FOV was located near the edge of a particle. To overcome large discontinuities within the FOV, surface profiles were taken on areas of the particle that were normal to the lens, minimizing lost data. The resolution of the system at the VSI mode is 10 nm. Scanning processing include subtracting the effect of the curvature of the particle surface.

Particles of each sand type were placed on a glass slide and inserted on to the sample stage. A lens with 10X zoom was used to locate a specific particle and the turret was rotated to the 50X lens with a 2.0X objective, resulting in an overall magnification of 100X and a 0.06 x 0.05 mm FOV. Figure 2.8 shows example 3D renderings of particles' surface profile of glass beads, #1 dry glass sand, and GS#40 Columbia sand. Approximately 30 particles from each of the sands were scanned, with 2 to 3 scans per particle. They were arbitrarily selected among each slide. The profilor is supplemented with computer software in which a series of mathematical algorithms are executed for

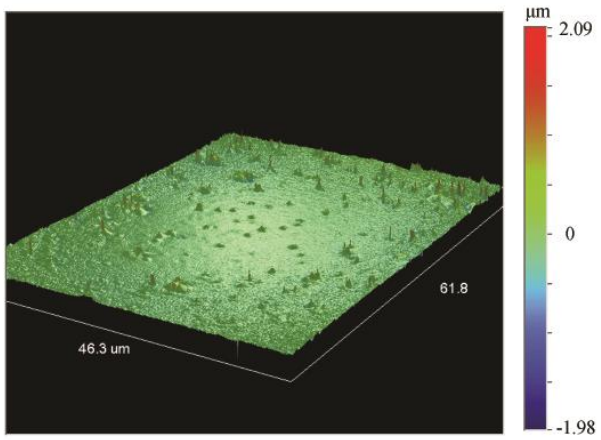

a) Glass Beads

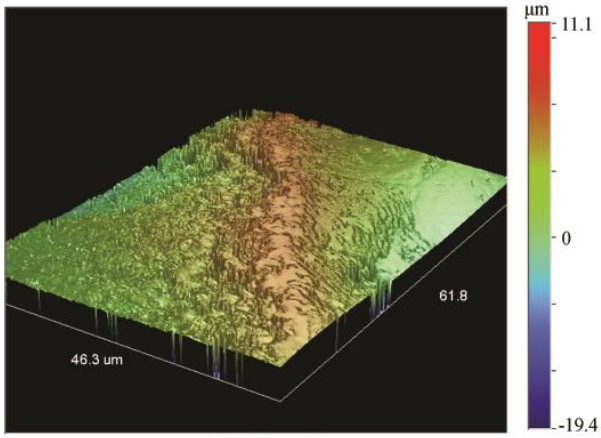

c) #1 Dry Glass

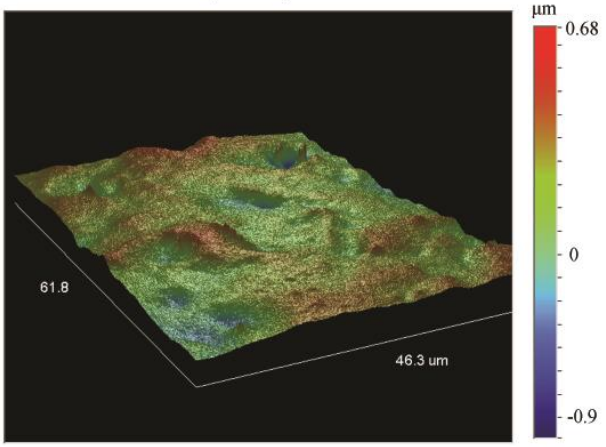

d) GS#40 Columbia Grout

Figure 2.8. Example surface profiles showing particle surface texture of glass beads, #1 dry sand, and GS#40 Columbia sand

each scan to estimate different texture indices. The following texture indices were calculated for each sand particle:

- Average texture (R_a): is the arithmetic mean of the absolute values of the surface departure from the mean plane.

$$R_a = \frac{1}{MN}\sum_{i=1}^{M}\sum_{j=1}^{N} Z_{ij} \qquad (2.6)$$

Where *M* and *N* are the number of pixels in X and Y direction, Z_{ij} is the surface height at a specific pixel relative to the reference mean plane. R_a is usually used to describe the texture of a finished surface, so it can be used to describe the texture of the sand particle surface. The main disadvantage that might be encountered here is, with average texture, the effect of a single spurious, non-typical peak or valley will be averaged out and have only small influence on the overall texture. So this index or average will give no information about the shape of the irregularities or the surface of the particle. For granular materials and particle–to–particle friction, R_a represents, to some extent, the overall texture used for friction calculations.

- Root mean square texture (R_q): is calculated as follows:

$$R_q = \sqrt{\frac{1}{MN}\sum_{i=1}^{M}\sum_{j=1}^{N} Z_{ij}^2} \qquad (2.7)$$

It represents the standard deviation of the surface heights. R_q has the same disadvantage as the R_a does. The advantage of using R_q over R_a is that R_q squares the heights, giving more significance to the valleys and peaks.

Table 2.3 lists a statistical summary of surface texture measurements of glass beads and the sands. One can notice that statistical parameters for R_q are slightly higher

than those for R_a for each of the sands and glass beads. As expected, the glass beads have the lowest surface texture. Toyoura sand has the lowest mean and SD of both R_a and R_q among sands, which corresponded with observations of SEM images (e.g., Figure 2.1e) where particles consisted of faceted relatively smooth surfaces. GS#40 Columbia sand has the highest SD of R_a and R_q values as well as the highest maximum values of both R_a and R_q.

Influence of Particle Morphology on Friction Angle of Granular Materials

The effect that sphericity, roundness, and surface texture have on the behavior of granular material is studied by comparing the friction angle of the relatively spherical, rounded, and smooth glass beads to that of the F35 sand, which is more angular and rough. To determine the friction angle, samples of glass beads and F35 sand were prepared at the same relative density and tested at the same confining pressure. The peak friction angle of the glass beads for the test was found to be 29.6^o and for F35 sand was 37^o. Figure 2.9 shows the friction angle of the two granular materials as a function of sphericity, roundness, and surface roughness and demonstrates that the friction angle seems to be impacted by sphericity and surface roughness. However, further analysis is warrented because the increase in friction angle could be a result from one, two, or all three of these measures. Therefore, a more detailed statistical study on the effects of

Table 2.3. Statistical parameters for Ra and Rq

Sand	Statistics	R_a (μm)	R_q (μm)	Sand	Statistics	R_a (μm)	R_q (μm)
Glass Beads	Minimum	0.048	0.082	GS#40 Columbia Grout	Minimum	0.081	0.102
	Maximum	6.994	8.051		Maximum	9.467	11.099
	Mean	0.248	0.381		Mean	1.504	1.923
	Median	0.142	0.240		Median	1.189	1.581
	Root mean square	0.859	1.015		Root mean square	2.228	2.754
	SD	0.829	0.947		SD	1.654	1.986
	Standard error	0.100	0.114		Standard error	0.191	0.229
F-35 Ottawa	Minimum	0.175	0.235	Toyoura	Minimum	0.381	0.499
	Maximum	9.259	11.284		Maximum	3.930	4.901
	Mean	1.612	2.084		Mean	1.436	1.847
	Median	1.291	1.649		Median	1.265	1.660
	Root mean square	2.124	2.677		Root mean square	1.616	2.065
	SD	1.392	1.693		SD	0.748	0.932
	Standard error	0.165	0.201		Standard error	0.097	0.120
#1 Dry Glass	Minimum	0.282	0.386	Hostun RF	Minimum	0.275	0.362
	Maximum	3.976	5.273		Maximum	3.711	4.862
	Mean	1.570	1.990		Mean	1.505	1.972
	Median	1.319	1.701		Median	1.333	1.715
	Root mean square	1.823	2.287		Root mean square	1.692	2.207
	SD	0.933	1.135		SD	0.781	1.001
	Standard error	0.108	0.131		Standard error	0.103	0.133

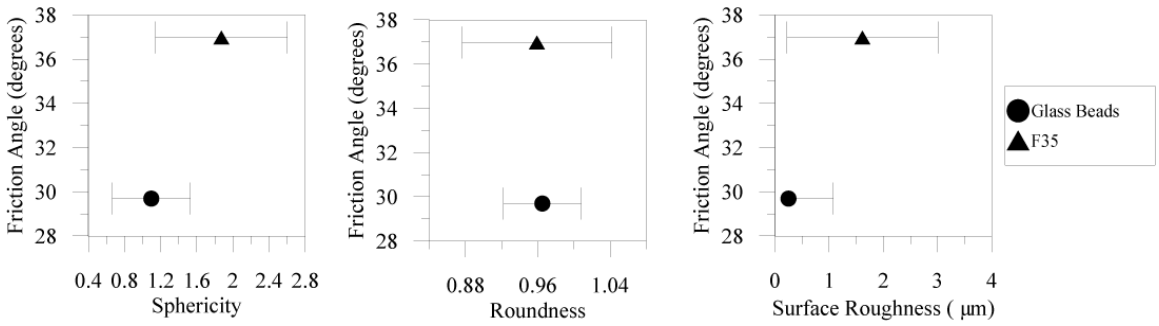

Figure 2.9. Example of the effects that sphericity, roundness, and surface roughness on friction angle of a granular material

sphericity, roundness, and surface roughness on the shear strength and particle kinematics will soon be conducted in order to better quantify the individual and combined effects of these measures.

Summary and Conclusions

Morphology of five sands and glass beads were quantified and discussed in this paper. 3D synchrotron micro computed tomography was used to acquire high-resolution images of particles of sands and glass beads. New sphericity and roundness indices are introduced to calculate roundness and sphericity using 3D SMT images of particles. They are independent measures that represent two different morphological properties of granular materials. The use of 2D images give different results when compared to 3D images if particles are not spherical and do not have a smooth surface, therefore it is necessary to use 3D images to obtain accurate measures of roundness and sphericity.

Surface texture was also accurately quantified for the sands and glass beads using optical interferometry technique. Texture parameters were defined and calculated for the sands and glass beads used in the study. It is apparent that particle morphology and surface roughness can play a role in the friction angle of granular material, and a more detailed analysis of these effects on the strength of granular material is justified and will soon be conducted.

References

Al-Raoush, R. (2007). “Microstructure characterization of granular materials.” *Physica A,* A377, 545-558.

Al-Rousan, T., Masad, E. Tutumluer, E. and Pan, T. (2006). “Evaluation of Image Analysis Techniques for Quantifying Aggregate Shape Characteristics.” *Elsevier, Construction and Building Materials*, 21, 978-990.

Alshibli, K. A. and Alsaleh, M. (2004). “Characterizing Surface Roughness and Shape of Sands Using Digital Microscopy.” *ASCE, Journal of Computing in Civil Engineering*, 18(1), 36-45.

Alshibli, K.A. and Reed, A. (ed.) *Advances in Computed Tomography for Geomaterials: Geox2010*. ISTE – John Wiley & Sons, Inc., 2010.

Bessa, I. S., Castelo Branco, V. T. F., and Soares, J. B. (2012). “Evaluation of different digital image processing software for aggregates and hot mix asphalt characterizations.” Constr Build Mater, 37(0), 370-378.

Bloom, M., Russell, M., Kustau, A., Mandayam, S., and Sukumaran, B. “An X-ray computed tomography technique for the measurement of packing density in granular particles.” Proc., Instrumentation and Measurement Technology Conference, 2009. I2MTC '09. IEEE, 74-79.

Content, P. and Ville, JF. (1995). “Surfascan 3D–An Industrial 3D Surface Texture Characterization Instrument.” *Int. J. Mach. Tools Manufacturing,* 35,151-156.

Cox, M. R., and Budhu, M. (2008). “A practical approach to grain shape quantification.” Engineering Geology, 96(1–2), 1-16.

Desrues, J., Viggiani, G., and Besuelle, P. (ed.) *Advances in X-ray Tomography for Geomaterials*. ISTE, Great Britain, 2006.

Duttine, A., Tatsuoka, F., Kongkitkul, W., and Hirakawa, D. (2008). “Viscous Behavior of unbound Granular Materlas in Direct Shear.” *Soils and Foundations,* 48(3), 297-318.

Fonseca, J., O’Sullivan, C., Coop, M. R., and Lee, P. D. (2012). "Non-invasive characterization of particle morphology of natural sands." Soils and Foundations, 52(4), 712-722.

Garboczi, E. J., and Bullard, J. W. (2013). "Contact function, uniform-thickness shell volume, and convexity measure for 3D star-shaped random particles." Powder Technology, 237, 191-201.

Garbout, A., Munkholm, L. J., and Hansen, S. B. (2013). "Temporal dynamics for soil aggregates determined using X-ray CT scanning." Geoderma, 204, 15-22.

Grigoriev, A. Y. A., Chizhik, S.A. , and Myshkin, N. K. (1998). “Texture Classification of Engineering Surfaces with Manoscale Roughness.” *Int. J. Mach. Tools Manufacturing,* 38(5-6), 719-724.

Hong, H-K., Myung, Y-C, and Choi, J-S. (1999). “3-D Analysis of Projective Textures Using Structural Approaches.” *Pattern Recognition* 32, 357-364.

James P. H. and Vallejo, L. E. (1997). “Fractal Analysis of the Roughness and Size Distribution of Granular Materials.” *Engineering geology*, 48, 231-244.

Kinney, J. H. and Nichols, M. C. (1992). Annual Review of Materials Science. 22, 121.

Komba, J., Anochie-Boateng, J., and van der Merwe Steyn, W. (2013). "Analytical and Laser Scanning Techniques to Determine Shape Properties of Aggregates." Transportation Research Record: Journal of the Transportation Research Board, 2335(-1), 60-71.

Kwan, A. K. H., Mora, C. F., and Chan, H. C. (1999). "Particle shape analysis of coarse aggregate using digital image processing." Cement Concrete Res, 29(9), 1403-1410.

Lee, Y-G., Lee, J-H., amd Hsueh, Y-C. (1998). “Texture Classification Using Fuzzy Uncertainty Texture Spectrum.” *Neurocomputing*, 20, 115-122.

Masad, E., Olcott, D., White, T. and Tashman, L. (2001). “Correlation of fine Aggregate imaging shape indices with asphalt mixture performance.” *Transportation Research Board*, 1757, 148-156.

Otani, J. and Obara, Y. (ed.) (2004). *X-Ray CT for Geomaterials: Soils, Concrete, Rocks*. Swets & Zeitlinger B.V., Lisse, The Netherlands, 2004.

Pettijohn, F. J. (1949). Sedimentary Rocks. Harpers and Brothers, New York.

Powers, M. C. (1953). “A New Roundness Scale for Sedimentary Particles.” *Journal of Sedimentary Petrology*, 23(2), 117-119.

Powers, M. C. (1982). “Comparison Charts for Estimating Roundness and Sphericity.” *AGI Data Sheets*, American Geological Institute.

Russel, R. D. and Taylor, R. E. (1937). “Roundness and Shape of Mississippi River Sands.” *Journal of Geology*, 45, 225-267.

Smith, M.L. (1999). “The analysis of surface texture using Photometric stereo acquisition and gradient space domain mapping.” *Image and Vision computing*, 17, 1009-1019.

Sukumaran, B., and Ashmawy, A. K. (2001). "Quantitative characterisation of the geometry of discret particles." Géotechnique, 619-627.

Sun, W., Wang, L., and Tutumluer, E. (2012). "Image Analysis Technique for Aggregate Morphology Analysis with Two-Dimensional Fourier Transform Method." Transportation Research Record: Journal of the Transportation Research Board, 2267(-1), 3-13.

Wadell, H. (1932). “Volume Shape and Roundness of Rock Particles.” *Journal of geology*, 40, 443-488.

Wang, L.B., Wang, X., Mohammad, L., and Abadie, C. (2005), "Unified method to quantify aggregate shape angularity and texture using fourier analysis", *Journal of Materials in Civil Engineering, ASCE*, 17(5): 498-504.

Zavala, J. M. R. (2012). "Particle Shape Quantities and Influence on Geotechnical Properties - A Review." Ph.D. , Luleå University of Technology Luleå , Sweeden.

CHAPTER 3

3D FINITE ELEMENT MODELING OF SAND PARTICLE FRACTURE BASED ON IN SITU X-RAY SYNCHROTRON IMAGING

A version of this chapter was originally published in: Druckrey, A. M., and Alshibli, K. A. (2016). "3D finite element modeling of sand particle fracture based on in situ X-Ray synchrotron imaging." *International Journal for Numerical and Analytical Methods in Geomechanics*, 40(1), 105-116.

My primary contributions to this paper include (i) formulating objectives and evaluating current research in the area, (ii) conducting experiments during in-situ SMT imaging, (iii) development of methodology to conduct finite element analysis on real particle shapes using SMT imaging, (iv) implementation of fracture model to simulate experimental particle fracture, (v) analysis of experimental and finite element simulation results, (vi) most of the writing.

Abstract

Compressive loading of granular materials causes inter-particle forces to develop and evolve into force chains that propagate through the granular body. At high-applied compressive stresses, inter-particle forces will be large enough to cause particle fracture, affecting the constitutive behavior of granular materials. The first step to modeling particle fracture within force chains in granular mass is to understand and model the fracture of a single particle using actual three-dimensional (3D) particle shape. In this paper, fracture mode of individual silica sand particles was captured using 3D x-ray radiography and Synchrotron Micro-computed Tomography (SMT) during in situ compression experiments. The SMT images were used to reconstruct particle surfaces through image processing techniques. Particle surface was then imported into Abaqus

finite element (FE) software where the experimental loading setup was modeled. The constitutive behavior of the particle was modeled using the extended finite element method (XFEM) where particle fracture was compared to experimental fracture mode viewed in radiograph images that were acquired during experimental loading. Load-displacement relationships of the FE analysis were also compared with experimental measurements. 3D FE modeling of particle fracture offers an excellent tool to map stress distribution and monitors crack initiation and propagation within individual sand particles.

Introduction

Particle fracture plays a significant role in the constitutive behavior of granular materials at high applied stresses. For example, McDowell and Bolton (1998) updated the relative density index proposed by Bolton (1986) to include the mean tensile strength of particles because it provides a more micromechanical insight into the dilatant behavior of crushable soils. More micromechanical insight can be achieved by determining the interaction of particles and how force chains develop and evolve during meso-scale testing. The geometry of force chains in a granular material mass is influenced by the fabric, boundary conditions, and applied stresses. Fabric or structure is defined here as the arrangement of particles, particle groups, and the associated pore space. It is directly affected by particle morphology (e.g. Edwards and Grinev 1999; Maeda et al. 2010; Tordesillas and Muthuswamy 2009; Wang et al. 2011). As applied compressive stresses increase, force chains transmit larger forces between particles, eventually leading to

particle fracture. The first step to modeling particle fracture within force chains in a granular material using actual particle morphology is to model and understand the micromechanics of compression and fracture of a single particle.

Many theories and approaches have been reported in the literature to describe particle fracture, and most common approach is to try to relate the failure stress within the particle to the applied failure force on the particle or granular mass. For example, Brzesowsky et al. (2011) have developed theoretical models that describe particle strength and flaw size using Weibull statistics based on failure data obtained from experiments. Cavarretta and O'Sullivan (2012) used a micromechanical approach to describe the compression of individual particles and developed models that incorporated frictional sliding, bulk particle compression, and fragmentation based on geometry and kinematic degradation of stiffness. More recently, Alshibli et al. (2013) used 3D x-ray diffraction to measure strains within individual silica particles in compression and calculated the stresses based on particle strain.

The objective of this paper is to import a high-resolution 3D representation of a single particle from an SMT image into FE modeling Abaqus software and model particle fracture using the XFEM. Crack initiation and propagation is modeled and compared to radiograph images that capture fracture of individual silica sand particles. The radiograph images are fast enough to capture live in situ images of particle fracture whereas accurate high-resolution 3D volume representation of particles is created using the SMT technique. Similar achievements have been reported in the medical field F(e.g. Barrett et

al. 2010; Cattaneo et al. 2001; Tajima et al. 2009; Tsuda et al. 2008); however to the best our knowledge, SMT images of individual sand particles have not been collected during in-situ compression and fracture.

Experimental measurements

Unconfined Compression Experiments

One-dimensional (1D) unconfined compression experiments were conducted on individual particles of ASTM 20-30 Ottawa sand using the apparatus shown in Figure 3.1. ASTM 20-30 Ottawa sand is a natural silica sand with rounded to sub-rounded particles with particle size between US sieve #20 (0.85 mm) and sieve #30 (0.59 mm). The particle is placed between two 0.4 mm diameter aluminum plates (#4 and #7 in Figure 3.1) that are kept concentric using an aluminum cylindrical guide tube (#5 in Figure 3.1). The bottom loading plate is fixed to the bottom plate of the loading cell whereas the top loading plate rests freely on the particle. A stepper motor drives the top end plate at a constant displacement rate of 1 μm/minute and a 90 lb load cell was used to record the axial load with resolution of 0.1%. An initial load of 0.3 N was first applied to stabilize the particle during the first x-ray SMT scan that was acquired to obtain a high-resolution reconstructed image of the particle. Since it takes few minutes to acquire SMT images and we wanted continuous loading up to fracture stage to capture particle fracture initiation and propagation; multiple radiographs were collected while loading the particle. Radiographs represent 2D projection image of the particle and takes a fraction of second

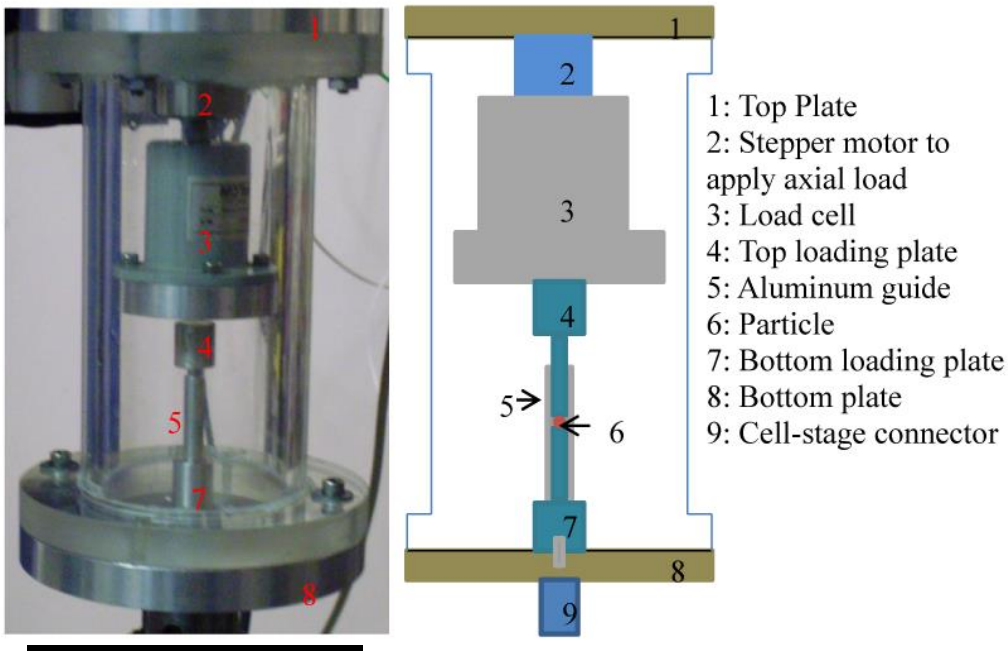

Figure 3.1. Experimental 1D unconfined compression test setup for a single sand particle

to acquire each. Displacements during experiments were measured with SMT images and radiographs to very high accuracy.

Imaging Acquisition and Post-Scan Processing

SMT is a non-destructive high-resolution imaging technique that can produce 3D images of the particle using x-ray transmission. The specimen is placed between the x-ray source and the detector, and a high-energy monochromatic x-ray beam produced by synchrotron sources is attenuated as it travels through the particle. The absorption level primarily depends on the properties of the scanned object (chemical composition and geometry) and the energy level of the x-ray. A scintillator converts the transmitted beam to visible light which is projected onto a detector and recorded by a camera system (Figure 3.2).

The x-ray SMT and radiograph images were collected at GeoSoilEnviroCARS (GSECARS) of the Advanced Photon Source (APS), Argonne National Laboratory (ANL), Illinois, USA. Beamline 13D was used to collect the data using a beam size of 1.38 mm horizontal × 1.03 mm vertical. Scans were acquired at 1^{o} rotation increments by rotating the specimen between 0^{o} and 180^{o} with 1 second exposure time, resulting in a set of 2D radiographs with spatial resolution of 1.98 μm/voxel (see (Rivers et al. 2010) for more information about the setup of beamline 13BMD). An example radiograph image of a particle is shown in Figure 3.3a. The reconstructed SMT data provides an accurate 3D image of the particle as depicted in Figure 3.3b. Each voxel has a unique attenuation

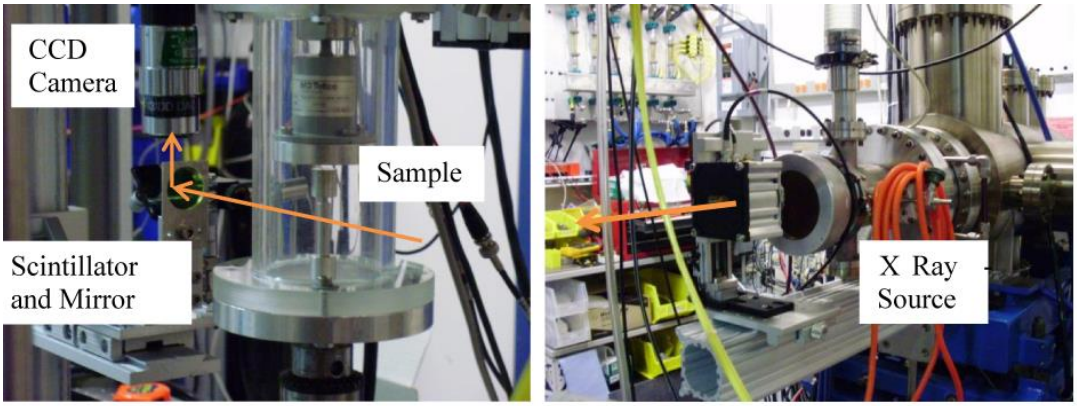

Figure 3.2. GSECARS Beamline 13BMD Experimental Hutch Setup

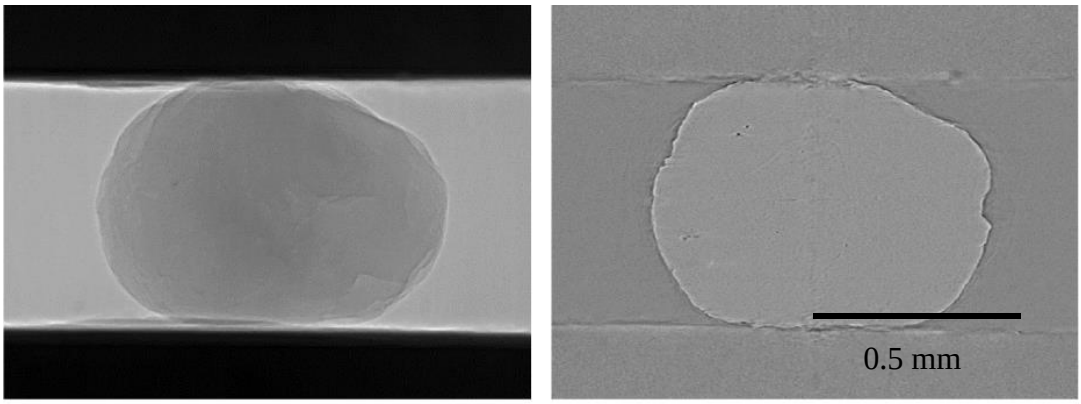

Figure 3.3. Images of (a) corrected preprocessed data (radiograph) and (b) slice of 3D reconstructed SMT image.

coefficient based on the x-ray attenuation of that particular voxel resulting in different shades of greyscale.

The goal of post-scan image processing is to create an accurate 3D triangulated surface of only the particle by eliminating the surrounding air and loading plates. A filter within Avizo Fire software was first applied to smooth the images while preserving the boundary contrast. A comparison of the original image and filtered image is depicted in Figure 3.4a&b. Next the image was binarized for further image processing. Since there was a small contrast between the background and particle, the entire image excluding the boundary between particle and air was segmented (Figure 3.4c). Small holes within the image were then filled (Figure 3.4d) and the particle was separated from the surrounding air and loading plates (Figure 3.4e). Finally, borders were deleted leaving only a binary image of the particle (Figure 3.4f).

A 3D surface of the particle was generated using Avizo Fire software so that a tetrahedral volume mesh can be implemented in the finite element analysis software. The surface is generated using triangular elements that are smoothed to inhibit the voxelated nature of the 3D image. The smoothing is necessary to mimic the physical particle surface more realistically and is valid since the voxel size is significantly smaller than the size of any pertinent surface features of the particle. The triangulated surface of the particle (Figure 3.5) is completely closed and saved as a stereolithography (STL) file in order to be exported to Abaqus Finite Element (FE) software.

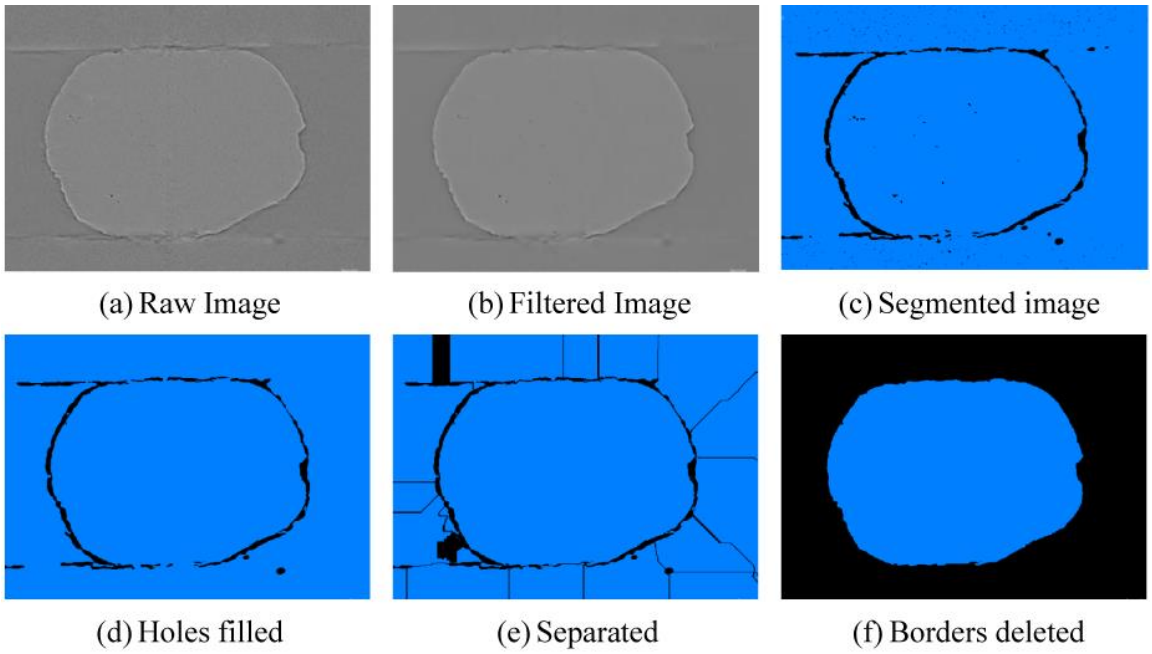

Figure 3.4. Workflow of the image post-processing steps

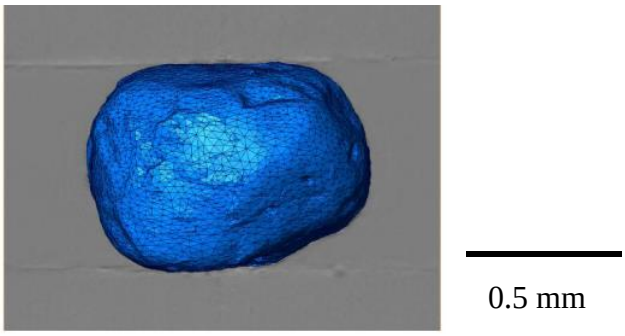

Figure 3.5. Triangulated particle surface with greyscale ortho-slice

Finite Element (FE) Analysis

Model Setup

Abaqus FE software was used to model particle fracture behavior. The STL file of the triangulated surface was imported into Abaqus through a plug-in tool of Abaqus. Using the edit mesh toolset, the 3D shell of triangular elements was converted into a solid mesh of tetrahedral elements. The mesh is constructed to optimize the efficiency of each element and the tetrahedral element faces are approximately the same size as the triangular elements. 3D revolved discrete rigid shell surfaces were created and assembled on the particle to simulate the experimental setup of the loading plates. Discrete rigid shells do not deform but can measure contact force at each node, similar to the interaction between the experimental load cell and the particle.

The general contact algorithm in Abaqus-Standard was implemented to define contact between the loading plates and the particle. The particle was defined as the slave mesh and the loading plates were the master. Contact properties were assigned to not allow the meshes to overlap. Because of the rough nature between the loading plate and particle as seen in the x-ray SMT images (Figure 3.3), the tangential behavior in the model was defined to be rough. When friction was used in the model with penalty friction formulation, the particle completely separated from the loading plates during analysis even when a high friction coefficient was assumed. Therefore rough friction formulation was adopted to model the experiment.

Material Properties

Elements are assumed to have a linear isotropic elastic behavior before failure. Although silica sand particles have slight anisotropic material properties, no crystalline structure data was collected on these particular particles and anisotropy could not be implemented in the FE model. The Young's elastic modulus and Poisson's ratio of silica sand are assumed to be 94.4 GPa and 0.118, respectively (Heyliger et al. 2003). In this paper the cracks are modeled as enriched features using XFEM since it allows for the detection of crack initiation and propagation and the crack can be visualized within the particle. Fracture and propagation of a discrete crack in XFEM is based on stresses (or strains) within the particle and the crack is mesh-independent. However, the material and geometrical nonlinearities introduced during fracture requires extremely small time steps and step stabilization for convergence as the crack propagates through the particle.

XFEM mitigates problems of meshing cracked surfaces which occur in traditional FE fracture models and allows for a solution-dependent path without the requirement of remeshing. XFEM was first introduced by Belytschko and Black (1999)) as an extension to the FE method that incorporates nodal enrichment functions based on the concept of partition of unity. Nodal enrichment functions allow discontinuities within the continuum by enriching degrees of freedom with special displacement functions u (ABAQUS 2011):

$$u = \sum_{I=1}^{N} N_I(x)[u_I + H(x)a_I] \qquad (3.1)$$

where $N_I(x)$ are the FE shape functions, u_I is the nodal displacement vector of the continuum observed in standard FE solutions, $H(x) = \begin{cases} 1 \; if \; (x - x*).n \geq 0 \\ -1 \; otherwise \end{cases}$ is the

discontinuous jump function where x is a Gauss point, x* point on the crack closest to that Gauss point and n is the unit outward normal to the crack at x, and a_I is the nodal enriched degree of freedom vector. The first term within the brackets applies to all nodes within the enriched part of model as normal and the second term applies when nodes within the shape function are cut by the crack. Near-tip asymptotic singularity is not considered within this approach because the computational effort for a propagating crack is too demanding, requiring the crack to propagate across an entire element at a time while not having to follow mesh contours. This assumption is valid in the current research because we are more interested in determining how cracks propagate through the particle rather than analyzing exact stresses at the crack tip.

The XFEM approach used in this research is based on traction-separation cohesive behavior and phantom nodes, which is very general and can be used for modeling brittle or ductile fracture (ABAQUS 2011). The phantom node is completely constrained to the real node when the element is intact. When a crack propagates through the element, the element splits into two parts connected by the phantom node but free to move apart. The cohesive law input into the model determines the magnitude of separation of the real and phantom nodes until element degrades to zero cohesive strength. Modifying the cohesive law controls whether the fracture is brittle or ductile and determines the rate of crack propagation.

Maximum nominal stress criterion was used to determine the initiation of fracture in the particle. Purely compressive states will not initiate damage and the tensile and

shear stresses at failure are required for the model, which coincides with particles fracturing because of tensile forces. Cracks are introduced or extended when the fracture criterion, $f = max\left\{\frac{t_n}{t_n^o}, \frac{t_s}{t_s^o}, \frac{t_t}{t_t^o}\right\}$, reaches one within a small tolerance. t_n is the stress normal to the crack (tensile stress) and t_s and t_t are the shear stresses to the cracked surface in the simulation. The failure stresses are input as t_n^o, t_s^o, and t_t^o. Stresses within particles of silica sand during compression were determined experimentally by Alshibli et al. (2013) using high-energy synchrotron diffraction up to fracture. The results of their research provided nominal normal and shear stresses at the failure stage of individual particles. The tensile stress at failure was determined to be 25.3 MPa and the two shear components were determined to be 12.6 MPa and 8.7 MPa. The crack will initiate and/or propagate when stress within the particle reaches the specified failure stresses.

After initial damage (i.e. fracture criterion is reached) particles of silica sand, a natural quartz, are known to fail via a brittle mode (Bieniawski 1967; Chelidze et al. 1994) therefore, damage evolution (crack propagation) in the model should reflect this behavior. Damage evolution in Abaqus can be defined in many ways for a brittle material and the methods for choosing damage evolution are rather empirical. In this paper, the damage evolution law is based on the rate of degradation of cohesive stiffness after damage is initiated. Mode-independent fracture energy with linear softening was defined with relatively small fracture energy to represent the quick and brittle nature of the crack. The cohesive strength of the real and phantom nodes will quickly reach zero after failure stresses are reached.

Boundary Conditions

To simulate experimental loading, the bottom load plate in the model was fixed with zero degrees of freedom throughout the analysis. The top plate was allowed one degree of freedom in the vertical direction, while the particle was unrestrained and permitted to move and rotate during loading. A constant displacement was applied on the top plate to load the particle in the same way as the experiment. The FE simulations were ran until crack onset and propagation.

Results

2D Mesh Analysis

An initial mesh sensitivity analysis was first conducted on a 2-dimensional (2D) particle to assess the effect of mesh size on particle loading and failure mode. A 2D model of a disc with diameter of 0.8 mm (close to size of analyzed particles) was used to simulate a particle. All material properties were kept the same for each of the simulations, varying only the approximate global seed size for mesh generation. FE analysis was conducted on the 2D particle with varying mesh sizes until divergence occurred. Divergence occurs as the crack quickly propagates through the particle (brittle failure) because of numerical instabilities inherent in the model, therefore cracks propagate to different lengths. Crack length in the 2D model was not of much concern because once initial damage occurs (crack initiation), the failure mode is brittle and the crack would theoretically propagate entirely through the particle with minimal increase in the load.

The 2D analysis could not capture the entire crack propagation because of model divergence, and the results for several mesh sizes (above and below element sizes used for 3D analysis) are depicted in Figure 3.6. The crack in each of the 2D FE simulations initiates immediately next to the contact area between the particle and loading plate when failure tensile stress is reached within a small tolerance. The crack initiates closer to the center of the particle for the smaller mesh sizes but the difference is negligible. The stress distribution before initiation of fracture is best defined in the finest mesh, but the differences are also negligible.

The force-displacement relationships for each of the 2D mesh simulations is shown in Figure 3.7 where no load was recorded at the beginning of the simulation because the loading plates had not yet made contact with the particle. Once contact was initiated, the force increased almost linearly until failure (peak of each curve). Again, the failure happens when a crack is initiated and subsequently propagated through the particle without any increase in the load. Most FE simulations failed at approximately the same load, while the simulation with the smallest element size resulted in a slightly larger load. Because of the small differences between local fracture and global loading curves, 3D meshes were created with approximately the same element size as the 2D particle meshed with a global seeding size of 0.03.

Behavior of a Spherical Particle

It is common to model the behavior of granular materials using ideal spheres. Here, we will perform FE analysis on spherical particles and compare it to the behavior

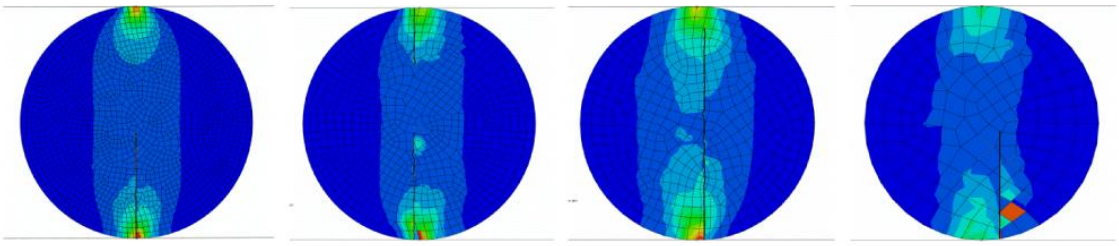

Figure 3.6. 2D mesh size analysis of XFEM cracking when analysis diverged

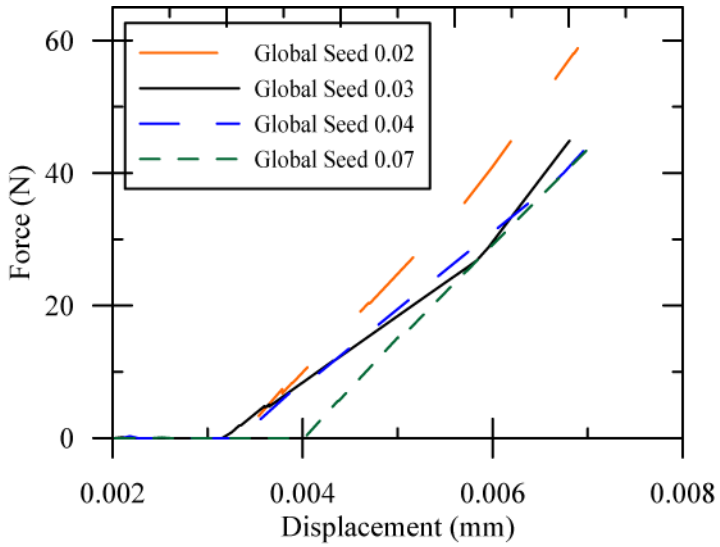

Figure 3.7. Force-displacement relationships of top plate for 2D mesh analysis

of actual shapes of sand. A 3D FE model was developed to compress an ideal spherical particle with no flaws or imperfections. A particle with a 0.8 mm diameter was analyzed. Cracking and fracture of the sphere occurred in several phases with increasing load as shown in Figure 3.8. As the top plate moves downward at a constant displacement rate, cracks initiated at the top and bottom of the particle next to the contact area with the loading plates which is similar to the failure mode of 2D simulations. After initiation at both ends, the cracks propagated until they met in the middle of the particle as viewed in yellow in Figure 3.8b. Upon further loading, the crack began to split open (Figure 3.8c) and then the particle fractured into what would be many small pieces (Figure 3.8d).

Particle Failure based on Experimental Radiograph Images

The small loading rate during in-situ radiograph imaging permitted experimental monitoring of fracture initiation and propagation within the particle. The top loading plate moves only ~0.0167 μm between consecutive radiograph images, allowing time to collect radiographs immediately before and after fracture. Due to the brittle nature of sand fracture, it takes only a fraction of second for the particle to disintegrate into small fragments. Figure 3.9 shows the radiographs of Particle 1 immediately before and after the fracture. Particle 1 in Figure 3.9 developed two cracks next to the contact between the particle and the loading plates, where the highest tensile stresses occurs (Kschinka et al. 1986; Shipway and Hutchings 1993). This indicates that tensile stresses in these locations reach the failure point and the particle fractured. The second particle where radiograph

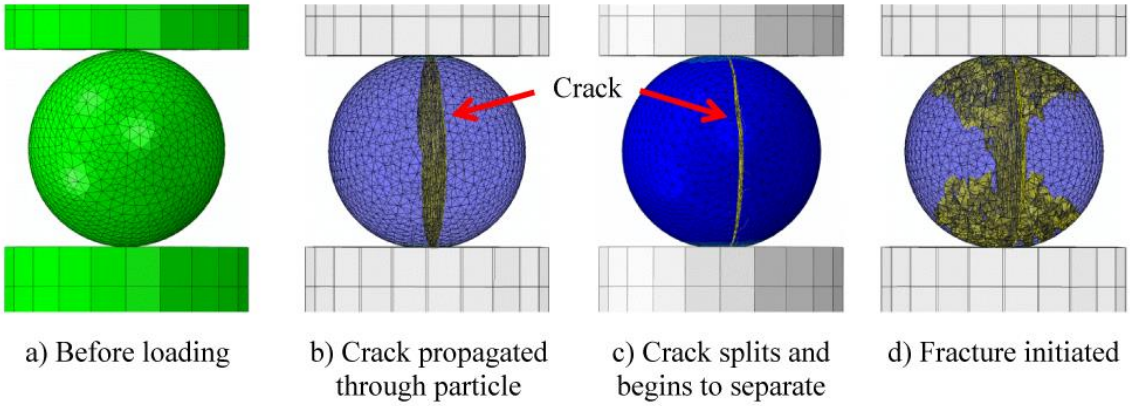

Figure 3.8. Visualization of ideal spherical particle loading and fracture mode

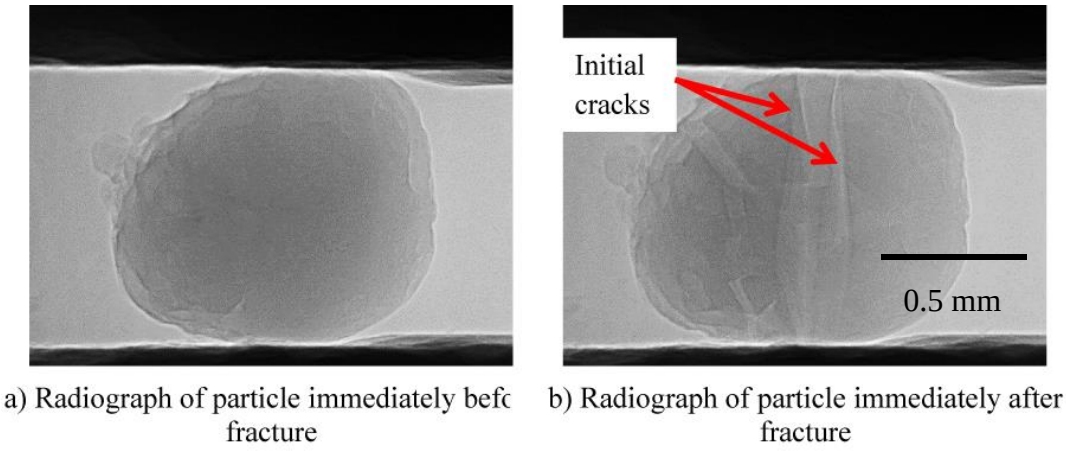

Figure 3.9. Radiograph visualization of first fracture within Particle 1

data was collected also demonstrated that fracture occurred immediately outside of the area of contact with end plates.

XFEM Using Physical Particle Shapes

SMT imaging of particles during in-situ loading helps to better understand the fracture mode that occurs and gives a baseline for model validation. The objective of particle fracture modeling in this paper is to accurately determine crack location and measure the force during loading and fracture using actual particle shapes. Understanding fracture at the particle level is the first step to growing the model to multi-particles and laboratory sized samples, leading to development of better constitutive models that involve particle fracture.

Particles experience elastic deformation before failure. The Von Mises stress distribution as the load increases from FE analysis of Particle 1 is shown in Figure 3.10. The stress concentration occurs at the contacts and propagates as the compressive load increases, which is similar to other theories such as the well-known Hertzian contact theory. Once a crack is initiated, the XFEM model in Abaqus required extremely small time steps and several days of computation time because of the discontinuous nature of cracking from geometrical and contact nonlinearities. Figure 3.11 displays the first crack locations within the two different particles from the XFEM model and radiograph images. Cracks initiated outside the contact area when the tensile stress reached the failure tensile stress. Once fracture is initiated, the propagation of the cracks occurred almost instantaneously in real time (not compute time) and are nearly perpendicular to

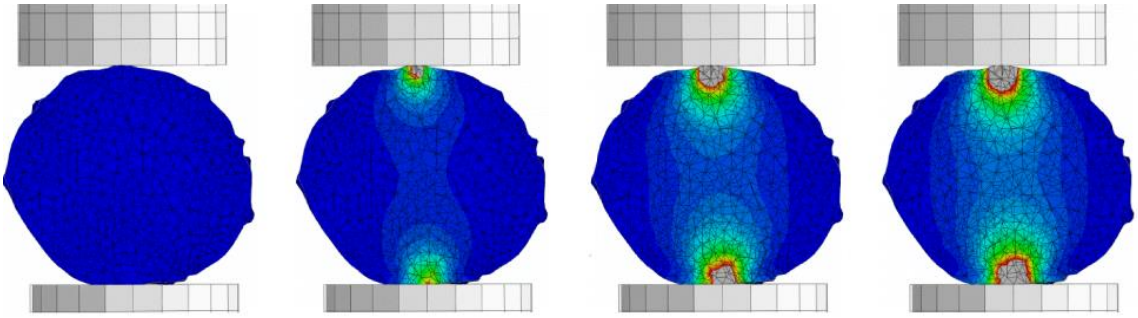

Figure 3.10. Stress distribution within Particle 1 at increasing load increments before fracture

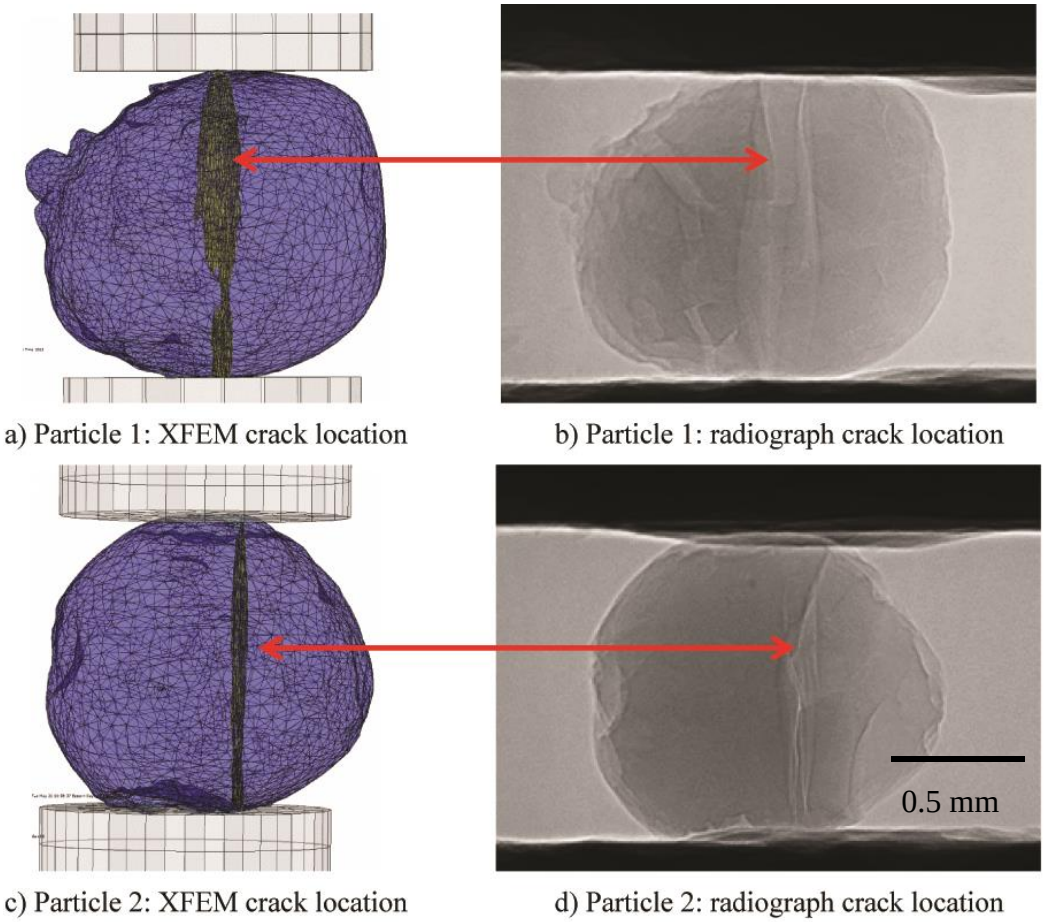

a) Particle 1: XFEM crack location

b) Particle 1: radiograph crack location

c) Particle 2: XFEM crack location

d) Particle 2: radiograph crack location

Figure 3.11. Crack locations of the two particles analyzed from (a) XFEM results and (b) radiographs during experiments

the loading plates. There are, however, slight differences between cracking in the model and the experiment. These differences could be due to the material being slightly anisotropic while an isotropic material was assumed in the model or imperfections in the sand grains or the experimental setup that are not captured by the model.

Initially, the particles rotated in the model and experiment and did not record a significant load until rigid body stability was achieved. Following initial rotation, particles undergo an elastic response until initial fracture (Figure 3.12). The ideal spherical particle experienced a relatively smooth elastic response until fracture which occurred at higher load and displacement when compared to experiments and FE simulations using real particle shapes. In the experiment, several asperities are damaged in Particle 1 before complete failure and the load-displacement curve reflects fracturing of the asperities via multiple small reductions in load. After asperity fracture, elastic response of the particle occurred until a major splitting failure. The XFEM model of Particle 1 did not capture the asperity fracture of the experiment, but replicates the major splitting fracture very well.

Particle 2 had the same fracture stresses input to the model as Particle 1, but required a larger force to fracture it with a behavior similar to an ideal sphere. Particle 2 also had sphericity and roundness indices closer to that of a sphere. The XFEM model of Particle 2 has more particle motion and rearrangement during loading, resulting in local peaks of the force-displacement curve prior to failure. From these results, it is clear that

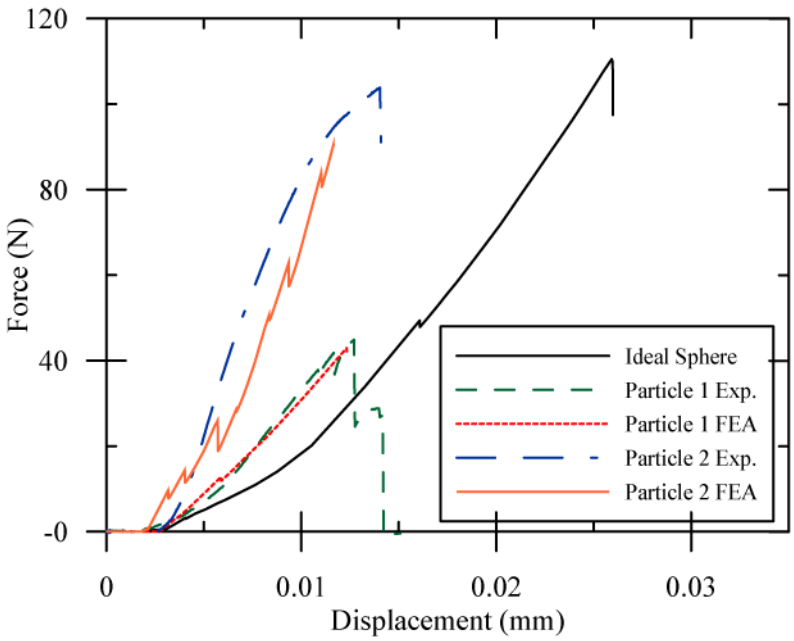

Figure 3.12. Load-displacement relationships from experiments and FE model for ideal sphere and the two analyzed particles

particle shape influences its fracture behavior and modeling sand particles using spheres does not give the best match for experimental measurements.

Conclusion

Synchrotron x-ray radiography and 3D SMT techniques were used to collect images of individual particles of silica sand during in-situ unconfined compression experiments. Radiograph images allowed for the visualization of cracks in the particles, giving insight into fracture patterns caused by compression. The cracks initiated next to the contact area between the loading plates and the particle, indicating that tensile stresses reached failure in these locations. Once fracture is initiated, the built up elastic stressed in the particle suddenly released causing an abrupt, brittle major splitting failure through the particle.

The XFEM model works well to capture the cracking and fracture behavior of an ideal spherical particle. The initial elastic response was relatively smooth until fracture load which was higher than fracture loads of FE simulations of real particle shapes and experiments. A crack propagated entirely through the particle and then began to separate. Shortly after the crack began to separate, complete fracture occurred in the ideal sphere.

The XFEM model analysis on the actual particle shape simulated fracture of the particle very similar to what was visualized using the radiograph images during compression. Fracture predicted by the model was in the same location as the experimental fracture. With the assumed parameters, XFEM analysis on actual particle produced a load-displacement curve similar to the experimental curve. Rotation of the

particle was captured, along with the elastic response and fracture mode. Finally, shape of sand particles influences their fracture behavior and modeling sand particles using spheres does not give the best match for experimental measurements.

References

ABAQUS (2011). "ABAQUS Documentation." Dassault Systemes, Providence, RI, USA.

Alshibli, K., Cil, M., Kenesei, P., and Lienert, U. (2013). "Strain tensor determination of compressed individual silica sand particles using high-energy synchrotron diffraction." *Granular Matter*, 1-14.

Barrett, M., Snow, M., Chizari, M., and Wang, B. (2010). "Mechanical aspects of a single-bundle tibial interference screw fixation in a tendon graft ACL reconstruction." *Biomedical Engineering: Applications, Basis and Communications*, 22(04), 271-278.

Belytschko, T., and Black, T. (1999). "Elastic crack growth in finite elements with minimal remeshing." *International Journal for Numerical Methods in Engineering*, 45(5), 601-620.

Bieniawski, Z. T. (1967). "Mechanism of brittle fracture of rock: Part I—theory of the fracture process." *International Journal of Rock Mechanics and Mining Sciences & Geomechanics Abstracts*, 4(4), 395-406.

Bolton, M. D. (1986). "The strength and dilatancy of sands." *Geotechnique*, 36, 65-78.

Brzesowsky, R. H., Spiers, C. J., Peach, C. J., and Hangx, S. J. T. (2011). "Failure behavior of single sand grains: Theory versus experiment." *Journal of Geophysical Research: Solid Earth*, 116(B6), B06205.

Cattaneo, P. M., Dalstra, M., and Frich, L. H. (2001). "A three-dimensional finite element model from computed tomography data: a semi-automated method." *Proc Inst Mech Eng H*, 215(2), 203-213.

Cavarretta, I., and O'Sullivan, C. (2012). "The mechanics of rigid irregular particles subject to uniaxial compression." *Geotechnique*, 62(8), 11.

Chelidze, T., Reuschle, T., and Gueguen, Y. (1994). "A theoretical investigation of the fracture energy of heterogeneous brittle materials." *Journal of Physics: Condensed Matter*, 6(10), 1857.

Edwards, S. F., and Grinev, D. V. (1999). "The statistical-mechanical theory of stress transmission in granular materials." *Physica A: Statistical Mechanics and its Applications*, 263(1–4), 545-553.

Heyliger, P., Ledbetter, H., and Kim, S. (2003). "Elastic constants of natural quartz." *The Journal of the Acoustical Society of America*, 114(2), 644-650.

Kschinka, B. A., Perrella, S., Nguyen, H., and Bradt, R. C. (1986). "Strengths of Glass Spheres in Compression." *Journal of the American Ceramic Society*, 69(6), 467-472.

Maeda, K., Sakai, H., Kondo, A., Yamaguchi, T., Fukuma, M., and Nukudani, E. (2010). "Stress-chain based micromechanics of sand with grain shape effect." *Granular Matter*, 12(5), 499-505.

McDowell, G. R., and Bolton, M. D. (1998). "On the micromechanics of crushable aggregates." *Geotechnique*, 48, 667-679.

Rivers, M. L., Citron, D. T., and Wang, Y. (2010). "Recent developments in computed tomography at GSECARS." *SPIE*, 3, 780409-780409.

Shipway, P. H., and Hutchings, I. M. (1993). "Attrition of brittle spheres by fracture under compression and impact loading." *Powder Technology*, 76(1), 23-30.

Tajima, K., Chen, K. K., Takahashi, N., Noda, N., Nagamatsu, Y., and Kakigawa, H. (2009). "Three-dimensional finite element modeling from CT images of tooth and its validation." *Dent Mater J*, 28(2), 219-226.

Tordesillas, A., and Muthuswamy, M. (2009). "On the modeling of confined buckling of force chains." *Journal of the Mechanics and Physics of Solids*, 57(4), 706-727.

Tsuda, A., Filipovic, N., Haberthur, D., Dickie, R., Matsui, Y., Stampanoni, M., and Schittny, J. C. (2008). "Finite element 3D reconstruction of the pulmonary acinus imaged by synchrotron X-ray tomography." *J Appl Physiol*, 105(3), 964-976.

Wang, Z., Yang, X., Chen, Q., Zhang, Y., and Zhao, Y. "Study of the contact forces and grain size distribution during grain crushing." *Proc., Multimedia Technology (ICMT), 2011 International Conference on*, 2617-2622.

CHAPTER 4

EXPERIMENTAL FRACTURE OF INDIVIDUAL SAND PARTICLES AT HIGH LOADING RATES AND ASSESSMENT USING 3D X-RAY IMAGING

A version of this chapter is under revision in the Journal of Dynamic Behavior of Materials. The author list is: A. Druckrey, K. Alshibli, D. Casem, E. Huskins.

My primary contributions to this paper include (i) development of problem based on overall research objectives at various length scales, (ii) conduction of all experimental aspects of paper, (iii) waveform data analysis to force and velocity versus displacement, (iv) development of non-linear multivariable statistical models to predict fracture forces, (v) simulation of particle fracture using finite element analysis, (vi) analysis of all results, (vii) most of the writing.

Abstract

High strain rate loading conditions such as blast, impact, or projectile penetration cause major damages to infrastructure and soils. Sand particles will likely fracture if they are exposed to such loading conditions. Modeling the constitutive behavior of sands when subjected to dynamic loading requires a high-fidelity particle-scale analysis, calibration, and validation using experimental measurements. In this paper, natural sand particles with varying morphology, mineralogy, and grain size were randomly selected from the bulk material and separated based on particle size and mineralogy. Intact particles were first imaged using a desktop x-ray computed tomography (CT) scanner to obtain morphology and provide further input to the mineralogy and internal structure. Each particle was then placed between incident and transmitter bars of a Kolsky bar setup and two optical images (side and top views) were collected to visualize the loading geometry and direction. Each particle was then dynamically compressed to failure and

load, compression, and compression rate were measured. Recovered particle fragments were imaged using synchrotron micro-computed tomography (SMT) to determine the fracture mode and fracture surface. Weibull statistics were performed and multivariable nonlinear regression was implemented with particle characteristics as predictors. Also, a finite element model was used to simulate particle fracture at the strain rate reported in this paper and particle fracture stresses were compared with theoretical particle strength. The paper discusses the influence of morphology, mineralogy, internal structure and size of particles on dynamic particle failure strength.

Introduction

Fracture and comminution of sand particles is well known to affect the constitutive and deformation behavior of granular material during quasi-static loading as well as high-rate loading conditions (Allen et al. 1957; Antoun 2012; Cooper and Breaux 2010; Iskander et al. 2015) . During blast loading, energy dissipates partially through sand particle fracture and comminution (Børvik et al. 2011; Braslau 1970). Fracture of individual particles could affect the dynamic behavior of the ejecta resulting from buried explosives (Regueiro et al. 2014) and therefore affect the loading applied to an object such as an armored vehicle or structures close to the explosive source. Particle fracture may occur in many other high strain rate (HSR) loadings on granular materials such as projectile penetration into sand (Allen et al. 1957; Cole 2010; Cooper and Breaux 2010), drilling and mining applications, and impact. In this paper, intermediate and HSR for granular materials is considered to be between 10%/s and 10^7%/s. Assessing dynamic

properties of fracture at the particle level is an essential step in understanding the behavior of bulk granular materials that experience high strain rates and plays a critical role in improving design against such dynamic forces. Constitutive behavior of granular materials at the macro-scale is highly influenced by the material properties at the particle scale. For example, it is well known that quasi-static loading of a granular material causes force chains to develop that carry the majority of the applied external loads. Particle fracture takes place within those force chains when jamming occurs within the system. Jamming is when other phenomenon including initial compression of the grains, particle-particle friction, and particle rearrangement due to such particulate friction are suppressed (Cil and Alshibli 2014; Cooper 2011; Peters et al. 2005; Wang et al. 2011). Individual particle properties significantly affect macroscopic properties in these particulate assemblies (Antony 2007; Yoshida 2005).

The HSR behavior of sand has been investigated using various techniques. Suescun-Florez et al. (Suescun-Florez et al. 2015) compiled a comprehensive review on HSR testing of granular soils, including different dynamic testing techniques and selected results. Many researchers have utilized techniques such as the Kolsky bar, also known as split-Hopkinson pressure bar (SHPB), on laboratory-scale specimens (e.g. Knodel et al. 1990; Luo et al. 2011; Martin et al. 2009). Luo et al. (2011) found that the grain size distribution shifted significantly, suggesting that many particles fractured during Kolsky testing at HSR. Force chains have also been found to develop within granular material during dynamic loading, although dynamic structures differentiate from those during

static and quasi-static loading (Behringer et al. 2014; Dwivedi et al. 2008; Felice and Gupta 2009; Omidvar et al. 2012). Similar to static and quasi-static loading, particles within these dynamic force chains experience the largest stresses and are the first to fracture. Particles within dynamic force chains have less time to rearrange, which increases stresses within the particles, but also have less time to fracture (Suescun-Florez et al. 2015). Therefore, particle stress at fracture would be theoretically larger during dynamic loading than quasi-static.

Extensive research on experimental fracture mechanics at the single particle level has been conducted using quasi-static loading using a variety of experimental methods and theories (e.g. Brzesowsky et al. 2011; Cavarretta and O'Sullivan 2012; Cil and Alshibli 2012; Druckrey and Alshibli 2015; McDowell and Bolton 1998; Mitchell et al. 2007; Zhao et al. 2015). For example, Druckrey and Alshibli (2015) modeled the fracture behavior of real particle shapes using 3D finite element (FE) analysis based on 3D images that were acquired using SMT imaging during quasi-static compression. Zhao et al. (2015) reported a comprehensive investigation of quasi-static single particle fracture using x-ray CT. However, quasi-static fracture of individual particles do not account for dynamic processes and do not account for any strain rate effect that might be present.

High rate testing of individual sand particles provides the initial particle-scale information that can be used in dynamic modeling across the scales. In particular, HSR tests can be used to calibrate and validate high fidelity particle-scale poly-ellipsoidal discrete element models (DEM) that include particle fracture, which in turn can be used

to develop lower fidelity soil blast models at larger scale to replace costly and time consuming full scale testing (Antoun 2012). Important input parameters to the particle-scale DEM modeling include particle shape, loading direction, fracture strength, and fracture mode resulting from high-rate loading. Furthermore, high-rate finite element analysis (FEA) of real particle shapes would further describe actual stresses within particles at fracture which has thus far been difficult to measure. Few studies have been published to investigate the behavior of single particle failure under dynamic loading. Parab et al. (2014) used a confined Kolsky bar to dynamically compress particles during in-situ high speed phase contrast imaging (PCI). Two confined approximately spherical Ottawa sand particles were placed in a hollow cylindrical aluminum housing and were subjected to dynamic load while 2D radiographs and load versus time data were collected. Visual assessments of damage propagation were conducted and when particles were dry, one of the two particles had extensive interfacial cracking followed by pulverization. Wet sand particles broke into large fragments followed by pulverization. Borg et al. (2015) used uniaxial compression to fracture 20 particles while acquiring images with a high-speed camera and used particle reflectivity to visualize fracture. Assuming spherical grains and Hertzian contact, approximate particle strains were calculated from the images and based on the force at fracture approximate particle stresses were calculated. Borg et al. (2015) observed similar phenomena between dynamic single particle fracture and particle fracture within a granular media during dart penetration.

This paper uses 3D imaging and recently developed mini-Kolsky bar techniques to assess the dynamic behavior of non-spherical natural sand particles with different mineralogy and morphology. To capture the initial morphology of the particles, 3D CT images of intact particles before testing were acquired using a desktop x-ray CT system. Each particle was then placed in an unconfined mini-Kolsky bar setup similar to (Casem et al. 2014; Casem et al. 2012) with a normal displacement interferometer (NDI) to measure the low-magnitude transmitted pulse in the transmitter bar. Optical images were taken with the particle in place before loading, and the fragments were collected after loading for post-test SMT imaging. Multivariable nonlinear regression was performed to determine a combined effect of particle properties in determining the fracture force. Also, Weibull statistical analysis was performed on particle characteristic tensile strengths with good statistical correlation. FEA was performed to validate the fracture and loading of particles at the experimental displacement rate, where fracture stresses determined from FEA were compared with the assumed characteristic tensile strength of each particle. This procedure provides essential information about alignment of the particle in any numerical analysis, collection of the load-displacement and velocity measurements as well as 3D analysis of particle fracture mode. Determining particle fracture strength and/or forces required to fracture a particle is an important first step in hierarchical upscaling to laboratory specimen size scale and eventually to field scale simulations.

Experimental Procedure

The experiments reported in this paper were developed as a contribution to a larger project described in Regueiro et al. (2014), an integrated experimental mechanics and multiscale computational model concurrent with a multiscale approach to simulate soil ejecta. The project required the use of natural sand in experiments and modeled using continuum finite element and discrete element methods to provide robust multiscale measurements. The research objectives of Regueiro et al. (2014) are to numerically predict (a) the propagation of blast waves in soils (accounting for particle scale physics), (b) explosive device fragmentation interaction with soil, and (c) the triphasic soil deformation, fracture, fragmentation and ejecta resulting from the detonation in various types of soil. This research was conducted to experimentally and numerically validate and verify DEM particle fragmentation at the pore-grain-scale (Scale I) as well as determine the forces on particles and the intra-particle stresses that develop and cause fracture during higher rate loading. Larger meso-scale HSR experiments are being concurrently conducted, and some of the results can be found in (Luo et al. 2014; Luo et al. 2011) for SHPB testing of sand. Current DEM modeling efforts can be found in Regueiro et al. (2014) and other numerical simulations based on this natural sand that include hierarchical upscaling in (Homel et al. 2015; Huq et al. 2016; Meyer Jr and Brannon 2012). The materials, experimental procedure, and modeling involved in this paper were chosen based on the needs of the parent research project.

Material

A natural sand from a quarry in Longmont, Colorado (Colorado Materials, Inc.), known as mason sand, was selected in this study because of its heterogeneous grain properties as a representative of a natural sand deposit. It is not a typical "research" sand which is generally uniform and has well-defined properties. This sand was chosen to provide experimental inputs for the development of robust particle-scale and multi-scale models. X-ray powder diffraction was performed on the full spectrum of Mason sand (without excluding any particles) and diffraction curves were analyzed using RockJock quantitative mineralogy software (Eberl 2003). The sand is composed of 27.8% quartz and 24.8% tridymite; a polymorph of quartz, 15.6% plagioclase, 15.4% potassium feldspar (denoted Kspar), 5.6% ferrihydrite, 3.2% pyroxene, 2.5% mica, 2% psilomelane, 1.4% hornblende, 1% calcite, and 0.7% other minerals. Particles were also separated by color (an approximate means of mineralogy) and additional powder diffraction curves were collected on each color and were analyzed in order to aid in visual mineral identification of individual particles that were tested. The particle size distribution of mason sand is shown in Figure 4.1 and it is classified as a poorly graded sand (SP) with D_{10} = 0.15 mm, D_{30} = 0.3 mm, D_{60} = 0.52 mm, C_c = 1.15, and C_u=3.47 according to ASTM-D2487 standard classification system.

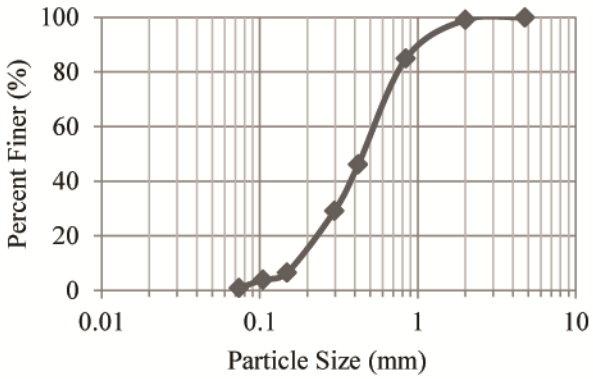

Figure 4. 1. Particle size distribution of Mason sand

Pre-Loading Imaging

To provide information on the initial properties of each particle, 3D CT scans were acquired using a commercial SkyScan 1172 microCT x-ray scanner. Ten particles were placed on a sample holder using double sided tape and care was taken to keep track of the orientation of the particles relative to the x-ray beam. The sample holder was placed in the x-ray machine and 720 projections were collected at 0.25° rotation increments. Projections were reconstructed to create a 3D image with a resolution of 4.02 μm/voxel (volumetric pixel). Grayscale images of the intact particles were processed and individual particle sizes of axis lengths (short, intermediate, and long) and volume were computed according to the method reported in Druckrey et al. (2016) and presented in Table 4.1. Morphology of each of the tested particles was calculated based on Alshibli et al. (2014) and are also presented in Table 4.1 in terms of sphericity (I_{sph}) and roundness (I_R). A large variation of sphericity was present among the tested particles (as well as in Mason sand as a whole). Individual particle morphology affects how the particle will be loaded and influences its fracture mode. Each particle had a unique morphology (therefore unique loading parameters such as contact points on the loading bars) and 3D images of the intact particles are used to construct, verify, and validate fracture models. Examples of fracture modeling using FEA are presented later in this paper.

The internal structure of a particle, which indirectly relates to the particle mineralogical composition, affects its fracture behavior. Internal flaws create stress

Table 4.1. Summary of particle properties obtained from CT imaging, XRD, and visual photographs

Particle Number	Particle Short Axis, d_s (mm)	Particle Int. Axis, d_i (mm)	Particle Long Axis, d_l (mm)	Particle Volume (mm^3)	I_{sph}	I_R	Internal Structure Classifi-cation	Visual Mineral Classifi-cation[1]
1	0.67	0.80	0.96	0.22	1.39	1.03	5	Biotite Mica
2	0.59	0.80	1.15	0.24	2.23	0.93	5	Granite
3	0.64	0.84	1.02	0.22	1.60	0.86	6	Granite
4	0.90	1.16	1.45	0.59	1.52	0.95	4	Granite
5	1.03	1.33	1.67	0.82	1.44	0.93	5	Granite
6	1.36	1.98	2.06	2.25	1.70	0.96	4	Granite
7	1.40	1.52	1.72	1.48	1.03	0.92	5	Granite
8	1.26	1.57	2.21	1.73	1.65	0.90	4	Kspar Orthoclase
9	0.77	0.78	1.07	0.26	1.06	0.93	3	Kspar Orthoclase
10	1.21	1.31	1.77	1.07	1.15	0.89	4	Kspar
11	1.47	1.60	2.50	2.27	1.36	0.88	4	Kspar Orthoclase
12	0.44	0.93	1.01	0.17	3.83	0.74	3	Kspar Orthoclase
13	0.58	0.61	1.45	0.19	1.78	0.75	3	Kspar Orthoclase
14	0.63	1.09	1.24	0.32	2.44	0.79	3	Kspar Orthoclase
15	0.68	1.03	1.22	0.30	1.84	0.74	4	Kspar Orthoclase
16	0.97	1.26	2.05	0.93	1.93	0.82	2	Kspar Orthoclase
17	0.98	1.04	1.62	0.77	1.59	0.99	2	Kspar Orthoclase
18	1.19	1.56	2.55	1.78	2.00	0.78	3	Kspar Orthoclase
19	1.29	2.01	2.22	2.01	1.76	0.89	3	Kspar Orthoclase
20	0.94	1.42	2.18	1.43	3.29	0.95	5	Muscovite Mica
21	1.18	1.51	2.00	1.14	1.32	0.83	3	Plagioclase
22	0.57	1.01	1.28	0.24	2.44	0.78	4	Plagioclase Albite
23	0.52	0.92	1.25	0.26	3.56	0.66	5	Plagioclase
24	0.57	0.81	1.30	0.32	3.36	0.86	6	Plagioclase
25	0.61	0.80	1.10	0.17	1.37	0.74	6	Plagioclase
26	0.87	1.17	1.51	0.67	1.90	0.90	6	Plagioclase
27	1.17	1.19	1.74	1.01	1.20	0.93	6	Plagioclase
28	0.72	1.06	1.10	0.33	1.68	0.83	4	Pryoxene Augite
29	0.91	1.64	1.90	1.48	3.68	0.76	2	Psilomelane
30	0.50	0.72	1.46	0.24	3.60	0.82	3	Pyroxene

[1]Pre-experiment CT images and optical images aided in mineral identification

Table 4.1 Continued. Summary of particle properties obtained from CT imaging, XRD, and visual photographs

Particle Number	Particle Short Axis, d_s (mm)	Particle Int. Axis, d_i (mm)	Particle Long Axis, d_l (mm)	Particle Volume (mm^3)	I_{sph}	I_R	Internal Structure Classifi-cation	Visual Mineral Classifi-cation[1]
31	1.00	1.39	1.57	0.80	1.53	0.80	4	Pyroxene
32	0.64	0.81	1.24	0.21	1.55	0.75	1	Quartz
33	0.60	0.98	1.28	0.27	2.30	0.78	1	Quartz
34	0.79	1.17	1.44	0.61	2.33	0.86	1	Quartz
35	0.72	1.04	1.25	0.31	1.60	0.79	2	Quartz
36	0.75	0.94	1.12	0.27	1.22	0.89	1	Quartz
37	1.15	1.70	2.13	1.06	1.34	0.75	1	Quartz
38	1.12	1.57	1.98	1.12	1.52	0.81	1	Quartz
39	1.09	1.42	1.61	0.94	1.40	0.86	2	Quartz
40	0.74	1.50	1.68	0.84	3.94	0.96	2	Quartz
41	1.21	1.47	1.52	0.96	1.05	0.92	2	Tridymite
42	0.82	1.37	2.31	1.35	4.66	0.99	2	Tridymite
43	1.36	1.51	2.46	2.23	1.70	0.90	2	Tridymite

[1]Pre-experiment CT images and optical images aided in mineral identification

concentrations within a particle upon loading and/or provide initial fracture planes (if flaws are micro-cracks). To quantify the internal structure of each particle, a rating system from one to six was developed based on the overall internal structure. The internal structure of a particle can include flaws such as voids, micro-cracks, or inclusions. Inclusions are various minerals embedded within the particle that create a mineral boundary and possible fracture plane. Figure 4.2 shows examples of each of the six internal structure ratings. Only flaws or inclusions with sizes greater than that of the image resolution can be detected, and any flaws smaller than the resolution were ignored at this level. A rating of 1 (Figure 4.2a) is a nearly solid internal structure with no apparent flaws. Rating 2 has few very small internal flaws (Figure 4.2b) and rating 3 (Figure 4.2c) has small sporadic flaws throughout the particle. A rating of 4 has several flaws within the particle (Figure 4.2d). A rating of 5 (Figure 4.2e) has many concentrated flaws and micro-cracks, while rating of 6 (Figure 4.2f) means that the particle is internally covered with flaw and micro-cracks. Internal flaws occasionally manifest towards the surface of a particle (especially for particles with ratings of 4-6), and the optical images aided in determining the internal structure rating. Rating for all of the tested particles is shown in Table 4.1.

Based on the optical images, XRD mineralogy results, and internal structure rating, a visual mineral classification for each of the tested particles is also listed in Table 4.1. It was obvious from the CT and optical images that some of the particles were not a pure mineral. Rather, they were a mixture of several different minerals. Those particular

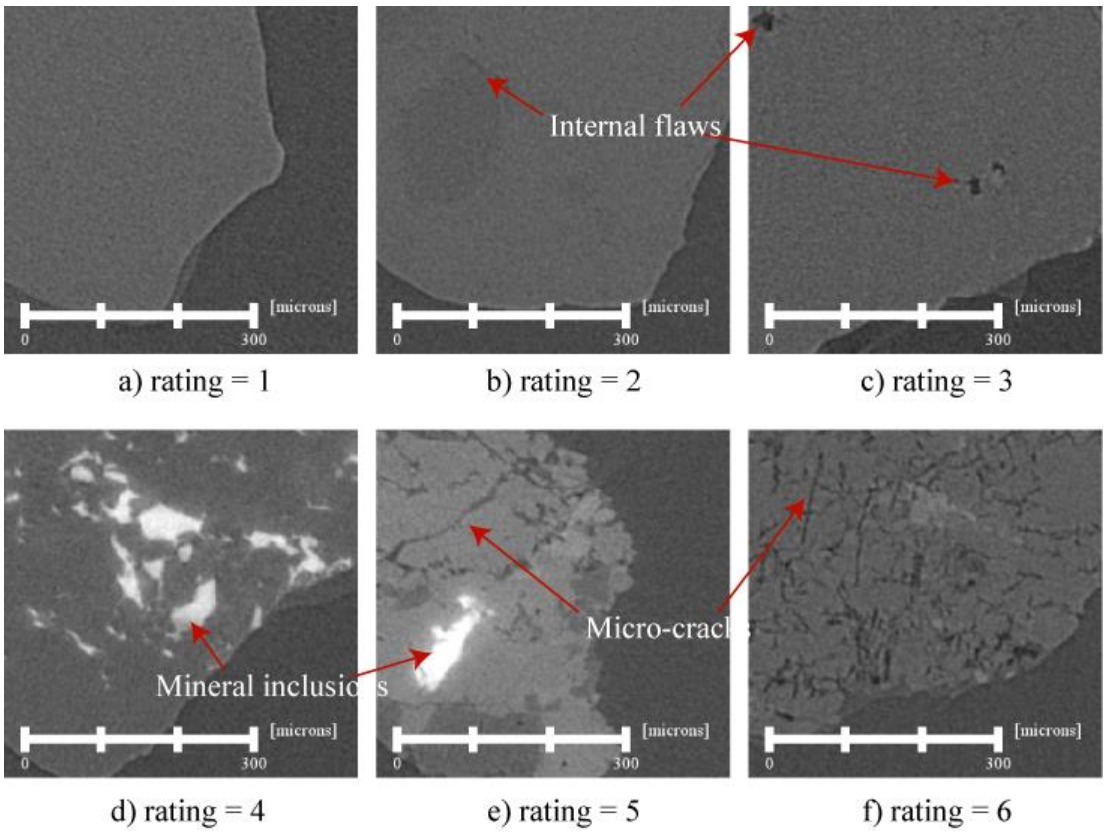

Figure 4.2. Examples of internal structural rating system for particles

particles were labeled as granite, which have inclusions of iron and occasional micro-cracks at mineral boundaries.

Kolsky Bar Experiments

A Kolsky bar (Figure 4.3) was used for the high rate compression experiments. Individual sand specimens were compressed directly between the incident and transmitter bars. The bars were both made from high strength steel, sufficiently strong that they were undamaged after testing the specimen (no platens were needed). The incident bar was made of Maraging-350 steel (c_0 = 4908 m/s, ρ = 8095 kg/m^3) and was 508 mm long and 4.77 mm in diameter. A set of strain gauges was mounted 403.2 mm from the specimen end to measure the incident and reflected signals[1]. The output bar is also made from Maraging-350 steel but measures 1.58 mm in diameter and 76 mm in length. A smaller diameter was selected to increase the magnitude of the transmitted signal due to compression of the relatively weak samples. Because of the small diameter, strain gages could not be used accurately on the transmitter bar and so instead a Normal Displacement Interferometer (NDI) was used in its place, similar to that done in (Casem and Zellner 2013). The end of the transmitter bar is polished to a specular finish and serves as the moving mirror in the interferometer. The incident beam (532 nm) is aligned perpendicular to the end of the bar and split to a fixed reference leg using the B1 beam splitter, and recombined to two photodetectors (Thorlabs PDA10A) using the B2 beam

[1] Note the strain gauges are not centered in the typical fashion to permit measurement of longer loading pulses than would be measurable from centered gauges, at the expense of measuring the reflected pulse. These longer duration experiments are not discussed in this paper.

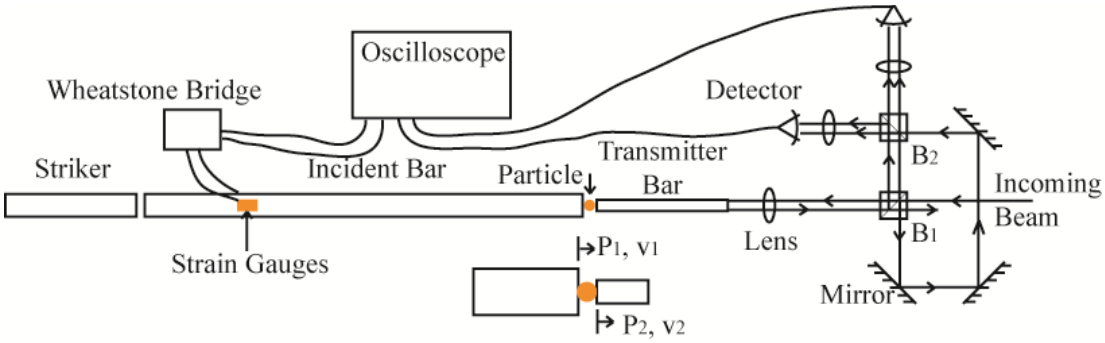

Figure 4.3. Schematic of mini-Kolsky bar setup with NDI to measure displacement of transmitter bar due to transmitted pulse (after Casem et al., 2012)

splitter. The data collected by the detectors (redundant) is due to the interference of the two beams and is correlated to the motion of the end of the bar, ultimately providing a measurement of free-end velocity. This essentially replaces the typical measurement of strain due to the transmitted pulse. Using a common analysis approach, velocity of the interface between the incident bar and the sample (v_1) can be determined as:

$$v_1 = c_{0,i}(\varepsilon_i - \varepsilon_r) \tag{4.1}$$

where $c_{0,i}$ is the elastic wave speed of the incident bar, ε_i is the strain due to the incident pulse , and ε_r is the strain due to the reflected pulse. In principle, the force (P_1) at this interface can be calculated as:

$$P_1 = (\varepsilon_i + \varepsilon_r)E_iA_i \tag{4.2}$$

where E_i and A_i are the elastic modulus and cross sectional area of the incident bar. However, Equation 4.2 is inaccurate because of the relatively low loads required to fail the particle in comparison to the impedance of the incident bar. Force and velocity at the interface between the specimen and the transmitter bar with time ($P_2(t)$ and $v_2(t)$, respectively) can be determined as described in Casem et al. (2012):

$$v_2(t) = v(-L_T, t) = \frac{1}{2}\left[v_f\left(\frac{L_T}{c_0} + t\right) + v_f\left(\frac{-L_T}{c_0} + t\right)\right] \tag{4.3}$$

$$P_2(t) = P(-L_T, t) = \frac{A_t\rho_t c_0}{2}\left[v_f\left(\frac{L_T}{c_0} + t\right) - v_T\left(\frac{-L_T}{c_0} + t\right)\right] \tag{4.4}$$

where v_f is the velocity of the free surface, and L_T, A_t, ρ_t, and c_0 are the length, cross sectional area, density and wave speed of the transmitter bar. As mentioned above, the rationale behind the reduced area of the transmitter bar is that it increases the magnitude of the transmitted signal and increases the resolution of the force measurement. This is

further enhanced by the use of the NDI, which is several orders of magnitude more sensitive than standard strain gauges. A similar approach was adopted in Casem et al. (2014). In addition, the force measurement in Equation 4.4 is valid for all time as long as there is NDI data. Such approach allows identification of any reloading of the particle after the initial loading pulse from reverberating stress waves in the bars.

Each particle was placed between the incident and transmitter bar with the help of a thin film of vacuum grease, typically allowing the particle to freely fall after fracture as a result of the initial pulse in the incident bar applied by the striker bar. A housing was placed around the particle, without touching it, to collect fragments after the experiment. Striker bar speed was initially varied by changing the pneumatic pressure that launches the striker to determine the optimum pulse transmitted to the particle. Once the optimum pulse was identified, all tests were conducted using the same pressure to launch the striker bar. Pulse lengths were 35 micro-seconds and strain rates were on the order of 1000 to 3500 s^{-1}, similar to larger scale experiments conducted on bulk material.

Figure 4.4 shows a sample of the transformed data for the NDI waveform and combined strain gauge signals. The transformed NDI signal is indicative of loading of the particle and repeats throughout sampling, unless a reload occurs. If a particle is reloaded by a secondary waveform, a change in the transformed NDI signal is present and can be analyzed. The strain signal displays the first incident pulse and concurrent reflected pulses from reflection off of the bar's free ends. The first reflected pulse is off of the loading end of the incident bar and the second reflected pulse is the one reflected from

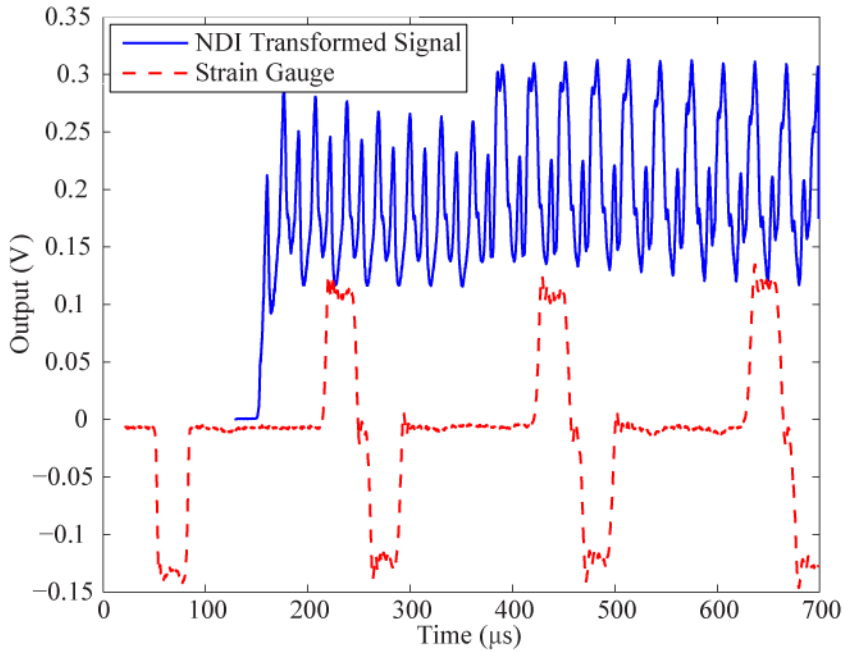

Figure 4.4. Waveform data collected from strain gauges and transformed NDI signal during particle loading

the free surface opposite to where the particle is loaded. First and second reflected pulses are close because the wave travels 104.8 mm from the free end of the bar the strain gauges, while traveling in the other direction the pulse travels 403.2 mm to reflect from the loading end of the incident bar. Incident and first reflected pulses are easily separable from others and are used in the analysis of the loading curve applied to the particle.

By detecting the local maxima and minima of the fringes from the NDI waveform, displacement of the free end of the bar was calculated using the concepts presented in Casem et al. (2012) and displacements converted to velocity according to Equation 4.3. Incident and reflected pulses were truncated and separated by user inspection of the data, as well as the free end velocity that resulted from loading of the first incident pulse. Pulses and truncated velocity were then shifted in the time domain to overlay over the same time (Figure 4.5a). Strain gauge pulses were typically shifted approximately 0.08 ms and the NDI pulse shifts were approximately 0.0175 ms. With the shifted pulses and truncated free end velocity, loading displacement and loading velocity applied to the particle were calculated based on the difference between the displacements of the loading end of the incident bar and loading end of the transmitter bar. Force was also calculated from the incident pulse, resulting in force-displacement and velocity-displacement relationships for each particle (e.g., Figure 4.5b). To check whether a particle was re-loaded, fringes from the NDI were analyzed for the entire duration of the data collection. Force based solely on NDI measurements (Equation 4.4) was calculated

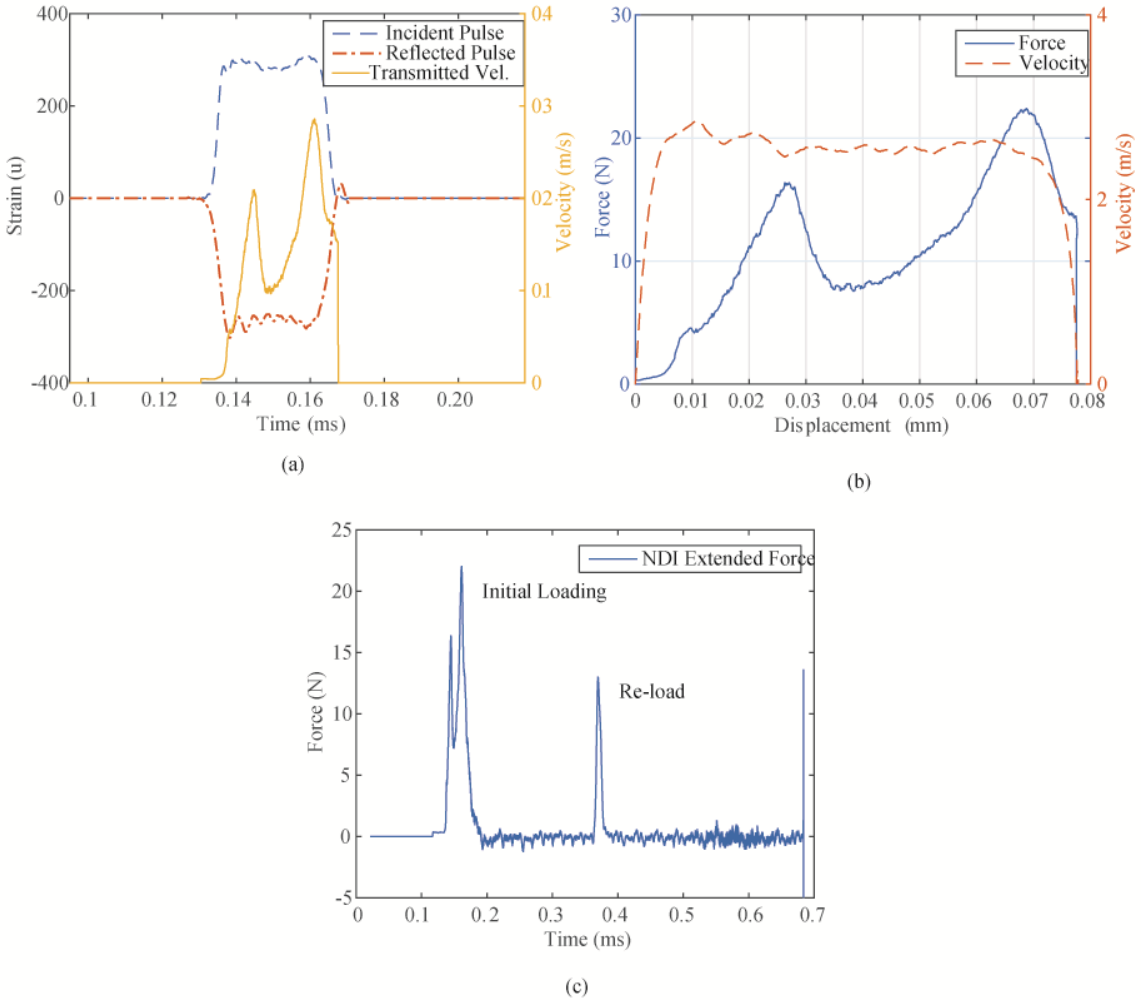

Figure 4.5. Analysis and results of particle loading: (a) truncated, shifted incident and reflected pulses and transmitted free end velocity, (b) force and velocity vs. displacement applied to particle and (c) NDI force over duration of experiment

and peaks after the initial loading infers the particle was re-loaded by a secondary reflected wave as shown in Figure 4.5c.

SMT Image Collection of Particle Fragments

To accurately examine fracture mode of the particles, SMT images of the fragments collected from the tested particles were acquired using the bending magnet beamline 13D (13 BMD) at the Advanced Photon Source (APS), Argonne National Laboratory (ANL), Chicago, Illinois, USA. Fragments belonging to a particle were glued onto a wooden dowel rod for stability and were clamped using a drill chuck mounted on the translation/rotation stage in the beam line. A parallel x-ray beam with high brilliance was sized and tuned to 28.1 keV energy by two upstream slits and a monochromator. X-rays were then attenuated by the particle fragments as they passed through them, converted to visible light by a scintillator, and reflected off a 45° mirror into a Grasshopper3 charged coupled device (CCD) detector, resulting in a radiograph image. 720 radiographs were acquired at 0.25° rotation increments. Radiographs were then pre-processed and reconstructed according to (Rivers et al. 2010), resulting in 3D SMT images with a resolution of 2.06 μm/voxel. High quality SMT images facilitate 3D qualitative analysis of the fracture mode and visualization of the fracture surface. Due to beam time restraints, not all fractured particles were imaged.

Experimental Results

3D images of intact particle, dynamic loading curve and velocity with optical image for loading direction, and 3D image of collected fragments can be used in modeling fracture behavior of individual particles, which in turn can be used as input to model dynamic loading on granular materials. Figure 4.6 shows an example of full experimental results for a particle. The CT image of the intact particle was post-processed to a binary image and a 3D surface reconstruction was generated. Surface reconstructions were aligned to match experimental alignment using two optical images of each particle after it was placed on the bar. Post-fracture SMT images obtained at APS were used to determine the fracture mode and describe the fracture surface, as well as create 3D surface reconstructions of the fractured particle. Experimental results of tested particles are summarized in Table 4.2. The loading diameter, or distance between the incident and transmitter bars, was measured using the optical images and is also presented in Table 4.2. When placed in-between transmitter and incident bars, particles generally rearrange such that their short or intermediate axis length is close to the loading diameter. Whether each particle was loaded in a triangular manner or not is also noted in Table 4.2. Triangular loading of a particle arises when one bar contacts the particle at two or three spread out contact points and the opposite bar contacts the particle at a location centralized between the spread contact points. This can occur when a particle is very angular and/or concave and is an indirect result of its morphology. Initial fracture loads

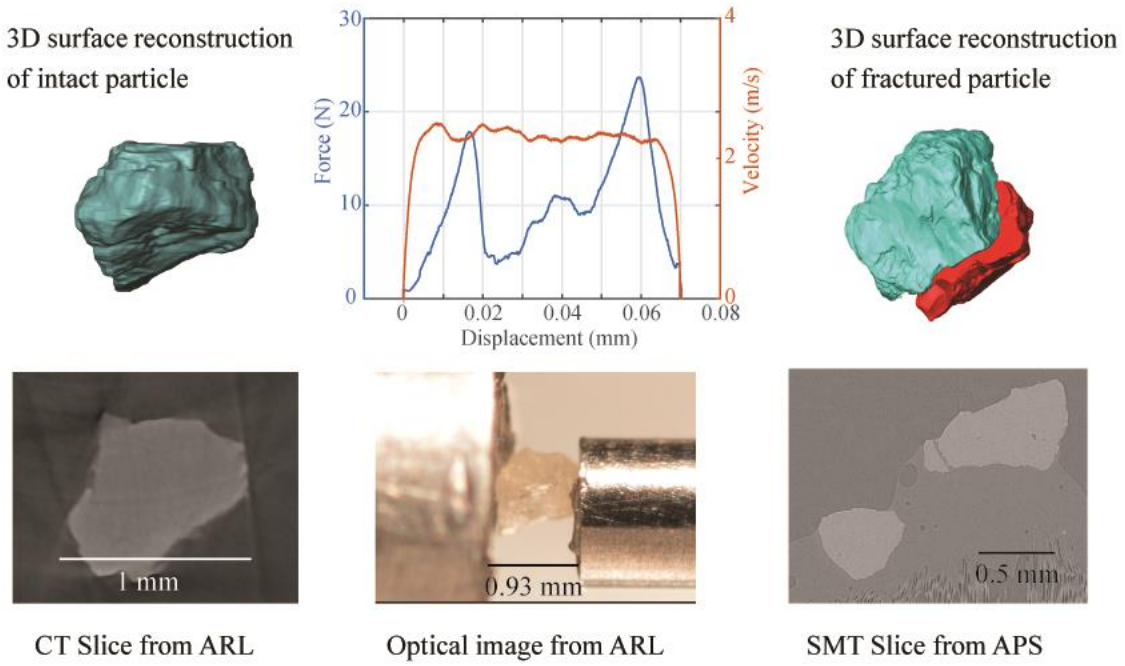

Figure 4.6. Example of experimental results from mini-Kolsky bar testing and particle imaging at Army Research Lab (ARL) and Advanced Photon Source (APS)

Table 4.2. Results of dynamic particle fracture using mini-Kolsky and imaging techniques

Particle Number	Loading Diameter d_{load} (mm)	Triangle Loading? (y/n)	Fracture Load (N)	Loading Velocity (m/s)	Reload?	Max Reload (N)	Fracture Mode[1]	Fracture Surface[1]
1	0.67	yes	10.5	2.25	yes	29	4	angular
2	0.59	yes	9.15	2.5	yes (2x)	7	4	rough/angular
3	0.64	yes	11.75	2.5	yes (2x)	14	4	rough/angular
4	1.04	no	19	2.1	no	n/a	n/a	n/a
5	1.18	no	15.4	2.5	no	n/a	n/a	n/a
6	1.36	no	40.4	2.25	yes	8	3	rough/angular
7	1.45	no	16.5	2.5	yes	13.5	4	rough
8	1.26	no	28.5	2.22	no	n/a	n/a	n/a
9	0.78	no	21.3	2.75	no	n/a	4	angular
10	1.39	yes	3.98	2.5	yes (2x)	7.4	4	rough/angular
11	1.49	no	29	2.25	no	n/a	3	rough/angular
12	0.44	yes	7.55	2.5	no	n/a	3	smooth/ang.
13	0.67	yes	4	2.25	yes	4.5	n/a	n/a
14	0.67	no	24.8	2.15	no	n/a	3	rough/angular
15	0.78	yes	6.08	2.57	yes	4.84	n/a	n/a
16	0.97	no	68.8	2.25	no	n/a	4,2	angular
17	0.98	yes	19.6	2.5	yes	17.5	n/a	n/a
18	1.19	no	26	2.5	no	n/a	3	angular
19	1.29	no	38.65	2.5	yes	31.3	n/a	n/a
20	0.96	no	46.6	2	no	n/a	n/a	n/a
21	1.18	no	19.8	2.3	no	n/a	3	angular
22	0.74	yes	12	2.1	yes	14.8	n/a	n/a
23	0.56	no	16.3	2.75	yes	13	3	rough
24	0.61	yes	3.25	2.25	yes (2x)	18.5	3,2	angular
25	0.74	no	2.75	2.5	yes (2x)	16.75	2	rough/angular
26	0.90	no	15	2.4	yes (2x)	13	3	rough/angular
27	1.17	yes	4.2	2.75	yes	4.25	4	rough/angular
28	1.13	yes	3.85	2.4	yes (2x)	15	1	angular
29	0.92	no	82	2.75	no	n/a	4	angular
30	0.93	yes	4.5	2.5	yes	1.3	n/a	n/a

[1]Refer to Figure 4.8 for fracture description. Not all tested particles were imaged post-mortem.

Table 4.2 Continued. Results of dynamic particle fracture using mini-Kolsky and imaging techniques

Particle Number	Loading Diameter d_{load} (mm)	Triangle Loading? (y/n)	Fracture Load (N)	Loading Velocity (m/s)	Reload?	Max Reload (N)	Fracture Mode[1]	Fracture Surface[1]
31	1.00	no	32.5	2.25	no	n/a	1	rough/angular
32	0.64	yes	2.8	2.3	no	20.5	3	smooth
33	0.67	yes	2.6	2.4	yes	17.4	3,1	smooth
34	0.86	no	86	2	no	n/a	3,2	smooth/ang.
35	0.93	no	17.1	2.3	yes (2x)	10.5	3	angular
36	1.03	yes	6.48	2.55	no	n/a	n/a	n/a
37	1.15	no	42.5	2.25	no	n/a	3	smooth
38	1.22	yes	27	2.55	yes	21.75	n/a	n/a
39	1.33	no	20.75	2.5	no	n/a	1	angular
40	1.63	yes	7.3	2.3	no	n/a	n/a	n/a
41	1.21	no	29.15	2	no	n/a	3	rough/angular
42	1.25	no	58.2	2.5	no	n/a	2	smooth
43	1.51	no	62.3	2.5	no	n/a	n/a	n/a

and loading velocities are also listed in Table 4.2, along with whether or not each particle was reloaded and the severity of the reload.

Based on Nakata et al. (2001) and other literature, Parab et al. (Parab et al. 2014) summarized the different types of failure mechanisms that occur within a particle is loaded to and beyond failure stage and classified failure into 5 modes: (1) single abrasion fracture; (2) multiple abrasion fractures; (3) major splitting into two or more particles; (4) breakage of sub-particles; and (5) pulverization into many small pieces (Figure 4.7a). Dynamic loading mechanisms such as blast or impact loading causes many particles to fracture in a pattern similar to groups 3 and 4, which is the realm of this paper. Luo et al. (Luo et al. 2014) observed shifts in particle size distribution before and after HSR loading using SPHB testing that corresponded to particle fracture mostly in modes 3 and 4. Loading speed was optimized such that most of the particles would fail by these two failure modes, allowing the capability to collect fractured particle fragments. The fracture mode and fracture surface were qualitatively described based on SMT images (if collected) of particle fragments. Fracture surfaces are described as smooth, rough, angular, or a combination of these modes (Figure 4.7b). The fracture mode and surface description of imaged particles are presented in Table 4.2.

Individual assessment of the influence of quantitative parameters such as particle size, volume, internal structure, morphology, and contact points (to determine if particle is triangularly loaded) each exhibit a trend with fracture loads but do not yield a strong statistical correlation. Therefore, a multivariable nonlinear regression was conducted with

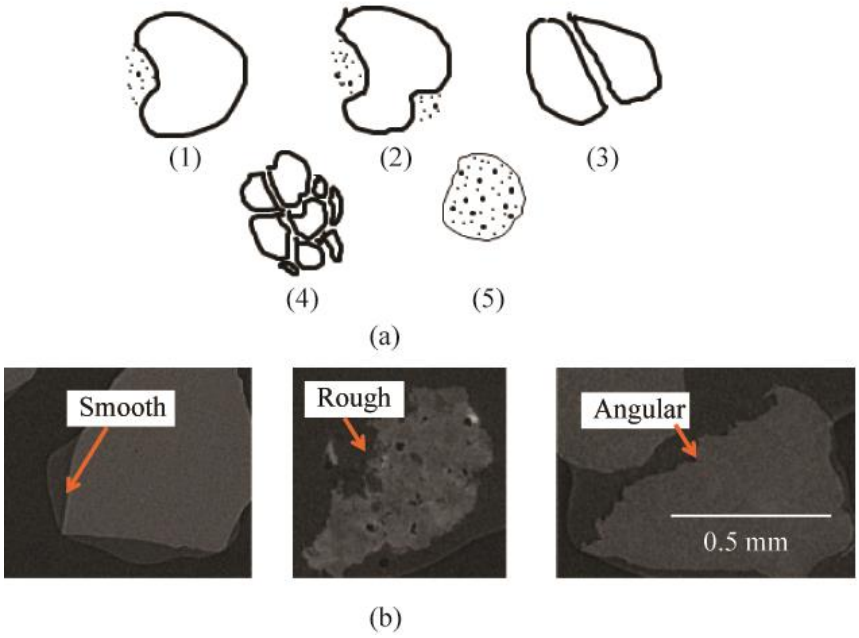

Figure 4.7. Description of particle failure based on (a) (1) single abrasion fracture (2) multiple abrasion fractures (3) major splitting into two or more particles (4) breakage of sub-particles (5) pulverization into many small pieces orders of magnitude smaller than the original particle (after Nakata et al. 2001; Parab et al. 2014) and (b) Fracture surface description examples

predictors of loading diameter, axis lengths, particle volume, internal structure rating, sphericity, roundness, and whether or not the particle was triangularly loaded (0 or 1) for the 43 observations. Other combinations of predictors were also investigated, but these predictors resulted in the most accurate predictions. To fit the trend of the fracture data and demonstrate the validity of the statistical analysis, an exponential model function in the following form was used:

$$f(b,x) = exp(b_1x_1 + b_2x_2 + \cdots + b_nx_n) \quad (4.5)$$

where b is an estimate for each of the n = 9 coefficients for each predictor value x. Predictors and fracture loads were analyzed using Matlab software to generate the multivariable nonlinear model. A summary of coefficients and their standard error (SE), p value, and 95% confidence interval are listed in Table 4.3. The predictive model had a root mean squared value (RMS) of 8.26 N, and R squared value of 0.88 and adjusted R squared value of 0.852. When the predictors with large p value were removed (d_i, d_l, and volume) individually or removed in any combination, the fit (in terms of R squared, adjusted R squared and RMS) became worse. The model can potentially be scaled up to predict individual particle fracture based on forces on the particle in larger scale specimens, provided CT data is available.

Another and more common analysis method of single particle fracture results is the use of Weibull statistics. To characterize failure stress of a particle many researchers (e.g. Brzesowsky et al. 2011; Cil and Alshibli 2012; McDowell and Amon 2000; McDowell and Bolton 1998; Nakata et al. 2001) have followed Jaeger (1967) (or a variation thereof) that defines the characteristic tensile stress of a particle as:

Table 4.3. Results of dynamic particle fracture using mini-Kolsky and imaging techniques

Predictor	Coefficient (*b*)	SE	p Value	95% CI
d_{load}	-4.628	0.574	<0.001	-5.79 to -3.46
d_s	4.585	0.999	<0.001	2.56 to 6.61
d_i	-0.426	0.363	0.25	-1.16 to 0.31
d_l	0.398	0.230	0.09	-0.07 to 0.87
Volume	0.162	0.219	0.47	-0.28 to 0.61
Int. Struct.	-0.458	0.052	<0.001	-0.56 to -0.35
I_{sph}	0.441	0.127	<0.001	0.18 to 0.70
I_R	4.577	0.750	<0.001	3.05 to 6.10
Tria. Loading	-0.241	0.049	<0.001	-0.34 to -0.14

$$\sigma_f = \frac{F_f}{d^2} \tag{4.6}$$

where σ_f is the characteristic tensile stress at failure, F_f is the force required to fracture the particle, and d is particle length in the loading direction. Weibull (1951) proposed a statistical distribution function that has been used in the literature to describe probability of survival as:

$$P_s = exp\left[-\left(\sigma_f/\sigma_{0f}\right)^{m_f}\right] \tag{4.7}$$

where P_s is the probability of survival for a particular particle ($P_s = \frac{\#\ of\ particles\ crushing\ at\ \sigma \geq \sigma_f}{total\ \#\ of\ particles}$), m_f is the Weibull modulus, and σ_{0f} is the characteristic tensile stress at which the probability of survival is 37%, which can be determined from the plot of $\ln(\sigma_f)$ versus $\ln\left[\ln\left(1/P_s\right)\right]$ as shown in Figure 4.8a. The Weibull modulus is the slope of the best fit line and the characteristic tensile stress is the intersection of the best fit line with the x axis. The Weibull modulus and σ_{0f} of this data are 1.25 and 26.86, respectively, and has a good statistical fit. Weibull statistics were also performed on quasi-static experiments of 23 Mason sand particles (Figure 4.8b). Weibull modulus and σ_{0f} of quasi-static experiments data are 1.25 and 27.0, respectively. No significant difference is observed between loading rates using Weibull statistics.

FEA Modeling of Single Particle Fracture

Five particles (Particles #32, 34, 35, 41, 42) were analyzed using FEA. Particles with relatively solid internal structures were selected here because of difficulties in

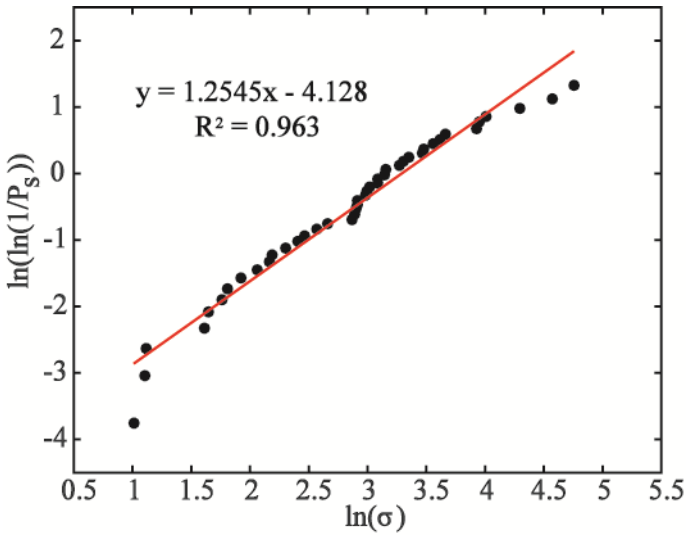

a) 2.5 m/s experiments

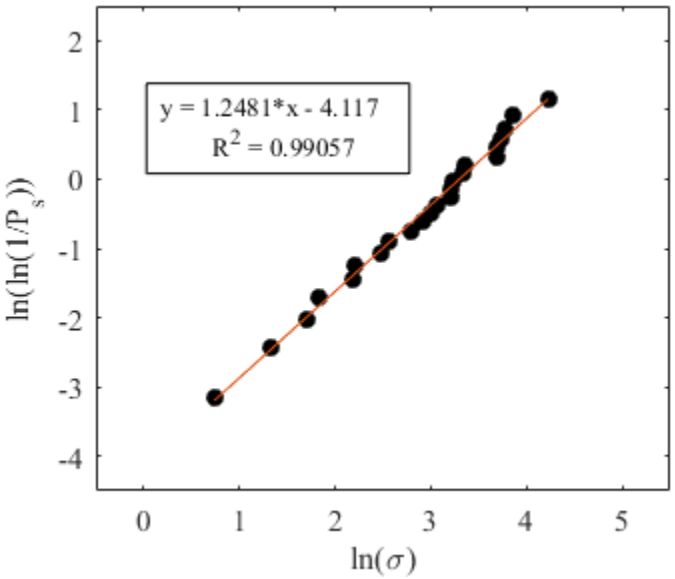

b) Quasi-static experiments

Figure 4.8. Wiebull distribution of characteristic tensile stresses for Mason sand particles

capturing internal flaws in FE meshes. External features and particle morphology can be easily captured and particles can be aligned similar to the experiment. The FEA model for particle fracture was setup with similar methodology as Druckrey and Alshibli (2015). Triangulated particle surfaces were generated from binary images of intact particles, imported into Abaqus FEA software, and filled with volumetric tetrahedral elements. The FE simulated particles in this paper contained approximately 45,000-70,000 tetrahedral elements per particle depending on the particle size. Each particle was assigned linear elastic material properties and density to simulate particle behavior before fracture. Discrete rigid bars were generated to represent the incident and transmitter bars of the experiment, and aligned on the particle based on the optical images that were collected during experiments. General contact in Abaqus Explicit was defined with hard normal contact and frictional tangential behavior. Load was generated by applying velocity to the incident bar in the simulation that matches the velocity for each experiment.

Determination of stresses within a particle as well as the failure strength during high rate loading is an important first step to modeling the fundamental behavior of granular material subject to HSR loading. Currently there are very few experimental techniques to quantify stresses within natural sand particles with complex morphology during loading, including determination of the fracture strength of a particle (without making considerable assumptions). One method is to use x-ray crystalline diffraction during loading such as in Alshibli et al. (2013), but this is currently limited to quasi-static loading and stress averaged throughout the particle (no determination of stress

concentrations). Brittle sand particles typically fail due to tensile stresses, and to represent this, the brittle cracking model was adopted to in the simulations. The failure stress was initially assumed and was adjusted until the loading curves from the FE simulations reasonably matched experimental loading curves. The final failure stress (when the loading curves match) can be a good representation of the actual failure stress of the particle. Post-failure behavior was implemented with brittle shear and brittle failure. Brittle shear is represented by a shear retention facture at a certain crack opening strain. For particles in this research, the shear retention factor is 1 before the particle fails (zero crack opening strain) and 0 when the crack opening strain is very small. Brittle failure was used within the model to remove elements that have failed, allowing a particle to break apart and/or comminute, and allowing post-failure behavior to be captured in the FE simulations. When brittle failure is implemented, a particle can break in half and the fragments continue to carry load, similar to what would occur in high strain-rate experiments.

The force-displacement relationships for the experiment and FE simulation for particle 35 are depicted in Figure 4.9. In the experiment, initial fracture occurs at ~0.017 mm displacement and the load drops. After initial fracture, particle fragments are then loaded until the fragments fracture. This trend is successfully simulated in FEA over the loading duration from the first incident wave. Fracture of the particle in the FE simulation is shown in Figure 4.10. Figure 4.10a is the particle before fracture occurs, Figure 4.10b shows the initial fracture of the particle (after the first major drop of load in the loading

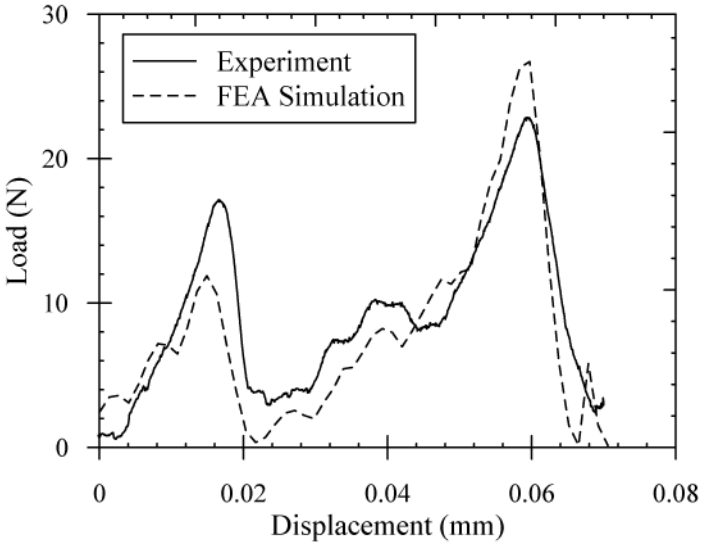

Figure 4.9. Experimental and FEA simulated force-displacement curves for particle 35

curve at ~0.018 mm displacement), and Figure 4.10c displays successive secondary fracture of the particle (after the second large drop in load observed from the loading curve). Simulations were thoroughly inspected to confirm that observations in loading curve pertained to physical observations in the simulation, such as particle rotation or fracture. Changes in the loading curve were therefore contributed to phenomena observed at the particle scale and not to simulated dynamic waves.

Failure stresses for the 5 particle simulations are listed in Table 4.4, along with the characteristic tensile stress from Equation 4.6. The characteristic tensile stress may work well enough for relatively spherical particles, but can lead to a large error for particles with more complex morphology, especially when triangular loading of a particle is present. The characteristic tensile stress of the particles significantly underestimates the failure stress of all particles, especially when triangular loading occurs (particle 32). Also, the averaged stress in the particle does not take into account any stress concentrations, which may have contributed to underestimating tensile failure stresses. Observed differences in FE simulation failure stress may also be due to material heterogeneities or flaws not observable at the current resolution.

Also included in Table 4.4 are failure stresses determined from FEA for two silica Mason sand particles subject to quasi-static compression. Observed failure of quasi-static particle 1 was a large fragment fracture, while quasi-static particle two was bulk failure near the center of the particle. Failure stresses observed during quasi-static compression of the two particles were less than the observed failure stresses in the 2.5 m/s

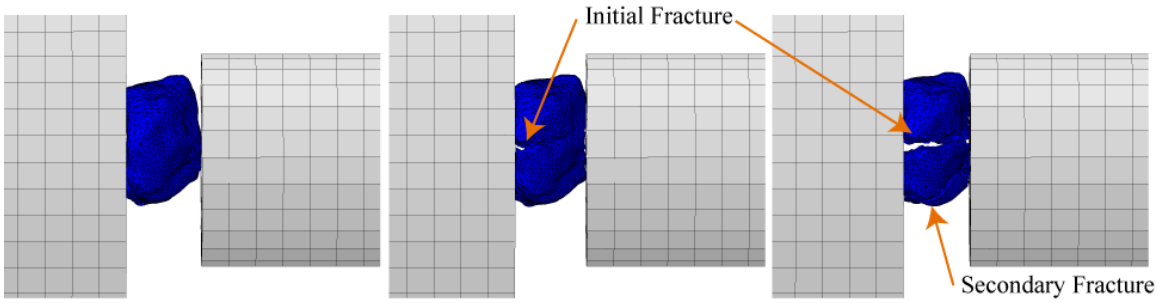

a) 0 displacement b) 0.018 mm displacement c) 0.065 mm displacement

Figure 4.10. Simulation results of particle 35 a) before fracture, b) after initial fracture, and c) after secondary fracture

Table 4.4. FEA simulation failure stress results compared with conventional failure stress techniques

Particle Number	Experimental Failure Load (N)	Failure tensile stress determined by FEA (MPa)	Characteristic tensile stress $\sigma = \frac{F_f}{d^2}$ (MPa)
32	2.8	78	6.8
34	86	156	115.2
35	17.1	212	19.7
41	29.15	75	19.9
42	58.2	112	37.5
Quasi-static 1	8.7	68	11.9
Quasi-static 2	54.1	56	47.0

experiments. Although the fracture loads for each of the quasi-static particles were significantly different, fracture stresses were similar. Actual fracture stresses of particles at higher loading rate may be larger because of less time to fracture, but more data is required for a comprehensive conclusion.

Discussion

A wide range of peak loads were measured within the tested particles and is attributed to the complex morphology, particle size, internal structure (a form of mineralogy), and loading geometry imposed onto particles. In this paper, these parameters are known quantitatively or at least qualitatively. The load required to fracture particles at the strain-rate reported in this paper generally increased with particle size (loading diameter, particle lengths and volume) and with increasing sphericity, and decreased with increasing internal structure rating and decreased significantly when loaded triangularly. Generalized trends are apparent from the data but the fracture loads do not correlate strongly with any individual parameter and include a lot of scatter.

An internal structure rating from 1 to 6 was assigned to each individual particle (Figure 4.2 and Table 4.1). Particles with less flaws (more solid internal structure) generally exhibited higher fracture loads, and the internal structure of the particles related to the mineralogy of each particle. Silica particles (quartz and tridymite) had relatively solid internal structures and were rated 1 or 2. Fracture surfaces of these particles were typically smooth to sub-conchoidal and generally fractured into only a few fragments or had asperities fracture. For example, Figure 4.11a shows an optical image of quartz

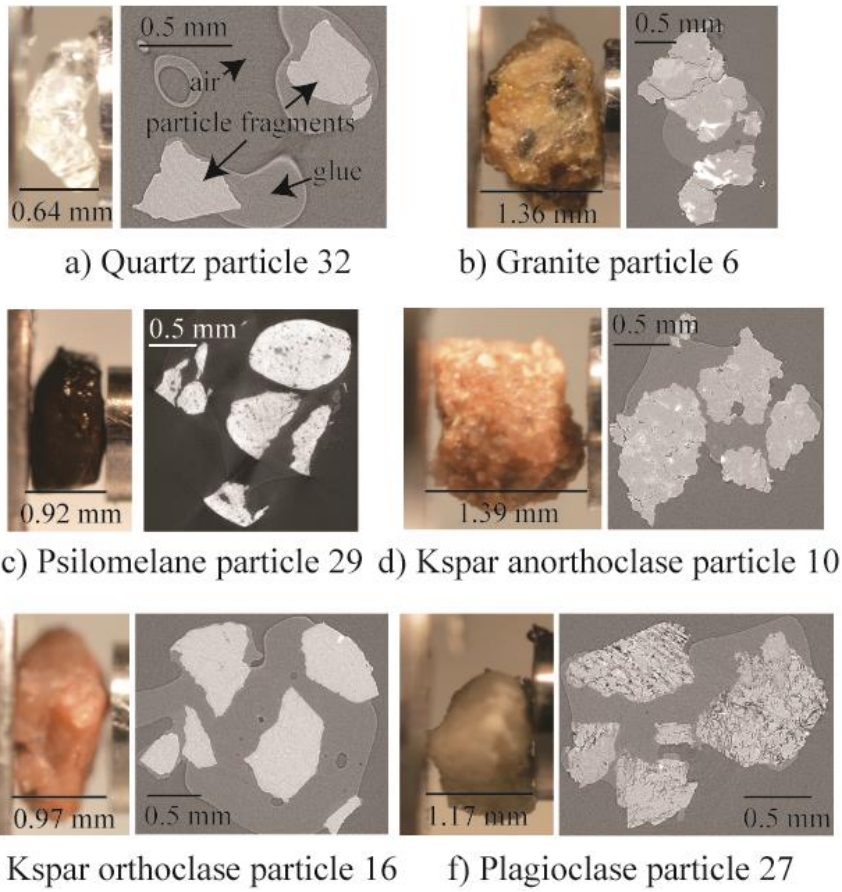

Figure 4.11. Optical images before testing and SMT slices of select fractured particles

particle 32 before testing and an SMT image of the fractured particle that shows locations of air, glue, and particle fragments. This particle was loaded triangularly, where it has two spread out contact on the transmitter bar and a central concentrated contact on the incident bar and split into two major fragments and one smaller fragment.

Granite particles were a mixture of several minerals, and typically had iron inclusions within each particle, resulting in internal structure ratings from 4 to 6. Inclusions created mineral boundaries on which fracture could occur by separation of minerals at the boundaries. Figure 4.11b shows an optical image and fractured CT slice of granite particle 6. The bright spots within the CT image are iron inclusions and internal mineral boundaries became exposed after fracture. Fracture surfaces of these types of particles were hackly. The only psilomelane particle tested (particle 29, Figure 4.11c) has a high CT attenuation (due to mineralogy) and has very few internal voids/inclusions. This particle fractured into many fragments and has angular fracture surfaces. The internal structure of Kspar particles ranged from 2 to 4, of which most flaws were small internal voids or concentrations of internal voids.

The Kspar anorthoclase particle 10 has a rating of 4 and is shown in Figure 4.11d, which was also loaded in a triangular manner. Fracture surfaces of this particle were rough and angular. A Kspar orthoclase particle is shown in Figure 4.11e, which had an internal structure rating of 2 and angular fracture surfaces, similar to the rest of the Kspar orthoclase particles.

The plagioclase group of particles ranged from 3 to 6 depending on the type of plagioclase, some with many internal flaws. Figure 4.11f shows an example of a plagioclase particle. The internal structure has many flaws, and the roughness manifests on the surface of the particle. Plagioclase particles exhibited rough and angular fracture surfaces. Both mica particles (biotite-particle 1 and muscovite-particle 20) have many flaws (rating of 5) with concentrations of flaws and micro-cracks. Pyroxene particles had internal structure rating of 3 or 4 and rough/angular fracture surfaces.

Although there are no strong individual trends between any of the quantitative parameters and fracture load, a relatively accurate multivariable nonlinear statistical model to predict fracture load was developed based on the quantitative parameters as predictors. In the model, each predictor is interrelated with all other predictors such that one predictor might not have as much effect on the results if other predictors are altered. Overall, the strongest predictor was whether or not particle was loaded in a triangular manner, which is also evident in the low fracture loads observed experimentally for particles with triangular loading configuration. The loading diameter and particle short axis (combined) also effected fracture load prediction significantly. When they deviate from each other (i.e. particle short axis is progressively smaller than loading diameter) the predicted force required to fracture the particle decreases significantly. That is, when a particle is loaded along its short axis it will require more force to fracture than if it were loaded on its intermediate or long axis. When loaded along short axis stress is distributed along a larger cross-sectional area, which may contribute to higher fracture forces.

Particle intermediate axis length, long axis length, and volume do not contribute significantly to the predicted load, but are necessary to form a more accurate prediction and statistically viable model. Sphericity, roundness, and internal structure play an intermediate role in prediction of the fracture force, depending on the loading diameter, short axis length, and triangular loading.

A more traditional approach to analyze the fracture stress, Weibull statistics, was also performed based on the characteristic tensile stress of a particle (Equation 6) and the Weibull statistical distribution function (Equation 7). The Weibull modulus for these experiments was 1.25 and the characteristic tensile stress corresponding to 37% probability of survival (σ_{0f}) was 26.86 MPa. These particles have a much lower Weibull modulus and σ_{0f} than the relatively spherical and homogeneous ASTM 20/30 sand during quasi-static testing reported in (Cil and Alshibli 2012). The lower Weibull modulus is due to a greater variance in characteristic tensile stress attributed to the particles. Also, the more angular and non-spherical particles generally require a lower fracture load than spherical particles, resulting in lower σ_{0f}.

To determine fracture tensile strength of a particle (other than the assumption in Equation 4.6), FE simulations of particle compression on actual particle shapes was conducted using a loading rate similar to the experiments. FEA tensile strength exhibited a similar trend to the tensile strength calculated from Equation 4.6, but Equation 4.6 significantly underestimated the tensile strength. Several factors contribute to this observation. Equation 4.6 does not account for low fracture loads due to triangular

loading or for the morphology of the particle. FEA on the actual particle shapes inherently accounts for particle morphology and loading geometry and leads to more accurate internal stresses. Also, Equation 4.6 is an average stress for the entire particle, when in actuality stress concentrations occur and are captured by FEA and incorporated into the tensile strength.

Summary and Conclusions

Natural sand particles with complex morphology and mineralogy were imaged using 3D CT imaging and dynamically compressed in an unconfined Kolsky bar. Particle fragments were collected and analyzed using SMT imaging to determine the fracture mode and fracture surface properties. Dynamic force required to fracture a particle is highly influenced by particle properties and loading conditions which is affected by particle morphology. Although the effect of individual particle properties do not correlate well with fracture load, multivariable nonlinear regression with all of the predictors discussed in this paper lead to a fairly accurate statistical model. Loading configuration, loading diameter, particle short axis diameter, and particle sphericity are the major parameters that influence the force required to fracture a particle, while including the other parameters mentioned in this paper lead to a more accurate statistical model. All parameters interact with each other in the model to predict the fracture force. Another predictor that can eventually be added is the loading rate to determine the effect of loading rate on the force required to fracture a particle. Analyzing loading rate effect is beyond the scope of this paper. However, CT data can be used to quantify all of the

predictors within a sample and/or distributions can be assumed to upscale from single particle to determining particle fracture forces in bulk granular material.

Particle fracture at the loading rate described in this paper also follows Weibull statistical distribution well, resulting in a Weibull modulus of 1.25 and σ_{0f} of 26.86 MPa. These values can be used to compare the fracture strength of particles to other loading rates, particle morphologies, size, or internal structure and is subject for future work.

FEA was used to simulate the experimental particle fracture using actual particle shapes and loading rate. At this loading rate, FEA captured the fracture of an individual particle that was similar to experimental fracture, and the experimental loading curve was matched from the simulation with relatively good accuracy. Fracture strength determined from FEA is significantly higher than using the characteristic tensile strength from Equation 4.6, which was developed for quasi-static loading. Current assumed particle tensile strength formulations, such as that in Equation 4.6 or variations thereof, do not account for stress concentrations within a particle. Therefore, actual stresses within a particle at fracture are higher than assumed stresses and FEA demonstrates fracture stresses more accurately.

References

Allen, W. A., Mayfield, E. B., and Morrison, H. L. (1957). "Dynamics of a Projectile Penetrating Sand." *Journal of Applied Physics*, 28(3), 370-376.

Allen, W. A., Mayfield, E. B., and Morrison, H. L. (1957). "Dynamics of a Projectile Penetrating Sand. Part II." *Journal of Applied Physics*, 28(11), 1331-1335.

Alshibli, K., Cil, M., Kenesei, P., and Lienert, U. (2013). "Strain tensor determination of compressed individual silica sand particles using high-energy synchrotron diffraction." *Granular Matter*, 1-14.

Alshibli, K., Druckrey, A., Al-Raoush, R., Weiskittel, T., and Lavrik, N. (2014). "Quantifying Morphology of Sands Using 3D Imaging." *Journal of Materials in Civil Engineering*, 04014275.

Antony, S. J. (2007). "Link between single-particle properties and macroscopic properties in particulate assemblies: role of structures within structures." *Phil. Trans. R. Society*, 365, 12.

Antoun, T., Herbold, E., Johnson, S. (2012). "Dynamic Behavior of Sand: Annual Report FY 11." Lawrence Livermore National Laboratory.

Behringer, R. P., Bi, D., Chakraborty, B., Clark, A., Dijksman, J., Ren, J., and Zhang, J. (2014). "Statistical properties of granular materials near jamming." *Journal of Statistical Mechanics: Theory and Experiment*, 2014(6), P06004.

Borg, J. P., Van Vooren, A., and Morrissey, M. (2015). "Chapter 6 - In Situ Characterization of Projectile Penetration into Sand." *Rapid Penetration into Granular Media*, Elsevier, Oxford, 187-227.

Børvik, T., Olovsson, L., Hanssen, A. G., Dharmasena, K. P., Hansson, H., and Wadley, H. N. G. (2011). "A discrete particle approach to simulate the combined effect of blast and sand impact loading of steel plates." *Journal of the Mechanics and Physics of Solids*, 59(5), 940-958.

Braslau, D. (1970). "Partitioning of energy in hypervelocity impact against loose sand targets." *Journal of Geophysical Research*, 75(20), 3987-3999.

Brzesowsky, R. H., Spiers, C. J., Peach, C. J., and Hangx, S. J. T. (2011). "Failure behavior of single sand grains: Theory versus experiment." *Journal of Geophysical Research: Solid Earth*, 116(B6), B06205.

Casem, D., and Zellner, M. (2013). "Measurements of Particle Velocity Within a Kolsky Bar with Applications to Wave Separation." *Dynamic Behavior of Materials, Volume 1*, V. Chalivendra, B. Song, and D. Casem, eds., Springer New York, 57-65.

Casem, D. T., Dwivedi, A. K., Mrozek, R. A., and Lenhart, J. L. (2014). "Compression response of a thermoplastic elastomer gel tissue surrogate over a range of strain-rates." *International Journal of Solids and Structures*, 51(11–12), 2037-2046.

Casem, D. T., Grunschel, S. E., and Schuster, B. E. (2012). "Normal and Transverse Displacement Interferometers Applied to Small Diameter Kolsky Bars." *Exp Mech*, 52(2), 173-184.

Cavarretta, I., and O'Sullivan, C. (2012). "The mechanics of rigid irregular particles subject to uniaxial compression." *Geotechnique*, 62(8), 11.

Cil, M. B., and Alshibli, K. A. (2012). "3D assessment of fracture of sand particles using discrete element method." *Géotechnique Letters*, 161-166.

Cil, M. B., and Alshibli, K. A. (2014). "3D evolution of sand fracture under 1D compression." *Géotechnique*, 351-364.

Cole, R. P. (2010). "Ballistic Penetration of a Sandbagged Redoubt Using Silica Sand and Pulverized Rubber of Various Grain Sizes." M.S.M.E., University of South Florida.

Cooper, W. (2011). "Communication of Stresses by Chains of Grains in High-Speed Particulate Media Impacts." *Dynamic Behavior of Materials, Volume 1*, T. Proulx, ed., Springer New York, 99-107.

Cooper, W., and Breaux, B. (2010). "Grain fracture in rapid particulate media deformation and a particulate media research roadmap from the PMEE workshops." *International Journal of Fracture*, 162(1-2), 137-150.

Druckrey, A. M., and Alshibli, K. A. (2015). "3D finite element modeling of sand particle fracture based on in situ X-Ray synchrotron imaging." *International Journal for Numerical and Analytical Methods in Geomechanics*.

Druckrey, A. M., Alshibli, K. A., and Al-Raoush, R. I. (2016). "3D characterization of sand particle-to-particle contact and morphology." *Computers and Geotechnics*, 74, 26-35.

Dwivedi, S. K., Teeter, R. D., Felice, C. W., and Gupta, Y. M. (2008). "Two dimensional mesoscale simulations of projectile instability during penetration in dry sand." *Journal of Applied Physics*, 104(8), 083502.

Eberl, D. D. (2003). "User's guide to RockJock -- A program for determining quantitative mineralogy from powder x-ray diffraction data." U.S. Geological Survey, Boulder, CO.

Felice, C. W., and Gupta, Y. M. (2009). "Penetration Physics at the Meso-Scale." U. S. A. F. O. o. S. Research, ed.

Homel, M. A., Brannon, R. M., and Guilkey, J. (2015). "Controlling the onset of numerical fracture in parallelized implementations of the material point method (MPM) with convective particle domain interpolation (CPDI) domain scaling." *International Journal for Numerical Methods in Engineering*, n/a-n/a.

Huq, F., Brannon, R., and Graham-Brady, L. (2016). "An efficient binning scheme with application to statistical crack mechanics." *International Journal for Numerical Methods in Engineering*, 105(1), 33-62.

Iskander, M., Omidvar, M., and Bless, S. (2015). "Chapter 2 - Behavior of Granular Media Under High Strain-Rate Loading." *Rapid Penetration into Granular Media*, Elsevier, Oxford, 11-63.

Jaeger, J. (1967). "Failure of rocks under tensile conditions." *International Journal of Rock Mechanics and Mining Sciences & Geomechanics Abstracts*, 4(2), 219-227.

Knodel, P. C., Charlie, W. A., Ross, C. A., and Pierce, S. J. (1990). "Split-Hopkinson Pressure Bar Testing of Unsaturated Sand." *Geotech. Test. J.*, 13(4), 291.

Luo, H., Cooper, W. L., and Lu, H. (2014). "Effects of particle size and moisture on the compressive behavior of dense Eglin sand under confinement at high strain rates." *International Journal of Impact Engineering*, 65, 40-55.

Luo, H., Lu, H., Cooper, W. L., and Komanduri, R. (2011). "Effect of Mass Density on the Compressive Behavior of Dry Sand Under Confinement at High Strain Rates." *Experimental Mechanics*, 51(9), 1499-1510.

Martin, B. E., Chen, W., Song, B., and Akers, S. A. (2009). "Moisture effects on the high strain-rate behavior of sand." *Mechanics of Materials*, 41(6), 786-798.

McDowell, G. R., and Amon, A. (2000). "THE APPLICATION OF WEIBULL STATISTICS TO THE FRACTURE OF SOIL PARTICLES." *SOILS AND FOUNDATIONS*, 40(5), 133-141.

McDowell, G. R., and Bolton, M. D. (1998). "On the micromechanics of crushable aggregates." *Geotechnique*, 667-679.

Meyer Jr, H. W., and Brannon, R. M. (2012). "A model for statistical variation of fracture properties in a continuum mechanics code." *International Journal of Impact Engineering*, 42, 48-58.

Mitchell, M. R., Link, R. E., Luscher, W. G., Hellmann, J. R., Segall, A. E., Shelleman, D. L., and Scheetz, B. E. (2007). "A Critical Review of the Diametral Compression Method for Determining the Tensile Strength of Spherical Aggregates." *Journal of Testing and Evaluation*, 35(6), 100793.

Nakata, Y., Hyodo, M., Hyde, A. F. L., Kato, Y., and Murata, H. (2001). "MICROSCOPIC PARTICLE CRUSHING OF SAND SUBJECTED TO HIGH PRESSURE ONE-DIMENSIONAL COMPRESSION." *Journal of the Japanese Geotechnical Society : soils and foundation*, 41(1), 69-82.

Nakata, Y., Kato, Y., Hyodo, M., Hyde, A. F. L., and Murata, H. (2001). "ONE-DIMENSIONAL COMPRESSION BEHAVIOUR OF UNIFORMLY GRADED SAND RELATED TO SINGLE PARTICLE CRUSHING STRENGTH." *Journal of the Japanese Geotechnical Society : soils and foundation*, 41(2), 39-51.

Omidvar, M., Iskander, M., and Bless, S. (2012). "Stress-strain behavior of sand at high strain rates." *International Journal of Impact Engineering*, 49, 192-213.

Parab, N. D., Claus, B., Hudspeth, M. C., Black, J. T., Mondal, A., Sun, J., Fezzaa, K., Xiao, X., Luo, S. N., and Chen, W. (2014). "Experimental assessment of fracture of individual sand particles at different loading rates." *International Journal of Impact Engineering*, 68, 8-14.

Peters, J. F., Muthuswamy, M., Wibowo, J., and Tordesillas, A. (2005). "Characterization of force chains in granular material." *Physical Review E*, 72(4), 041307.

Regueiro, R., Pak, R., McCartney, J., Sture, S., Yan, B., Duan, Z., Svoboda, J., Mun, W., Vasilyev, O., Kasimov, N., Brown-Dymkoski, E., Hansen, C., Li, S., Ren, B., Alshibli, K., Druckrey, A., Lu, H., Luo, H., Brannon, R., Bonifasi-Lista, C., Yarahmadi, A., Ghodrati, E., and Colovos, J. (2014). "ONR MURI Project on Soil Blast Modeling and Simulation." *Dynamic Behavior of Materials, Volume 1*, B. Song, D. Casem, and J. Kimberley, eds., Springer International Publishing, 341-353.

Regueiro, R. A., Zhang, B., and Shahabi, F. (2015). " Micromorphic continuum stress measures calculated from three-dimensional ellipsoidal discrete element simulations on granular media." *Proc., Geomechanics from Micro to Macro*, CRC Press, London, 195-200.

Rivers, M. L., Citron, D. T., and Wang, Y. (2010). "Recent developments in computed tomography at GSECARS." *SPIE*, 3, 780409-780409.

Suescun-Florez, E., Omidvar, M., Iskander, M., and Bless, S. (2015). "Review of High Strain Rate Testing of Granular Soils."

Wang, Z., Yang, X., Chen, Q., Zhang, Y., and Zhao, Y. "Study of the contact forces and grain size distribution during grain crushing." *Proc., Multimedia Technology (ICMT), 2011 International Conference on*, 2617-2622.

Weibull, W. (1951). "A Statistical Distribution Function of Wide Applicability." *Journal of Applied Mechanics*, 18(3), 293-297.

Yoshida, Y. (2005). "Force chains and the fragmentation of granular materials." MSCE Master's Thesis, University of Pittsburgh.

Zhao, B., Wang, J., Coop, M., Viggiani, G., and Jiang, M. (2015). "An investigation of single sand particle fracture using X-ray micro-tomography." *Géotechnique*, 65(8), 625-641.

CHAPTER 5

3D STRAIN LOCALIZATION AND LOCAL SHEAR BAND EVOLUTION IN SHEARED GRANULAR MATERIALS USING SYNCHROTRON MICRO-COMPUTED TOMOGRAPHY

A version of this chapter has been submitted to Geotechnique. The author list is: A. Druckrey, K. Alshibli.

My primary contributions to this paper include (i) development of problem statement, (ii) conduction of most experiments during in-situ SMT imaging, (iii) processing and quantification of SMT images, (iv) development of code to track particles and quantify kinematics, (v) development of relative displacement code to expose intricate areas of localized strain, (vi) processing, analysis, and interpretation of experimental data, (vii) most of the writing.

Abstract

It is well known that the constitutive behavior of granular materials is highly influenced by strain localization into zones of intensive shearing known as shear bands. The failure mode of specimens tested under axisymmetric triaxial compression is commonly manifested through single or multiple shear bands or diffuse bifurcation (bulging). The ability to monitor the evolution of strain localization has been enhanced by measuring particle kinematics using discrete element method or 3D imaging techniques such as x-ray computed tomography. However, particle kinematics cannot expose intricate localized shearing during pre-peak regime and internal granular material behavior before reaching the peak deviator stress is still unknown. This paper presents the results of 3D synchrotron micro-computed tomography (SMT) scans of sand and glass beads that were acquired at multiple strains during triaxial experiments. Individual particles were identified and tracked through multiple strains and particle translations

were calculated. Each particle's neighboring particles were identified, and translation fields for each of the neighboring particles were calculated. The second order norm between the particle translation vector and neighboring particles translation vectors were averaged, resulting in a relative displacement value for each particle. The relative displacement concept is effective to uncover the onset of localized shearing within sheared granular materials. Progression of local shearing into a final well-defined single or multiple shear bands provides a micro-mechanics insight into mechanisms that describe the failure mode of sheared granular materials.

Introduction

Granular materials are composed of discrete particles that translate and rotate against neighboring particles when they are subjected to global stresses applied at the laboratory specimen or soil mass boundaries. Rowe (1962) thoroughly discussed the approach of treating granular materials as a set of discrete 2D particles rather than a continuum, where strength and volume change of the material is influenced by micro-scale properties that cause local shearing. Loading of soils will eventually cause the soil mass to fail through shearing along zones of intensive shearing known as shear bands. Localization of plastic shear strains and subsequent development of shear bands initiates during the pre-peak regime in true triaxial experiments, as detected through sudden strength reduction, and failure is a consequence of shear band (bifurcation) rather than a constitutive response of the material itself (Lade 2002).

Investigations of mechanisms leading to strain localization in granular material experiments have been difficult to quantify until the emergence of discrete or distinct element method (DEM) (Jiang et al. 2010; Kuhn and Bagi 2004; Oda and Iwashita 2000; Oda et al. 1997), digital image correlation (DIC) (Hall et al. 2009; Rechenmacher and Finno 2004), x-ray computed tomography (CT) (Andò et al. 2012; Druckrey and Alshibli 2014; Fu et al. 2008; Hall et al. 2010; Hasan and Alshibli 2012; Sjödahl et al. 2012), as well as theoretical and numerical methods (Alsaleh et al. 2006; Alshibli et al. 2006; Walker et al. 2013). For example, Oda and Iwashita (2000) developed a modified DEM approach and laboratory biaxial experiments to investigate onset of shear bands in granular materials. Local strains exposed mini shear bands at peak stress state that eventually developed into a single major shear band during the critical state. Column-like structures parallel to the major principal stress direction nucleated and collapsed during strain pre-peak and were regenerated during post-peak PSR softening by means of particle rolling. Also, stress states were found to be different across shear band boundaries. Jiang et al. (2010) noticed the birth of mini shear bands near peak stress state that enetually developed into a single shear band after the phase-change point during DEM simulations of biaxial experiments. Hall et al. (2009) found evidence of complex evolving internal structures consisting of bands of localized deformation on specimen surfaces using DIC of biaxial experiments. Hall et al. (2010) applied 3D volume digital image correlation (V-DIC) to x-ray micro-tomography (XRCT) images and observed and quantified the onset and evolution of localized deformation in sand. X-ray images were

acquired at multiple compressive axial strains and V-DIC was used to characterize shear band development throughout the experiment using grain scale kinematics of displacements and rotations. Using particle kinematics, the final shear band in the experiments reported by Hall et al. (2010) was well defined during the post-peak PSR softening and critical state. Andò et al. (2012) expanded on the work of Hall et al. (2010) and developed ID-track, a computer code that discretized each particle within an XRCT image and tracked particle kinematics throughout subsequent images of an experiment. Using this method, final shear bands were initially apparent near the peak principal stress ratio (PSR) that fully developed during the post-peak PSR softening and critical state of the experiments.

Experimental quantification of 3D particle kinematics can be useful in micromechanical quantifications such as shear band thickness that are important for strain localization and bifurcation models that incorporate strain localization at failure. However, traditional particle kinematics alone do not uncover intermittent strain localization during pre-peak regime or the evolution of strain localization into a single shear band at failure. Andò et al. (2012) presented an interesting concept at the particle level by differentiating particles displacing upward and downward, but important particle level features were still relatively masked as localized strains were not observed until peak stress state and no localized strain was observed during the pre-peak regime. Such techniques have led to particle-scale and meso-scale discoveries of the onset and evolution of failure in granular material via shear bands that have proved valuable in

developing theories that account for strain localization and bifurcation (Da Cruz et al. 2002; Nicot and Darve 2007; Nicot et al. 2009)

Few researchers have investigated intermittent micro-band formation during pre-peak phase using 2D DEM and DIC techniques. Kuhn (1999) used DEM experiments to investigate local void-based fabric parameters and found that thin obliquely trending bands were the predominant deformation structures in which slip deformation was most intense. These thin structures, named microbands, appeared at the beginning of the test and spontaneously throughout loading. Unlike shear bands, micro-bands are relatively thin (one to four times the mean particle size (d_{50}) in thickness) and are neither static nor persistent. Kuhn (2003) and Kuhn (2005) expanded on the DEM microband concept using strain gradients in granular materials and concluded that strain localization is not an isolated phenomenon and microbands and non-persistent shear bands develop before the final stationary band. These microbands can be modeled using second-gradient linear models, while a more complex non-linear model can predict the deformation profile of a non-persistent shear band during pre-peak. Few researchers have found experimental evidence of micro-bands within biaxial experiments using DIC. Based on surface observations on biaxial experiments, Rechenmacher (2006) noticed that multiple and conjugate shear bands initiated during the pre-peak regime, but the persistent final shear band was not fully obvious until post-peak PSR softening. Bouil et al. (2014) was able to detect extremely small heterogeneous strains (of the order of 10^{-5}) with DIC of biaxial experiments, finding intermittent microband development and subsequent collapse

between 2.5% axial strain and peak deviator stress, where a final persistent shear band dominates. Structured deformations such as microbands seem to occur sporadically during the pre-peak phase of a given experiment especially biaxial specimens and eventually lead to the development of a persistent shear band during post-peak PSR softening and critical states. Evidence of micro-bands has been detected using DEM and DIC; however, traditional discrete particle kinematics fall short in determining micro-band formation in experiments on sand. Also, if failure of the granular material is through diffuse bifurcation, detection of localized shearing using particle kinematics is difficult during critical state. To the author's best knowledge, 3D experimental micro-band analysis is not reported in the literature.

This paper uses 3D measurements of individual particle kinematics during axisymmetric triaxial experiments to track the onset of strain localization within granular material using synchrotron micro-computed tomography (SMT). A new technique is proposed to calculate the displacement vectors of individual particles relative to displacement vectors of neighboring particles using the second order norm, or Euclidian length difference, which gives the particle's discrete relative displacement. Particle relative displacement (*rd*) is a measure of how much a particle translates relative to all of its contacting neighbors. rd technique uncovered the onset of multiple micro-bands that develop during the pre-peak phase and eventually evolve into fewer persistent shear bands. The paper discusses the influence of particle morphology and confining pressure on the failure mode of triaxial experiments in 3D.

The concept of critical state has been disputed and defended by many in the literature (e.g. Been et al. 1991; Mooney et al. 1998; Riemer and Seed 1997; Verdugo and Ishihara 1996). Critical state will be referred to in this paper, and the rest of this dissertation, as the point during the experiment where strength behavior of the material reaches steady-state. At this point deformation behavior may or may not be at steady state, depending on the material. Using particle relative displacements, this paper exposes that shear banding within the material reaches a steady –state when strength behavior of the material reaches critical state. Formation and destruction of internal shear bands no longer occurs within the specimen at critical-state and failure only occurs within areas of localized shearing that have already formed.

Materials Description and Experiments

Four granular materials of different morphologies described in Alshibli et al. (2014) were used in this paper. Three silica sand known as F-35 Ottawa sand, GS#40 Columbia grout, and #1 dry glass, along with glass beads with particle sizes between U.S. sieves #40 (0.429 mm) and #50 (0.297 mm) were used in the experiments. Average micro-scale particle morphology properties of sphericity and roundness based on 3D images of particles are presented in Alshibli et al. (2014) and summarized in Table 5.1. The glass beads have average sphericity (I_{sph}) of 1.096 and roundness (I_R) of 0.965; closest to unity, being the most spherical and least angular of the four granular materials. F-35 sand has the highest sphericity value (least spherical, I_{sph} = 1.872), followed by #1 dry glass sand (I_{sph} = 1.704) and GS#40 Columbia grout sand (I_{sph} = 1.674), which are

relatively close in sphericity to each other. Of the three sands, F-35 has a roundness index closest to unity (I_R = 0.959) after glass beads, followed by the more angular dry glass sand (I_R = 0.937) and the most angular GS#40 sand (I_R = 0.924).

A small triaxial apparatus described in Hasan and Alshibli (2012) and Druckrey and Alshibli (2014) was setup in beamline 13BMD of Advanced Photon Source (APS), Argonne National Laboratory (ANL), Illinois, USA. Specimens are cylindrical and initially measure about 10 mm in diameter by 20 mm in height. Eight axisymmetric triaxial compression experiments were conducted on very dense dry specimens under drained condition at two confining pressures ($\sigma_3 = 15\ kPa\ or\ 400\ kPa,$ Table 5.1). Specimens were prepared in 5 lifts, lightly tamping each lift using 9 mm rod to densify before adding the next lift. The prescribed σ_3 was applied to the specimen and the apparatus was mounted on the stage of the x-ray beam for SMT imaging.

Advantages of SMT imaging are summarized in Druckrey et al. (2016), some of which are high resolution and sharp particle edges. Individual scans were acquired at increasing displacements, pausing the experiment to collect 900 radiograph images at 0.2° rotation increments, and radiographs were reconstructed to create 3D SMT images. Resolution for images in each experiment are listed in Table 5.1. More information on image collection and reconstruction can be found in (Rivers 2012; Rivers et al. 2010). An initial image was acquired, the top end plate was moved at a constant compressive displacement rate of 0.2 mm/minute to a predetermined target displacement, loading was paused and the next image was acquired. It took approximately 50 minutes to collect

Table 5.1. Summary of the experiments

Material	Exp.	I_{sph}	I_R	Initial void ratio	σ_3 (kPa)	D_r (%)	Resolution (μm/voxel)
F-35 Ottawa sand (F35)	F35-15kPa	1.872	0.959	0.510	15	131	11.14
	F35-400kPa			0.531	400	120	11.18
#1 Dry glass sand (DG)	DG-15kPa	1.704	0.937	0.637	15	134	11.14
	DG-400kPa			0.667	400	121	11.18
GS#40 Columbia grout sand (GS40)	GS40-15kPa	1.674	0.924	0.627	15	126	11.14
	GS40-400kPa			0.644	400	119	8.16
Glass beads (GB)	GB-15kPa	1.096	0.965	0.518	15	170	11.14
	GB-400kPa			0.556	400	144	11.18

one SMT scan. Particle kinematics can be determined between each of these incremental displacements (or strains), as particles translate and rotate as a result of the global loading. Strain increments are hereafter referred to as the interval between successive images.

Compressive Load and displacement measurements were also collected during each of the experiments and the principal stress ratio (PSR = σ_1/σ_3) and volume change (ε_v) versus nominal axial strain (ε_1) relationships for all experiments are presented in Figure 5.1. Markers in Figure 5.1 label axial strains at which SMT scans were acquired (marks were omitted on ε_v curves for clarity). Under relatively high confining pressure (σ_3 = 400 kPa), all specimens exhibited a gradual increase in PSR to a peak state followed by a small post-peak PSR softening (Figure 5.1a). The #1 dry glass sand (DG-400kPa) exhibited the highest peak PSR of 4.2 at $\varepsilon_1 = 7.1\%$, followed by a small post-peak PSR softening. The F35-400kPa sand specimen reached a peak PSR of 3.9 at $\varepsilon_1 = 4.9\%$, followed by relatively more post-peak PSR softening. The GS40-400kPa specimen closely followed F35-400kPa where it reached the peak PSR of 3.8 at $\varepsilon_1 = 5.0\%$ followed by a small post-peak PSR softening. The glass beads specimen reached a peak PSR of 2.8 at $\varepsilon_1 = 3.7\%$ followed by a very small post-peak PSR softening. Of the four materials under σ_3 = 400 kPa, DG-400kPa experiment was the only specimen that did not exhibit a well-defined single shear band at critical state. Specimens tested under low confining pressure (σ_3 = 15 kPa) did not exhibit a peak PSR but rather an initial increase in PSR followed by a smaller rate of increase as compression

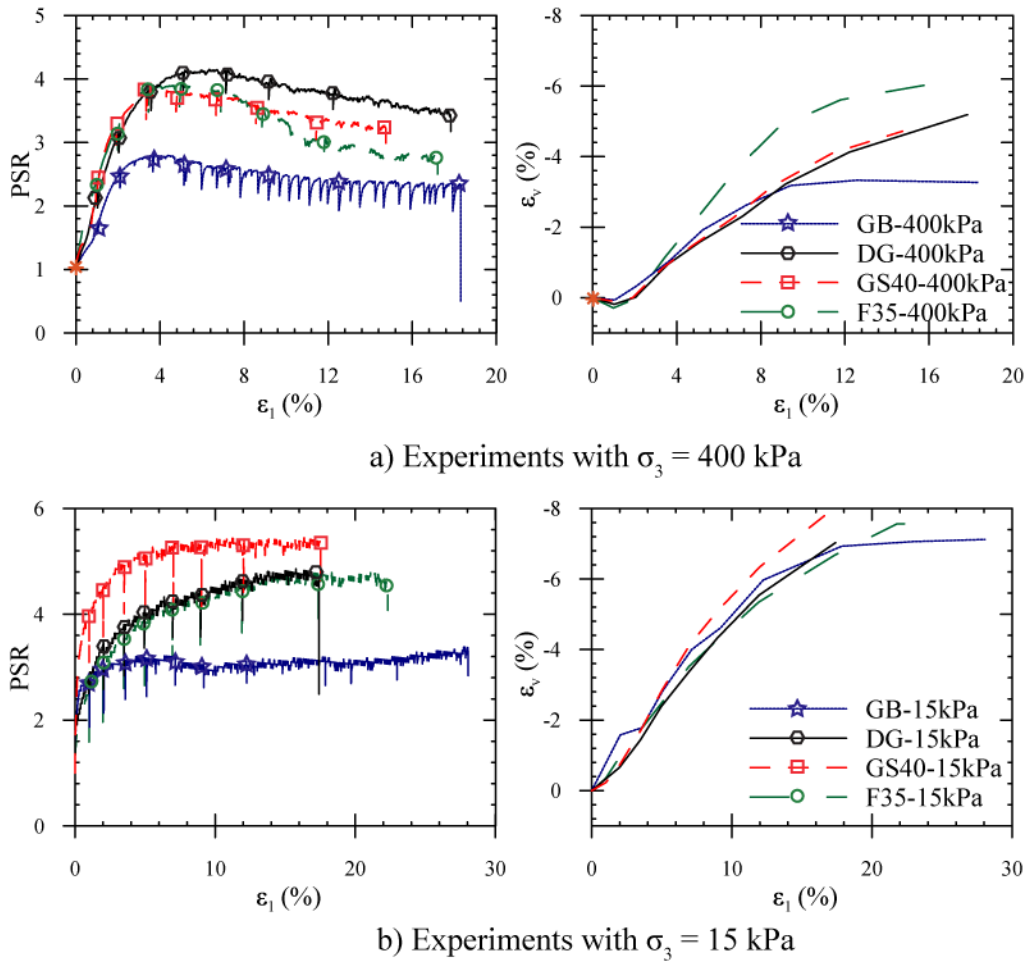

Figure 5.1. Principal stress ratio (PSR) versus axial strain and volumetric strain versus axial strain for the experiments

progressed and leveling off at critical state (Figure 5.1b); a typical behavior of a very dense specimen tested at low confining pressure. The 400 kPa experiments exhibit a volume increase after a small initial contraction whereas the 15 kPa experiments dilate throughout the experiments with no initial contraction.

Image Processing and Particle Tracking

To quantify discrete particle kinematics at multiple strains, images must be processed to uniquely label each particle within the image. Image processing was conducted using the procedure described in Druckrey et al. (2016). Grayscale SMT images were initially filtered and binarized, and particles were separated using a combination of watershed, distance transform, and numerical reconstruction algorithms that removed small areas of contact between particles. With particles no longer in contact, each particle was assigned a unique label number and contacts were restored. Example grayscale and final labeled images are shown in Figure 5.2 for the initial scan of F35-400kPa experiment. SMT technique produced high quality grayscale images that resulted in accurate particle identification after processing. Images at each axial strain increment were then quantified using the code described in Druckrey et al. (2016) and particle centroid, volume, surface area, short axis length, intermediate axis length, long axis length, and contact information were extracted and saved for each particle. In addition, orientation of the particle long, intermediate, and short axes were computed and

saved in output files for further analysis. Initial void ratios were calculated from the images based on the volumetric ratio of voids (within the membrane encasing the

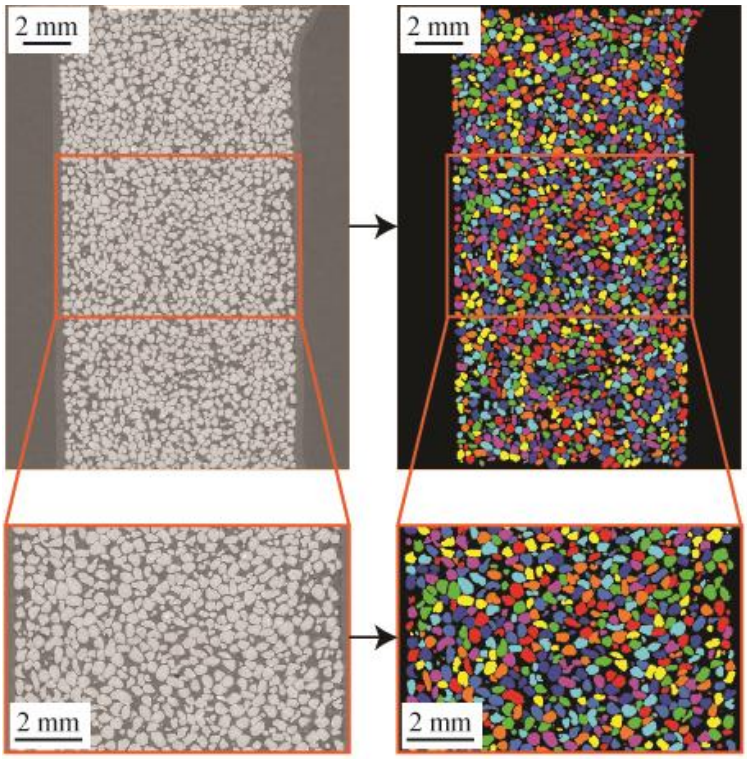

Figure 5.2. Example SMT grayscale image and labeled image after processing it

specimen) to total particle volume and are listed in Table 5.1, as well as the relative density (D_r) that was calculated from the specimen void ration, the maximum and minimum index densities for calculating relative densities that were measured according to ASTM-D4253 and ASTM-D4254 standard procedures, respectively. It is interesting to notice that specimens have D_r values higher than 100%. Lo Presti et al. (1992) reported similar observations.

The same particle is assigned a different number in different images which is caused by rearrangement of particles during experimentation and the nature of computer algorithm used to identify particles, which labels particles in an image from the top to bottom. In order to quantify particle kinematics between strain increments, each particle needs to be identified from one strain increment to the next. An incremental particle tracking code was developed to track individual particles using particle morphology data, similar to the particle tracking code in Druckrey and Alshibli (2014). A search box large enough to consider particle displacement from global loading was first isolated around the centroid of the particle of interest in the first SMT image. Particles in the next SMT image within the search box were compared to the particle of interest using particles' surface area, volume, and the three particle lengths. If particles within the search box matched all particle properties within the certain tolerance set by the user, they were considered for matching. If no particles were matched, they were omitted for that increment. Typically, only one particle matched the particle of interest within all set tolerances, but occasionally more than one particle would be a match (especially if

particles are very uniform) and occasionally zero matches occurred. In the case of multiple matching particles, the particle in the second SMT image with the closest matching features was considered as the counterpart to the particle of interest in the first SMT image. The magnitude of particle displacement was then calculated as the distance between the centroid of a particle in the first SMT image (x_1, y_1, z_1) and the centroid of the matching particle in the second SMT image (x_2, y_2, z_2) as:

$$displacement = \sqrt{(x_1 - x_2)^2 + (y_1 - y_2)^2 + (z_1 - z_2)^2} \qquad (5.1)$$

Particle rotations were also calculated based on differences in long axis orientations between the increments. Applying this particle kinematics analysis to an entire specimen at multiple strains is similar to 3D digital volume correlation. An example of particle kinematics for F35-D-400kPa experiment is shown in Figure 5.3 in the plane parallel to specimen shear band at critical state, displaying the shear band at its narrowest point of view. Particle displacements shown in Figure 5.3 are normalized for each strain increment by the axial displacement of the specimen top plate (i.e., global compression). The specimen failed via a single well-defined shear band that initiated near the peak PSR (ε_1~ 4.9%) and is easily identified from particle displacements and rotations during the post-peak PSR softening (ε_1 = 8.9%-11.8%) and critical state (ε_1 = 8.9%-11.8%) of the experiment. Particle rotations do not exhibit localization during earlier stages of the experiment. Particle displacements show a nucleation of the shear band, but are not definitively localized until post-peak PSR softening. Such conventional particle kinematics can be used to analyze and quantify failure shearing behavior of

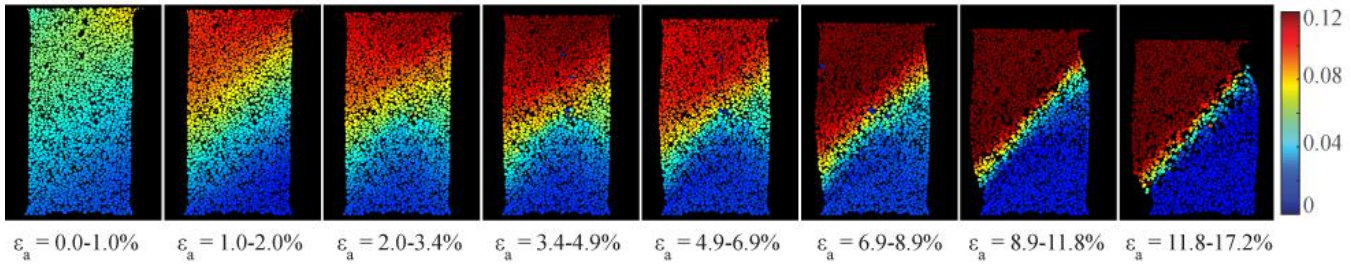

a) Normalized particle displacements

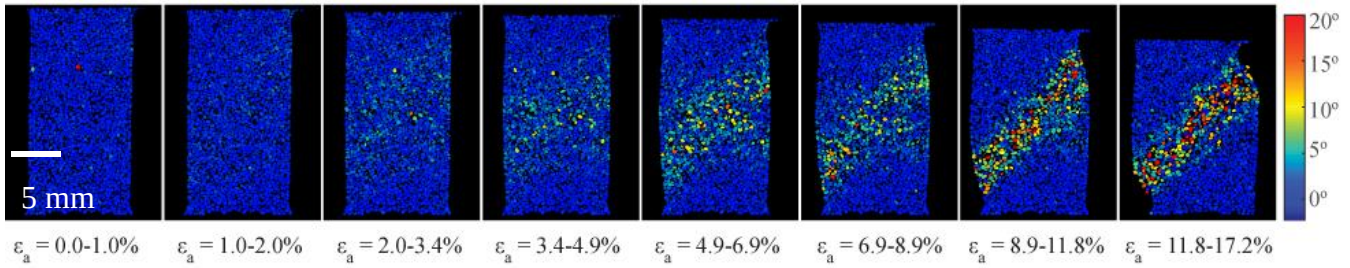

b) Particle long axis rotations

Figure 5.3. Particle kinematics of F35-400kPa experiment

granular material, but mask many intricacies and lesser intermittent localized strains (micro shear bands, MSB) during pre-peak that lead to failure, especially if a specimen fails through bulging.

Intricate zones of localized strain within a specimen that are not exposed by particle kinematics can be mined from the data by comparing a particle's displacement vector with that of all of its neighboring particles. The concept of relative particle displacement branches from kinematic displacements and relates a particle displacement vector (δ) to that of all neighboring particles in contact with that particle (δ_1, δ_2, …, δ_n), using the second order norm of vector differences:

$$rd_i = norm(\delta - \delta_i) \quad (5.2)$$

$$rd = \frac{1}{n}\sum_{i=1}^{n} rd_i \quad (5.3)$$

where rd_i is the magnitude of relative displacement for a single contacting neighboring particle and *n* is the number of contacting particles. The overall magnitude of relative displacement is the average of all individual relative displacement vectors (*rd*). Figure 5.4 shows an illustration of particle relative displacement, where particles 1, 2, and 3 have displacements δ_1, δ_2, and δ_3, respectively. Quantifying particle displacements (as in Figure 5.3) would not show a quantifiable difference between particle 1 and the other two particles in either Figure 5.4a or 4b because the magnitude of displacements are all the same. Relative displacement for particle 1 would be zero for the case demonstrated in Figure 5.4a (same direction and magnitude of displacements) and a larger value for the case demonstrated in Figure 5.4b because direction is considered in calculating particle

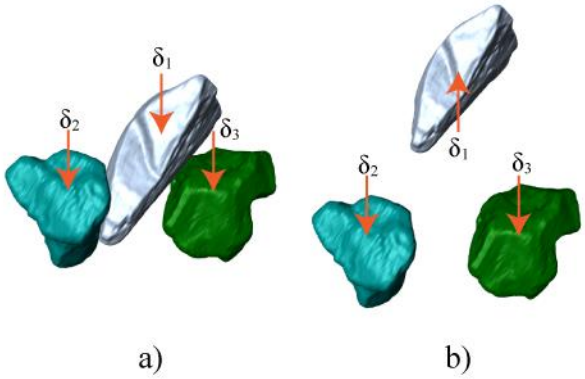

Figure 5.4. Illustrative example of particle relative displacements having a) the same relative displacement and b) different relative displacements

relative displacement. Relative displacement not only differentiates vertical displacements, but localized displacement in any 3D direction. Relative displacement better captures the shear between particles, exposes small localized strains within a granular material, and allows for quantification and visualization of local MSB throughout the experiment as well as analysis of mechanisms that contribute to the onset and growth of the major shear band if any.

Results

Very dense specimens tested under high confining pressure ($\sigma_3 = 400$ kPa)

Incremental relative displacements of individual particles were calculated from the SMT images where the previous SMT image was taken as the reference for relative displacement of particles in the current SMT image. Relative displacements are normalized by the global axial compression imposed by the top end plate. Figure 5.5 displays the Incremental relative displacements for F35-400kPa experiment (slices are taken normal to final shear band for better visualization). Strain pre-peak for this experiment took place between ε_1 = 0-4.9%, peak PSR was reached between ε_1 = 4.9% - 6.9%, followed by post-peak PSR softening between ε_1 = 6.9% - 11.8%, and critical state transpires thereafter (Figure 5.1a). Zones of localized strain, not necessarily shear bands, sporadically developed as early as the first strain increment (ε_1 = 0-1%). Then at ε_1 = 1%-2%, strains localized into multiple MSB with thicknesses of $1d_{50}$ to $3d_{50}$, where d_{50} is the mean particle size (0.36 mm). The MSB exhibited preferred orientations parallel

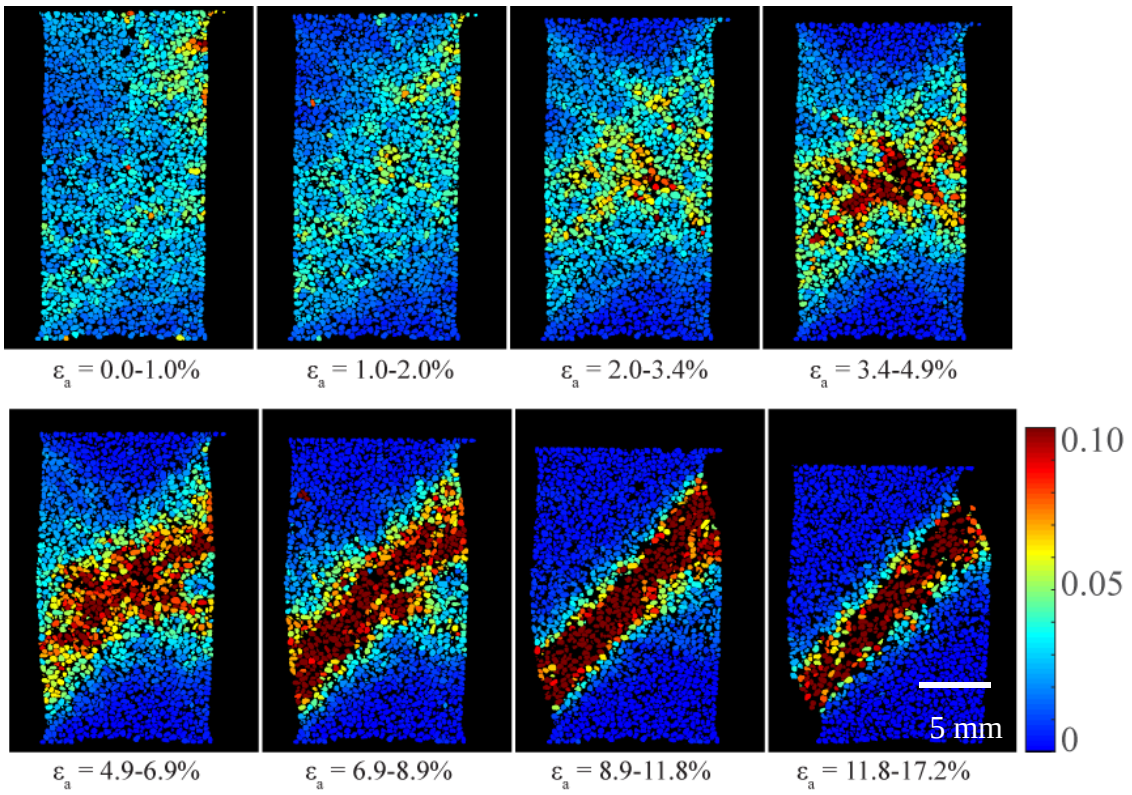

Figure 5.5. Normalized relative displacements for F35-400kPa experiment

and perpendicular to the inclination of the of final major shear band that would develop at a higher strain. The MSB became more developed and more defined in the third strain increment (ε_1 = 2%-3.4%), where multiple cross-hatched MSB develop in multiple directions. These multiple intersecting MSB typically extend over the entire width of the specimen in conjugate directions with orientations similar to the final shear band. The MSB began to retreat and merge into a zone of entropy near the center of the specimen at the end of strain pre-peak phase of the experiment (ε_1 = 3.4%-4.9%). MSB within this strain increment have thicknesses of $2d_{50}$ to $5d_{50}$. The zone of highly disordered particle relative displacements near the end of pre-peak is still in the general direction of the final shear band, although MSB in other directions are still growing from the zone of disarray. During the peak PSR phase (ε_1 = 4.9%-6.9%), most MSB have merged into a large zone of disordered relative displacements that has an overall inclination of the final major shear band, while few minor MSB were still extend from the zone of intensive shearing. The final major shear band fully develops during the post-peak PSR softening phase of the experiment and continues through the critical state phase. Particles within the final major shear band exhibit a high relative displacement values which uncovers an interesting experimental evidence that intensive shearing and interaction takes place between particles within the shear band. The thickness of the shear band is $9d_{50}$ to $10d_{50}$ and edges are delineated by transition bands with a thickness of d_{50} to $3d_{50}$ that have slightly less relative displacements than particles within the major shear band.

Relative displacements show much more intricate detail of particle behavior during pre-peak than conventional particle kinematics approach. The onset of multiple MSB in several directions is exposed using relative displacements that are not apparent when quantifying particle displacements or rotations of experiment F35-400kPa. The MSB merge and contribute to the development of the final shear band in a very complex shear evolution process, which is not captured based on calculating particle displacements or rotations. The final shear band is well defined and delineated with high relative displacements, while conventional particle displacement calculations and rotations do not expose the d_{50} to $3d_{50}$ delineation with as much detail. Figure 5.6 displays slices that are parallel to the final shear band (orthogonal to those shown in Figure 5.5). During pre-peak and peak PSR phases, MSB initiate and progress similar to the orthogonal direction, suggesting a complex 3D network of MSB formation and evolution. During post-peak PSR softening and critical state, Figure 5.6 shows that the MSB merge and form the final shear band, as evident in the centralized zone of localized strain at ε_1 = 8.9%-11.8% in Figure 5.6.

Relative displacements for GB-400kPa experiment are depicted in Figure 5.7. Strain pre-peak takes place between ε_1 = 0-3.7%, peak PSR was reached between ε_1 = 3.7% - 5.2%, followed by post-peak PSR softening between ε_1 = 5.2% - 7.3%, and critical state transpires thereafter (Figure 5.1b). The increment containing the final image (ε_a = 12.5-18.3%) is not included in the analysis due to difficulty in tracking relatively spherical particles over such a large strain increment. Critical state was reached during

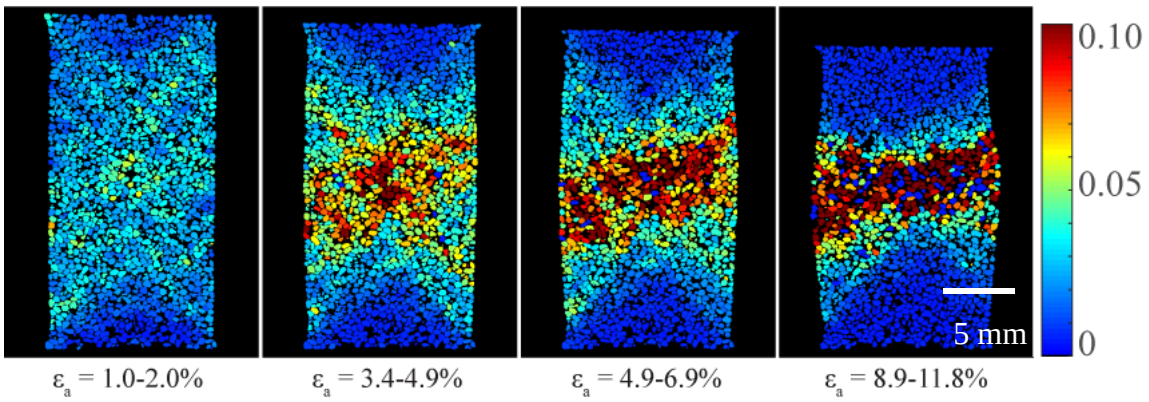

Figure 5.6. Normalized relative displacements parallel to final shear band for F35-400kPa experiment

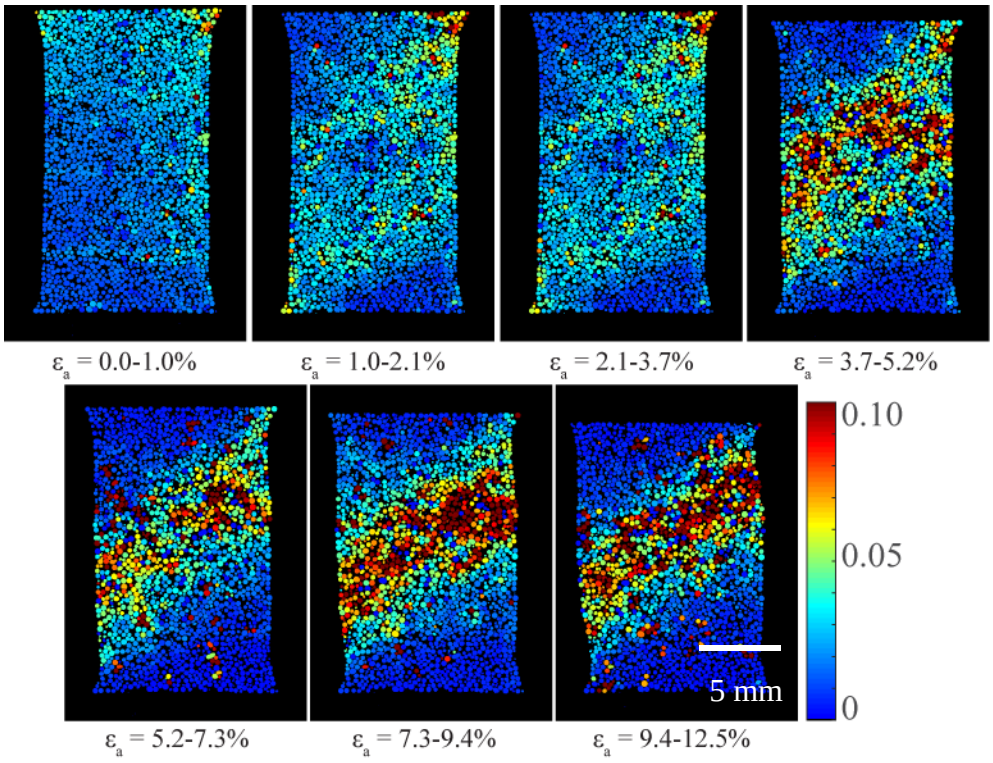

Figure 5.7. Normalized relative displacements for GB-400kPa experiment

the previous two increments and the final increment did not uncover many changes in relative displacements; therefore omitting the last increment does not impact the results. Similar to the F3-400kPa experiment, zones of localized strain emerged during the first ε_1 increment (ε_1 = 0-1%) and MSB with thickness $3d_{50}$ to $5d_{50}$ began to nucleate during the second ε_1 increment (ε_1 = 1%-2.1%) and continued to grow throughout the pre-peak phase. The thickness of MSB in this experiment is larger than F35-400kPa and are not as well defined as the F35-400kPa experiment. The majority of MSB within GB-400kPa experiment typically orient in the same direction as the final single shear band, while few MSB develop at the same inclination and opposite direction of the major shear band. During the peak PSR phase (ε_1 = 3.7%-5.2%), most MSB merged into a large zone of disorder within the specimen and align in the direction of the final major single shear band. During post-peak PSR softening, the disorder localizes into the final well-defined single shear band that continues to evolve and develop during the critical state. The final shear band is much thicker ($13d_{50}$ to $14d_{50}$) than that of the less spherical and more angular F35 sand (Figure 5.5) and is not as well defined. There are also some sporadic particles with large relative displacement outside of major shear band. Large relative displacement of individual (or small groups of) particles outside MSB or the major shear bands is attributed to stick-slip nature of glass beads at critical state, as reflected by frequent drops in the PSR response in Figure 5.1a. Alshibli and Roussel (2006) presented a detailed experimental investigation of slick-slip phenomena in glass beads which is not limited to particles within the shear band.

Relative displacements for GS40-400kPa experiment are shown in Figure 5.8. The experiment exhibits strain pre-peak up to ε_1 = 4.7%. Peak PSR phase for this experiment is broad and endures through increments 5 and 6 (ε_1 = 4.7-6.7% and ε_1 = 6.7-8.6%), while slight post-peak PSR softening occurs during increment 7 (ε_1 = 8.6-11.4%), and critical state thereafter. The initial ε_1 increment (ε_1 = 0-1%) did not show an evidence of MSB where only two horizontal layers of larger relative displacement are apparent as a result of image processing errors and should not be considered as strain localization. Through increments 2 and 3 during strain pre-peak phase, a complex network of MSB emerges similar to those in F35-400kPa experiment, and had thicknesses of $2d_{50}$ to $4d_{50}$. Many MSB develop in conjugate directions with inclinations similar to the final major shear band, some of MSB extend through the entire specimen. Near the end of strain pre-peak (increment 4, ε_1 = 3.3%-4.7%) the MSB began to merge and show a preferential alignment with that of the final major shear band. During peak PSR phase, few MSB remain and the final shear band is nearly fully developed. Full development of the final shear band commenced during the minor post-peak PSR softening and continued through critical state phase. The final shear band for GS40-400kPa experiment have a thickness of $10d_{50}$ to $13d_{50}$, and is not as well defined nor as delineated as the shear band for F35-400kPa experiment (that have a thickness of $9d_{50}$ to $10d_{50}$). However, the final shear band for GS40-400 kPa experiment is more delineated and better defined than the shear band in GB-400kPa experiment (thickness $13d_{50}$ to $14d_{50}$), advocating the influence of particle morphology on the onset and growth of shear

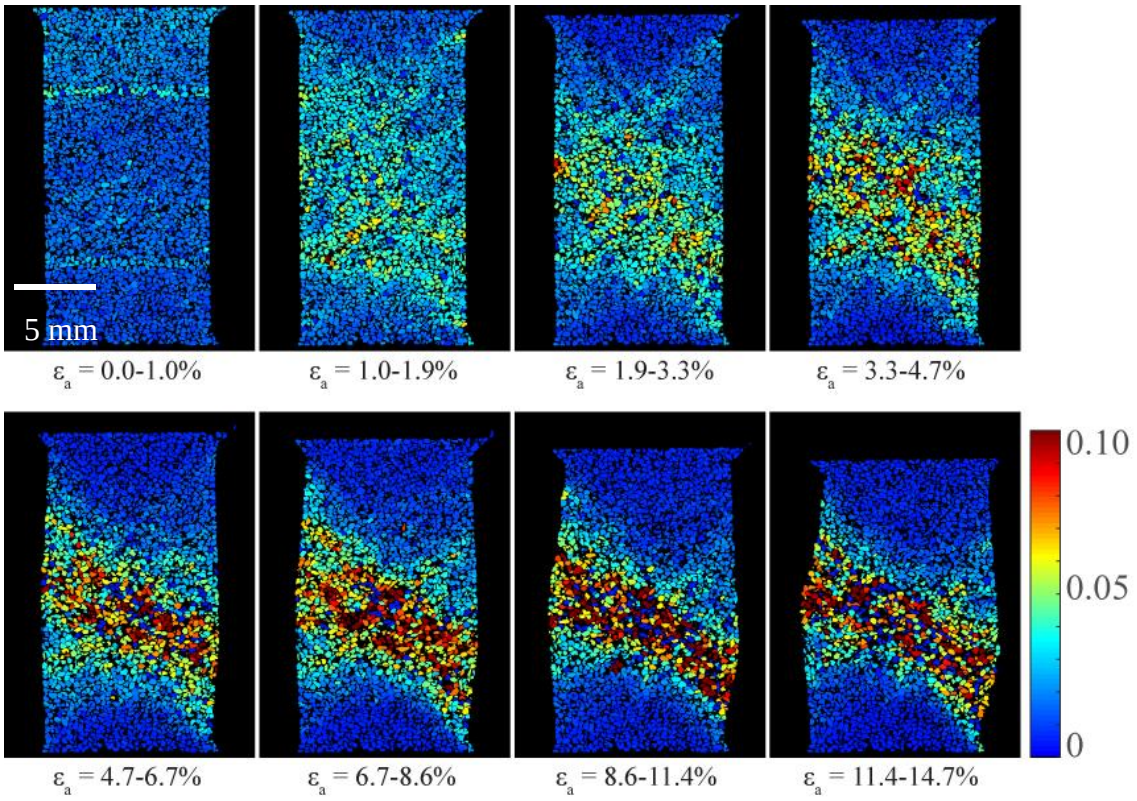

Figure 5.8. Normalized relative displacements for GS40-400kPa experiment

bands in granular materials. Of the three 400 kPa experiments that exhibited a final shear band, the thickness of the final shear band for the least spherical material (F35 sand, I_{sph} = 1.872) was the thinnest, followed by GS40 sand (I_{sph} = 1.674) and the final shear band in glass beads (I_{sph} = 1.096) was the thickest. This trend was also apparent for MSB thicknesses, where F35 sand had the thinnest MSB, followed by GS40 sand and glass beads. Interlocking and rotation between less spherical particles result in thinner shear bands than that of specimens with more spherical particles, which have to translate around each other (less particle interlocking).

Relative displacements for DG-400kPa experiment are displayed in Figure 5.9. This experiment experienced strain pre-peak up to ε_1 = 5%, peak PSR at ε_1 = 6.9%, and very minor post-peak PSR softening into critical state during increment 6 (ε_1 = 6.9%-8.9%). Failure of this specimen was characterized as bulging based on specimen surface deformation, but more complex internal failure modes occur. Strain localization began to form during the first ε_1 increment (ε_1 = 0-1%). In the second ε_1 increment (ε_1 = 1%-2%), MSB have formed in a diagonal direction through the specimen, which seemingly would be early evidence of a major well-defined single shear band. However, during the third ε_1 increment (ε_1 = 2%-3.5%) several MSB develop throughout the specimen in the opposite direction and began to compete with the previously developed MSB. MSB in this 3rd increment have thicknesses of $3d_{50}$ to $4d_{50}$. During the 4th ε_1 increment (ε_1 = 3.5%-5%) a complex network of MSB emerges with a preferential inclination; however intersecting MSB cause a relatively large zone of disorder in the middle of the specimen. In the

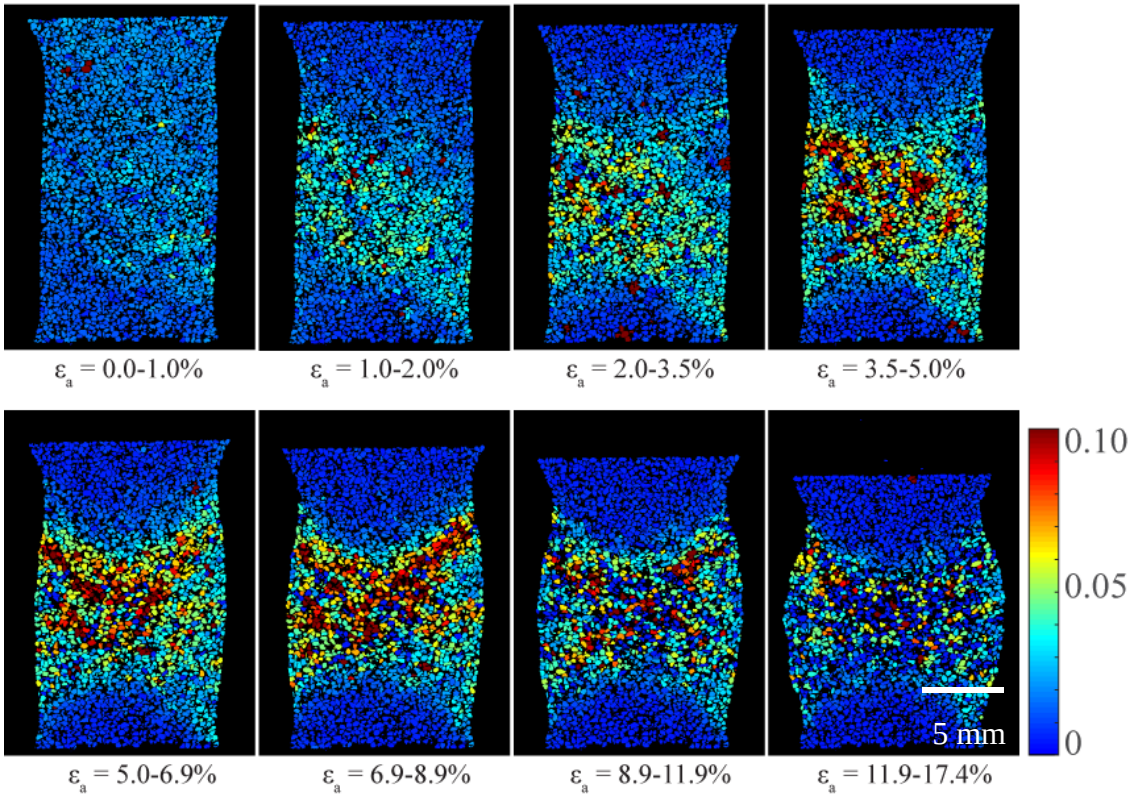

Figure 5.9. Normalized relative displacements for DG-400kPa experiment

increment approaching peak PSR (ε_1 = 5%-6.9%) MSB develop in opposite directions resulting in the development of two conical shearing surfaces near the top and bottom of the specimen and a large amount of disarray in the middle part of the specimen. Conflicting MSB in a cross-hatched pattern continue to battle throughout the remainder of the experiment, retaining the conical shaped shearing zones near the top and bottom of the specimen and many MSB in the central zone. Cross-hatching of MSB force other lateral MSB to manifest and push outward toward the specimen surface, as well as push groups of particles outward, resulting in specimen bulging at the surface. During the last two increments, particle disorder was very high in the central part of the specimen resulting in difficulty in tracking particles, leading to many particles with zero relative displacement in that zone.

Very dense specimens tested under low confining pressure ($\sigma_3 = 15$ kPa)

The failure mode of very dense specimens sheared at relatively low confining pressure ($\sigma_3 = 15$ kPa) was through bulging based on observations of the specimens' surface. F35-15kPa experiment (Figure 5.10) showed early signs of randomly oriented MSB with thicknesses of $2d_{50}$ to $3.5d_{50}$ concentrated in the central part of the specimen until approximately ε_1 = 3.5%-5%, where MSB have mostly merged into a centralized zone, with the exception of conical shearing zones near the top and bottom of the specimen. Subsequently, F35-15kPa experiment (Figure 5.10) retained the conical zones of shearing at the top and bottom of the specimen, with shearing concentrated between the two conical zones. As shearing progressed, a centralized hourglass-like (x-shaped in

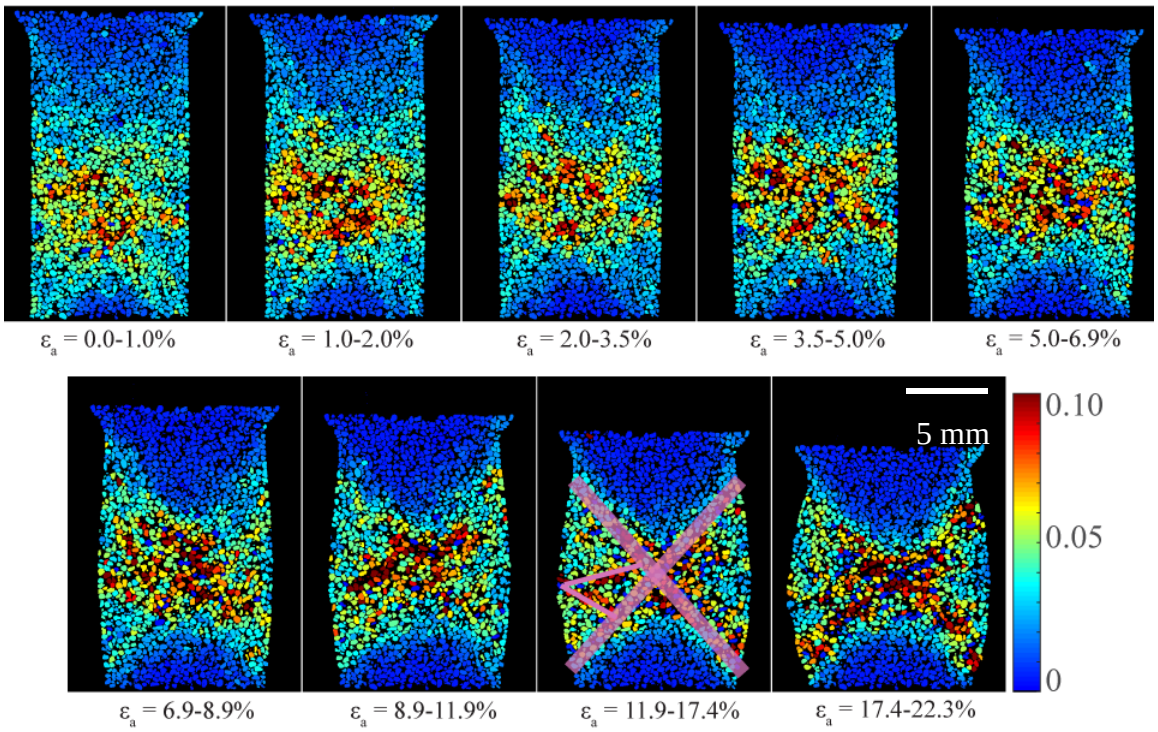

Figure 5.10. Normalized relative displacements for F35-15kPa experiment

2D slice visualizations) shearing pattern dominates the internal microstructure, forcing particles outwards toward the surface of the specimen in the lateral direction where some of these particles were part of MSB (see Figure 5.10, increment 8, ε_1 = 11.9%-17.4%, where thick transparent markers are added to the image to show hourglass pattern and thin lines show structured MSB being forced outwards). The outthrust of particles and MSB cause specimen surface bulging. Cross sectional slices within the conical shearing zones at the top and bottom of the specimen as well as a cross section near the mid height of the specimen for ε_1 = 11.9%-17.4% increment are displayed in Figure 5.11. The circular pattern within the top and bottom cross-sectional slices reveals that the shape of the failure zone is in fact conical. The middle cross sectional slice shows disarray between the conical shearing zones and multiple MSB with no preferred orientation other than random relative particle displacement outward in the lateral direction (axisymmetric plane of the specimen).

GS40-15kPa experiment (Figure 5.12) also exhibited early signs of MSB development (thicknesses of $3.5d_{50}$ to $4d_{50}$) and retained several major MSB after ε_1 = 5% with inclination similar to the conical shape observed at the top and bottom of F35-15kPa experiment, resulting in a centralized cross-hatched shearing pattern. Ends of the MSB pushed towards the specimen surface and particles outside those shearing zones were forced to move outwards in the lateral direction resulting in bulging at the specimen surface. A similar failure mode is observed in DG-15kPa experiment at early strains

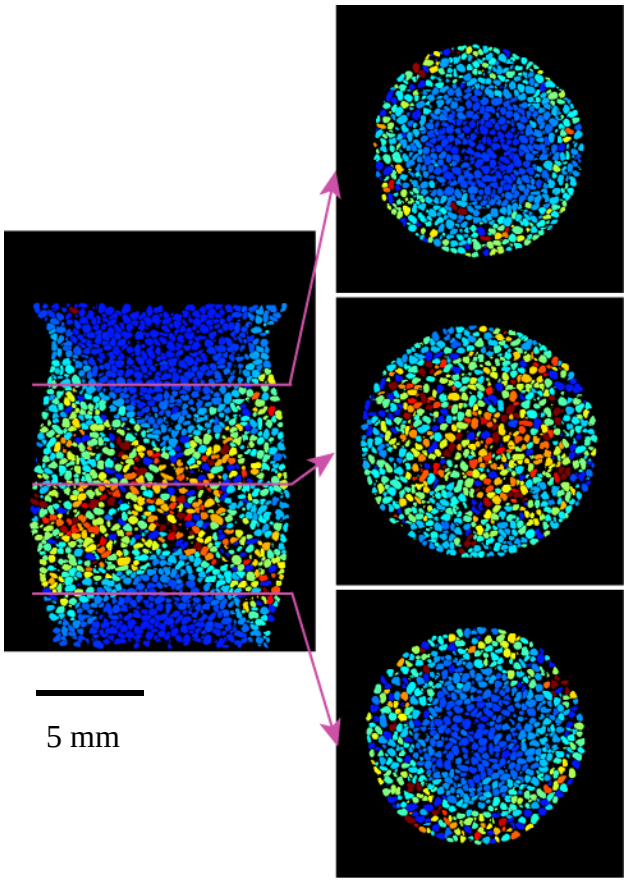

Figure 5.11. Slices of strain increment ε_1 = 11.9-17.4% for F35-15kPa experiment displaying conical shearing zones and lateral MSB and particle group expulsion

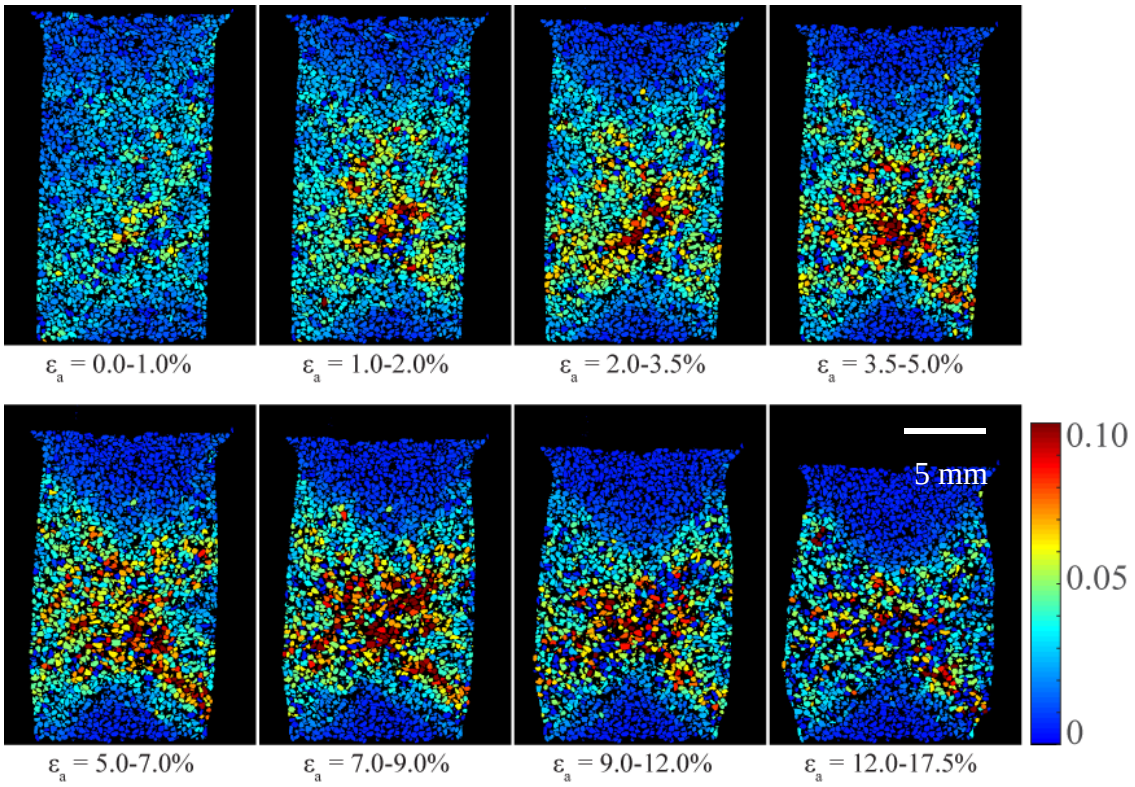

Figure 5.12. Normalized relative displacements for GS40-15kPa experiment

(Figure 5.13), with MSB thicknesses of $3d_{50}$ to $3.5d_{50}$. A cross-hatched MSB pattern forms and conical shearing zones at the top and bottom of the specimen develop and persist. However, particle relative displacements eventually show a large centralized zone of particle entropy pushing particle groups outward in the lateral direction to cause specimen bulging. GB-15kPa experiment (Figure 5.14) exhibited many distributed MSB and zones of localized shearing throughout the experiment, many of which are sporadically distributed throughout the specimen. Thicknesses of MSB at early strain increments are $3d_{50}$ to $5d_{50}$. Some structure is retained in cross-hatched MSB; however some of the structured deformation is randomly orientated and shearing zones near the top and bottom of the specimen do not have a well-defined conical structure. Specimen bulging is caused by MSB ends pushing out towards the specimen surface as well as pushing groups of particles in the lateral direction.

The role of confining pressure on internal shearing mechanisms of granular material is significant. A cross-hatched MSB failure pattern develops during strain pre-peak for both low ($\sigma_3 = 15$ kPa) and high ($\sigma_3 = 400$ kPa) confining pressures. However, under lower confining pressure, MSB are thicker and shearing zones are not as well structured as under a higher confining pressure. This is attributed to a more stable microstructure imposed by higher confining pressure. With exception of experiment DG-D-400kPa, where a high confining pressure typically forces MSB and shearing zones to merge into a single well-defined shear band during peak PSR and post-peak PSR softening phases. In experiments conducted at low confining pressure, the failure was

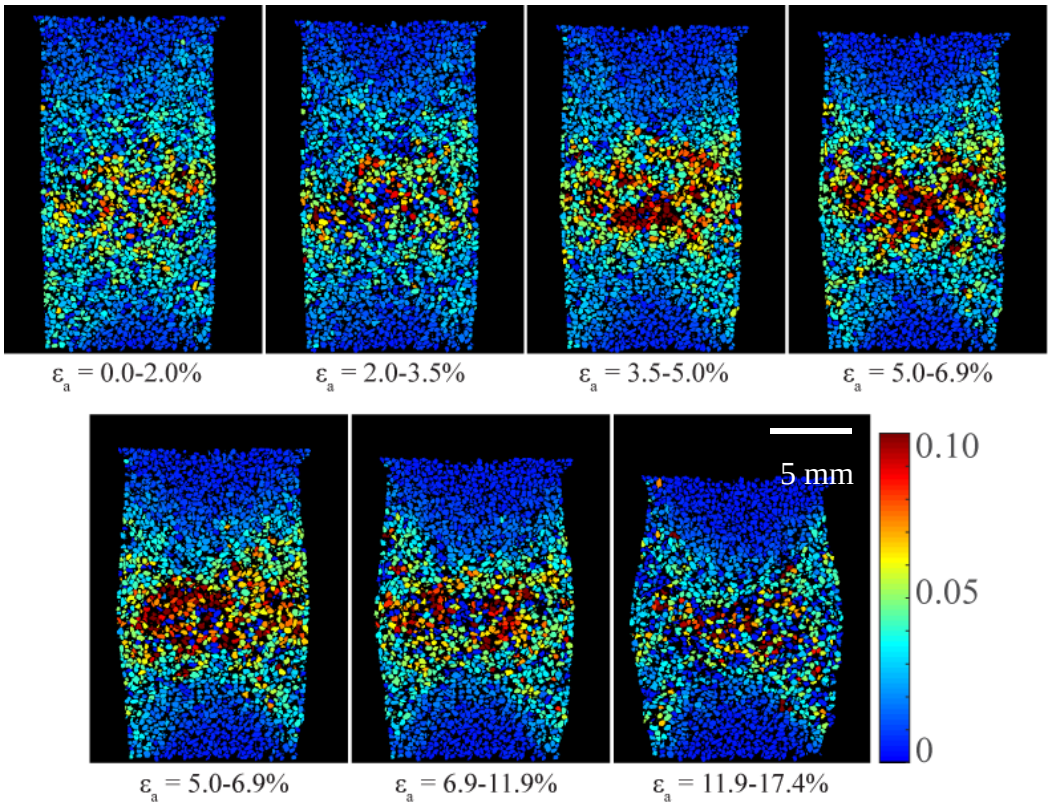

Figure 5.13. Normalized relative displacements for DG-15kPa experiment

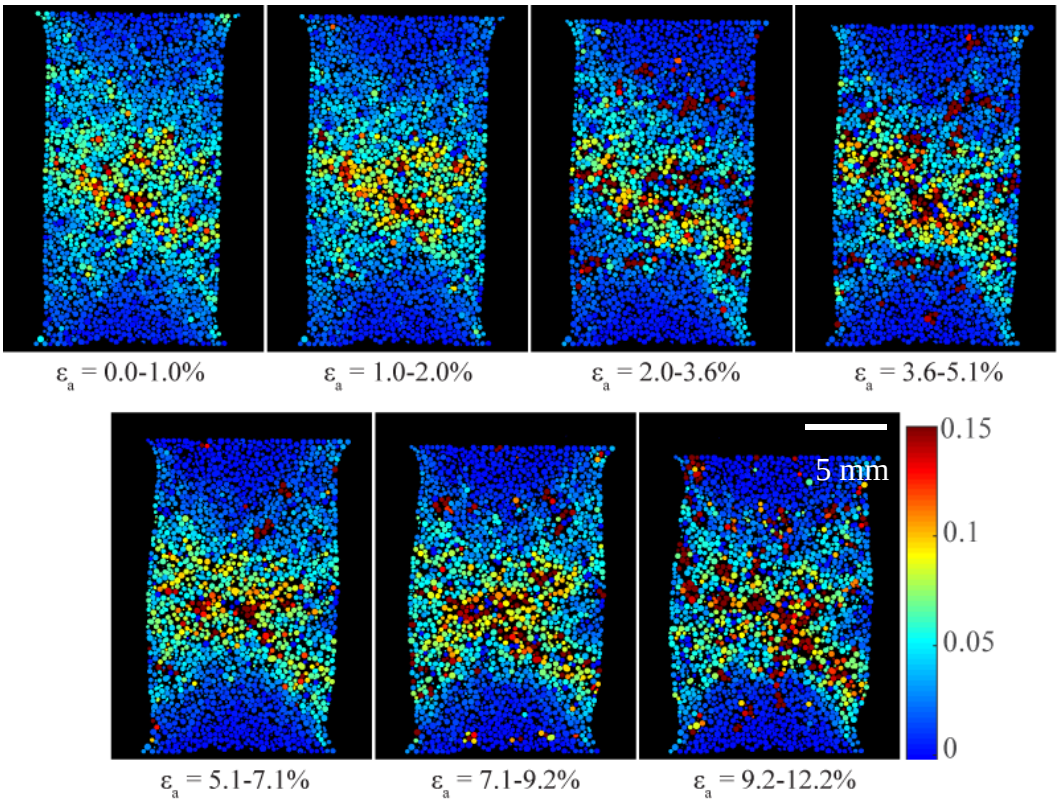

Figure 5.14. Normalized relative displacements for GB-15kPa experiment

manifested in bulging of the specimen surface with a complex network of internal MSB. Cross-hatched MSB were the typical mode of internal failure mode (singular hourglass pattern in F35-D-15kPa experiment), where the cross-hatched MSB forced groups of particles and lateral MSB outward and conical shearing zones at the top and bottom of the specimens. Particle morphology, mainly I_{sph}, influenced the thicknesses of MSB during pre-peak as well as the thicknesses of critical state shear bands (in experiments that developed critical state shear bands). In all cases, glass beads (most spherical) had the thickest MSB, followed by GS#40 and #1 dry glass sands, which have intermediate I_{sph}. F35 sand was the least spherical particles and exhibited the thickest MSB.

Conclusions

3D SMT was used to capture the evolution of failure mode of triaxial specimens composed of uniform sands and glass beads. The concept of relative particle displacement is introduced and used to visualize and quantify intricate zones of localized strains and micro shear bands that cannot be exposed when one uses particle translation and rotation alone. The following conclusions are drawn from this paper:

a) Micro shear bands in triaxial experiments can be better analyzed and quantified in 3D using the second order norm of differences in displacement vectors. This technique exposes more intricate strain localizations than conventional particle kinematics approach.
b) All experiments developed MSB during strain pre-peak. In specimens that exhibit a single well defined shear band at failure, persistent MSB that nucleate and mature

during the pre-peak phase merge to form the single shear band. In specimens that exhibit bulging, MSB develop into either a cross-hatched or hourglass pattern that push groups of particles and small lateral MSB outwards in the lateral direction.

c) Particle morphology influences thickness and delineation of MSB. Specimens with less spherical particles have thinner well-defined MSB and critical state shear bands, caused by interlocking of the less spherical particles

d) Confining pressure influences the thickness and delineation of MSB. MSB that develop during strain pre-peak are more structured and better defined when the specimen is tested at a high confining pressure.

References

Alsaleh, M. I., Voyiadjis, G. Z., and Alshibli, K. A. (2006). "Modelling strain localization in granular materials using micropolar theory: mathematical formulations." *International Journal for Numerical and Analytical Methods in Geomechanics*, 30(15), 1501-1524.

Alshibli, K., Druckrey, A., Al-Raoush, R., Weiskittel, T., and Lavrik, N. (2014). "Quantifying Morphology of Sands Using 3D Imaging." *Journal of Materials in Civil Engineering*, 04014275.

Alshibli, K. A., Alsaleh, M. I., and Voyiadjis, G. Z. (2006). "Modelling strain localization in granular materials using micropolar theory: numerical implementation and verification." *International Journal for Numerical and Analytical Methods in Geomechanics*, 30(15), 1525-1544.

Alshibli, K. A., and Roussel, L. E. (2006). "Experimental investigation of slip-stick behaviour in granular materials." *International Journal for Numerical and Analytical Methods in Geomechanics*, 30(14), 1391-1407.

Andò, E., Hall, S., Viggiani, G., Desrues, J., and Bésuelle, P. (2012). "Grain-scale experimental investigation of localised deformation in sand: a discrete particle tracking approach." *Acta Geotechnica*, 7(1), 1-13.

Andò, E., Hall, S. A., Viggiani, G., Desrues, J., and Bésuelle, P. (2012). "Experimental micromechanics: grain-scale observation of sand deformation." *Géotechnique Letters*, 2(3), 107-112.

Been, K., Jefferies, M. G., and Hachey, J. (1991). "The critical state of sands." *Géotechnique*, 41(3), 365-381.

Bouil, A., Amon, A., Sangleboeuf, J.-C., Orain, H., Bésuelle, P., Viggiani, G., Chasle, P., and Crassous, J. (2014). "A biaxial apparatus for the study of heterogeneous and intermittent strains in granular materials." *Granular Matter*, 16(1), 1-8.

Da Cruz, F., Chevoir, F., Bonn, D., and Coussot, P. (2002). "Viscosity bifurcation in granular materials, foams, and emulsions." *Physical Review E*, 66(5), 051305.

Druckrey, A., and Alshibli, K. (2014). "3D Behavior of Sand Particles Using X-Ray Synchrotron Micro-Tomography." *Geo-Congress 2014 Technical Papers*, 2814-2821.

Druckrey, A. M., Alshibli, K. A., and Al-Raoush, R. I. (2016). "3D characterization of sand particle-to-particle contact and morphology." *Computers and Geotechnics*, 74, 26-35.

Fu, Y., Wang, L., Tumay, M. T., and Li, Q. (2008). "Quantification and Simulation of Particle Kinematics and Local Strains in Granular Materials Using X-Ray Tomography Imaging and Discrete-Element Method." *Journal of Engineering Mechanics*, 134(2), 143-154.

Hall, S. A., Bornert, M., Desrues, J., Pannier, Y., Lenoir, N., Viggiani, G., and BéSuelle, P. (2010). "Discrete and continuum analysis of localised deformation in sand using X-ray μCT and volumetric digital image correlation." *Geotechnique*, 315-322.

Hall, S. A., Muir Wood, D., Ibraim, E., and Viggiani, G. (2009). "Localised deformation patterning in 2D granular materials revealed by digital image correlation." *Granular Matter*, 12(1), 1-14.

Hasan, A., and Alshibli, K. (2012). "Three dimensional fabric evolution of sheared sand." *Granular Matter*, 14(4), 469-482.

Jiang, M., Zhu, H., and Li, X. (2010). "Strain localization analyses of idealized sands in biaxial tests by distinct element method." *Frontiers of Architecture and Civil Engineering in China*, 4(2), 208-222.

Kuhn, M. R. (1999). "Structured deformation in granular materials." *Mechanics of Materials*, 31(6), 407-429.

Kuhn, M. R. (2003). "An experimental method for determining the effects of strain gradients in a granular material." *Communications in Numerical Methods in Engineering*, 19(8), 573-580.

Kuhn, M. R. (2005). "Are granular materials simple? An experimental study of strain gradient effects and localization." *Mechanics of Materials*, 37(5), 607-627.

Kuhn, M. R., and Bagi, K. (2004). "Alternative Definition of Particle Rolling in a Granular Assembly." *Journal of Engineering Mechanics*, 130(7), 826-835.

Lade, P. V. (2002). "Instability, shear banding, and failure in granular materials." *International Journal of Solids and Structures*, 39(13–14), 3337-3357.

Lo Presti, D., Pedroni, S., and Crippa, V. (1992). "Maximum Dry Density of Cohesionless Soils by Pluviation and by ASTM D 4253-83: A Comparative Study." *ASTM Geotechnical Testing Journal*, 15(2), 180-189.

Mooney, M. A., Finno, R. J., and Viggiani, M. G. (1998). "A Unique Critical State for Sand?" *Journal of Geotechnical and Geoenvironmental Engineering*, 124(11), 1100-1108.

Nicot, F., and Darve, F. (2007). "A micro-mechanical investigation of bifurcation in granular materials." *International Journal of Solids and Structures*, 44(20), 6630-6652.

Nicot, F., Sibille, L., and Darve, F. (2009). "Bifurcation in granular materials: An attempt for a unified framework." *International Journal of Solids and Structures*, 46(22–23), 3938-3947.

Oda, M., and Iwashita, K. (2000). "Study on couple stress and shear band development in granular media based on numerical simulation analyses." *International Journal of Engineering Science*, 38(15), 1713-1740.

Oda, M., Iwashita, K., and Kakiuchi, T. (1997). "Importance of particle rotation in the mechanics of granular materials." *Proc., Powder and Grains*, A A Balkema Publishers, Rotterdam, Netherlands, 207-210.

Rechenmacher, A., and Finno, R. (2004). "Digital Image Correlation to Evaluate Shear Banding in Dilative Sands."

Rechenmacher, A. L. (2006). "Grain-scale processes governing shear band initiation and evolution in sands." *Journal of the Mechanics and Physics of Solids*, 54(1), 22-45.

Riemer, M. F., and Seed, R. B. (1997). "Factors Affecting Apparent Position of Steady-State Line." *Journal of Geotechnical and Geoenvironmental Engineering*, 123(3), 281-288.

Rivers, M. L. "tomoRecon: High-speed tomography reconstruction on workstations using multi-threading." 85060U-85060U-85013.

Rivers, M. L., Citron, D. T., and Wang, Y. (2010). "Recent developments in computed tomography at GSECARS." *SPIE*, 3, 780409-780409.

Rowe, P. W. (1962). "The Stress-Dilatancy Relation for Static Equilibrium of an Assembly of Particles in Contact." *Proceedings of the Royal Society of London A: Mathematical, Physical and Engineering Sciences*, 269(1339), 500-527.

Sjödahl, M., Siviour, C. R., and Forsberg, F. (2012). "Digital Volume Correlation Applied to Compaction of Granular Materials." *Procedia IUTAM*, 4(0), 179-195.

Verdugo, R., and Ishihara, K. (1996). "THE STEADY STATE OF SANDY SOILS." *Journal of the Japanese Geotechnical Society : soils and foundation*, 36(2), 81-91.

Walker, D., Tordesillas, A., and Rechenmacher, A. (2013). "Transmission of kinematic information in dense granular systems: local and nonlocal network sensing." *Acta Geotechnica*, 8(5), 547-560.

CHAPTER 6

3D EXPERIMENTAL QUANTIFICATION OF FABRIC EVOLUTION OF SHEARED GRANULAR MATERIALS USING SYNCHROTRON MICRO-COMPUTED TOMOGRAPHY

A version of this chapter is under review in Granular Matter Journal. The author list is: A. Druckrey, K. Alshibli.

My primary contributions to this paper are (i) formulating objectives and evaluating current research in the area, (ii) conducting most experiments during in-situ SMT imaging, (iii) quantifying particle contact normal vectors and fabric tensors based on contact normal vectors (iv) comparison fabric evolution for various granular materials, (v) most of the writing.

Abstract

Experimental studies have established that mechanical response of granular materials is highly influenced by micro-structural fabric and fabric evolution. In the literature, theories and quantification of fabric evolution have been developed based on microstructural observations using discrete element modeling (DEM) or simple two-dimensional experiments with simple particle shapes. Emergence of x-ray computed tomography (CT) technique has made quantification of such experimental microstructural properties possible. This paper used synchrotron micro-computed tomography (SMT) to collect 3D images during in-situ triaxial compression experiments on granular materials with different morphologies to experimentally quantify fabric and fabric evolution. Effects of confining pressure, and particle morphology on the initial fabric and fabric evolution are presented. The results show that particle morphology plays a significant role on initial anisotropy of granular material (fabric is a measure of internal anisotropy) as well as the magnitude of fabric evolution throughout triaxial compression experiment.

Relatively higher applied confining pressure causes less anisotropic initial state in granular materials of any morphology, and fabric evolves in correspondence with evolution of strength; if material strength peaks and reaches a steady-state, fabric will also peak and become constant shortly thereafter.

Introduction

Micro-scale properties and particle-to-particle association of granular materials contribute to its macroscopic strength and dilatancy behavior as well as other engineering properties. An important micro-scale property is the internal structure, or fabric, which describes its internal anisotropy. Fabric is defined as the arrangement of particles, particle groups and associated pore space. Experimental and discrete element methods have demonstrated that fabric anisotropy greatly influences mechanical properties of granular material when varying the fabric of the material or the loading direction (Oda 1972; Oda et al. 1985; Lam and Tatsuoka 1988; Yimsiri and Soga 2001; Li and Yu 2009; Yimsiri and Soga 2010; Li and Yu 2014). For example, Oda (1972) used various sands, preparation methods, and 2D thin section microscopy to find that initial fabric anisotropy is a direct result of particle shape and sample preparation technique, differences in initial fabric greatly influence mechanical properties, and specimens with contact normal vectors preferential orientation toward the direction of loading have a more stable fabric. Li and Zeng (2014) used experimental bender element techniques and found that fabric anisotropy is affected by sand morphology and density, and fabric affects the shear modulus of the material. Furthermore, Yimsiri and Soga (2010) used DEM and showed

that initial fabric has profound effects on stiffness, strength, and dilation properties of granular materials. Although the importance of initial fabric and fabric evolution resulting from particle deposition, morphology, and applied loadings is well documented in the literature, they remain difficult to completely and effectively quantify and model experimentally in 3D.

Fabric tensors characterize the geometric arrangement of granular material microstructure and quantify internal anisotropy of the material. Any micro-scale directional data of granular material used to represent fabric can be used in quantitative analysis of fabric tensors. Several different microstructural quantities have been used in formulating fabric tensors. Directional microstructural data such as particle long axis orientations, branch vectors, particle contact normal vectors, and void vectors are commonly used to define fabric of granular materials. To analyze the different microstructural fabric tensor parameters, Fonseca et al. (2013) terminated triaxial experiments at different axial strain levels during shearing and impregnated the specimens with epoxy resin. Cores were then extracted from several locations within the specimens and CT scans were acquired to quantify and compare microstructural data using rose diagrams and an eigenvalue analysis of fabric tensors, as well as analyze evolution of fabric in the specimens. Li et al. (2009) developed a new anisotropic fabric tensor based on void cell anisotropy that correlated with the macro behavior of granular material via numerical simulations and stated that it is a more effective definition than those based on particle orientations or contact normal. Few researchers have found a

strong correlation between fabric tensors based on contact normal vectors and void space vectors (Theocharis et al. 2014; Fu and Dafalias 2015), but contact normal tensors have had the disadvantage of being difficult to accurately quantify experimentally (Theocharis et al. 2014). However, forces transmit through a mass of granular material via contact normals and force chains (e.g. Oda et al. 2004; Peters et al. 2005; Peña et al. 2009; Tordesillas and Muthuswamy 2009), and accurate experimental contact normal tensors would prove valuable for micro-mechanics constitutive models. Experimental contact normal tensors inherently incorporate other particle-scale properties if accurate characterization of contact in 3D space is quantified.

Many researchers have adopted a form of fabric tensor quantification for granular materials based on, or similar to, 2^{nd} order (rank 2) fabric tensors of the first or second kind that was proposed by Kanatani (1984). They are symmetric tensors that provide the structural anisotropy of directional data. It been shown that 4^{th} order tensors better represent material anisotropy, but are not commonly utilized due to difficulty in calculating and analyzing the 4^{th} order tensors (Millet et al. 2009; Stershic et al. 2015). Interpretation of fabric tensor parameters has not been consistent in the literature, but generally attempts to quantify material fabric resistance to loading with fabric direction and magnitude relative to the global stress direction applied at specimen boundaries (e.g. Barreto et al. 2009; Li and Dafalias 2011; Fonseca et al. 2013; Zhao and Guo 2013; Theocharis et al. 2014; Fu and Dafalias 2015). Li and Dafalias (2011) introduce a fabric anisotropy variable (FAV) A which is a tensorial product of the normalized fabric tensor

F (normalized such that at critical state $F_c = \sqrt{\mathbf{F}:\mathbf{F}} = 1$) and the unit-norm deviatoric tensor-valued loading direction **n**, where FAV $A = \mathbf{F}:\mathbf{n}$. *A* accounts for fabric direction and magnitude relative to loading direction for all possible loading combinations.

Several researchers have incorporated initial fabric and fabric evolution into constitutive modeling of granular material. For example, Nemat-Nasser (2000) developed a robust micromechanically-based constitutive model that accounts for pressure sensitivity, friction, dilatancy, and, most importantly, fabric and fabric evolution. Model parameters were estimated in Nemat-Nasser and Zhang (2002) based on results of cyclic shearing experiments and then were used to predict other experimental results with good correlation. Li and Dafalias (2000) developed a micro-mechanical constitutive model for cohesionless soils (without fabric input) and later developed the anisotropic critical state theory (ACST) that incorporates fabric anisotropy in the model using FAV *A* integrated into the state parameter (Li and Dafalias 2011).

Theoretical values of fabric and models of fabric evolution were assumed in the current literature based on rudimentary experimentation or DEM, with no 3D experimentally quantified fabric tensors to validate them. This paper provides 3D experimental measurements of contact normal fabric and fabric evolution for a series of axisymmetric triaxial compression experiments on granular materials of different morphologies while utilizing in-situ SMT. The influences confining pressure, particle morphology, and tensor quantification parameters are analyzed and discussed. Results of this study can be used to formulate and validate constitutive models that incorporates

material anisotropy and fabric evolution. To the author's best knowledge, no other research of this kind is reported in the literature to supplement the models. 4^{th} order fabric tensors are also analyzed and compared to 2^{nd} order tensors that are commonly used in granular material research and modeling.

Materials Description and Experiments

Four granular materials described in Alshibli et al. (2014) were used in this paper. Three silica sands known as F-35 Ottawa sand, GS#40 Columbia grout, and #1 dry glass sand, along with glass beads with grain-size between U.S. sieves #40 (0.429 mm) and #50 (0.297 mm) were used in the experiments. Micro-scale particle properties of sphericity, roundness, and surface roughness are presented in Alshibli et al. (2014). Of these materials, glass beads have an average sphericity (I_{sph} = 1.096) and roundness indices closest to unity (spherical). F-35 sand has the highest sphericity value (least spherical, I_{sph} = 1.872), followed by #1 dry glass sand (I_{sph} = 1.7046) and GS#40 Columbia grout (I_{sph} = 1.674), which are relatively close in sphericity to each other. The three sands have similar average roundness indices.

A small triaxial apparatus described in (Hasan and Alshibli 2012; Druckrey and Alshibli 2014) was setup in beamline 13BMD of Advanced Photon Source (APS), Argonne National Laboratory (ANL), Illinois, USA. Ten axisymmetric triaxial compression experiments were conducted at various confining pressures as summarized in Table 6.1. Specimens were prepared in 4-5 lifts, lightly tamping each lift to densify before adding the next lift. A constant confining pressure was applied to the specimen

Table 6. 1.Properties of the tested specimens

Material	Exp.	Initial void ratio (e)	σ_3 (kPa)	D_r[a] (%)	Scan acquired at axial strains (%)	Resolution (□m/voxel)
F-35 Ottawa sand (F35)	F35-15kPa	0.510	15	131	0.0, 1.0, 2.0, 3.5, 5.0, 6.94, 8.9, 11.9, 17.4, 22.3	11.14
	F35-400kPa	0.531	400	120	0.0, 1.0, 2.0, 3.4, 4.9, 6.9, 8.9, 11.8, 17.2	11.18
#1 Dry glass sand (DG)	DG-15kPa	0.637	15	134	0.0, 2.0, 3.5, 5.0, 6.9, 8.9, 11.9, 17.4	11.14
	DG-400kPa	0.667	400	121	0.0, 1.0, 2.0, 3.5, 5.0, 6.9, 8.9, 11.9, 17.4	11.18
GS#40 Columbia grout sand (GS40)	GS40-15kPa	0.627	15	126	0.0, 1.0, 2.0, 3.5, 5.0, 7.0, 9.0, 12.0, 17.5	11.14
	GS40-400kPa	0.644	400	120	0.0, 1.0, 1.9, 3.3, 4.7, 6.7, 8.6, 11.4, 14.7	8.16
Glass beads (GB)	GB-15kPa	0.518	15	170	0.0, 1.0, 2.0, 3.6, 5.1, 7.1, 9.2, 12.2	11.14
	GB-400kPa	0.556	400	144	0.0, 1.0, 2.1, 3.7, 5.2, 7.3, 9.4, 12.5, 18.3	11.18

[a]D_r = Relative Density = $\frac{e_{max}-e}{e_{max}-e_{min}}$

and the test cell was mounted on the stage of the x-ray beam for SMT imaging. Experiments with 400 kPa confining pressure were conducted on F-35 sand (experiment F35-400kPa), glass beads (experiment GB-400kPa), GS#40 sand (experiment GS40-400kPa), and dry glass sand (experiment DG-400kPa). Similarly, experiments with 15 kPa confining pressure were conducted on F-35 sand (experiment F35-15kPa), glass beads (experiment GB-15kPa), GS#40 sand (experiment GS40-15kPa), and dry glass sand (experiment DG-15kPa).

The advantages of SMT imaging are summarized in Druckrey et al. (2016). Multiple scans were acquired at increasing displacements, pausing the experiment to collect 900 radiograph images at 0.2° rotation increments for each scan, and radiographs were reconstructed to create 3D SMT images with resolutions listed in Table 6.1. Information on image collection and reconstruction can be found in (Rivers et al. 2010; Rivers 2012). Load and compression displacement data were also collected during each of the experiments. SMT images were acquired at increasing axial strains for each experiment listed in Table 6.1. Initial void ratios were calculated from the images based on the volumetric ratio of voids (within the membrane encasing the specimen) to total particle volume and are listed in Table 6.1, as well as the relative density (D_r) that was calculated from the specimen void ration, the maximum and minimum index densities for calculating D_r that were measured according to ASTM-D4253 and ASTM-D4254 standard procedures, respectively. It is interesting to notice that specimens have D_r values higher than 100%. Lo Presti et al. (1992) reported similar observations.

Quantifying fabric and fabric evolution

In order to quantify fabric, 3D SMT images were processed and data was extracted using the procedure described in Druckrey et al. (2016). Each loading step of all experiments was processed to individually label each particle. Labeled images were then processed using the code described in Druckrey et al. (2016), producing microstructural data of particle lengths (short, intermediate, and long axes), volume, surface area, orientation, coordination number, contact locations, contact normal vectors, and contact tangent vectors for each particle in the entire specimen. Specimens contained 25,000 to 50,000 particles depending on the material and density. Failure via a well-defined shear band was observed in experiments F35-400kPa, GB-400kPa and GS40-400kPa by means of particle kinematics and visual inspection. Experiment DG-400kPa, as well as all experiments with 15 kPa confining pressure exhibited bulging failure. In order to additionally quantify fabric within and outside of the shear band (to differentiate from global fabric), shear bands in the 400 kPa experiments were identified during critical state and volume of interests (VOI) were extracted from locations within the shear band and outside of the shear band. An example of VOI locations within cross sectional grayscale and labeled images for experiment F35-400kPa at 11.8% axial strain are depicted in Figure 6.1, where VOI 1 contains particles outside of the shear band whereas VOI 2 contains particles within the shear band. Particles within the VOI's were tracked throughout the entire experiment for analysis of fabric on those specific particles. For experiment DG-400kpa that did not exhibit a single well-defined shear band, a VOI was

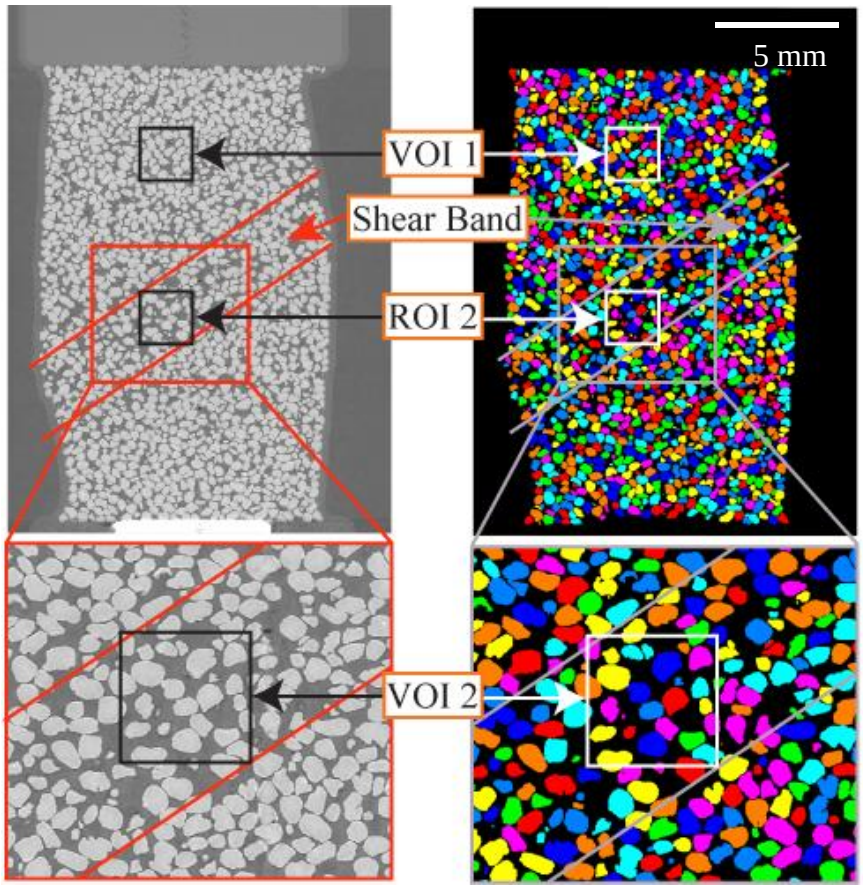

Figure 6.1. Grayscale and labeled slices through experiment F35-400kPa at 11.8% axial strain and depiction of VOI selection

chosen in the middle of the specimen at failure, where intersecting bands in an hourglass pattern was the cause of bulging, and another VOI was chosen outside of the shearing zone. VOI's contain approximately 600 to 800 particles.

Distribution of Contact Normal Vectors

Contact normal vectors and their distribution have been extensively used in the literature for fabric quantification and were correlated to other parameters such as void vectors to quantify fabric. Transmission of force takes place through contacts and is commonly associated with stiffness and strength (Kuhn et al. 2015). Therefore, 3D unit contact normal vectors, quantified with x, y, and z components, were extracted from the SMT images and were used in fabric quantification. For visualization of the distribution of contact normal vectors, all contact normal vectors were projected onto the YZ plane (Z axis is the major principal stress direction) and plotted in 2D rose diagrams. The YZ plane is perpendicular to the critical state shear band such that the band is well defined in the YZ plane. As demonstrated in Druckrey et al. (2016), contact normal vector rose diagrams initially have a greater degree of anisotropy than branch vectors and exhibit a greater degree of evolution throughout triaxial compression experiments. Also, force transmission through contacts in granular materials, justifying contact normal-based fabric as a more desirable parameter to quantify fabric for micro-mechanics constitutive models.

Fabric tensor calculation

Kanatani (1984) proposed a framework to quantify fabric tensors from any microstructural directional data, such as contact normal vectors. Fabric tensors of the first kind, also known as moment tensors, are conventionally used to define fabric in granular materials as (unweighted):

$$N_{ij} = \frac{1}{N}\sum_{\alpha=1}^{N} n_{i_1}^{\alpha} n_{i_2}^{\alpha} \dots n_{i_r}^{\alpha} \quad (6.1)$$

where n_i^{α} is the αth contact normal vector, N is the number of contacts, and r is the order of the tensor. Moment tensors can be calculated to any even order r. The second kind of fabric tensor most closely approximates the microstructural distribution function, and higher orders of fabric tensor $F_{i_1 \dots i_r}$ better represents the orientation distribution function, defined as (Moesen et al. 2012):

$$f(n) \sim \frac{1}{4\pi} F_{i_1 \dots i_r} n_{i_1} \dots n_{i_r} \quad (6.2)$$

Explicit definitions for second and fourth order fabric tensors of the second kind are (Kanatani 1984):

$$\boldsymbol{F}_{ij} = \frac{15}{2}\left(N_{ij} - \frac{1}{3}\delta_{ij}\right) \quad (6.3)$$

$$\boldsymbol{F}_{ijkl} = \frac{315}{8}\left(N_{ijkl} - \frac{2}{3}\delta_{(ij}N_{kl)} + \frac{1}{21}\delta_{(ij}\delta_{kl)}\right) \quad (6.4)$$

where δ is the Kronecker delta. Fabric tensors of the second kind are adopted in this paper. 2nd order fabric tensors are typically used to calculate and fabric in the literature, and all quantification of fabric in this paper will be executed using 2nd order fabric tensors. Surface representations of 2nd and 4th order fabric tensors will be plotted in a later Section to display differences between the two.

Quantification of fabric tensors

2nd order fabric tensors (2nd kind) are expressed in a 3×3 symmetric matrix that describes the internal anisotropy of the material and is decomposable into deviatoric and isotropic components. The deviatoric is the part of fabric that contributes to differences in material strength attributed to anisotropic fabric. The main constituents of micro-mechanical interpretations of fabric are direction and magnitude, which can be incorporated into a macroscopic continuum mechanics description. Li and Dafalias (2011) considers the norm of tensor **F** (norm $F \geq 0$) as a measure of the magnitude and the unit-norm deviatoric tensor-valued direction $\mathbf{n}_F$ of **F** to describe the direction of fabric, where

$$\boldsymbol{F} = F\boldsymbol{n}_F, \qquad F = \sqrt{\boldsymbol{F}:\boldsymbol{F}}, \quad \boldsymbol{n}_F:\boldsymbol{n}_F = 1, \quad tr\boldsymbol{n}_F = 0 \tag{6.5}$$

To incorporate the resistance of fabric against loading, Li and Dafalias (2011) included the unit-norm deviatoric tensor-valued loading direction **n**, where $\mathbf{n}:\mathbf{n} = 1$ and $\mathrm{tr}\mathbf{n} = 0$. FAV *A* is calculated as:

$$FAV\ A = \boldsymbol{F}:\boldsymbol{n} = F\boldsymbol{n}_F:\boldsymbol{n} = FN \tag{6.6}$$

F is normalized such that at critical state $F_c = 1$, resulting in FAV *A* to approach $A_c = 1$. Normalized FAV *A* will hereafter be referred to as FAV *A*. It accounts for both the orientation of fabric relative to loading direction as well as the magnitude of fabric and will be adopted in this paper to experimentally characterize fabric and its evolution.

Results

Contact normal rose diagrams

Full evolution of global contact normal vector distributions are represented in rose diagrams for 400 kPa specimens of F-35 sand (F35-400kPa) and glass beads (GB-400kPa) at axial strains (ε_a) where SMT images were acquired are shown in Figures 6.2 and 6.3, respectively. Experiment F35-400kPa (Figure 6.2) exhibited an initial preferential orientation (ε_a = 0.0%) of contact normal vectors towards the horizontal plane which is expected as particles lay along their long axis when they are deposited. Then, the global contact normal distribution evolved during early stages of loading (up to ~ε_a = 4.9%) into a more vertical orientation to resist the applied axial load. Minimal changes in global contact normal orientation occur after ε_a = 6.9%. Experiment GB-400kPa (Figure 6.3) has preferential contact orientation towards the horizontal and vertical directions. The spherical nature of the glass beads resulted in a more cubical packing of the particles, as manifested in the rose diagram of initial state. Although glass beads exhibit rather cubical packing (global contact normal vectors in the vertical and horizontal directions), the majority of contacts in the initial state slightly tend towards the horizontal direction rather than vertical. Glass beads used in this study are not completely spherical (see Alshibli et al. (2014)) and initial contact orientation preference indeed reflects it. Global contact normal orientation evolved to a more vertical preference until ~ε_a = 9.4% and becomes relatively consistent afterwards and retain cubical-like packing.

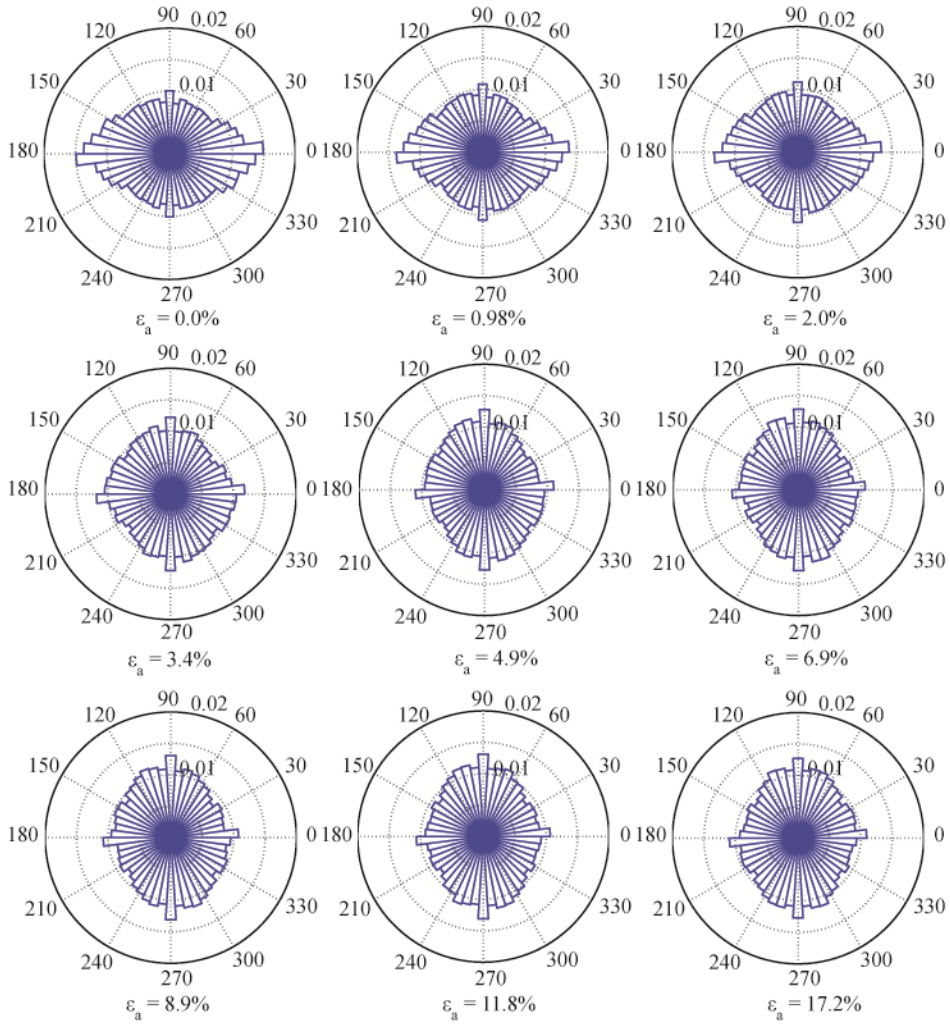

Figure 6.2. Global contact normal distribution rose diagrams for full evolution of F35-400kPa experiment

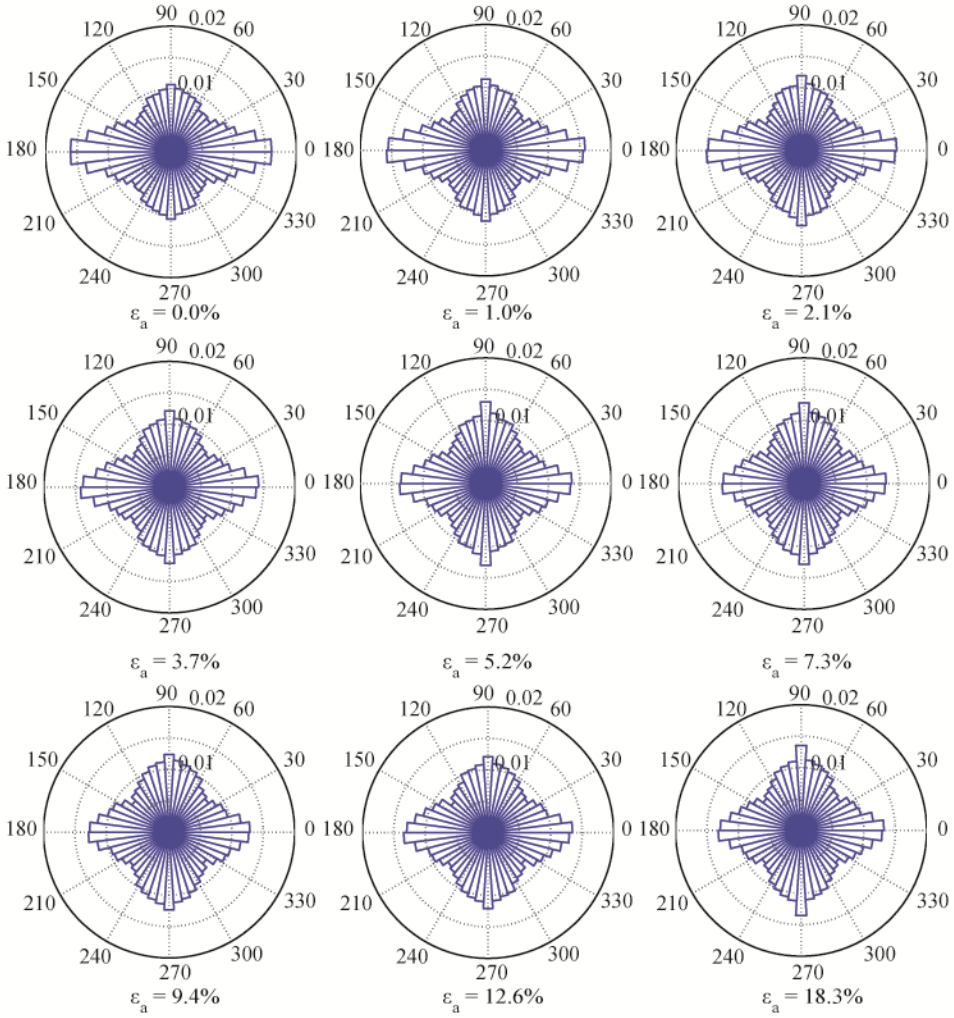

Figure 6.3. Global contact normal distribution rose diagrams for full evolution of t GB-400kPa experiment

Contact normal vector distributions in VOI's of experiments F35-400kPa and GB-400kPa are depicted in Figures 6.4 and 6.5, respectively. The initial contact distribution within the VOI's is similar to global distributions for both experiments. Throughout different compression strain stages, particle contacts outside of the shear band evolved similar to the global fabric; however, evolution towards the loading direction was less intense. In experiment F35-400kPa, contact normal vectors within the shear band evolved from horizontal preference to preferred orientation approximately perpendicular to the shear band, coinciding with formation of columnar structures within the band resisting global forces from particles above the shear band. Similar phenomenon was observed within the shear band of experiment GB-400kPa. Contacts evolved to prefer vertical orientation up to 9.4% axial strain with much less horizontal orientation preference than global or outside the shear band, and during critical state at ε_a = 18.3% orientations tended to align vertically as well as perpendicular to the shear band.

Global contact normal vector distributions for 400 kPa experiments on #1 dry glass sand (DG-400kPa) and GS#40 (GS40-400kPa) sand are depicted in Figure 6.6. Some strain stages are not included in Figure 6.6 since no major fabric changes took place between some compression stages. Global contact normal distribution of DG-400kPa specimen (Figure 6.6a) evolved from a horizontal to a vertical orientation until about ~ε_a = 6.9%, afterwards it became relatively constant. Similar trend was observed in GS40-400kPa specimen (Figure 6.6b) which evolved to resist vertical load up to ε_a = 6.9% and then became relatively constant distribution thereafter.

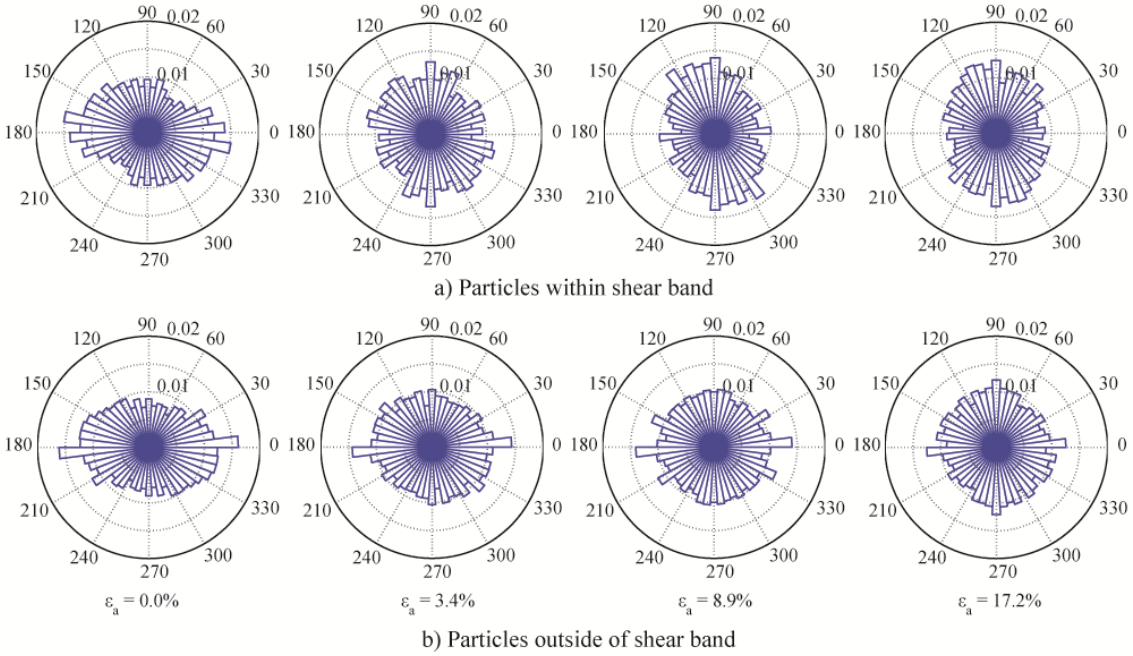

Figure 6.4. VOI contact normal distribution rose diagrams at various axial strains of experiment F35-400kPa for (a) Particles within the shear band; and (b) particles outside the shear band

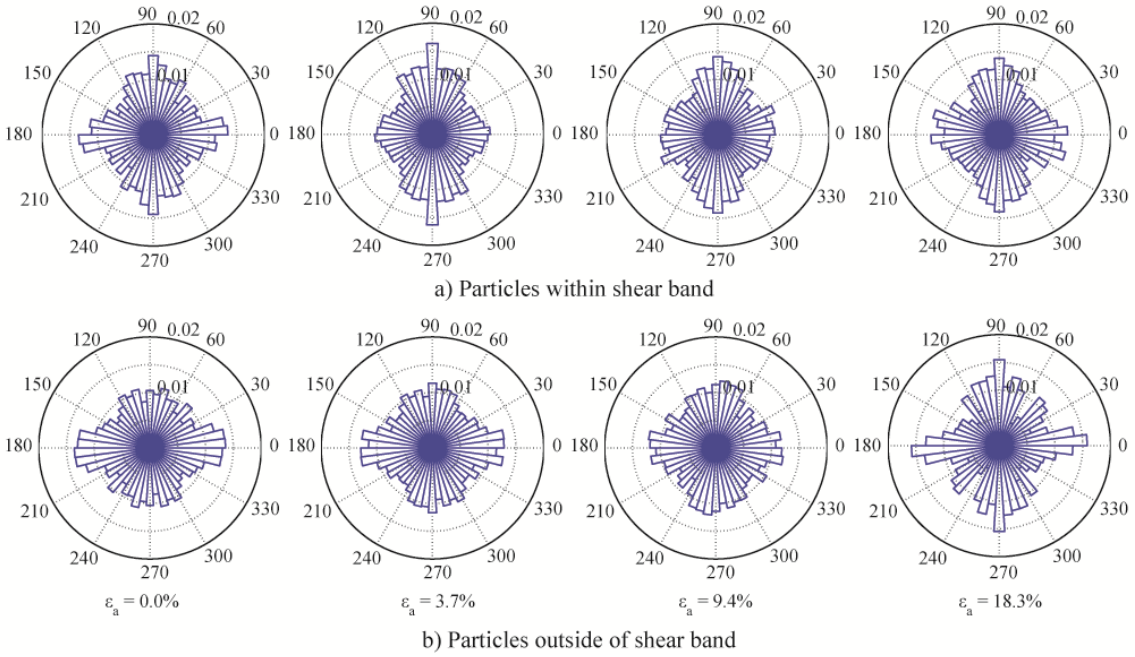

Figure 6.5. VOI contact normal distribution rose diagrams at various axial strains of experiment GB-400kPa for (a) Particles within the shear band; and (b) particles outside the shear band

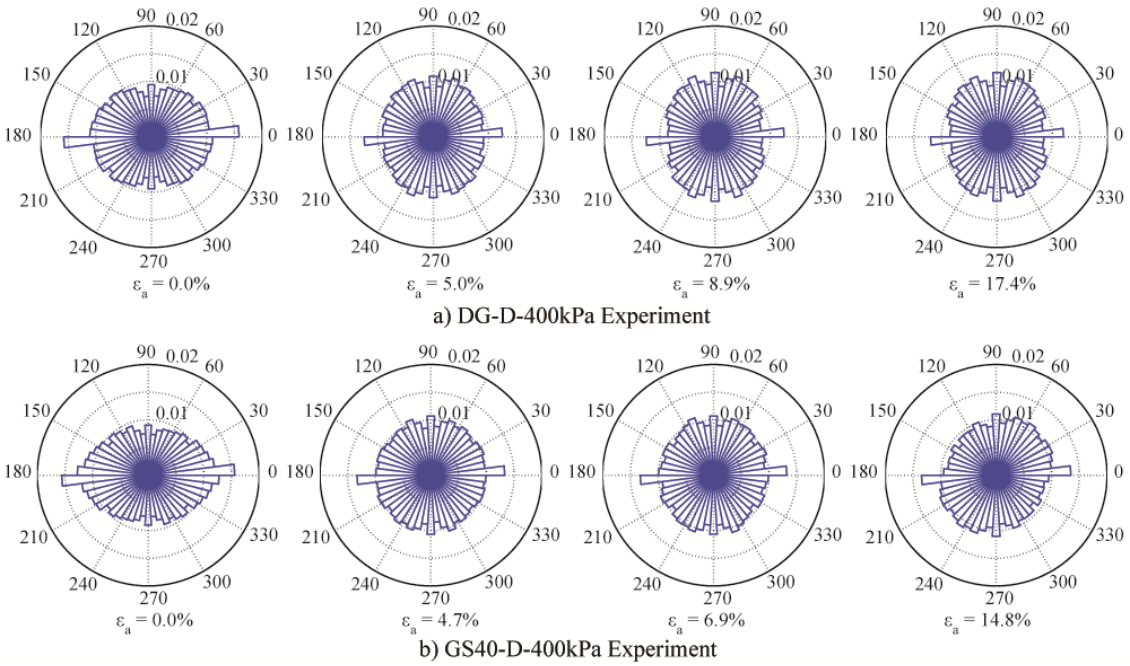

Figure 6.6. Global contact normal distribution rose diagrams at various axial strains for (a) DG-400kPa; and (b) GS40-400kPa experiments

Distributions of contact normal vectors within the VOI's for DG-400kPa and GS40-400kPa experiments are shown in Figures 6.7 and 6.8, respectively. Particles within all VOI's have similar initial contact distribution to the global trends, although slightly more disorganized (mainly due to the global fabric being an average of all particles' contacts). Particles within the centralized shearing zone of DG-400kPa (the specimen that bulged) develop contact distribution with two preferential directions approximately 45° from the vertical, somewhat perpendicular to the intersecting shear bands that developed within the specimen which caused bulging. Particles within the VOI outside of the shearing zone develop contact orientation that evolves from initially more horizontal to more vertical preference with increasing strain. Experiment GS40-400kPa failed through a major shear band associated with smaller secondary shear bands intersecting it. A high concentration of contact normal vectors distributed relatively perpendicular to the orientation of the major shear band, with a smaller amount of contact normal vector preference in the direction perpendicular to the minor band that develops at ε_a = 6.7% (Figure 6.8). Very little change is observed in the VOI outside of the shear band for the same experiment.

Global contact normal distributions for the 15 kPa specimens (prepared in same manner as 400 kPa specimens) are displayed in Figure 6.9 of initial state, two intermediate states, and at end of experiment. Distribution of global contact normal vectors in F35-15kPa experiment (Figure 6.9a) was initially extremely anisotropic with preference of contact normal vectors toward the horizontal. Contact evolved towards the

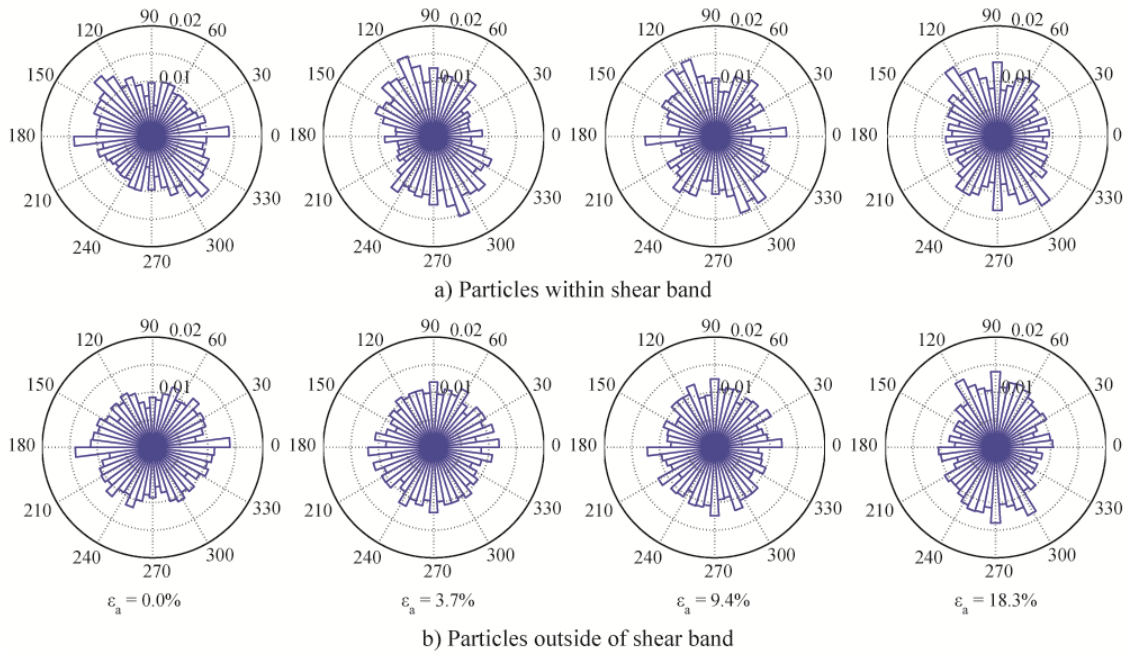

Figure 6.7. VOI contact normal distribution rose diagrams at various axial strains of experiment DG-400kPa for (a) Particles within the shear band: and (b) particles outside the shear band

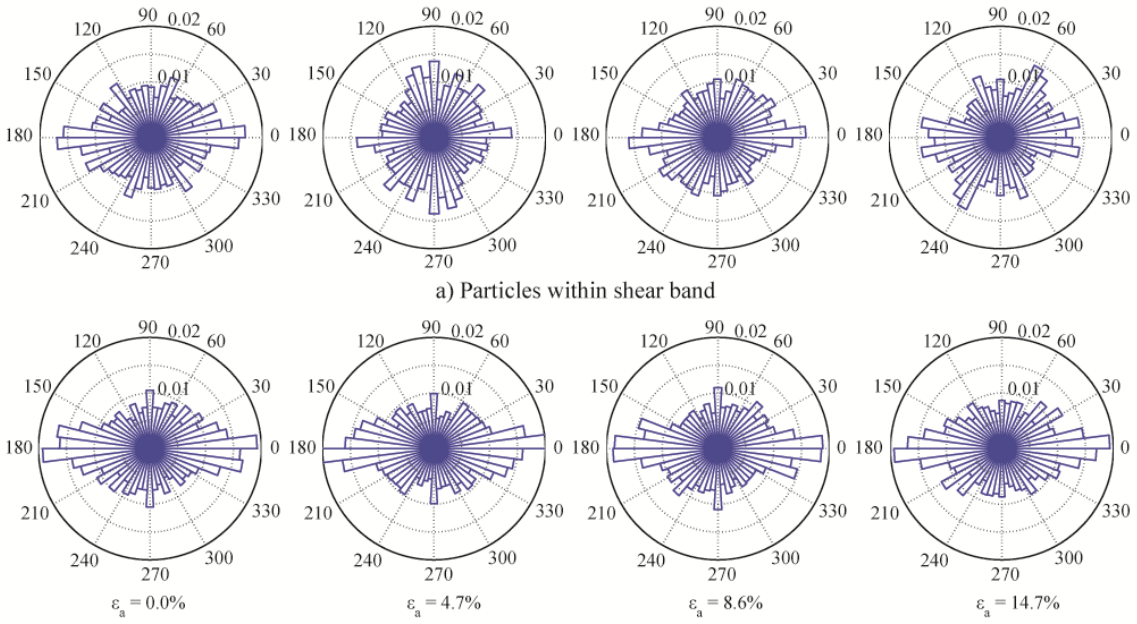

Figure 6.8. VOI contact normal distribution rose diagrams at various axial strains of experiment GS40-400kPa for (a) Particles within the shear band; and (b) particles outside the shear band

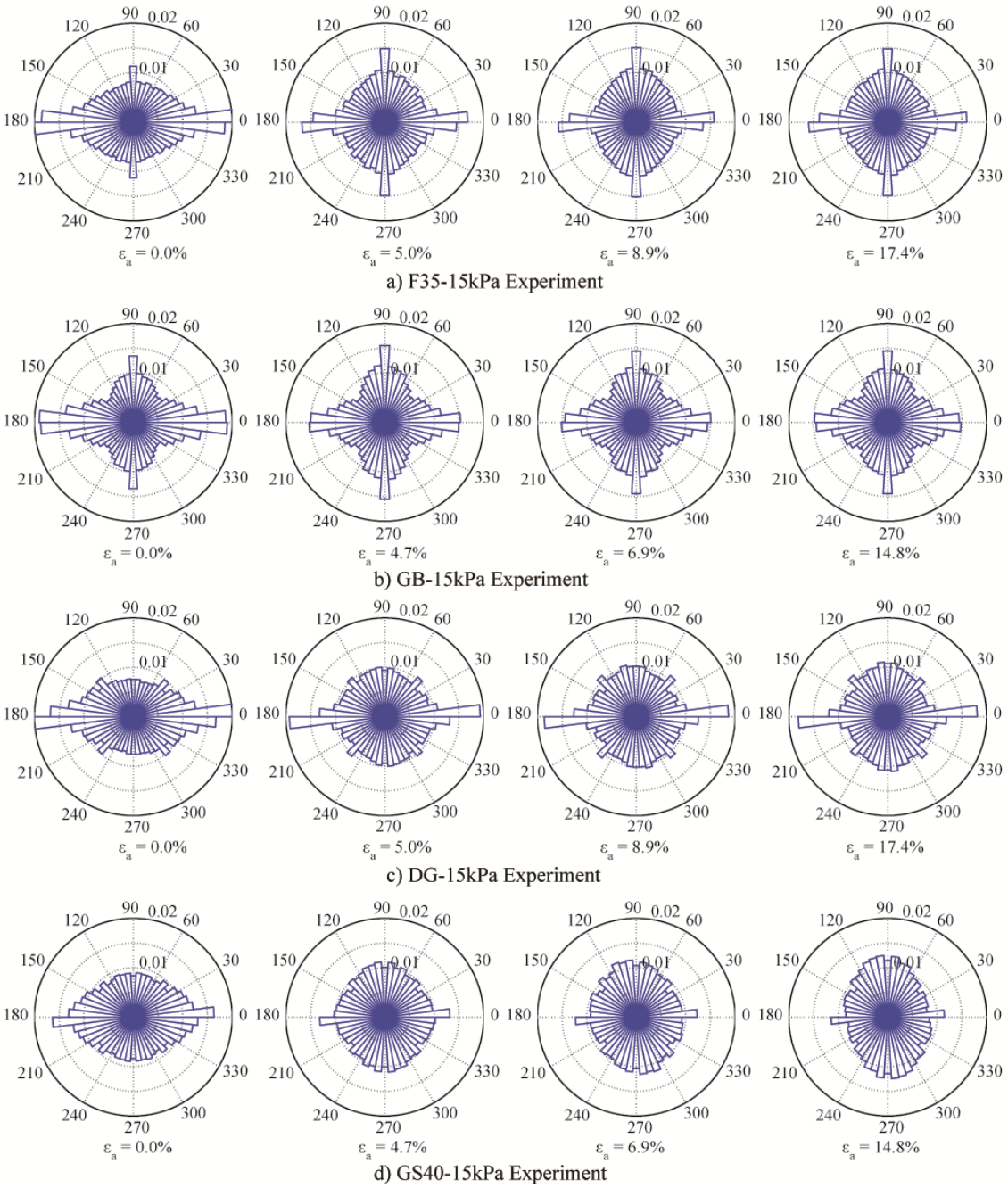

Figure 6.9. Global contact normal distribution rose diagrams at various strains for all 15 kPa experiments

vertical loading direction until ε_a = 11.9%, where distribution remained relatively unchanged for the remainder of the experiment. Glass beads (Figure 6.9b, experiment GB-15kPa) initially exhibited evidence of cubic packing with preference of contact normal vectors toward horizontal. Throughout the experiment, contacts aligned more toward the vertical, retaining evidence of cubic packing. #1 dry glass sand (Figure 6.9c, experiment DG-15kPa) had initial contact distribution similar to the F-35 sand, but the contact normal distribution did not reach a steady state and continuously evolved toward the vertical throughout the entire experiment. Similar contact distribution evolution was observed in the GS40 sand (Figure 6.9d, experiment GS40-15kPa), where the contact normal distribution was continuously evolving towards the vertical.

Influence of particle morphology on initial fabric

F-35 Ottawa sand has the highest overall sphericity index value (least spherical) of all the granular materials considered in this paper, and among the 400 kPa experiments had the highest initial contact normal anisotropy. Contact normal vectors were distributed more in the horizontal plane than any other of the granular materials as evident in the rose diagrams. #1 dry glass and GS#40 sands had similar initial anisotropic contact normal distributions, but not to the extent of F-35 sand. Cubical-like packing of glass beads (the most spherical of the materials) resulted in contacts being distributed more evenly between the horizontal and vertical directions with a slight initial bias towards the horizontal direction. These trends are also evident in the initial contact normal rose diagrams of 15 kPa experiments.

Influence of confining pressure on initial fabric

Experiments were prepared in the same manner before application of confining pressure. The influence of confining pressure on initial global fabric can be determined through investigating the initial contact normal distributions (Figures 6.2, 6.3, 6.6 and 6.9, $\varepsilon_a = 0.0\%$). All 15 kPa experiments have a more anisotropic fabric with preferential contact normal direction to the horizontal than the same granular material when confined with 400 kPa pressure. Application of a relatively higher confining pressure causes particle contact normal vectors to align into a more heterogeneous configuration to resist all-around loading. Application of a relatively large confining pressures (barring particle breakage) may induce an initially isotropic fabric of a granular material.

2nd and 4th order fabric surface representations

To illustrate the difference between 2nd and 4th order fabric tensors, recalling that 4th order tensors better represent material anisotropy, surface representations of fabric tensors for experiments F35-400kPa and GB-400kPa at various loading stages are shown in Figure 6.10. Shape of the surface representations depict the overall direction (and magnitude) of contact normal vectors, and would follow the shape of 3D rose diagrams. Surface representations of fabric tensors for both experiments show preferential alignment of fabric towards the horizontal and evolution towards the vertical (to resist the applied axial load), similar to the rose diagrams that were discussed earlier. 2nd order tensor surface representations are limited to ellipsoidal shapes, and the 2nd order tensors of F-35 sand (Figure 6.10a) begins elongated horizontally at the beginning of the

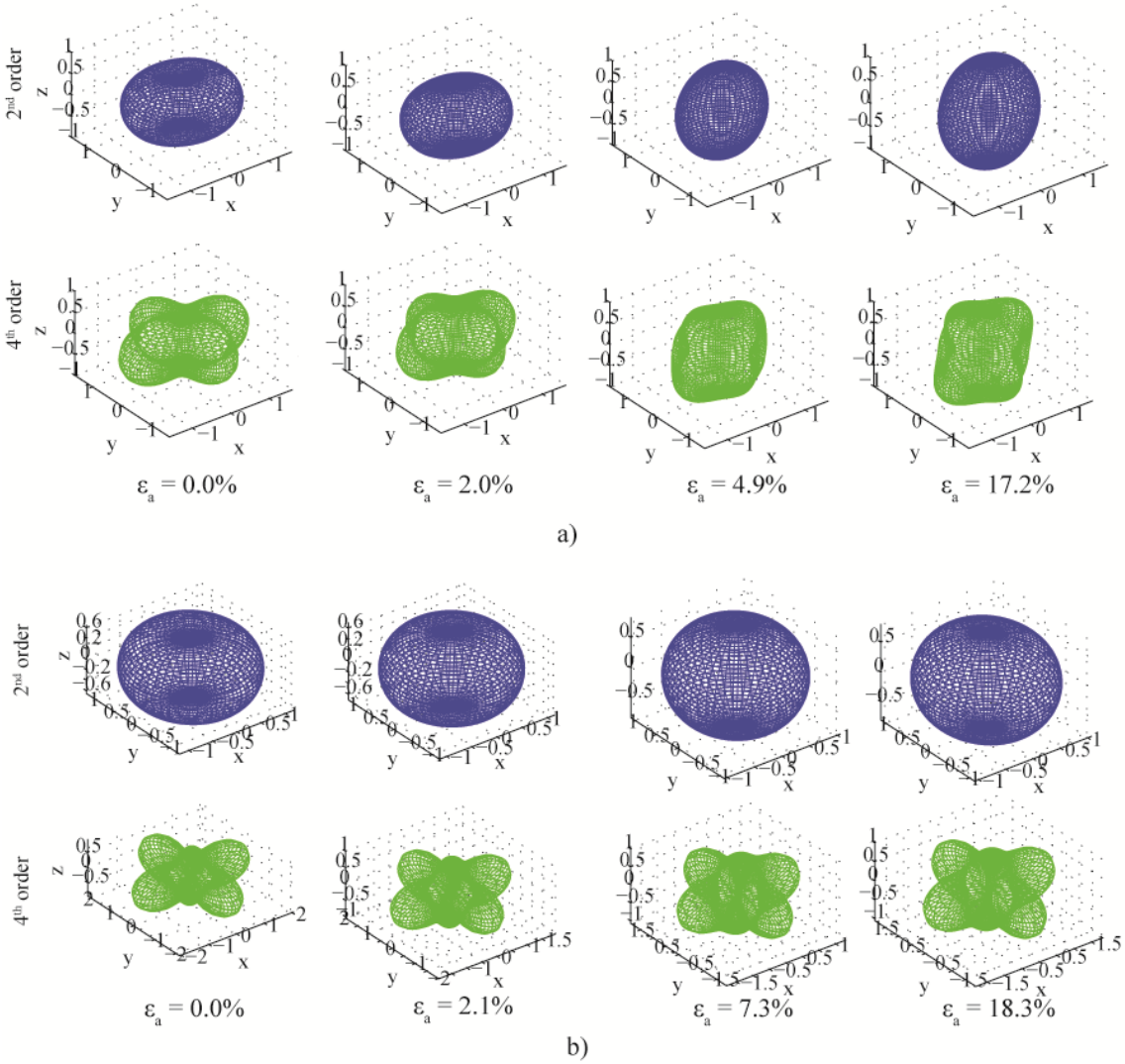

Figure 6.10. Evolution of 2nd and 4th order fabric tensor surface representations for (a) F35-400kPa experiment; and (b) GB-400kPa experiment

experiment and changes to more vertical orientation towards the end of the experiment. 4th order tensor surface representations for F-35 better capture 3D contact orientation anisotropy, especially for the initial fabric. The difference between orders is even more pronounced for the glass beads (Figure 6.10b), which initially have contact normal orientations tending towards cubic packing. Ellipsoidal representations cannot fully capture 3D contact orientations of cubical-type packing. Even though 4th order tensors better capture fabric anisotropy, conventional 2nd order fabric tensors are adopted for the remainder of this paper to coincide with the literature for use in current micromechanical models that incorporate fabric.

Evolution of FAV A

FAV *A* was calculated for each SMT image of all experiments listed in Table 6.1 and for the VOI's in the 400 kPa experiments, taking into account the unit-norm deviatoric tensor-valued loading direction **n** for triaxial compression. In order to compare with theoretical evolution of *F* and FAV *A* in (Li and Dafalias 2011), maximum FAV *A* for each experiment was normalized to unity ($A_c = A_{max} = 1$). Normalizing FAV *A* scales the initial fabric and does not affect fabric evolution. Evolution of FAV *A* and principal stress ratio (PSR = σ_1/σ_3) versus axial strain for all 400 kPa experiments considered in this paper are shown in Figure 6.11. Initial FAV *A* for F35-400kPa experiment is 0.22 and steadily increased until ε_a = 6.9%, where it began to approach unity shortly after the peak PSR. Initial FAV *A* for GB-400kPa experiment is 0.63 and increased at a smaller rate than F-35 sand. FAV *A* for glass beads peaked at ~ε_a= 8%,

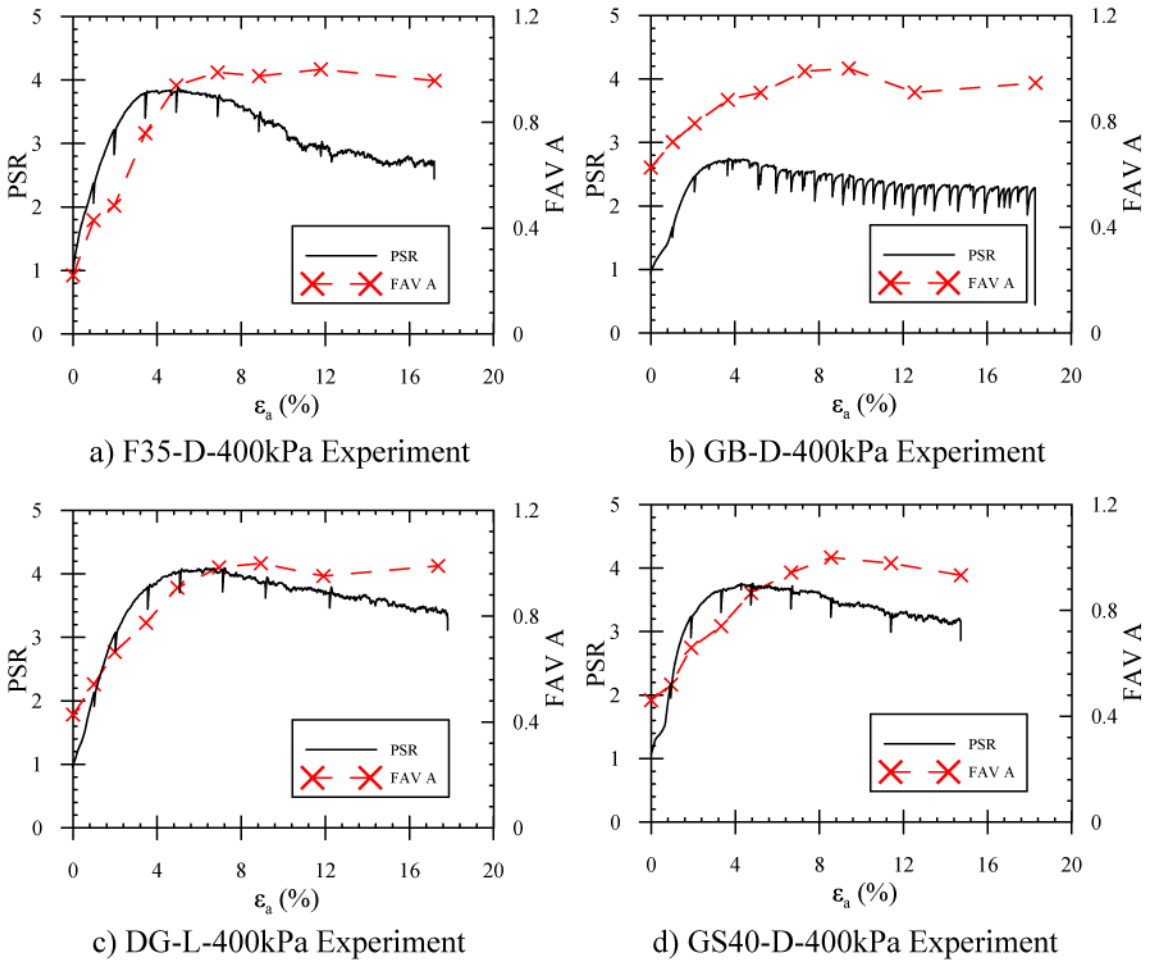

Figure 6.11. Evolution of PSR and global FAV A for 400 kPa experiments

which is about 4% after the peak PSR. In general, FAV *A* for specimens that were subjected to 400 kPa confining pressure peaked and remained relatively constant between 5%-10% axial strain. FAV *A* closely follows observations from contact normal rose diagrams and fabric tensor surface representations. Fabric evolved (in terms of FAV*A*) to the most stable configuration possible in the experiment at approximately the same axial strains as contact normal distributions become relatively constant.

Evolution of FAV *A* within the VOI's (Figure 6.12) exhibited different behavior than the global behavior, which is a representation of all particles whether they are within the shearing zone or not. FAV *A* for particle contacts within shear band/zone VOI show a strong peak near or slightly after peak PSR, while particle contacts in the VOI outside of shearing zones produce FAV *A* evolution that gradually increases throughout the experiment. The continual increase of FAV *A* of particle contacts outside of shearing zones agrees with theoretical evolution found in the literature, where particle contacts gradually orient to resist global load. FAV *A* in the shear band of experiment F35-400kPa (Figure 6.12a) peaks during the post-peak PSR softening, whereas shear band particle contact FAV *A* in the other 400 kPa experiments peak at the peak PSR. After the failure shear band or at the onset of shear band, FAV *A* within the shear zones is not consistent, implying a larger level of contact creation and destruction in several directions. In experiment GB-400kPa (Figure 6.12b), an initial decrease of FAV *A* (inside and outside of shear band) is noticed during the first strain increment which is not observed in the global FAV *A*. Such decrease corresponds to the slight PSR change observed as a result

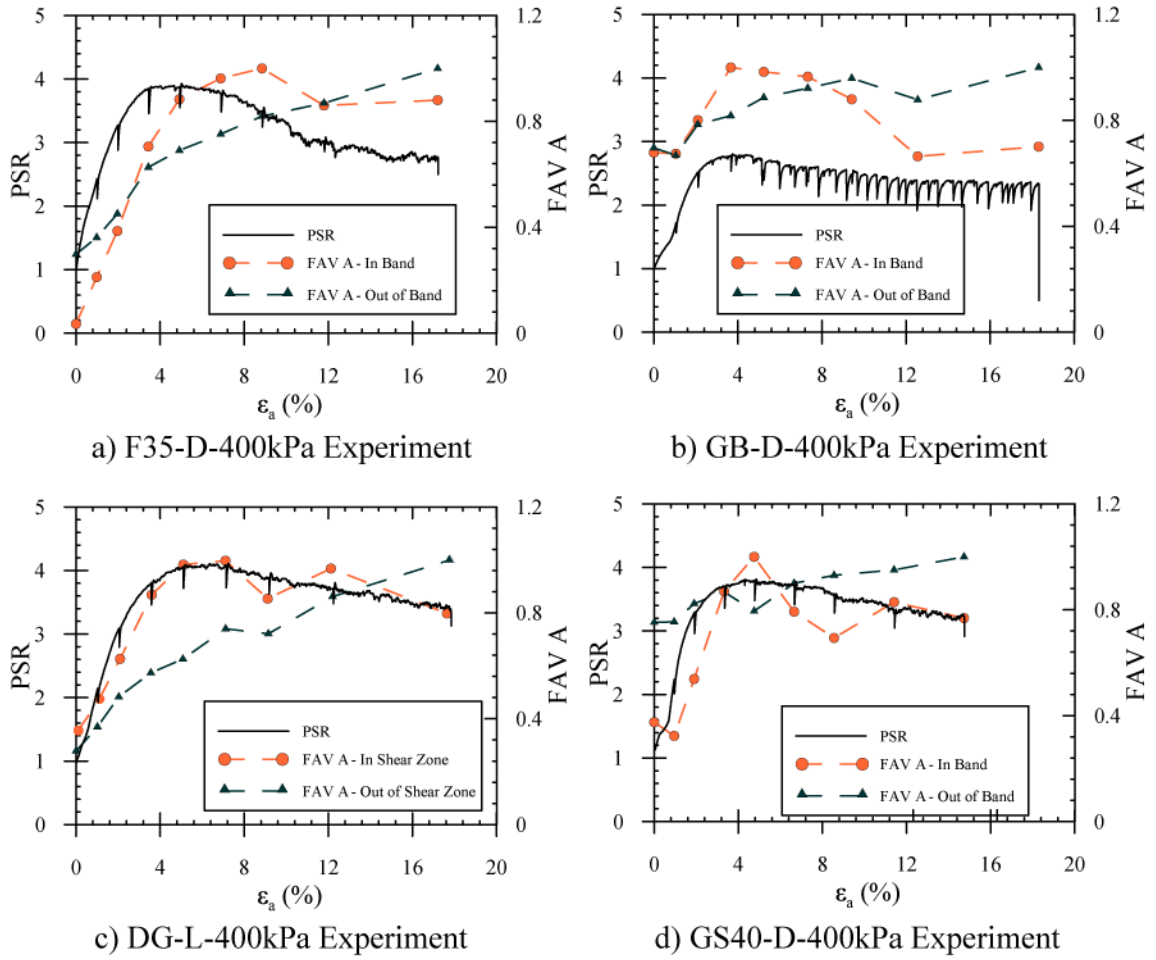

Figure 6.12. Evolution of PSR and VOI FAV A for 400 kPa experiments

of particle contacts rearrangment to a more stable state at low PSR before orienting to resist global load. The VOI chosen for particles outside of failure shear band is near the top end platen, where most initial activity occurs and small strain localizations develop near the center of the specimens in these experiments. Fabric evolves differently within and outside of the shear zones. Global fabric is a diluted combination of particles within the shear zone and outside the shear zone, masking many interesting localized changes.

Specimens subjected to 15 kPa confining pressure did not exhibit peak PSR states (Figure 6.13). All experiments had an initial sharp increase in PSR followed by a slow steady increase of PSR for the remainder of the experiment. Fabric of experiment F35-15kPa initially had FAV *A* of 0.27, increased to a local peak at ε_a = 5%, exhibited a slight decrease until ε_a = 7%, then increased to the maximum observed value at ε_a = 11.9%. Experiment GB-15kPa followed a similar trend, starting at an initial FAV *A* of 0.54 and had peaks at ε_a = 3.6 and ε_a = 9.2%. In general, fabric of DG-15kPa and GS40-15kPa experiments (initial FAV *A* of 0.25 and 0.23, respectively) followed a trend similar to the PSR curve, having an initially steep slope followed by more gradual continuous increase throughout the experiment. A sharp fabric peak is exhibited in experiment DG-15kPa at ε_a = 3.5%, but continued to follow the continually increasing trend afterwards. The observed peak is shortly after PSR slope changes when an intense area of strain localization initially formed in the specimen.

Although FAV *A* alone does not provide significant insight into initial fabric, it does amply describe evolution of fabric throughout an experiment under a given

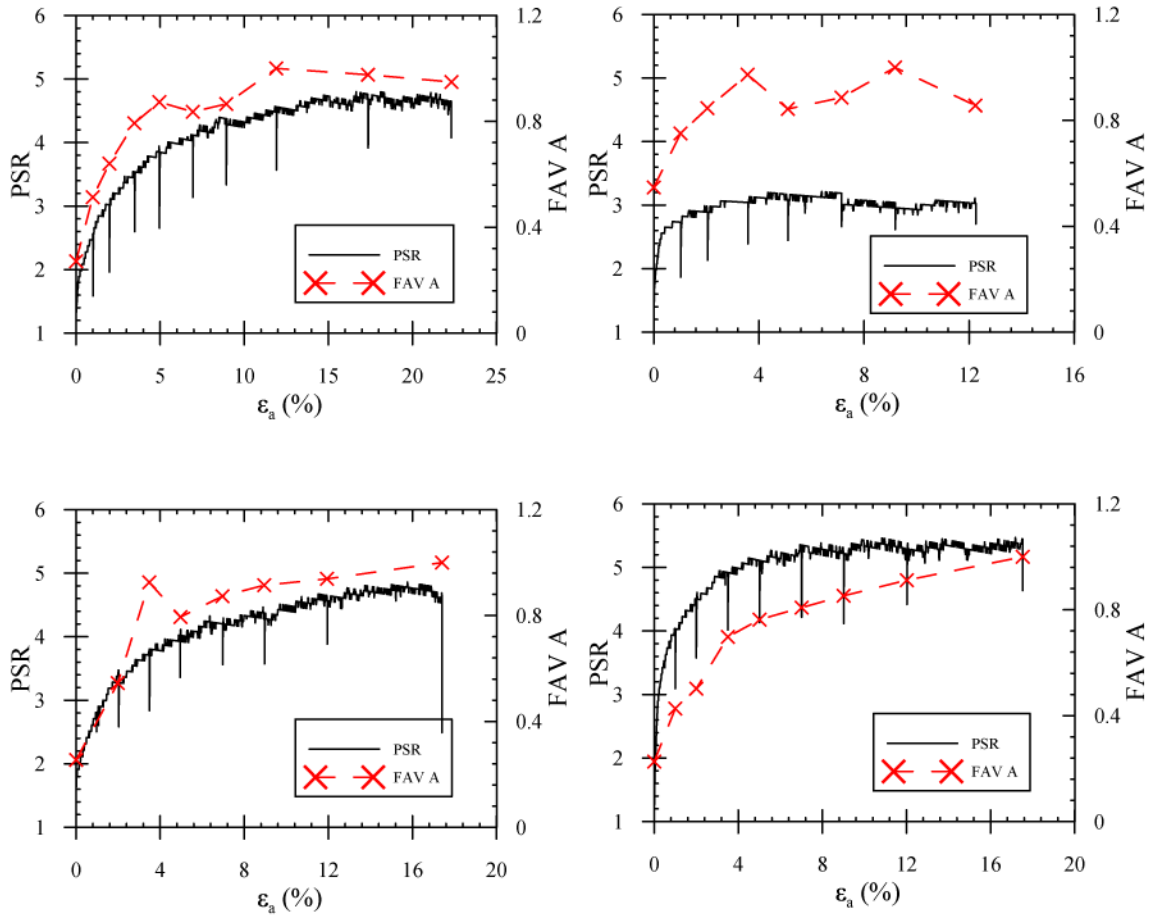

Figure 6.13. Evolution of PSR and global FAV A for 15 kPa experiments

conditions (i.e., confining pressure), especially if a maximum is reached and maintained for a reasonable amount of axial strain. Theoretical evolution of FAV *A* in (Li and Dafalias 2011) for triaxial compression approached unity near 100% shear strain ($\gamma = \varepsilon_1 - \varepsilon_3$) as a power function. This theoretical evolution agrees with experimental evolution of FAV *A* for fabric outside the shearing zones, and somewhat agrees for global FAV *A* of specimens that were subject to 15 kPa confining pressure, especially for #1 dry glass sand (experiment DG-15kPa without the anomalous peak at $\varepsilon_a = 3.9\%$) and GS#40 (experiment GS40-15kPa) specimens. The PSR of these two specimens is also continuously increasing throughout the experiment duration and global FAV *A* is a reflection of the PSR. 15 kPa experiments on the F-35 sand (F35-15kPa) and glass beads (GB-15kPa) exhibit a local minimum of FAV *A* in the experiment and a decrease in FAV *A* near the end of the experiment with no apparent strength variations. Lower confining pressure could result in less stability of the fabric, allowing for particles to rearrange more freely. FAV *A* enhances features of fabric that may not be discernable from visual inspection of contact normal orientation rose diagrams.

Global fabric (as described by FAV *A*) of the 400 kPa experiments tend to be much more stable. For all experiments, fabric evolved to a peak shortly after peak PSR and maintained somewhat uniform fabric for the remainder of the experiments. During strain hardening and peak stages of triaxial experiments on granular materials with 400 kPa confining pressure, particles throughout the specimen stabilize and allow the onset of a single shear band or multiple shear bands. After the development of a dominant shear

band or several shear bands, particle and contact arrangement is generally localized within the shear band(s). Zones of shearing (shear bands) within the specimen contain a small percentage of particles to not reflect in the overall contact normal distribution, therefore global rose diagrams and FAV *A* stabilize (as depicted in Figures 6.2-3, 6.6, and 12). The same cannot be deduced when analyzing particles solely within or outside of the shear band. A continual increase of fabric to resist loading is observed in particles outside the shear band, while fabric of particles with the shear band peak (near peak PSR or during softening), decreases, and becomes relatively unstable at critical state.

Of the 400 kPa experiments, F-35 sand exhibited the most intense initial increase of global FAV *A* and reached maximum at the lowest axial strain, while glass beads had the most gradual increase of global FAV *A* to a maximum value. Global fabric of #1 dry glass and GS#40 sands evolved at an intermediate rate, implying that particle sphericity affects the initial fabric and influences fabric evolution. Global fabric of glass beads had the least degree of fabric evolution when considering the difference between maximum (1) and minimum values of global FAV *A*. F-35 had the largest degree of fabric change among the 400 kPa specimens. Definitive conclusions on degree of fabric change cannot be formed for 15 kPa specimens because fabric for some of the experiments was still evolving upon termination of the experiments.

Initial FAV *A* values may not be an ideal indicator of initial fabric anisotropy as they are normalized, a variable of loading direction, and dependent on the intensity of fabric evolution. However, for the 400 kPa experiments, where global FAV *A* has a

definitive peak and steady-state, initial FAV *A* values coincide with particle sphericity. Glass beads have the highest initial FAV *A* and are the most spherical. F-35 sand has the lowest initial FAV *A* and is the least spherical, while dry glass and GS#40 sands have approximately equivalent sphericity and initial FAV *A* (Figure 6.11).

Fabric of granular material can be calculated from any quantifiable microstructural measurements, and contact normal vector based fabric is discussed extensively in the literature. Conventional 2^{nd} order fabric tensors may not fully capture the full anisotropy of a granular material, whereas 4^{th} order tensors capture more details of material anisotropy. Many factors influence granular material fabric and fabric evolution, which contribute to strength and volume change properties. Experimental data reported in this paper can be used to develop fabric evolution laws that can be incorporated in anisotropic material models.

Conclusions

A series of triaxial compression experiments were conducted on four different granular materials while acquiring in-situ SMT imaging. Experiments were conducted at two confining pressures and paused to acquire SMT images at multiple axial strains. Images were processed and analyze to quantify microstructural variables such as contact normal vectors. Contact normal vector distributions were analyzed and fabric tensors were calculated for each strain state of each experiment, and initial fabric and fabric evolution was analyzed for global contacts, contacts of shear zone particles, and contacts

of particles outside of shear zones. Based on the experimental contact normal distribution and fabric evolution, the following conclusions are drawn:

1. 4^{th} order fabric tensors are more accurate to quantify material anisotropy than conventional 2^{nd} order tensors found in the literature. Incorporating 4^{th} order tensors in micromechanical models would provide more accurate fabric insight.
2. For preparation methods used in this study, particle contact normal vectors have an initial bias towards the horizontal and globally evolve to resist the vertical applied stress.
3. Particle sphericity has a major influence on the initial fabric of granular material and the evolution of fabric. Less spherical materials produce a more anisotropic material and a larger work is required to evolve global fabric to a steady-state during shearing.
4. A higher confining pressure forces an initial arrangement of particle contact normal vectors into a more isotropic state.
5. Global fabric evolution, in terms of FAV *A*, is dependent on confining pressure. At 400 kPa confining pressure, fabric evolves to a constant state shortly after peak PSR is reached. At 15 kPa confining pressure, fabric continues to evolve as PSR increases.
6. Global fabric (not fabric solely within the shear band) reaches a steady-state shortly after PSR reaches a critical state.

7. Fabric of particles within shearing zones evolve much differently than fabric of particles outside of shearing zones. Contacts within the shearing zone orient themselves relatively perpendicular to shear bands (coinciding with columnar structure formation within band), while particles outside of the shear band continually orient towards the vertical loading direction. Global fabric is a combination of the two, which masks interesting localized fabric features.

References

Alshibli, K., Druckrey, A., Al-Raoush, R., Weiskittel, T., and Lavrik, N. (2014). "Quantifying Morphology of Sands Using 3D Imaging." *Journal of Materials in Civil Engineering*, 04014275.

Barreto, D., O'Sullivan, C., and Zdravkovic, L. (2009). "Quantifying the Evolution of Soil Fabric Under Different Stress Paths." *AIP Conference Proceedings*, 1145(1), 181-184.

Druckrey, A., and Alshibli, K. (2014). "3D Behavior of Sand Particles Using X-Ray Synchrotron Micro-Tomography." *Geo-Congress 2014 Technical Papers*, 2814-2821.

Druckrey, A. M., Alshibli, K. A., and Al-Raoush, R. I. (2016). "3D characterization of sand particle-to-particle contact and morphology." *Computers and Geotechnics*, 74, 26-35.

Fonseca, J., O'Sullivan, C., Coop, M. R., and Lee, P. D. (2013). "Quantifying the evolution of soil fabric during shearing using directional parameters." *Géotechnique*, 487-499.

Fu, P., and Dafalias, Y. F. (2015). "Relationship between void- and contact normal-based fabric tensors for 2D idealized granular materials." *International Journal of Solids and Structures*, 63(0), 68-81.

Hasan, A., and Alshibli, K. (2012). "Three dimensional fabric evolution of sheared sand." *Granular Matter*, 14(4), 469-482.

Kanatani, K.-I. (1984). "Distribution of Directional Data and Fabric Tensors." *Int. J. Engng Sci.*, 22(2), 149-164.

Kuhn, M. R., Sun, W., and Wang, Q. (2015). "Stress-induced anisotropy in granular materials: fabric, stiffness, and permeability." *Acta Geotechnica*, 10(4), 399-419.

Lam, W.-K., and Tatsuoka, F. (1988). "Effects of initial anisotropic fabric and σ_2 on strength and deformation characteristics of sand." *Soils and Foundations*, 28(1), 89-106.

Li, B., and Zeng, X. (2014). "Effects of fabric anisotropy on elastic shear modulus of granular soils." *Earthq. Eng. Eng. Vib.*, 13(2), 269-278.

Li, X., and Dafalias, Y. (2011). "Anisotropic Critical State Theory: Role of Fabric." *Journal of Engineering Mechanics*, 138(3), 263-275.

Li, X., and Yu, H.-S. (2009). "Influence of loading direction on the behavior of anisotropic granular materials." *International Journal of Engineering Science*, 47(11–12), 1284-1296.

Li, X., and Yu, H.-S. (2014). "Fabric, force and strength anisotropies in granular materials: a micromechanical insight." *Acta Mech*, 225(8), 2345-2362.

Li, X., Yu, H. S., and Li, X. S. (2009). "Macro–micro relations in granular mechanics." *International Journal of Solids and Structures*, 46(25–26), 4331-4341.

Li, X. S., and Dafalias, Y. F. (2000). "Dilatancy for cohesionless soils." *Géotechnique*, 50(4), 449-460.

Lo Presti, D., Pedroni, S., and Crippa, V. (1992). "Maximum Dry Density of Cohesionless Soils by Pluviation and by ASTM D 4253-83: A Comparative Study." *ASTM Geotechnical Testing Journal*, 15(2), 180-189.

Millet, O., Gu, S., and Kondo, D. (2009). "A 4th order fabric tensor approach applied to granular media." *Computers and Geotechnics*, 36(5), 736-742.

Moesen, M., Cardoso, L., and Cowin, S. C. (2012). "A symmetry invariant formulation of the relationship between the elasticity tensor and the fabric tensor." *Mechanics of Materials*, 54, 70-83.

Nemat-Nasser, S. (2000). "A micromechanically-based constitutive model for frictional deformation of granular materials." *Journal of the Mechanics and Physics of Solids*, 48(6–7), 1541-1563.

Nemat-Nasser, S., and Zhang, J. (2002). "Constitutive relations for cohesionless frictional granular materials." *International Journal of Plasticity*, 18(4), 531-547.

Oda, M. (1972). "Initial fabrics and their relations to mechanical properties of granular material." *Soils and foundations*, 12(1), 17-36.

Oda, M., Nemat-Nasser, S., and Konishi, J. (1985). "Stress-induced anisotropy in granular masses." *Soils and Foundations*, 25(3), 85-97.

Oda, M., Takemura, T., and Takahashi, M. (2004). "Microstructure in shear band observed by microfocus X-ray computed tomography." *Géotechnique*, 54(8), 539-542.

Peña, A. A., Herrmann, H. J., and Lind, P. G. (2009). "Force chains in sheared granular media of irregular particles." *AIP Conference Proceedings*, 1145(1), 321-324.

Peters, J. F., Muthuswamy, M., Wibowo, J., and Tordesillas, A. (2005). "Characterization of force chains in granular material." *Physical Review E*, 72(4), 041307.

Rivers, M. L. "tomoRecon: High-speed tomography reconstruction on workstations using multi-threading." 85060U-85060U-85013.

Rivers, M. L., Citron, D. T., and Wang, Y. (2010). "Recent developments in computed tomography at GSECARS." *SPIE*, 3, 780409-780409.

Stershic, A. J., Simunovic, S., and Nanda, J. (2015). "Modeling the evolution of lithium-ion particle contact distributions using a fabric tensor approach." *Journal of Power Sources*, 297, 540-550.

Theocharis, A., Vairaktaris, E., Fu, P., and Dafalias, Y. F. (2014). "Comparison of fabric tensors for granular materials." *Geomechanics from Micro to Macro*, K. Soga, K. Kumar, G. Biscontin, and M. Kuo, eds., CRC Press, 153-158.

Tordesillas, A., and Muthuswamy, M. (2009). "On the modeling of confined buckling of force chains." *Journal of the Mechanics and Physics of Solids*, 57(4), 706-727.

Yimsiri, S., and Soga, K. (2001). "Effects of Soil Fabric on Undrained Behavior of Sands." *International Conferences on Recent Advances in Geotechnical Earthquake Engineering and Soil Dynamics*San Diego, CA.

Yimsiri, S., and Soga, K. (2010). "DEM analysis of soil fabric effects on behaviour of sand." *Géotechnique*, 483-495.

Zhao, J., and Guo, N. (2013). "Unique critical state characteristics in granular media considering fabric anisotropy." *Géotechnique*, 63(8), 695-704.

CHAPTER 7

APPLICATION OF ANISOTROPIC CRITICAL STATE THEORY USING EXPERIMENTAL FABRIC EVOLUTION IN SAND TRIAXIAL COMPRESSION

A version of this chapter is in preparation for submittal to a technical journal. The author list is: A. Druckrey, K. Alshibli.

My primary contributions to this paper are (i) formulating objectives and evaluating current research in the area, (ii) conducting most experiments during in-situ SMT imaging (iii) incorporating fabric tensors obtained from Chapter 6 into the Anisotropic Critical State Theory model, (iv) analysis of influences on model behavior and comparison with experiments, (v) most of the writing.

Abstract

The concept of critical state soil mechanics has been adopted and implemented into many successful models without full understanding of material micro-mechanics. Some granular materials may not always approach a single critical state state depending on gradation, morphology, and applied stresses. Material fabric plays a major role in influencing the constitutive behavior of granular materials. Fabric evolution based on theoretical, numerical, and rudimentary experimental techniques has been successfully integrated into several models. However, a limited published research that utilizes a comprehensive 3D experimental quantification of evolution of fabric has been reported for granular material. This paper assesses the accuracy of the anisotropic critical state theory (ACST) model which incorporates fabric evolution using 3D experimental measurements of fabric evolution of dry axisymmetric triaxial compression experiments where fabric was quantified using synchrotron micro-computed tomography (SMT) and image processing techniques. Also, multivariable statistical models (using particle-scale

input determined from imaging) are proposed to estimate the critical state parameters. The ACST model was calibrated using a single experiment and was extended to predict the behavior of granular materials during axisymmetric triaxial compression at various initial mean stresses and densities with good accuracy.

Introduction

Critical state, also known as steady-state, is an important and widely used concept in soil mechanics and is considered to be the state where stress and void ratio approach a constant with increasing shear strain (Wood 1991). The concept of critical state has been successfully implemented into many soil constitutive models models without a comprehensive understanding of the contributing micro-mechanics properties (e.g. Bolton 1986; Gens and Potts 1988; Kurtay and Reece 1970; Roscoe et al. 1958). For granular materials, the concept of critical state based on a steady state void ratio has been difficult to implement because of non-unique void ratio at the critical state at varying densities and confining pressures (Been et al. 1991; Mooney et al. 1998; Riemer and Seed 1997; Verdugo and Ishihara 1996). Thus, other micro-properties such as particle interactions and kinematics, boundary conditions, and fabric anisotropy may contribute to the non-uniqueness of the critical state void ratio in granular materials. Isolating and experimentally measuring individual micro-mechanical properties of granular material and subsequent evolution that has been the subject of extensive research in recent years.

Fabric of granular material is defined as the geometrical arrangement of particles, particle groups and associated pore space. Fabric has been found to greatly influence

constitutive behavior of granular material (Lam and Tatsuoka 1988; Li and Yu 2009; Li and Yu 2014; Oda 1972; Oda et al. 1985; Yimsiri and Soga 2001; Yimsiri and Soga 2010). For example, Oda (1972) used various sands, preparation methods, and 2D thin section microscopy and found that initial fabric anisotropy is a direct result of particle shape and sample preparation technique where differences in initial fabric greatly influenced mechanical properties, and specimens with contact normal vectors preferential orientation toward the direction of loading have a more stable fabric. Li and Zeng (2014) used experimental bender element techniques and found that fabric anisotropy is affected by sand morphology and density, and fabric affects the shear modulus of the material. Furthermore, Yimsiri and Soga (2010) used discrete element modeling (DEM) to demonstrate that the initial fabric has profound influence on stiffness, strength, and dilation properties of granular materials. Although the importance of initial fabric and fabric evolution resulting from particle deposition, morphology, and applied loadings is well documented in the literature, they remain difficult to be accurately quantified and model experimentally in 3D.

Fabric is typically quantified using tensors, and any micro-scale directional data of granular material can be used to represent fabric. Many researchers have defined fabric using a variety of particle scale features. Fonseca et al. (2013) terminated triaxial experiments at different axial strain levels during shearing and impregnated the specimens with epoxy resin. Cores were then extracted from several locations within the specimens and CT scans were acquired to quantify and compare microstructural data

using rose diagrams and an eigenvalue analysis of fabric tensors, as well as analyzed evolution of fabric in the specimens. Li et al. (2009) developed a new anisotropic fabric tensor based on void cell anisotropy that was correlated with the macro behavior of granular material via numerical simulations and concluded that it is a more effective definition than those based on particle orientations or contact normal. Few researchers have found a strong correlation between fabric tensors based on contact normal vectors and void space vectors (Fu and Dafalias 2015; Theocharis et al. 2014); however, contact normal tensors have had the disadvantage of being difficult to accurately quantify experimentally (Theocharis et al. 2014). Forces transmit through a mass of granular material via contact normals and force chains (e.g. Oda et al. 2004; Peña et al. 2009; Peters et al. 2005; Tordesillas and Muthuswamy 2009), and accurate experimental measurements of contact normal tensors would prove valuable for micro-mechanics constitutive models. Experimental contact normal tensors inherently incorporate other particle-scale properties if accurate characterization of contact in 3D space is quantified.

Several researchers have incorporated initial fabric and fabric evolution into constitutive modeling of granular material. For example, Nemat-Nasser (2000) developed a robust micromechanics-based constitutive model that accounts for pressure sensitivity, friction, dilatancy, and, most importantly, fabric and fabric evolution. Model parameters were estimated in (Nemat-Nasser and Zhang 2002) based on results of cyclic shearing experiments and then were used to predict other experimental results with a good accuracy. However, most constitutive models that incorporate fabric evolution are based

on fabric properties obtained from theories, discrete element method, or rudimentary experiments. Experimental evolution of fabric in 3D has only recently began to emerge as new techniques such as x-ray computed tomography (CT) and synchrotron micro-computed tomography (SMT) were developed to quantify micro-scale properties of granular materials. This paper utilizes SMT imaging of axisymmetric triaxial compression experiments on dry sand specimens to quantify fabric evolution. Fabric evolution obtained from the experiments is used in the anisotropic critical state theory (ACST) to model the strength and deformation behavior of granular materials at various densities and initial mean stresses. Also, empirical multivariable statistical models that incorporate micro-scale particle parameters are developed and used for estimating the critical state parameters in the model.

Model Description

Li and Dafalias (2000) proposed a critical state soil mechanics model for granular materials that incorporated state dependent dilatancy to describe the internal state of the material. The state parameter was defined as the difference between the current void ratio and the critical state void ratio was shown to be an effective parameter to measure how far the material state is from the critical state. The model was modified by Li and Dafalias (2002) to include the influence of the initial fabric anisotropy of the material. Then, Li and Dafalias (2011) incorporated fabric evolution into the model of Li and Dafalias (2000) through the fabric anisotropy variable *A* (FAV *A*), which is a tensorial product of the normalized fabric tensor **F** (normalized such that at critical state $F_c =$

$\sqrt{\mathbf{F}:\mathbf{F}} = 1$) and the unit-norm deviatoric tensor-valued loading direction **n**. **F** is decomposable into magnitude *F* and unit-norm deviatoric tensor-valued direction $\mathbf{n}_F$ as:

$$\boldsymbol{F} = F\boldsymbol{n}_F, \qquad F = \sqrt{\boldsymbol{F}:\boldsymbol{F}}, \quad \boldsymbol{n}_F:\boldsymbol{n}_F = 1, \quad tr\boldsymbol{n}_F = 0 \tag{7.1}$$

To incorporate the resistance of fabric against loading, Li and Dafalias (2011) included the unit-norm deviatoric tensor-valued loading direction **n**, where $\mathbf{n}:\mathbf{n} = 1$ and $\mathrm{tr}\mathbf{n} = 0$. FAV *A* is calculated as:

$$FAV\ A = \boldsymbol{F}:\boldsymbol{n} = F\boldsymbol{n}_F:\boldsymbol{n} = FN \tag{7.2}$$

and FAV *A* accounts for fabric direction and magnitude relative to loading direction for all possible loading combinations.

The dilatancy state parameter (DSL, ζ) in Li and Dafalias (2011) replaces the state parameter originally proposed by Li and Dafalias (2000) and proposed an expression for fabric as:

$$\zeta = \psi - \psi_A = e - \hat{e}_c(p) - \hat{e}_A(e,p)(FAV\ A - 1) \tag{7.3}$$

where e is the current void ratio, $\hat{e}_c(p)$ is an expression for the critical state line (CSL) as a function of the means stress p, and $\hat{e}_A(e,p)$ assumed to be e_A, a constant independent of e and p, which is obtained from a parallel translation of the CSL by an amount equal to $e_A(FAV\ A - 1)$. The CSL is defined (Li and Wang 1998):

$$\hat{e}_c(p) = e_\Gamma - \lambda_c\left(\frac{p}{p_a}\right)^\xi \tag{7.4}$$

where e_Γ and λ_c are material parameters, ξ is a material constant and p_a is atmospheric pressure. The remaining model equations from Li and Dafalias (2011) are as follows for triaxial loading; elastic strain rates:

$$\dot{\varepsilon}_q^e = \frac{\dot{q}}{3G} \qquad and \qquad \dot{\varepsilon}_v^e = \frac{\dot{p}}{K} \tag{7.5}$$

with the elastic shear (G) and bulk (K) moduli as:

$$G = G_0 \frac{(2.97-e)^2}{1+e}\sqrt{pp_A} \qquad and \qquad K = G\frac{2(1+\nu)}{3(1-2\nu)} \tag{7.6}$$

where G_0 is a material constant and ν is Poisson ratio. The plastic strain rates are:

$$\dot{\varepsilon}_q^p = \frac{p}{K_p}\dot{\eta} \qquad and \qquad \dot{\varepsilon}_v^p = D\dot{\varepsilon}_q^p \tag{7.7}$$

where $\dot{\eta} = {\dot{q}}/{\dot{p}}$, D , and K_p are determined by:

$$D = d(M_c e^{m\zeta} - \eta) \quad and \quad K_p = h(M_c e^{-n\zeta} - \eta) \tag{7.8}$$

where parameters *m* and *n* can be determined at the phase transformation state (D = 0) and drained peak stress state (K_p = 0), respectively. The coefficients d and h were assumed to be:

$$d = \frac{d_0}{M_c} \qquad and \qquad h = \frac{G[h_1(1+FAV\ A)+h_2(1-FAV\ A)]}{\eta} \tag{7.9}$$

with d_0, h_1, and h_2 as model constants and M_c is the critical stress ratio for triaxial compression. Theoretical evolution of the fabric was proposed by Li and Dafalias (2011) as:

$$\dot{F} = c(\pm 1 - F)\left|\dot{\varepsilon}_q^p\right| \qquad or \qquad F = \pm 1 \mp (1 \mp F_{in})e^{-c\left|\varepsilon_q^p\right|} \tag{7.10}$$

where *c* is taken as a constant and F_{in} is the initial value of *F*. Li and Dafalias fabric and its evolution were used without 3D experimental verification. In this paper, theoretical fabric evolution is replaced with fabric evolution calculated from 3D experimental measurements.

Experimental Measurement of Fabric

Synchrotron Micro-Computed Tomography

To experimentally quantify fabric, a small triaxial apparatus described in (Druckrey and Alshibli 2014; Hasan and Alshibli 2012) was setup in beamline 13BMD of Advanced Photon Source (APS), Argonne National Laboratory (ANL), Illinois, USA. Drained axisymmetric triaxial compression experiments were conducted on dry dense specimens of angular F35 Ottawa sand and glass beads with initial mean stress (p'_0) of 400 kPa. Specimens were prepared in 4-5 lifts, lightly tamping each lift to densify before adding the next lift. Multiple scans were acquired for both experiments at increasing displacements, pausing the experiment to collect 900 radiograph images at 0.2° rotation increments for each scan, and radiographs were reconstructed to create 3D (SMT) images with resolution of 11.18 μm/voxel. Both experiments exhibited a single shear band at failure, and the stress ratio versus axial strain of the two experiments is shown in Figure 7.1. SMT imaging produces high resolution images with high clarity, and advantages of SMT imaging over conventional x-ray (CT) can be found in Druckrey et al. (2016).

3D SMT images were processed and data was extracted using the procedure described in Druckrey et al. (2016). Each loading step of all experiments was processed to individually label each particle. Labeled images were then processed using the code described in Druckrey et al. (2016), producing microstructural data of particle lengths (short, intermediate, and long axes), volume, surface area, orientation, coordination number, contact locations, contact normal vectors (CNV), and contact tangent vectors for

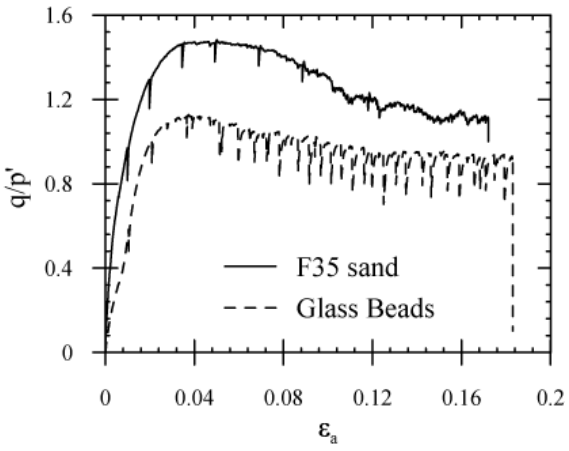

Figure 7.1. Stress ratio versus axial strain for experiments with in-situ SMT images

each particle in the entire specimen. In granular material, transmission of force takes place through particle contacts and is commonly associated with stiffness and strength (Kuhn et al. 2015). Also, CNV fabric has been found to correlate well with void vector fabric (a quasi-measure of deformation) (Fu and Dafalias 2015; Theocharis et al. 2014). Therefore, CNVs were used to quantify fabric in this paper. CNVs were quantified globally (all CNVs within specimen) as well as CNVs in a volume of interest (VOI) within the final shear band as well as a VOI outside the final shear band. CNVs in the VOIs were quantified by identifying the shear band at critical state, extracting particle contact information, and tracking those particles' contacts through decreasing strains. For visualization of the distribution of contact normal vectors, CNVs were projected onto the YZ plane (Z axis is the vertical or major principal stress direction) and plotted in 2D rose diagrams. Distribution of CNVs for the F35 sand is shown in Figure 7.2 at various strains for the VOI within the shear band as well as the global CNV network. CNVs demonstrate initial anisotropy with preference to the horizontal direction (direction of minor principal stress). Upon loading, they evolve to resist the vertical loading direction and near the peak deviator stress have preferential orientation towards the vertical. During softening and critical state, CNVs show some preference of orientation perpendicular to the shear band, which is evident in the distribution of CNVs of particles within the final shear band (Figure 7.2a).

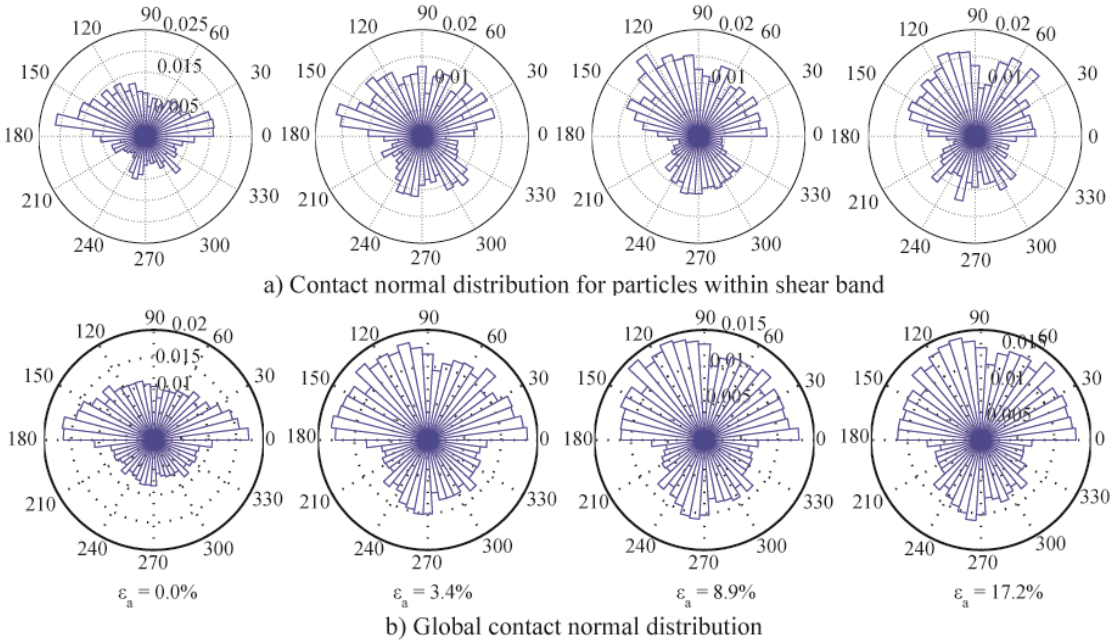

Figure 7.2. Rose diagrams of contact normal distribution for F35 sand at various axial strains

Fabric Quantification

Kanatani (1984) proposed a framework to quantify fabric tensors from any microstructural directional data, such as contact normal vectors. Fabric tensors of the first kind, also known as moment tensors, are conventionally used to define fabric in granular materials as (unweighted):

$$N_{ij} = \frac{1}{N}\sum_{\alpha=1}^{N} n_{i_1}^{\alpha} n_{i_2}^{\alpha} \dots n_{i_r}^{\alpha} \quad (11)$$

where n_i^{α} is the αth contact normal vector, *N* is the number of contacts, and *r* is the order of the tensor. Moment tensors can be calculated to any even order *r*. The second kind of fabric tensor most closely approximates the microstructural distribution function, and higher orders of fabric tensor $F_{i_1 \dots i_r}$ better represents the orientation distribution function, defined as (Moesen et al. 2012):

$$f(n) \sim \frac{1}{4\pi} F_{i_1 \dots i_r} n_{i_1} \dots n_{i_r} \quad (7.12)$$

Explicit definitions for second order fabric tensors of the second kind are (Kanatani 1984):

$$\boldsymbol{F}_{ij} = \frac{15}{2}\left(N_{ij} - \frac{1}{3}\delta_{ij}\right) \quad (7.13)$$

where δ is the Kronecker delta. Fabric tensors of the second kind are adopted in this paper. 2nd order fabric tensors are typically used in the literature to quantify fabric.

FAV A was quantified based on the fabric tensors at discrete strains throughout the experiments for all CNVs and CNVs in VOIs within and outside of the final shear band, all normalized such that maximum FAV *A* for each experiment was normalized to unity ($A_c = A_{max} = 1$). Normalizing FAV *A* scales the initial fabric and does not affect

fabric evolution, and FAV *A* for the triaxial experiment on F35 sand is presented in Figure 7.3a. Global fabric (in terms of FAV *A*) grew steadily until nearly reaching 1 at approximately ε_a =0.05, mirroring CNV evolution from horizontal preferential alignment to a preferential alignment towards the vertical loading direction during strain hardening. Fabric within the band evolved similarly to global evolution at early strains. However, during softening, a decrease in FAV *A* was observed until leveling at the critical state. This corresponds with CNV orientation shifting from initial horizontal bias to a preference towards the vertical loading direction at peak stress state. During softening, the final shear band develops and CNVs demonstrate some preferential alignment towards normal to the shear band rather than the vertical loading direction. FAV *A* of particles outside the shear band demonstrates a milder incline, most similar to theoretical evolution. Fabric is thus quantified at each strain point where an SMT image was acquired. In order to quantify a continuous evolution of FAV *A* with strain, two-term Fourier models were fit to each of the data sets to capture local maxima and minima within the evolution (Figure 7.3b). Cutoff strain values in the Fourier models (strain to which no more variation occurs) were determined to be where evolution of experimental FAV *A* became relatively constant. Theoretical evolution of FAV *A* based on eq. 7.10 with $F_{in} = 0.4$ and c = 5.7 is also presented in Figure 7.3b (constants were chosen to demonstrate differences in fabric evolution between Li and Dafalias (2011) and the current work). Evolution of FAV *A* for glass beads is presented in Figure 7.3c. The initial fabric of glass beads is larger than F35 sand, and band FAV *A* peaks and then decreases

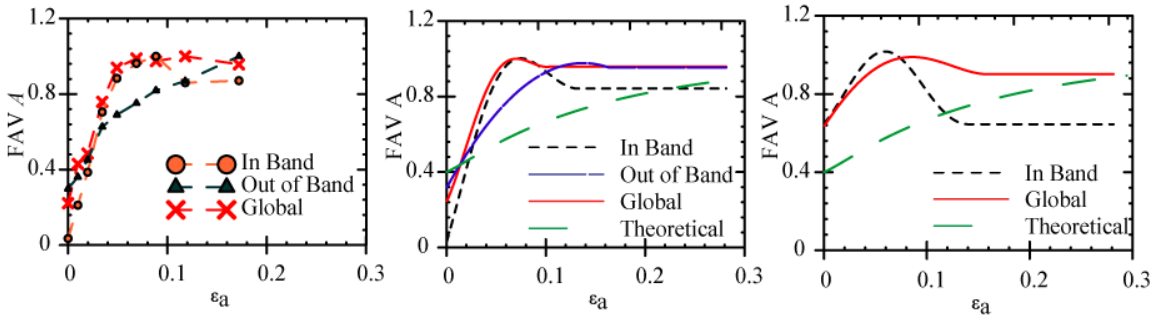

a) F35 Experimental evolution of FAV *A*

b) F35 Fourier series fit and theoretical evolution of FAV *A*

c) Glass beads Fourier series fit and theoretical evolution of FAV *A*

Figure 7.3. Experimental evolution of FAV A and two-term Fourier series fits to experimental fabric

to a steady state close to the initial value (F_{in}). Global evolution of glass beads FAV A is similar to that of global F35 sand. Experimental fabric evolves faster than the theoretical, which was assumed to reach 1 at very late strains. Theoretical fabric can be modified to closer match experimental by increasing the constant c, but cannot capture any decreases in fabric (such as fabric of CNVs within the shear band).

Critical State Model Parameters

This particular model is relatively sensitive to critical state inputs, and many experiments have shown that on the same sand, at different initial void ratios, initial mean stresses, and testing conditions, do not converge to a single critical state void ratio or critical state friction angle (e.g. Been et al. 1991; Ferreira and Bica 2006; Konrad 1990; Riemer and Seed 1997; Riemer et al. 1990; Shipton and Coop 2015). Similar observations were observed during drained triaxial experiments on dry F35 sand and glass beads used in this research, which are poorly graded and uniform (particle sizes between 0.3 mm to 0.425 mm, mean particle size, d_{50} = 0.36). Table 7.1 shows a summary of test initial conditions for F35 sand. Loose, medium dense, and dense experiments were subjected to initial mean stresses (p_0') of 15 kPa, 50 kPa, 100 kPa, and 400 kPa. Stress ratio (q/p') and void ratio (e) versus axial strain for these experiments are depcited in Figure 7.4. From the experiments, it is evident that the critical stress ratio (M_c = $(q/p')_{cs}$) used in eq. 8 and the critical void ratio (eq. 7.4) are variable with varying initial mean stress and initial void ratio. To estimate these parameters, empirical

Table 7.1. Summary of drained triaxial experimental conditions on dry F35 Ottawa sand

Experiment	Initial mean stress, p_0' (kPa)	Initial void ratio (e_0)
L15	15	0.735
L50	50	0.731
L100	100	0.726
L400	400	0.738
MD15	15	0.617
MD50	50	0.612
MD100	100	0.611
MD400	400	0.615
D15	15	0.491
D50	50	0.496
D100	100	0.498
D400	400	0.491

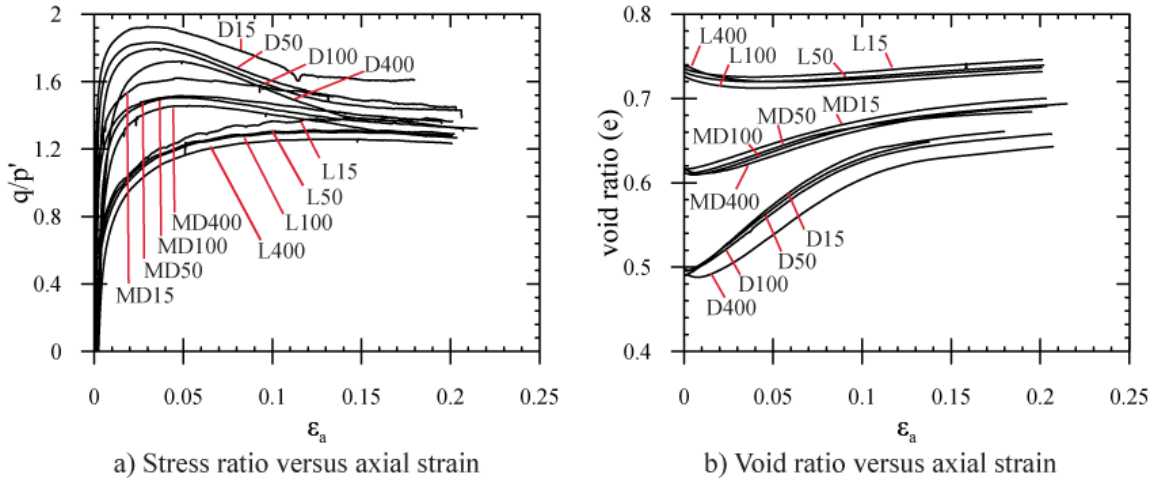

a) Stress ratio versus axial strain

b) Void ratio versus axial strain

Figure 7.4. Results of drained axisymmetric experimental at various densities and initial mean stresses for F35 sand

statistical models were developed using several granular material of varying morphology and size similar to those used in this research and are presented in the next Section.

Critical State Line

Void ratio and mean effective stress at critical state were determined from drained traixial experiments and data points were plotted in the $e - (p'/p_a)^{\alpha}$ plane following (Li and Wang 1998), where p_a is atmospheric pressure and $\alpha = 0.7$. Figure 7.5 shows results of F35 sand for each density state, indicating a nearly parallel shift in the critical state void ratio with density. The location of the best fit line crossing the y-axis corresponds to e_Γ in eq. 7.4. A total of 48 experiments were performed on four granular material (F35 sand, GS#40 sand, #1 Dry Glass sand, and glass beads) with varying morphologies and surface roughness (sphericity I_{sph}, roundness I_R, and surface roughness R_q) determined from Alshibli et al. (2014), each producing unique critical state void ratios. Each density state for each sand yielded unique e_Γ, and the results of relative density (D_r) versus e_Γ for all experiments are shown in Figure 7.6. e_Γ varies with density, and it is apparent that it varies with other material parameters.

To estimate e_Γ for poorly graded granular materials, a generalized multivariable linear regression model with predictors of I_{sph}, I_R, R_q, and D_r was constructed using values of each resulting e_Γ. The objective of this empirical model is to estimate e_Γ of similarly graded granular materials with known I_{sph}, I_R, R_q, and D_r. The model took the form of:

$$f(b,x) = b_1x_1 + b_2x_2 + \cdots + b_nx_n + b_{n+1} \qquad (7.14)$$

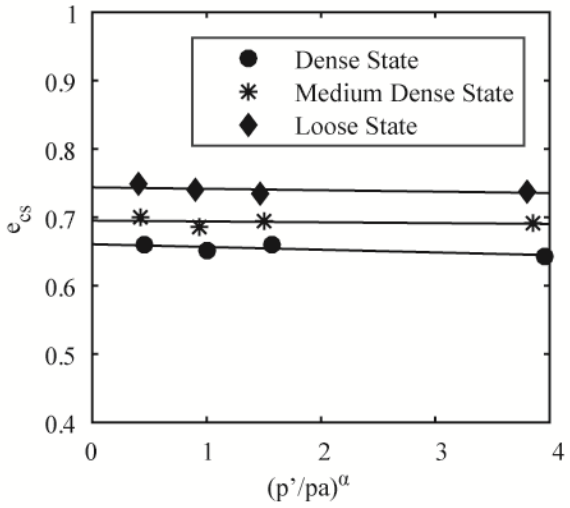

Figure 7.5. Results of $e - (p'/p_a)^{\alpha}$ for F35 sand at each density state demonstrating a nearly parallel shift in critical state void ratio with density (α = 0.7)

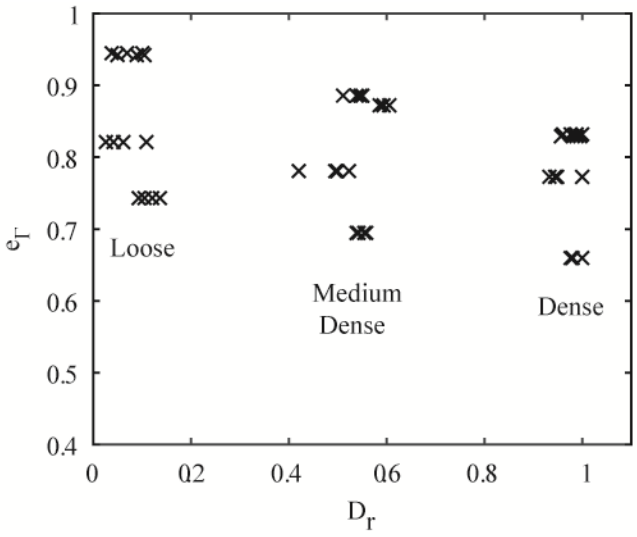

Figure 7.6. Experimental results of e_Γ versus D_r of four granular materials, demonstrating the effect of density and other variables on e_Γ

where $f(b,x)$ is e_Γ, b is an estimate for each of the n = 4 coefficients for each predictor value x and an additional statistical constant (b_{n+1}) was added for better statistical regression. The statistical constant has no physical meaning and is determined solely from the multiple regression. A summary of the coefficients, their standard error (SE), and p-values are listed in Table 7.2. Negative coefficients are a result of negative correlation of that predictor with e_Γ. The coefficient of determination of the model is 0.98, indicating a good statistical correlation.

Critical State Stress Ratio

For critical stress ratio, a multivariable model similar to eq. 7.4 was constructed to predict $f(b,x)$ = critical state friction angle φ_{cs}, where $M_c = \frac{6\sin\varphi_{cs}}{3-\sin\varphi_{cs}}$. An additional predictor, normalized mean stress (p_0'/p_a), was added to incorporate the effect of initial mean stress (note from Table 7.1 and Figure 7.4a that initial mean stress resulted in variation of M_c). Results from Toyora and Huston sands are also included in the critical stress ratio model, and a summary of the model is presented in Table 7.3 (n = 5 predictors). The coefficient of determination of the critical state friction angle model is 0.92. Results of experiments versus model predictions for e_Γ and φ_{cs} are shown in Figure 7.7, along with a 1:1 fit line. Predictions from the empirical statistical models will be input into the anisotropic critical state theory model for generalized behavior prediction of the granular materials and are presented in the next Section.

Table 7.2. Results of multivariable statistical model for e_Γ

Predictor	Coefficient (*b*)	SE	p Value
I_{sph}	-1.517	0.289	<0.001
I_R	0.419	0.382	0.279
R_q	0.641	0.044	<0.001
D_r	-0.100	0.003	<0.001
Statistical Constant	1.856	0.005	<0.001

Table 7.3. Results of multivariable statistical model for critical state friction angle φ_{cs}

Predictor	Coefficient (*b*)	SE	p Value
I_{sph}	5.805	2.968	0.055
I_R	-88.322	8.765	<0.001
R_q	0.787	1.321	0.553
Normalized p_0'	-0.793	0.113	<0.001
D_r	0.030	0.003	<0.001
Statistical Constant	105.12	7.878	<0.001

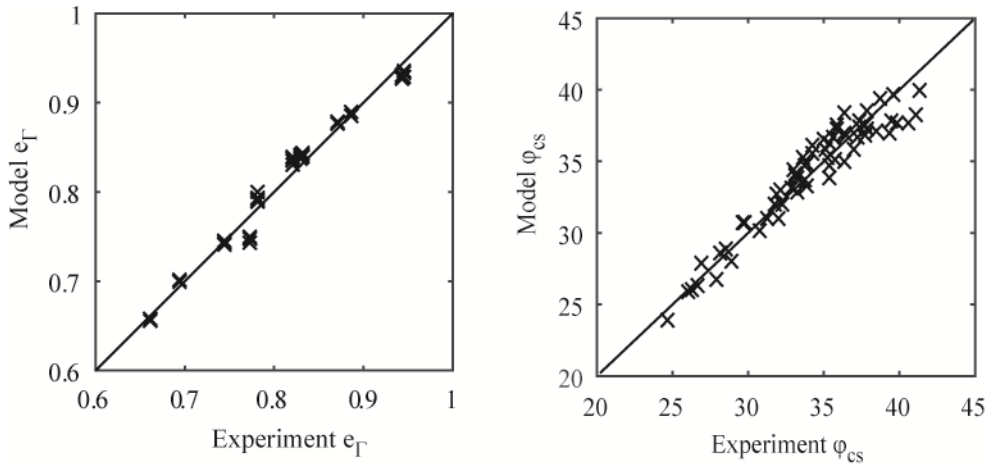

Figure 7.7. Experimental critical state parameters versus statistical model predictions

Model Results

The model was calibrated for F35 sand and glass beads using the experiments in which SMT images were acquired and fabric was quantified (Figs. 1 and 3), and model constants are shown in Table 7.4. Model results of the F35 triaxial experiment using global, shear band, and theoretical fabric evolution are shown in Figure 7.8. Axial strain versus deviatoric stress and volume change are presented, as well as void ratio versus deviatoric stress. Critical stress ratio used in the model predictions presented in Figure 7.8 was determined directly from the experiment, while the remaining critical state parameters were estimated using the proposed empirical statistical model. Model predictions are much more accurate using experimental fabric rather than theoretical fabric. Strength and deformation behavior of the sand predicted by the model is nearly identical to the experiment when experimental fabric is used. Experimental global fabric results result in slightly more accurate prediction of deformation behavior, while shear band fabric results in slightly more accurate strength behavior prediction.

Model predictions for experiments described in Table 7.1 and Figure 7.4 are presented in Figure 7.9 using model constants from Table 7.4. Critical state parameters were obtained from the statistical models presented earlier, and the only two remaining inputs are the initial void ratio and p_0'. Global fabric evolution of F35 sand (Figure 7.3) was used for dense and medium dense cases (Figure 7.9a and b), while fabric of particles not within the shear band produced the best results for loose cases (Figure 7.9c). Slight deviations in peak deviatoric stress were observed between experiments and the model

Table 7.4. Model constants for F35 sand and glass beads

Material	Elastic parameters	Dilatancy parameters	Hardening parameters
F35 Sand	$G_0 = 125$ $\nu = 0.05$	$d_0 = 1.8$ $m = 2$	$h_1 = 0.35$ $h_2 = 0.2$ $n = 3$
Glass Beads	$G_0 = 125$ $\nu = 0.05$	$d_0 = 1.8$ $m = 3$	$h_1 = 0.4$ $h_2 = 0.2$ $n = 3$

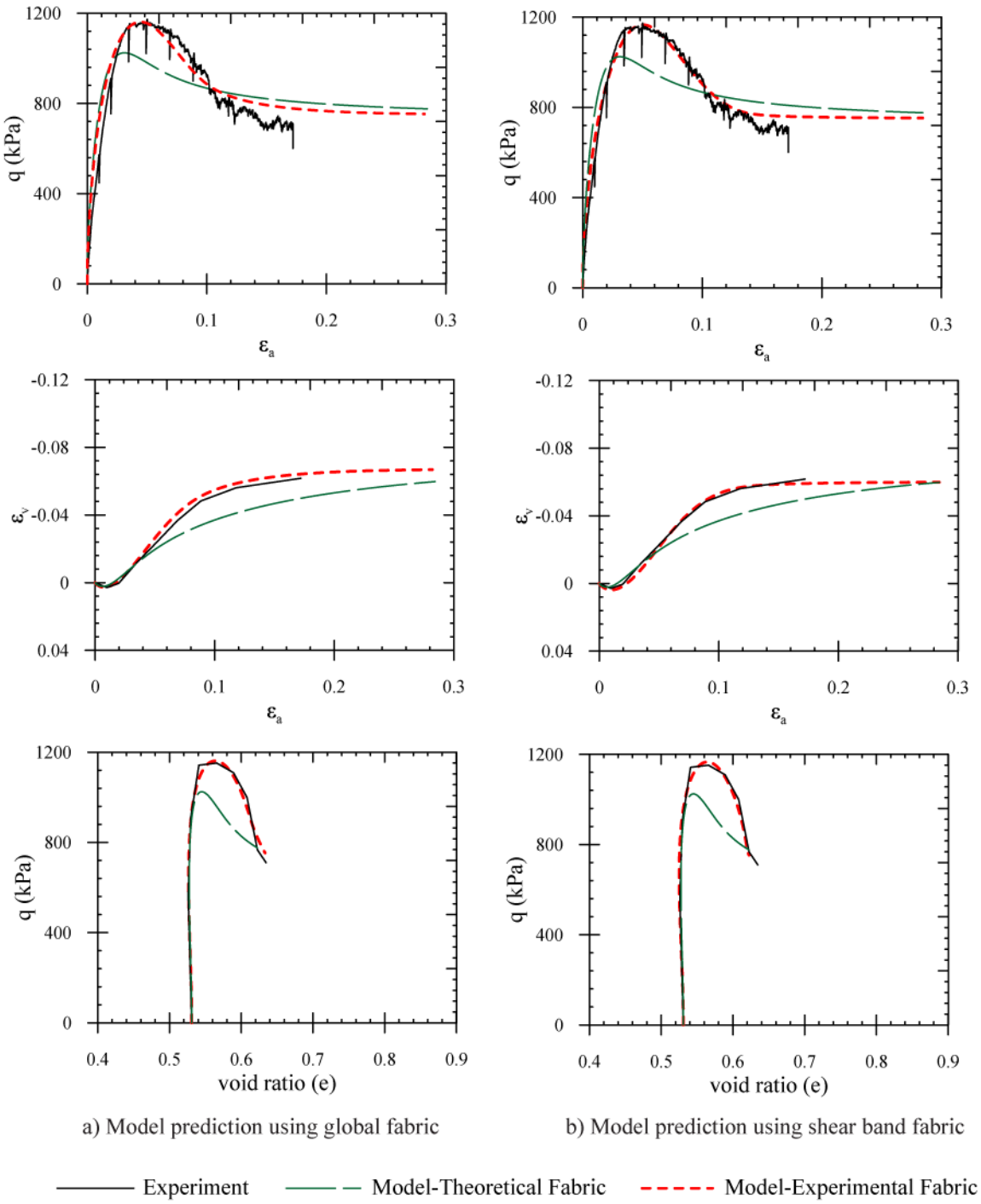

Figure 7.8. Results of ACST model using experimental fabric and theoretical fabric for F35 sand

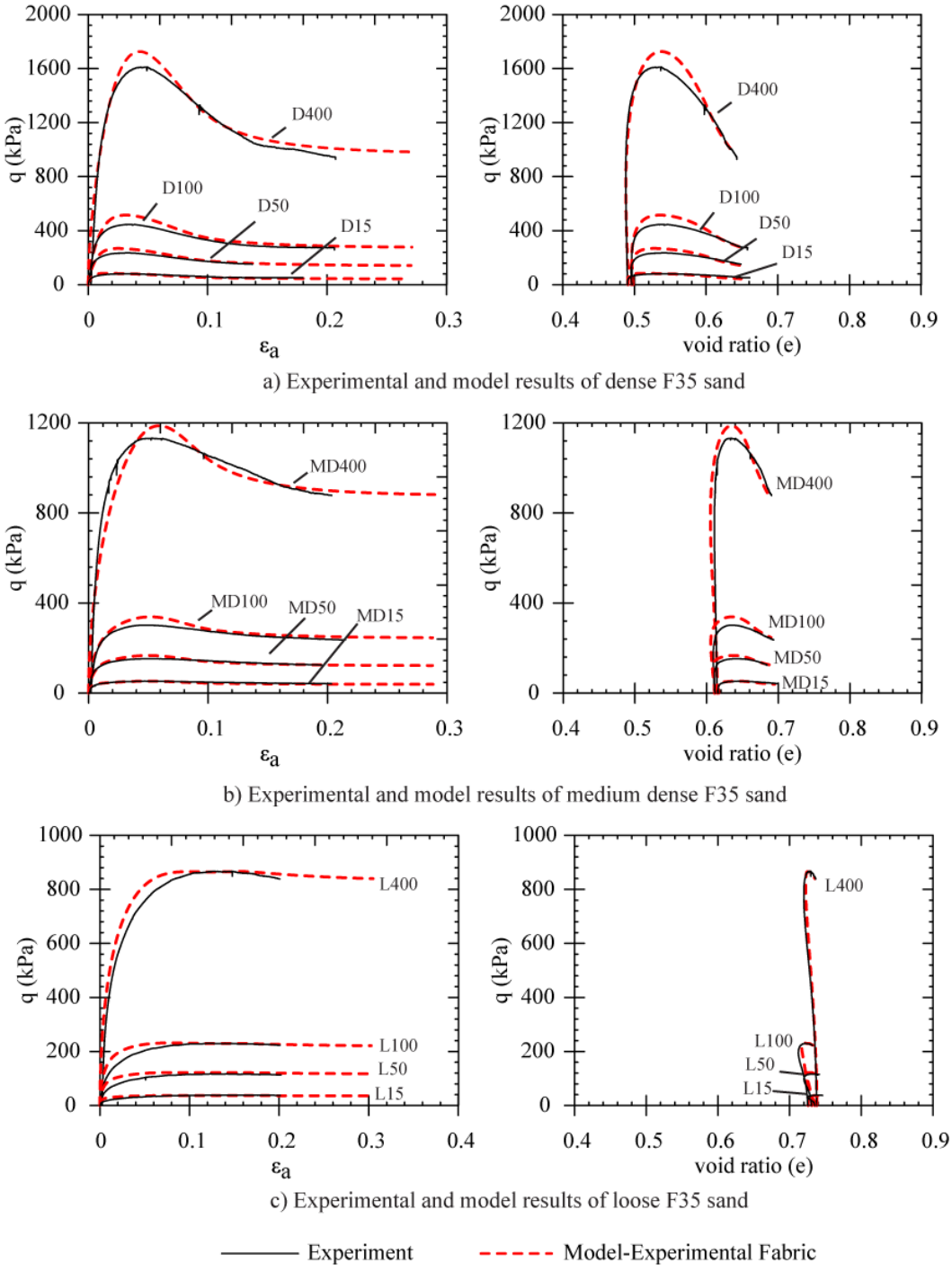

Figure 7.9. ACST Strength and void ratio prediction of F35 sand at various initial mean stress and void ratio using experimentally-estimated fabric evolution

for dense and medium dense cases at p_0' = 100 kPa and p_0' = 400 kPa. This deviation may be attributed to differences in fabric evolution of these experiments compared to experimental fabric determined in Figure 7.3. Currently there are no available in-situ methods to quantify fabric evolution in large scale specimens (without destruction of the specimen).

To test the validity of the model on more spherical granular material, conventional drained triaxial experiments were conducted on glass beads with various initial void ratios and p_0' = 100 kPa (Figure 7.10). Global experimental fabric was implemented into the model, critical state model parameters were obtained using the statistical models presented earlier, and remaining model constants for glass beads from Table 7.4 are used. Model predictions of deviatoric stress versus axial strain and void ratio are also presented in Figure 10. Model predictions are extremely accurate for the dense and medium dense cases (omitting stick-slip responses observed in experiments). Model results are more accurate for spherical material because fabric evolution for glass beads would be relatively consistent due to their spherical nature.

Summary and Conclusion

Anisotropic critical state theory model developed by (Li and Dafalias 2011) was implemented using experimental fabric evolution that was determined from SMT imaging and quantification for F35 Ottawa sand and glass beads. It has been found that global and shear band CNV based fabric (FAV *A*) in conventional drained triaxial experiments peaks during strain hardening (when shear band develops) and reaches

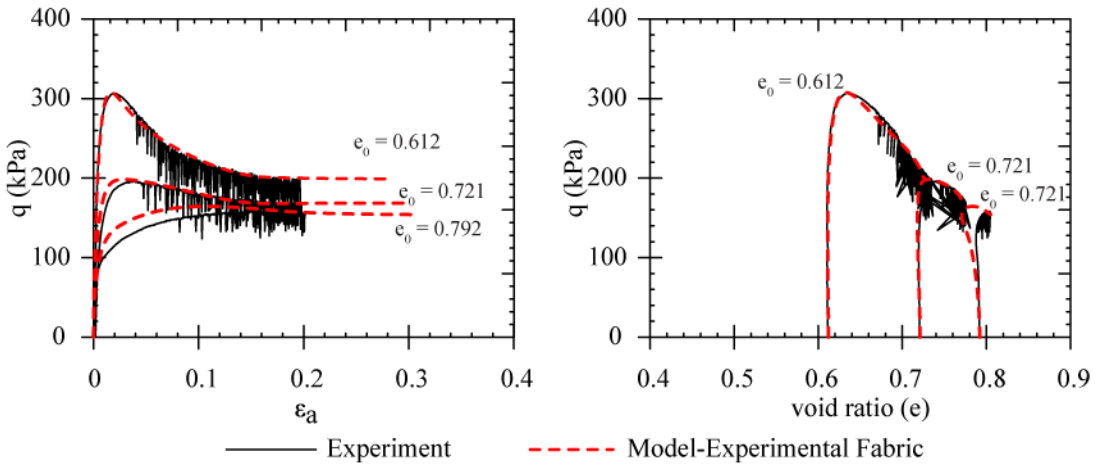

Figure 7.10. ACST Strength and void ratio prediction of glass beads using experimentally-estimated fabric evolution (p_0' = 100 kPa)

steady-state shortly thereafter. Fabric of particles within the shear band peaks and exhibits a decrease during shear band formation before reaching steady-state. Such local intricacies can be captured by two-term Fourier series fits with a limiting strain value for steady state fabric. Experimental fabric was found to evolve quite differently than either theoretical fabric evolution or fabric evolution observed by numerical simulations, where ultimate state was reached at large strains.

Empirical multivariable statistical models were developed to estimate critical state parameters of uniform sands with known average morphology (I_{sph}, I_R) and surface roughness (R_q) for input into the critical state model. The multivariable regressions fit the data very well, suggesting particle level characteristics of morphology and surface roughness, along with relative density and initial mean stress, are respectable input parameters for estimation of critical state parameters during drained triaxial compression on dry granular materials. Using critical state parameters measured from experiments (not estimated from statistical methods) lead to more accurate results (Figure 7.8), but the objective of a predictive model is to estimate behavior of the material at any initial mean stress or density without prior knowledge of the critical state parameters.

Modeling behavior of granular material during drained traixial compression using the anisotropic critical state theory with experimental fabric evolution produces more accurate results than using theoretical or numerical fabric evolution. One triaxial experiment during in-situ SMT imaging is required to quantify fabric evolution and particle morphology and determine model parameters, while critical state parameters can

be determined by statistical means mentioned previously. Using experimental fabric, critical state parameters, and model constant, granular material can be modeled accurately with any initial void ratio and initial mean stress.

References

Alshibli, K., Druckrey, A., Al-Raoush, R., Weiskittel, T., and Lavrik, N. (2014). "Quantifying Morphology of Sands Using 3D Imaging." *Journal of Materials in Civil Engineering*, 04014275.

Been, K., Jefferies, M. G., and Hachey, J. (1991). "The critical state of sands." *Géotechnique*, 41(3), 365-381.

Bolton, M. D. (1986). "The strength and dilatancy of sands." *Geotechnique*, 36, 65-78.

Druckrey, A., and Alshibli, K. (2014). "3D Behavior of Sand Particles Using X-Ray Synchrotron Micro-Tomography." *Geo-Congress 2014 Technical Papers*, 2814-2821.

Druckrey, A. M., Alshibli, K. A., and Al-Raoush, R. I. (2016). "3D characterization of sand particle-to-particle contact and morphology." *Computers and Geotechnics*, 74, 26-35.

Ferreira, P. M. V., and Bica, A. V. D. (2006). "Problems in identifying the effects of structure and critical state in a soil with a transitional behaviour." *Géotechnique*, 56(7), 445-454.

Fonseca, J., O'Sullivan, C., Coop, M. R., and Lee, P. D. (2013). "Quantifying the evolution of soil fabric during shearing using directional parameters." *Géotechnique*, 487-499.

Fu, P., and Dafalias, Y. F. (2015). "Relationship between void- and contact normal-based fabric tensors for 2D idealized granular materials." *International Journal of Solids and Structures*, 63(0), 68-81.

Gens, A., and Potts, D. M. (1988). "Critical state models in computational geomechanics." *Engineering Computations*, 5(3), 178-197.

Hasan, A., and Alshibli, K. (2012). "Three dimensional fabric evolution of sheared sand." *Granular Matter*, 14(4), 469-482.

Kanatani, K.-I. (1984). "Distribution of Directional Data and Fabric Tensors." *Int. J. Engng Sci.*, 22(2), 149-164.

Konrad, J. M. (1990). "Minimum Undrained Strength Versus Steady-State Strength of Sands." *Journal of Geotechnical Engineering*, 116(6), 948-963.

Kuhn, M. R., Sun, W., and Wang, Q. (2015). "Stress-induced anisotropy in granular materials: fabric, stiffness, and permeability." *Acta Geotechnica*, 10(4), 399-419.

Kurtay, T., and Reece, A. R. (1970). "Plasticity theory and critical state soil mechanics." *Journal of Terramechanics*, 7(3), 23-56.

Lam, W.-K., and Tatsuoka, F. (1988). "Effects of initial anisotropic fabric and σ_2 on strength and deformation characteristics of sand." *SOILS AND FOUNDATIONS*, 28(1), 89-106.

Li, B., and Zeng, X. (2014). "Effects of fabric anisotropy on elastic shear modulus of granular soils." *Earthq. Eng. Eng. Vib.*, 13(2), 269-278.

Li, X., and Dafalias, Y. (2011). "Anisotropic Critical State Theory: Role of Fabric." *Journal of Engineering Mechanics*, 138(3), 263-275.

Li, X., and Yu, H.-S. (2009). "Influence of loading direction on the behavior of anisotropic granular materials." *International Journal of Engineering Science*, 47(11–12), 1284-1296.

Li, X., and Yu, H.-S. (2014). "Fabric, force and strength anisotropies in granular materials: a micromechanical insight." *Acta Mech*, 225(8), 2345-2362.

Li, X., Yu, H. S., and Li, X. S. (2009). "Macro–micro relations in granular mechanics." *International Journal of Solids and Structures*, 46(25–26), 4331-4341.

Li, X. S., and Dafalias, Y. F. (2000). "Dilatancy for cohesionless soils." *Géotechnique*, 50(4), 449-460.

Li, X. S., and Dafalias, Y. F. (2002). "Constitutive Modeling of Inherently Anisotropic Sand Behavior." *Journal of Geotechnical and Geoenvironmental Engineering*, 128(10), 868-880.

Li, X. S., and Wang, Y. (1998). "Linear Representation of Steady-State Line for Sand." *Journal of Geotechnical and Geoenvironmental Engineering*, 124(12), 1215-1217.

Moesen, M., Cardoso, L., and Cowin, S. C. (2012). "A symmetry invariant formulation of the relationship between the elasticity tensor and the fabric tensor." *Mechanics of Materials*, 54, 70-83.

Mooney, M. A., Finno, R. J., and Viggiani, M. G. (1998). "A Unique Critical State for Sand?" *Journal of Geotechnical and Geoenvironmental Engineering*, 124(11), 1100-1108.

Nemat-Nasser, S. (2000). "A micromechanically-based constitutive model for frictional deformation of granular materials." *Journal of the Mechanics and Physics of Solids*, 48(6–7), 1541-1563.

Nemat-Nasser, S., and Zhang, J. (2002). "Constitutive relations for cohesionless frictional granular materials." *International Journal of Plasticity*, 18(4), 531-547.

Oda, M. (1972). "INITIAL FABRICS AND THEIR RELATIONS TO MECHANICAL PROPERTIES OF GRANULAR MATERIAL." *Soils and foundations*, 12(1), 17-36.

Oda, M., Nemat-Nasser, S., and Konishi, J. (1985). "STRESS-INDUCED ANISOTROPY IN GRANULAR MASSES." *Soils and Foundations*, 25(3), 85-97.

Oda, M., Takemura, T., and Takahashi, M. (2004). "Microstructure in shear band observed by microfocus X-ray computed tomography." *Géotechnique*, 54(8), 539-542.

Peña, A. A., Herrmann, H. J., and Lind, P. G. (2009). "Force chains in sheared granular media of irregular particles." *AIP Conference Proceedings*, 1145(1), 321-324.

Peters, J. F., Muthuswamy, M., Wibowo, J., and Tordesillas, A. (2005). "Characterization of force chains in granular material." *Physical Review E*, 72(4), 041307.

Riemer, M. F., and Seed, R. B. (1997). "Factors Affecting Apparent Position of Steady-State Line." *Journal of Geotechnical and Geoenvironmental Engineering*, 123(3), 281-288.

Riemer, M. F., Seed, R. B., Nicholson, P. G., and Jong, H. L. (1990). "Steady State Testing of Loose Sands: Limiting Minimum Density." *Journal of Geotechnical Engineering*, 116(2), 332-337.

Roscoe, K. H., Schofield, A. N., and Wroth, C. P. (1958). "On The Yielding of Soils." *Géotechnique*, 8(1), 22-53.

Shipton, B., and Coop, M. R. (2015). "Transitional behaviour in sands with plastic and non-plastic fines." *Soils and Foundations*, 55(1), 1-16.

Theocharis, A., Vairaktaris, E., Fu, P., and Dafalias, Y. F. (2014). "Comparison of fabric tensors for granular materials." *Geomechanics from Micro to Macro*, CRC Press, 153-158.

Tordesillas, A., and Muthuswamy, M. (2009). "On the modeling of confined buckling of force chains." *Journal of the Mechanics and Physics of Solids*, 57(4), 706-727.

Verdugo, R., and Ishihara, K. (1996). "THE STEADY STATE OF SANDY SOILS." *Journal of the Japanese Geotechnical Society : soils and foundation*, 36(2), 81-91.

Wood, D. M. (1991). *Soil Behaviour and Critical State Soil Mechanics*, Cambridge University Press.

Yimsiri, S., and Soga, K. (2001). "Effects of Soil Fabric on Undrained Behavior of Sands." *International Conferences on Recent Advances in Geotechnical Earthquake Engineering and Soil Dynamics*San Diego, CA.

Yimsiri, S., and Soga, K. (2010). "DEM analysis of soil fabric effects on behaviour of sand." *Géotechnique*, 483-495.

CONCLUSIONS AND RECOMMENDATIONS

Summary and Conclusions

In this dissertation, SMT imaging served as the foundation for quantification and analysis of granular material mechanics at micro- and meso-scales. At the micro-scale (single particle level), SMT images were used in fracture analysis of single particles at two loading rates (0.2 mm/min and ~2.5 m/s). 3D FEA was conducted on particles that closely match the real particle morphology to investigate crack onset and propagation as well as fracture stresses. Also, an empirical statistical model that incorporated micro-scale particle properties was developed to predict the fracture loads of particles subjected to unconfined compression at a loading rate of 2.5 m/s. Results from micro-scale fracture analysis can be implemented in up-scaled bulk material models that incorporate individual particle fracture.

At the meso-scale, an extension of particle kinematics, termed particle relative displacement, was developed to examine intricate strain localization during axisymmetric triaxial testing. Strain localization during hardening was observed and progression into softening and critical state was discussed. Also, at the meso-scale, fabric evolution was quantified during axisymmetric triaxial compression, and experimental fabric was implemented into the ACST model that resulted in a better accuracy in strength and behavior predictions. Influence of micro-scale quantifications (particle morphology) on meso-scale behavior was also studied. Micromechanical insight gained from this study

contribute to the overall objective of geotechnical engineering; accurate modeling of complex granular material systems.

The summary of findings of this dissertation are as follows:

1. Quantitative particle characteristics determined from SMT image processing and analyses provides valuable insight into the fabric and failure mechanisms of granular materials. Loading paths of granular material depend on particle shape, orientation, and contact, which are defined by Chapter 1. Results from this analysis can be used in many applications such as tracking particle kinematics at progressive loading, verifying numerical models, or input for force chain models, to name a few. This research provides a first step for future development of accurate micromechanical models that can eventually be used to design many different types of granular systems.
2. New morphology indices are proposed in Chapter 2 to calculate roundness and sphericity of particles using 3D SMT images. They are independent measures that represent two different morphological properties of granular materials. Surface texture was also accurately quantified for granular materials using optical interferometry technique. Particle morphology and surface roughness can be used as inputs into micro-mechanically based constitutive models.
3. The XFEM model was utilized to predict fracture within spheres and real particle shapes. Simulated fracture of the particle was very similar to what was experimentally visualized using the radiograph images of tested sand particles

during compression. Fracture predicted by the model was in the same location as the experimental fracture. With the assumed parameters, XFEM analysis on actual particle produced a load-displacement curve similar to the experimental measurements. Rotation of the particle was captured, along with the elastic response and fracture mode. Finally, shape of sand particles influences their fracture behavior and modeling sand particles using spheres does not give the best match for experimental measurements.

4. The dynamic force required to fracture a particle is highly influenced by particle properties and loading conditions which are affected by particle morphology. Although the effect of individual particle properties does not correlate well with fracture load, multivariable nonlinear regression with all of the predictors discussed in Chapter 4 lead to a fairly accurate statistical model.
5. At loading rate of 2.5 m/s, FEA captured the fracture of individual particles that was similar to experimental fracture, and the experimental loading curve was matched from the simulation with relatively good accuracy. Fracture strength determined from FEA is significantly higher than using the characteristic tensile strength from Equation 4.6, which was developed for quasi-static loading. Current assumed particle tensile strength formulations, such as that in Equation 4.6 or variations thereof, do not account for stress concentrations within a particle. Therefore, actual stresses within a particle at fracture are higher than assumed stresses and FEA determines fracture stresses more accurately.

6. Micro shear bands (MSB) in triaxial experiments can be better analyzed and quantified in 3D using the second order norm of differences in displacement vectors. This technique exposes more intricate strain localizations than conventional particle kinematics approach.
7. All experiments exhibited MSB during strain hardening. In specimens that exhibit a single well defined shear band at failure, persistent MSB that nucleate and mature during the hardening phase merge to form the single shear band. In specimens that exhibit bulging, MSB develop into either a cross-hatched or hourglass pattern that push groups of particles and small lateral MSB outwards in the lateral direction.
8. Particle morphology influences thickness and delineation of MSB. Specimens with less spherical particles have thinner well-defined MSB and critical state shear bands, caused by interlocking of the less spherical particles.
9. Confining pressure influences the thickness and delineation of MSB. MSB that develop during strain hardening are more structured and better defined when the specimen is tested at a high confining pressure.
10. For preparation methods used in this study, particle contact normal vectors have an initial bias towards the horizontal and globally evolve to resist the vertical applied stress. Global fabric (not fabric solely within the shear band) reaches a steady-state shortly after PSR reaches a critical state.

11. Particle sphericity has a major influence on the initial fabric of granular materials and the evolution of fabric. Less spherical materials produce a more anisotropic material and a larger work is required to evolve global fabric to a steady-state during shearing. Also, higher confining pressure forces an initial arrangement of particle contact normal vectors into a more isotropic state.
12. Global fabric evolution, in terms of FAV *A*, is dependent on confining pressure. At 400 kPa confining pressure, fabric evolves to a constant state shortly after peak PSR is reached. At 15 kPa confining pressure, fabric continues to evolve as PSR increases.
13. Fabric of particles within shearing zones evolve much differently than fabric of particles outside of shearing zones. Contacts within the shearing zone orient themselves relatively perpendicular to shear bands (coinciding with columnar structure formation within band), while particles outside of the shear band continually orient towards the vertical loading direction. Global fabric is a combination of the two, which masks interesting localized fabric features.
14. Modeling behavior of granular material during drained triaxial compression using the anisotropic critical state theory with experimental fabric evolution produces more accurate results than using theoretical or numerical fabric evolution. One triaxial experiment during in-situ SMT imaging is required to quantify fabric evolution and particle morphology and determine model parameters, while critical state parameters can be determined by statistical means mentioned previously.

Using experimental fabric, critical state parameters, and model constant, granular material can be modeled accurately with any initial void ratio and initial mean stress.

Limitations and Recommendations

Techniques and methodologies introduced in this dissertation were developed to solve specific problems while being as robust as possible. Many instances occur in which several (or many) techniques were executed for some cases. However certain limitations for each exist and are discussed here. In Chapter 1, physical particle characteristics and contacts were characterized through image processing and an analysis code. The first stipulation for production of accurate results using methodology presented in Chapter 1 is that high resolution images with little noise must be available. Lower resolution or noisy images will cause deviation from expected results. Concurrently, proper image processing techniques must be implemented to discretize particles and contacts. Errors resulting from inaccurate particle or contact characterization would lead to inability to track particle kinematics and quantify accurate fabric. Limitations from Chapter 1 propagate to all other chapters in the dissertation with regard to image processing.

Chapter 2 presented morphology and surface quantification of granular material. Morphology measurements were developed for 3D particles that are generally convex. Particles exhibiting concavity may cause erroneous results. Intricate 3D measures such as surface area are exploited in morphology measurements. Accurate particle quantification is a must for accurate morphology. Limitations also exist for surface roughness

measurements obtained and presented in Chapter 2. Sudden large changes on a particle surface may not be able to be measured by the optical profiler. The vertical limit of the profiler was 10 microns. Spherical convexity of particles is accounted for in surface roughness measurements.

Chapter 3 presented methodology to import real particle shapes into FEA software and simulate fracture. A large limitation of the current dissertation is inability to model flaws smaller than voxel size. Internal flaws on the order of several voxels can be meshed as internal voids in the mesh, but particles were chosen in this dissertation that did not have any visible internal flaws. Also, any slight variance of material properties influences fracture. This dissertation assumes homogeneous linear elastic material, when in actuality the crystalline structure of silica particles is somewhat heterogeneous. Loading silica in one direction may produce very different fracture results than another. Fracture model implemented in FEA will also effect simulations.

Limitations exist in the higher rate loading of particles in Chapter 4 additional to the FEA simulation limitations discussed for Chapter 3. Very little correlation exists between fracture force and any one measured characteristic, while the nonlinear multivariable model represents the data fairly well. Some inputs to the model are qualitative and highly variable (such as internal structure). Results are also limited to one particle sand, even though the sand is highly heterogeneous. Other types of sand particles may not exhibit the same behavior.

Chapter 5 presents relative particle displacement method that exposes intricate zones of strain localization. Accurate particle kinematics is required for this method. Relatively large global loading strains between images somewhat prevents analysis of MSB formation and progression. Henceforth, with the experiments and images presented in Chapter 5, it is difficult to precisely relate localized shearing to global strength and deformation behavior.

Fabric and fabric evolution of several granular materials during triaxial compression was presented in Chapter 6. As discussed in this dissertation, fabric is a generalized micromechanical parameter that groups all contact orientations into a single direction and magnitude (relative to loading direction). More micromechanical insight would be gained if individual contacts are analyzed. Pertaining to VOI fabric, only a small section of the shear band was analyzed. Although representative REV's were used, fabric of the entire shear band may deviate from observed results. Fabric within a VOI below the shear band may vary from the VOI's chosen above the shear band. Also, as observed in Chapter 5, strain localization exists outside the shear band and the VOI groups all intricate localized strains.

Chapter 7 was included in this dissertation to prove the effectiveness of using experimental fabric in a current model. However, many limitations of the model itself inherently exist and will not be discussed. Also, fabric evolution will slightly vary between conventional experiments and experiments during in-situ imaging exist to generalize fabric evolution for a certain material.

The following recommendations are proposed for future research:

1. Incorporating loading rate into the empirical statistical fracture force model presented in Chapter 4. SMT images during quasi-static fracture (similar to Chapter 3) would provide basis for input into the model and better micromechanical assessment of loading rate can be determined (rather than Weibull statistics).
2. A more thorough analysis of fracture stresses within particles at various loading rates. Specifically, incorporation of particle flaws into FEA and determination of their effect on fracture stress/load should be investigated.
3. Incorporation of strain localization during hardening and subsequent evolution into final shear band at critical state into bifurcation models for granular materials. The tools to investigate intricate zones of strain localization presented in this dissertation can be extended to develop/modify constitutive models based on micro-scale observations.
4. Analysis of fabric evolution with various initial fabric, initial density, loading conditions, and stress paths. Methodology presented in this dissertation can be extended to any initial fabric, density, and stress path provided that SMT images are available. Thorough analyses of these conditions are essential for robust input into anisotropic constitutive models.

VITA

Andrew Druckrey was born and raised in northeast Wisconsin. He attended the University of Wisconsin-Milwaukee, where he graduated with his bachelor of science degree in Civil Engineering in May 2010 and master's of science degree in geotechnical/pavement engineering in December 2011. Andrew started his Ph.D. work at the University of Tennessee-Knoxville under the supervision of Dr. Khalid Alshibli in January of 2012. His research interests include x-ray imaging of granular materials, 3D image processing and analysis, finite element analysis, and constitutive modeling of granular material.